Conference Proceedings of the Society for Experimental Mechanics Series

Alfred Wicks · Christopher Niezrecki *Editors*

Structural Health Monitoring, Damage Detection & Mechatronics, Volume 7

Proceedings of the 34th IMAC, A Conference and Exposition on Structural Dynamics 2016

SEM

Springer

Conference Proceedings of the Society for Experimental Mechanics Series

Series Editor

Kristin B. Zimmerman, Ph.D.
Society for Experimental Mechanics
Bethel, CT, USA

More information about this series at http://www.springer.com/series/8922

Alfred Wicks • Christopher Niezrecki
Editors

Structural Health Monitoring, Damage Detection & Mechatronics, Volume 7

Proceedings of the 34th IMAC, A Conference and Exposition on Structural Dynamics 2016

Springer

Editors
Alfred Wicks
Virginia Polytechnic Institute
& State University
Blacksburg, VT, USA

Christopher Niezrecki
Department of Mechanical Engineering
University of Massachusetts Lowell
Lowell, MA, USA

ISSN 2191-5644 ISSN 2191-5652 (electronic)
Conference Proceedings of the Society for Experimental Mechanics Series
ISBN 978-3-319-29955-6 ISBN 978-3-319-29956-3 (eBook)
DOI 10.1007/978-3-319-29956-3

Library of Congress Control Number: 2016941055

Printed on acid-free paper

This Springer imprint is published by Springer Nature
The registered company is Springer International Publishing AG Switzerland

Preface

Structural Health Monitoring, Damage Detection & Mechatronics represent one of ten volumes of technical papers presented at the 34th IMAC, A Conference and Exposition on Structural Dynamics, organized by the Society for Experimental Mechanics and held in Orlando, Florida, January 25–28, 2016. The full proceedings also include volumes on nonlinear dynamics; dynamics of civil structures; model validation and uncertainty quantification; dynamics of coupled structures; sensors and instrumentation; special topics in structural dynamics; rotating machinery, hybrid test methods, vibro-acoustics and laser vibrometry; and shock and vibration, aircraft/aerospace, energy harvesting, acoustics and optics, and topics in modal analysis and testing.

Each collection presents early findings from experimental and computational investigations on an important area within structural dynamics. *Structural Health Monitoring, Damage Detection & Mechatronics* are a few of these areas.

The organizers would like to thank the authors, presenters, session organizers, and session chairs for their participation in this track.

Blacksburg, VT, USA — Alfred Wicks
Lowell, MA, USA — Christopher Niezrecki

Contents

Chapter 1
Development and Characterization of an ITO Nanocomposite Film Sensor for Damage Detection

Breno Ebinuma Takiuti, Vicente Lopes Júnior, Michael J. Brennan, Walter Katsumi Sakamoto, José Antônio Malmonge, and Marcelo Ornaghi Orlandi

Abstract In order to secure the structural integrity of aeronautic structures, several structural health monitoring techniques have been studied throughout history. One of the most recent technologies developed involves the use of continuous sensors, made of thin films of nanocomposite material. Previous works proved that the ITO/PMMA nanocomposite sensor (ITO—indium tin oxide) nanobelts inserted in a matrix of PMMA (poly(methyl methacrylate)) was capable of detecting a certain damage by comparing the values of resistances between two points before and after the damage occurrence, however some uncertainties were found. Two problems were found during the development of the sensors: first of them was the difficulty to obtain uniformity of the coating material through its monitored area and; the second one was the influence of environmental changes on the measurements. The uniformity problem was solved by enhancing the nanocomposite synthetizing method, which resulted in more constant readings of resistances, although there were still variations on measurements taken on different days. To verify the cause of this oscillation, several tests were performed in an environmental chamber, in which the temperature and the humidity were controlled during the measurements, making it possible to find out which parameter would cause more changes on the readings.

Keywords Structural health monitoring • Nanocomposite • Continuous sensors • Neural network • ITO

1.1 Introduction

It is common knowledge in mechanical engineering that different materials can be combined in order to create an enhanced material, with properties specifically tailored for each application. Some examples of commonly found composite materials are carbon fiber, fiberglass and steel reinforced concrete.

With recent developments in the nanotechnology field, several nanomaterials have been studied, and with this knowledge nanocomposites have been developed. It allows the production of even more sophisticated and multifunctional materials. The main characteristic of a nanocomposite material is that the matrix material is a standard material, such as polymer, and the filler material consists of nanostructures or nanomaterials. This enables the composite material to have some of the properties of the filler, but with the addition of a considerably small amount of filler [1]. With this, the degradation in the mechanical properties caused by the filler is minimal, so the matrix is capable of maintaining its structural properties resulting in a better composite material.

Several papers describe the use of CNT (Carbon Nanotubes) nanocomposites for damage detection applications. In [2] the use of nanocomposite film made of a PMMA matrix and CNT fillers was proposed to detect surface damage through resistance monitoring. The use of a nanocomposite film sensor made of an epoxy matrix and CNT fillers to monitor the growth of a crack was studied by [3], and the creation of a net of CNT nanocomposite film ribbons to detect and locate the damage was proposed by [4].

B.E. Takiuti (✉) • V.L. Júnior • M.J. Brennan
Univ Estadual Paulista – UNESP, Department of Mechanical Engineering, CEP 15385-000, Ilha Solteira, SP, Brazil
e-mail: takiuti.breno@gmail.com

W.K. Sakamoto • J.A. Malmonge
Univ Estadual Paulista – UNESP, Department of Physics and Chemistry, CEP 15385-000, Ilha Solteira, SP, Brazil

M.O. Orlandi
Univ Estadual Paulista – UNESP, Department of Physical Chemistry, CEP 14801-970, Araraquara, SP, Brazil

A. Wicks, C. Niezrecki (eds.), *Structural Health Monitoring, Damage Detection & Mechatronics, Volume 7*,
Conference Proceedings of the Society for Experimental Mechanics Series, DOI 10.1007/978-3-319-29956-3_1

This work presents advances obtained after the paper published previously [5]. At that time the film sensor presented several flaws, such as uneven distribution of resistances throughout the coated area, lack of transparency and different ranges of resistances at each created film (no repeatability). The method presented this time was designed to overcome such deficiencies which would reflect in a much more efficient sensor, capable of detecting and locating the damage in a much more accurate manner.

1.2 Surface Damage Detecting Film Nanocomposite

Previous works [5], focused in proving that the proposed nanocomposite film sensor could be used for surface damage detection. Aside from a few flaws, it was proven that the sensor was effective in detecting damage. Afterward, the focus of the project was to try to improve the sensor and its synthesis process to overcome these problems. The first step to achieve this was to find the source of these deficiencies. By analyzing the process of the sensor synthesis, it was found that it is needed to strictly define all the synthesis's steps meticulously, so that every time the result would be the same. The main point was to define the exact proportion of solvent mixed with the ITO that would be poured over the PMMA layer. Since the amount of solvent is directly proportional to the time it would react with the polymer and allow the penetration of ITO. It was essential to define the exact conditions for this process, in order to obtain a predefined thickness of layer. With this, it was possible to obtain consistency in the synthesis of the nanocomposite. Figure 1.1 shows some examples of coated aluminum plates.

ITO nanostructures were synthetized by a carbothermal reduction method using the co-evaporation of oxides [6]. The starting materials were SnO_2 (Sigma-Aldrich, 99.9 % of purity) and In_2O_3 (Sigma-Aldrich, 99.99 % of purity) each of which was mixed in a molar portion of 1:1 with carbon black (Union Carbide, >99 % of purity) and placed side by side in a tube furnace (EDG, model FT-HI 40) with a N_2 gas flux to carry the vapors to the colder region of the tube [6, 7].

The ITO/PMMA mass proportion was fixed as 10 wt%, so that the sensor would have acceptable damage sensitivity, since the amount of ITO reflects directly to the sensor's conductivity.

Simply by looking at the obtained sensors, it can be noted that the coated area is far more uniform and transparent compared to the plates presented in [5].

1.3 Experimental Setup

As described in previous works, the method to detect the damage is based on the change on the measured resistances, as the damage would obstruct the travel of the current, therefore increasing the resistance. These resistances are formed by the alignment of the ITO nanobelts, forming paths as shown in Fig. 1.2. If the number of ITO nanobelts is too low (Fig. 1.2a) the probability for a conductive path to be formed between two given points are too low, making it inviable. On the other hand, if the number of nanobelts is too high (Fig. 1.2c) there would be too much paths formed between that given points and in this case if a damage severe one of the paths, there would still be many other paths to allow the conduction, therefore this is not acceptable either. Finally if the mass of ITO is just above the percolation threshold, the probability for the path to be

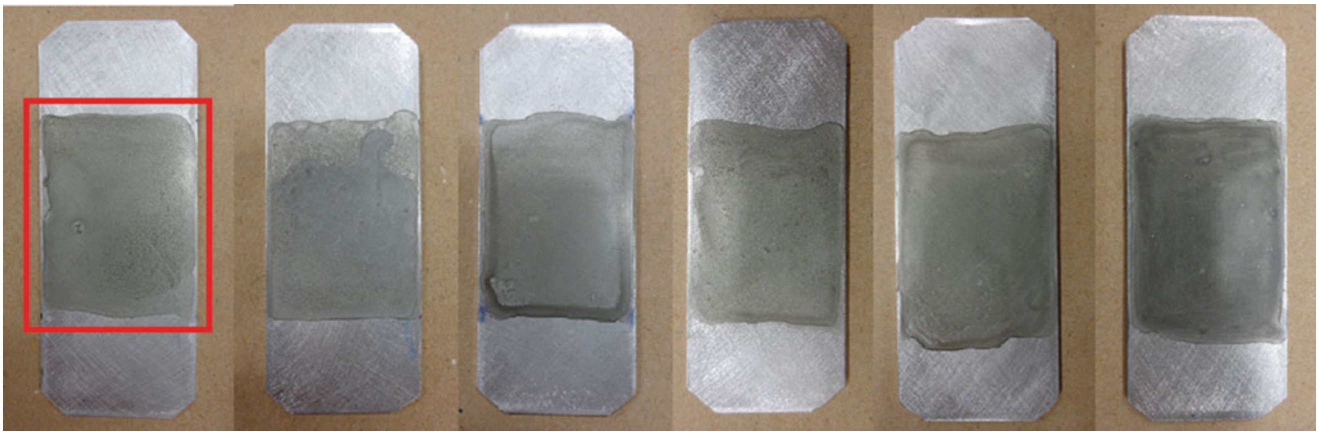

Fig. 1.1 Six coated aluminum plates obtained after the establishment of the coating method. The *red rectangle* shows the coated area

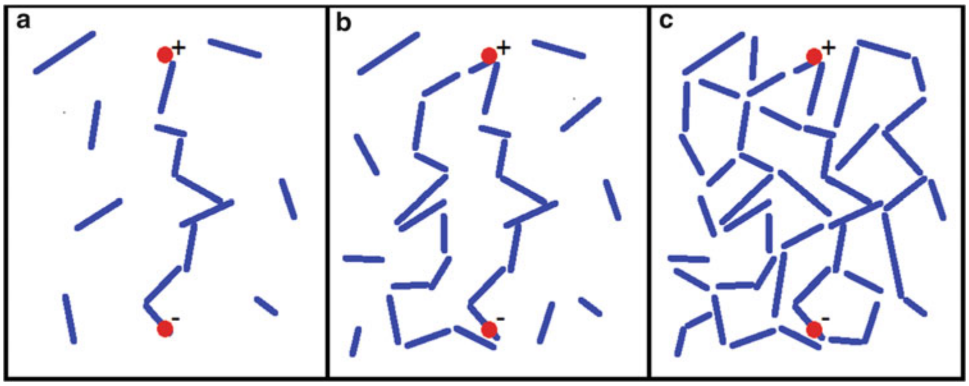

Fig. 1.2 Resistive paths formed by different amounts of ITO in PMMA. In (**a**) the amount of ITO per mass of PMMA is too low, in (**b**) the amount of ITO is just above the percolation limit and in (**c**) there is too much ITO, making it saturated

Fig. 1.3 Plate used for the tests

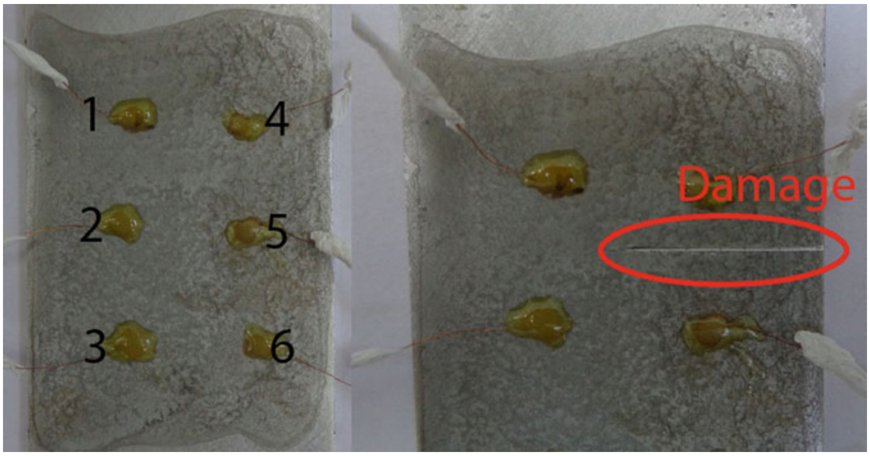

formed is fairly good and if a damage appears it would cause an detectable change in the measured resistance. The damage location method is based on Yun et al. (2005), in which a network of damage sensitive paths are established throughout the monitored area, and an specific set of steps are followed in order to pinpoint the location of the damage.

In order to take the resistance measurements, six copper wires were soldered over the nanocomposite (Fig. 1.3). The terminals were numbered from 1 to 6 and the measurements were taken by combining them in all possible ways, except for the reciprocals and the paths formed by the combination of two other paths. The measured paths were r12, r14, r15, r16, r23, r25, r26, r36, r42, r43, r45, r53 and r56 where the first number is the terminal number connected to the positive cable of the measurement instrument and the second one is the terminal number connected to the negative cable. With this configuration of terminals, it is possible to create a grid of measured paths, which can be used to detect the damage in several positions and by analyzing all of them; it is possible to find the location of the damage.

Since the resistance measurements had to be logged, a Keithley 236 SMU was used with a LabView® interface. For the humidity tests, the resistances were measured with the coated plate within an environmental chamber, where the temperature was kept constant and equal to 25 °C and the humidity varied from 20 to 100 % with 10 % intervals, and for the temperature tests, the humidity was fixed at 70 % and the temperatures varied from 10 to 50 °C with 10 °C intervals.

1.4 Results and Discussions

1.4.1 Surface Damage Detection

Since the main objective was to evaluate the damage detection and location capabilities of the sensor, all the resistive paths were measured at a fixed temperature and humidity (30 °C and 70 %) to establish a baseline (undamaged) value of resistance for each path. Following these measurements, damage, in a form of a razor cut between terminals 4 and 5, was created at the

Table 1.1 Resistance measurements before and after the damage

	Baseline (Ω)	Damaged (Ω)	Difference (%)
r12	3572	5087	42
r14	5148	5748	12
r15	4563	6169	35
r16	7087	8921	26
r23	1899	2213	17
r25	3023	3278	8
r26	5597	6182	10
r36	5299	5879	11
r42	5223	6909	32
r43	5199	6730	29
r45	5784	7796	35
r53	3239	3523	9
r56	6106	5910	−3

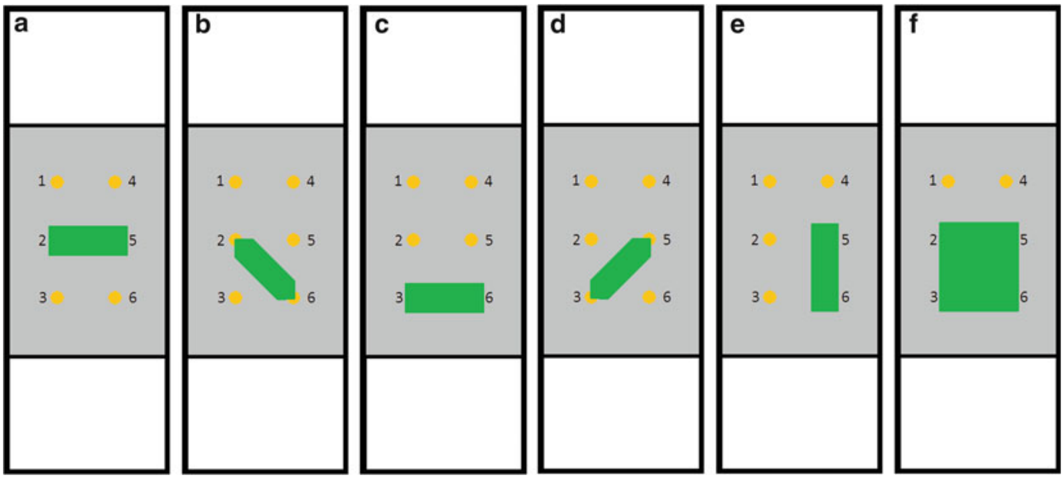

Fig. 1.4 Undamaged area analysis. The *green polygons* represents the undamaged paths

sensor as seen in Fig. 1.3. This cut was created so that it would damage the sensor and the plate. The variation of the resistances are shown in Table 1.1.

One of the problems found in previous works was the lack of transparency and an uncertainty to the resultant resistances. By looking at Fig. 1.3 it can be noted that the film has a clearer coloring and a much transparent look, and by evaluating Table 1.1 it can be noted that the resistances ranges from 1 to 8 kΩ, which indicates that the proportion of ITO per PMMA is just above the percolation threshold, therefore the sensor should provide a good sensitivity to the damage. It is clear that the sensor is useful for detecting the damage, since mostly all the resistances presented increasing resistances after the damage.

On the other hand, since the beginning of this research, damage location have been a challenge. In general, all paths tend to present some level of increase in their resistances. That happens because even though the path between each number is expected to be a straight line, generally it does not occur. Even after the improvements of the sensor, this scenario will only be achieved when the ITO are perfectly distributed and randomly oriented nanobelts. The outcome of this is that there are too much paths with increasing resistances, making it difficult to establish a pattern for the damage location.

One simple way to overcome this flaw is simply to evaluate the undamaged paths instead of the damaged paths. If a localized damage creates a generalized increase in the resistances, them a path with low changes are surely undamaged. In other words, the undamaged path takes precedence over damaged paths. By analyzing each undamaged areas and isolating them, the remaining region would have the damage. Figure 1.4 shows this analysis.

Looking at Fig. 1.4f it is clear that the damaged area was isolated by this method. Another observation to be taken is the fact that the sensor is not capable of locating damages smaller than one quadrant (a square of four terminals), but this is not a problem since the size of this quadrant can be modified for each case.

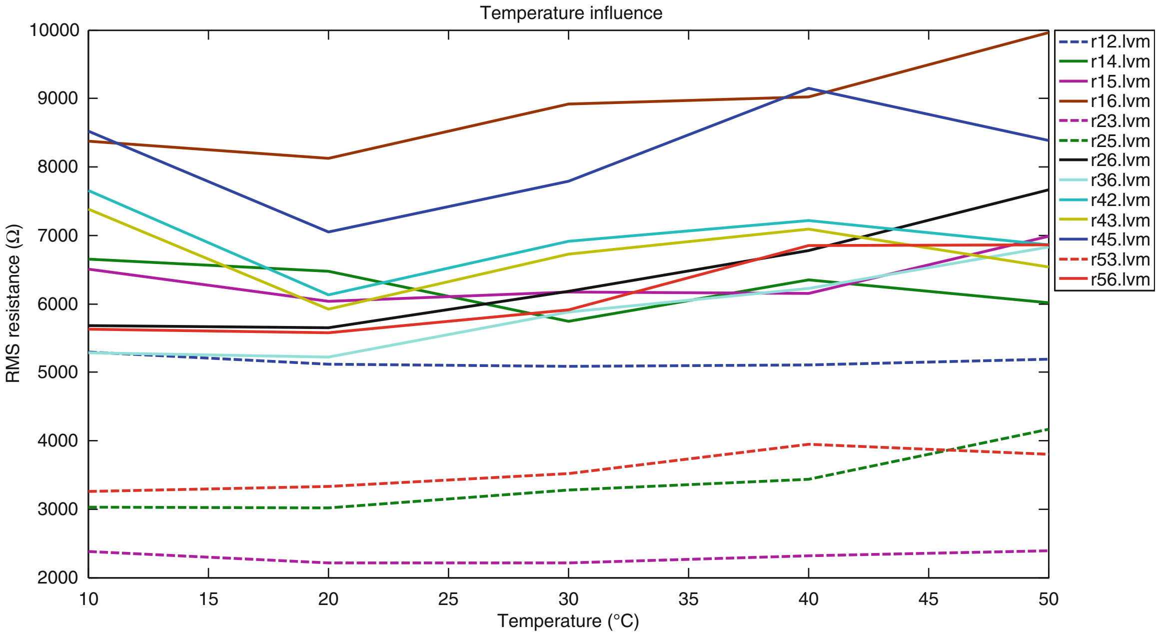

Fig. 1.5 RMS resistances variations with temperature of all paths

1.4.2 *Influence of the Temperature*

Initially it was proposed that three factors could influence the resistance measurements: temperature, humidity and strain to the aluminum plate. The first and second influences are evaluated in this work. Figure 1.5 shows the variation of the resistances with the increase of the temperature. It can be noted that the resistances tend to slightly increase with the temperature, but this increase is only perceptible if analyzed for larger differences of temperatures. If the change caused by increasing 10 °C is compared to the change caused by the damage, it can be concluded that the damage causes much more alteration, therefore the influence of the temperature can considered negligible.

1.4.3 *Influence of the Humidity*

Analyzing the results from the humidity variation (Fig. 1.6), it could be noted that the resistances slightly increased from 20 to 80 % of relative humidity. After 80 %, the resistances tend to decrease, getting to the lowest value at 100 %. This decrease can be caused by the formation of water drops over the surfaces at high humidity.

The experiment proved that the humidity could cause a little more influence to the resistances, especially at values higher than 80 %. Although it was clear that both parameters might cause variations at the resistances readings, it was found that the damage causes a much greater alteration than the environmental parameters.

1.5 Conclusion

Evaluating the results attained it can be concluded that the ITO/PMMA thin film nanocomposite damage sensor was successful at detecting the damage, while still maintaining some transparency. Although it still requires some fine-tuning, the method was able to identify the damage location, by evaluating all the altered and unaltered resistance measurements.

Although it was proven that the sensor works as an interconnected network in which a single damage could affect several measurements, this in fact contributed to the damage detection, which is the first and most important phase of the damage detection process. On the other hand this characteristic undermined the damage location capability by indicating more than

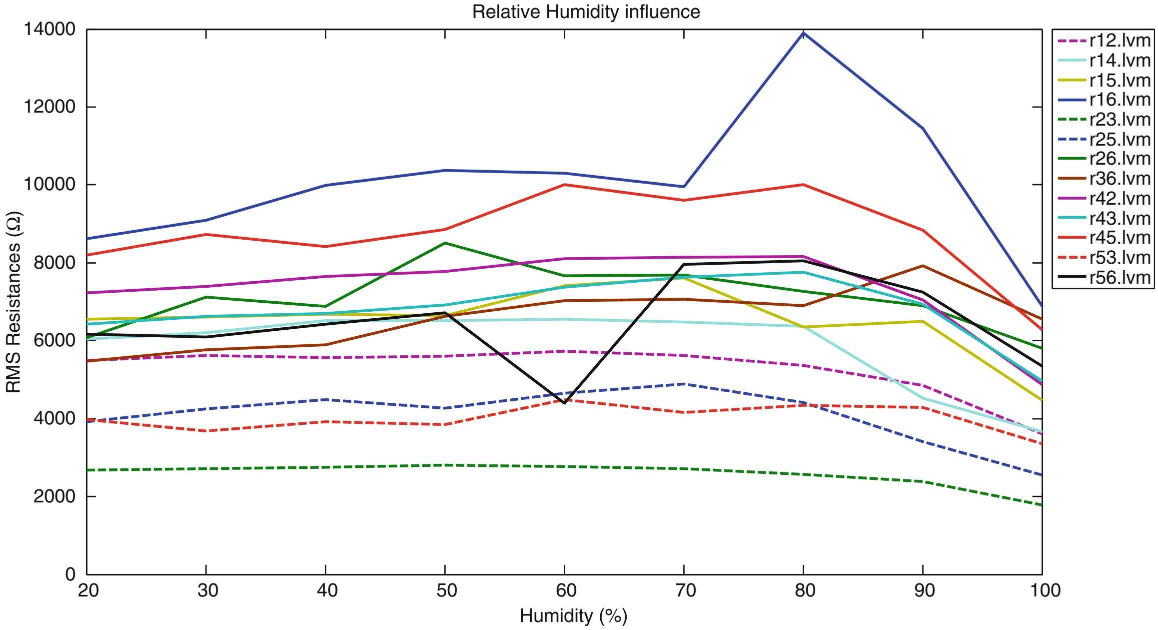

Fig. 1.6 RMS resistances variations with relative humidity of all paths

one possible area with the damage. This drawback can be solved by restricting the possible damaged area through the analysis of the paths with low resistance variations. Another solution would be to enhance the film production method, in order to create uniform films, with equal resistances in each path. This would make it easy to analyze the data and consequently yield more precise damage location results.

Regarding the humidity and temperature influence, it was found that influence of these parameters are low, although in the case of humidity it was concluded that the sensor is sensitive to water contact. This could be easily solved by applying a protective layer over the film sensor, avoiding the contact of the nanowires with any kind of humidity. Although each of these parameters varying separately may not cause much influence in the measurements, if both are changed, it may cause significant variations on the resistances, but still, it would be smaller than the change caused by the damage, so that these parameters can be neglected, although the contact with liquid water should be avoided.

This kind of damage detection method has proven to be promising, opening several research possibilities. The next steps for this line of study would be to enhance the sensor's damage location capabilities, to apply this sensor in a larger area (which is a challenge in most of nanocomposite practical application cases) and to find an easy practical way to produce and apply this film to any kind of surface.

Acknowledgements The authors would like to thank the FAPESP (Process number: 2012/25153-1) for its financial support and the CNPq and FAPEMIG for partially funding the present work through the INCT-EIE.

References

1. Winey, K.I., VAIA, R.A.: Polymer nanocomposites. MRS Bull. **32**(04), 314–322 (2007)
2. Kang, I., Heung, Y.Y., Kim, J.H., Lee, J.W., Gollapudi, R., Subramaniam, S., Narasimhadevara, S., Hurd, D., Kirikera, G.R., Shanov, V., Schulz, M.J., Shi, D., Boerio, J., Mall, S., Ruggles-Wren, M.: Introduction to carbon nanotube and nanofiber smart materials. Composites Part B **37**(6), 382–394 (2006)
3. Ashrafi, B., Johnson, L., Martinez-Rubi, Y., Martinez, M., Mrad, N.: Single-walled carbon nanotube–modified epoxy thin films for continuous crack monitoring of metallic structures. Struct. Health Monit. Lond. **11**(5), 589–601 (2012)
4. Yun, Y.-H., Kang, I., Gollapudi, R., Lee, J. W., Hurd, D., Shanov, V. N., Schulz, M. J., Kim, J., Shi, D., Boerio, J. F., Subramaniam, S.: Multifunctional carbon nanofiber/nanotube smart materials. In: Proceedings of the Smart Structures and Materials 2005: Smart Electronics, MEMS, BioMEMS, and Nanotechnology. SPIE, San Diego (2005)
5. Takiuti, B.E., Lopes Júnior, V., Brennan, M.J., Arlindo, E.P.S., Orlandi, M.O.: Damage detection and quantification using thin film of ITO nanocomposites. In: Structural Health Monitoring, Volume 5: Proceedings of the 32nd IMAC, A Conference and Exposition on Structural Dynamics, 2014. Structural Health Monitoring, Springer International Publishing. 5(23), 207–213 (2014)

6. Orlandi, M.O., Aguiar, R., Lanfredi, A.J.C., Longo, E., Varela, J.A., Leite, E.R.: Tin-doped indium oxide nanobelts grown by carbothermal reduction method. Appl. Phys. A (Washington) **80**(1), 23–25 (2005)
7. Arlindo, E.P.S., Lucindo, J.A., Bastos, C.M.O., Emmel, P.D., Orlandi, M.O.: Electrical and optical properties of conductive and transparent ITO@PMMA nanocomposites. J. Phys. Chem. C (Washington) **116**(23), 12946–12952 (2012)

Chapter 2
Fiber Optic Sensor Arrays for Real-Time Virtual Instrumentation and Control of Flexible Structures

Hector Gutierrez, Behzad Shariati Javani, Daniel Kirk, Weihua Su, Michael Wolf, and Edwin Griffin

Abstract Launch vehicles and aerospace structures trend towards slender and more lightweight designs to reduce mass and aerodynamic drag. Slender structures are more affected by structural vibrations that interfere with both inertial sensing and navigation performance. Slender aerospace structures (launch vehicles, aircraft, and others) would greatly benefit from means for real-time monitoring of the flexible dynamics: real time modal sensing, as well as estimation of acceleration and rate of rotation at any point in the structure. This paper proposes the use of fiber-Bragg (FBG) sensor arrays for real-time monitoring and control of a flexible subscale test article representative of a launch vehicle. A virtual sensor for estimating acceleration and rate of rotation at any point in the structure is presented: the FBG Inertial Measurement Unit. The FBG-IMU is a real-time estimator based on a finite element model of the structure, the state-space equations of the flexible dynamics, and a finite number of strain measurements provided by the FBG array. The FBG-IMU allows accurate estimation of the states of the flexible structure with no need of estimation of load forces or damping matrix, as current structural models of flexible structures are forced to assume. The FBG-IMU is a contribution to the real-time estimation of the flexible dynamics in structures without the need of estimating loads or damping.

Keywords Fiber optic strain gage • Real-time modal analysis • Structural dynamics • Real-time estimation and control of flexible structures

2.1 Introduction

Next generation launch vehicles will trend towards slender and more lightweight designs. This natural trend has been limited due to the associated increase in flexible effects on the structure. Undesired vibrations affect structural health and also degrade control performance, in particular since the Inertial Measurement Unit (IMU) onboard the launch vehicle is affected by both the flexible dynamics as well as the rigid body motion, and feeds both signals into the control loop. Another important challenge in launch vehicle simulation and control is given by the time-varying mass and inertia of the vehicle, and the corresponding changes in modal frequencies and modal shapes of the structure as propellant is exhausted. To stabilize the trajectory of a rocket while considering its flexible dynamics, the estimation of displacement, rate of rotation and acceleration at any point on launch vehicle is of great value for both mission planning and controller design [1].

Fiber Optic Bragg Grating (FBG) sensor arrays are lightweight, insensitive to EM noise, and can be embedded in large numbers in a single fiber with no additional penalty in weight or complexity. Large numbers of FBG sensors can be multiplexed at the speed of light at the interrogator, enabling the potential use of FBG sensor arrays to develop systems which can accurately predict the dynamic characteristics of the structure in real time. This can be coupled with various control systems techniques for real time estimation and vibration control in launch vehicles.

Until recently, the use of FBG sensor systems was limited to semi-static measurements of strain in multiple points of a structure due to the fact that optical interrogation equipment had limited bandwidth (typically below 10 Hz) and used output buffers that further delayed the availability of updated readings. Recently, fiber optic sensor array interrogation systems with

---

H. Gutierrez (✉) • B.S. Javani • D. Kirk
Department of Mechanical and Aerospace Engineering and Department of Electrical and Computer Engineering,
Florida Institute of Technology, Melbourne, FL 32905, USA
e-mail: hgutier@fit.edu

W. Su
Department of Aerospace Engineering and Mechanics, The University of Alabama, Tuscaloosa, AL 35487, USA

M. Wolf • E. Griffin
NASA Kennedy Space Center, Launch Services Program, Washington, DC 20546, USA

A. Wicks, C. Niezrecki (eds.), *Structural Health Monitoring, Damage Detection & Mechatronics, Volume 7*,
Conference Proceedings of the Society for Experimental Mechanics Series, DOI 10.1007/978-3-319-29956-3_2

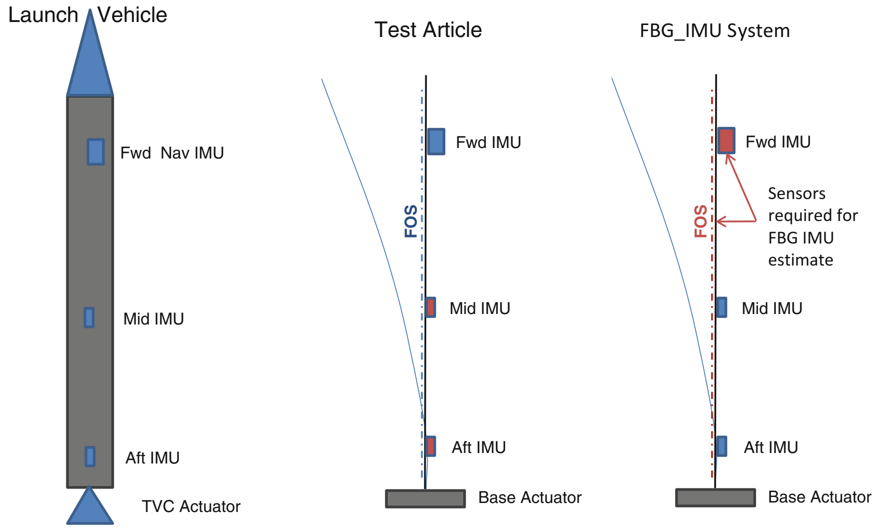

Fig. 2.1 FBG-IMU system vs. standard launch vehicle body bending configuration

capabilities in excess of 1000 Hz have become available. Such systems, combined with the fact that multiplexed interrogation of optical gratings occurs at the speed of light, provides a potential breakthrough in dynamic monitoring of large structures: the strain at hundreds of points within a structure can now be monitored almost simultaneously at high sampling rates. Fiber optic sensor technology with high interrogation rate and unbuffered output therefore has the potential to provide real-time estimation of flexible dynamics. This, combined with distributed auxiliary actuators and advanced control algorithms opens the path for the real time control of the flexible dynamics of future aerospace structures [2].

A typical standard launch vehicle body-bending sensor configuration consists of three ring laser gyros (RLG). The primary objective of this paper is to propose two novel approaches for the estimation of acceleration and rate of rotation at any point in the structure based on a FBG strain sensor array plus a forward placed IMU, compared to the standard launch vehicle body bending sensor configuration shown in Fig. 2.1.

The proposed algorithms enable prediction of deflection, rate of rotation and acceleration of any point in the flexible structure relative to the rigid body frame, and are based on modal matrices $\{[M], [k], [\Phi], [\Theta]\}$ that are calculated using only a finite element model of the structure. The estimation is based on direct measurements of strain in multiple points in the structure, which allows accurate estimation of the states of the flexible structure with no need of estimation of load forces or a damping matrix, or no need to assume that the damping is linear and viscous, as current structural models of flexible structures are forced to assume (Fig. 2.2).

2.2 Approach

To validate the proposed algorithms on a setup with only one degree of freedom, the flexible launch vehicle is first simplified to a clamped-free uniform flexible cantilever beam that only deflects transversely. A linear motor air-bearing stage is used to introduce vibrations as base motion, as shown in Fig. 2.3. Although cantilever beam equations predict the bending shape of the cantilever beam correctly, these simplified mathematical equations fall short when additional components are added to the bare beam, such as thrusters, the wiring harness and the sensor arrays. ANSYS finite element analysis software was used to create a more accurate model of the test article that can be transferred to and implemented in MATLAB/Simulink to develop a state-space model of the structure.

2.3 Finite Element Analysis

The goal of developing a finite element analysis of the test article is to define the damping, stiffness and mass matrices that can be used to create a benchmark model of the structure that can be used for comparison, namely:

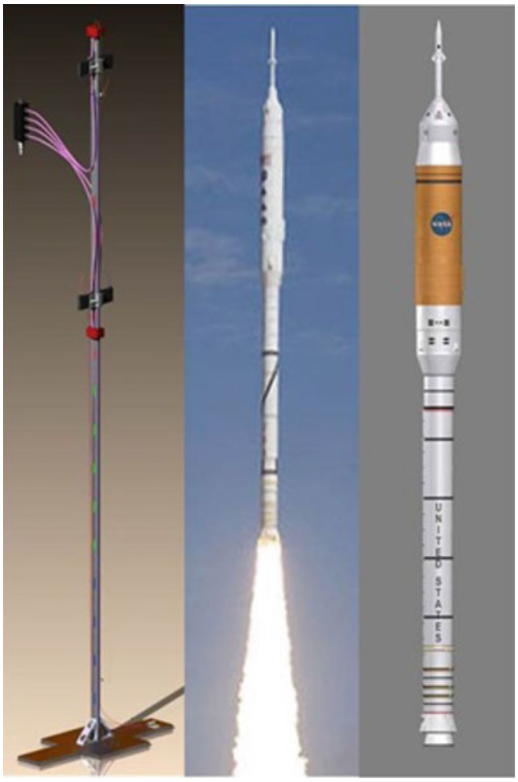

Fig. 2.2 Test article design analogous to slender flexible launch vehicle

$$[\mathrm{M}]\{\ddot{\mathrm{x}}\} + [\mathrm{C}]\{\dot{\mathrm{x}}\} + [\mathrm{K}]\{\mathrm{x}\} = 0 \tag{2.1}$$

$$[\mathrm{I}]\{\ddot{\theta}\} + [\mathrm{C}]\{\dot{\theta}\} + [\mathrm{K}]\{\theta\} = 0 \tag{2.2}$$

Where $[M]$, $[C]$, $[K]$, $[I]$ are the mass, damping, stiffness and rotational inertia matrices and $[x]$, $[\theta]$ are the translational and rotational degrees of freedom respectively. Dimensions of the test article were chosen based on the first three weak natural frequencies. The structural model reflects the integrated test article including every component, such as gas thrusters, FBG sensors, IMUs, plumbing and wiring harness. The mass of all items installed on the beam was considered in the FEM model, and the ANSYS model was designed such that each FBG sensor is collocated with a FEM node as shown in Fig. 2.4.

Although the proposed models in this paper do not require estimation of damping, this was done as part of the benchmark state-space model of the test article. Damping measurements were done using the half power method to estimate damping ratio at each natural frequency. The damping ratio for each modal frequency is estimated as shown in Eq. (2.3):

$$\zeta = \frac{f_2 - f_1}{2f_{res}} \tag{2.3}$$

Where f_{res} is the corresponding resonant peak and f_1, f_2 are the frequencies corresponding to the peak amplitude divided by the square root of two. According to Raleigh damping theory, the damping matrix $[C]$ can be calculated based on two coefficients $\{\alpha, \beta\}$ that are calculated using a two-equation with two-unknown system based on the first two natural frequencies of a the test article as shown in Eq. (2.4).

$$\zeta = \frac{1}{2}\left(\frac{\alpha}{\omega_r} + \beta\omega_r\right) \Rightarrow [C] = \alpha[M] + \beta[K] \tag{2.4}$$

After $\{\alpha, \beta\}$ are updated in the ANSYS model, the C matrix can be extracted from ANSYS to provide the set of beam model matrices {M (mass), K (stiffness), C (damping)}. The beam model matrices were verified in the frequency domain by comparing against the measured frequency response function (FRF) as shown in Fig. 2.5. The experimental FRF was measured by using input base motion with band limited noise displacement (PRBS), 0.01–30 Hz, and displacement, rate of rotation and acceleration output at node 69/80.

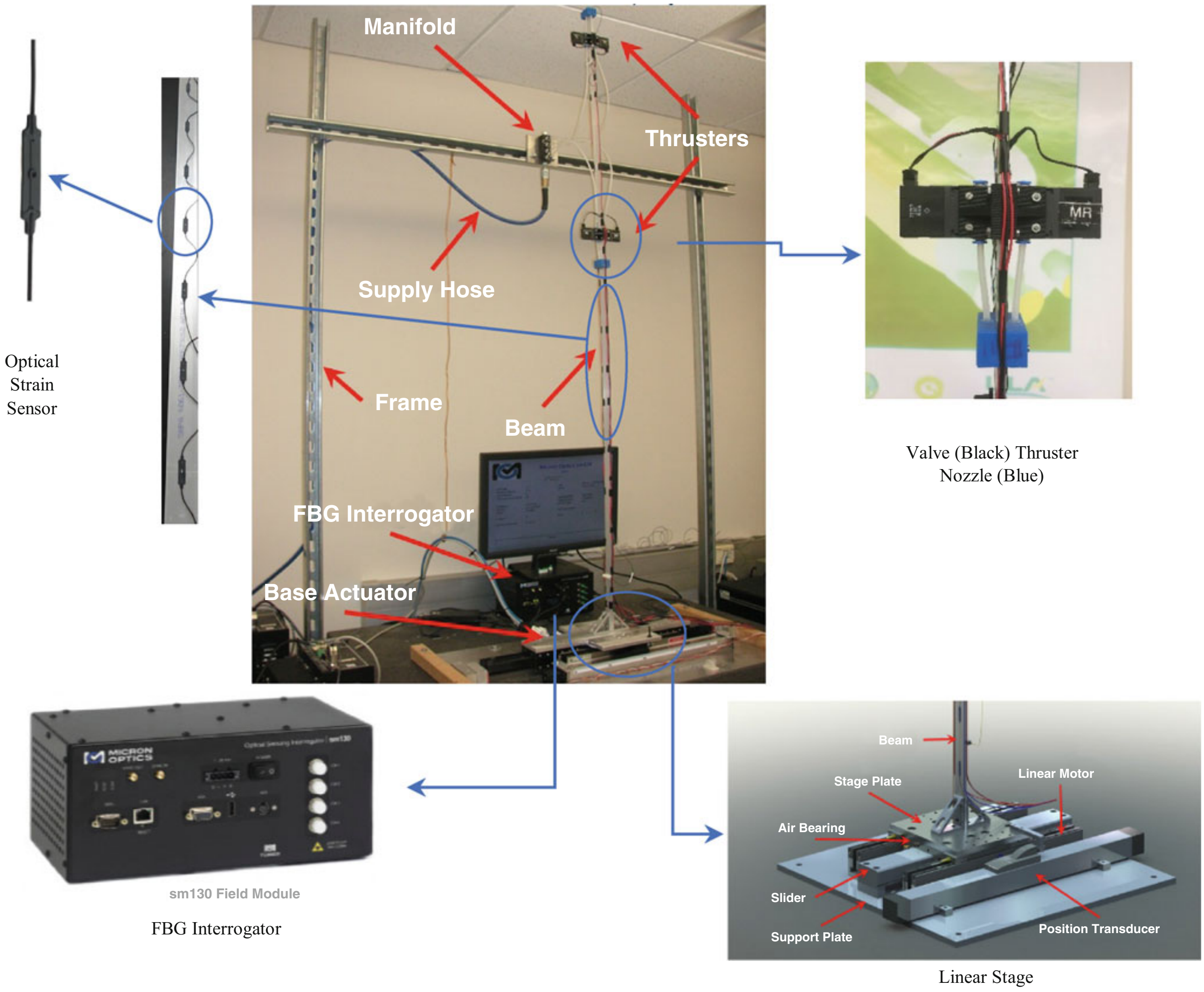

Fig. 2.3 Full test article setup

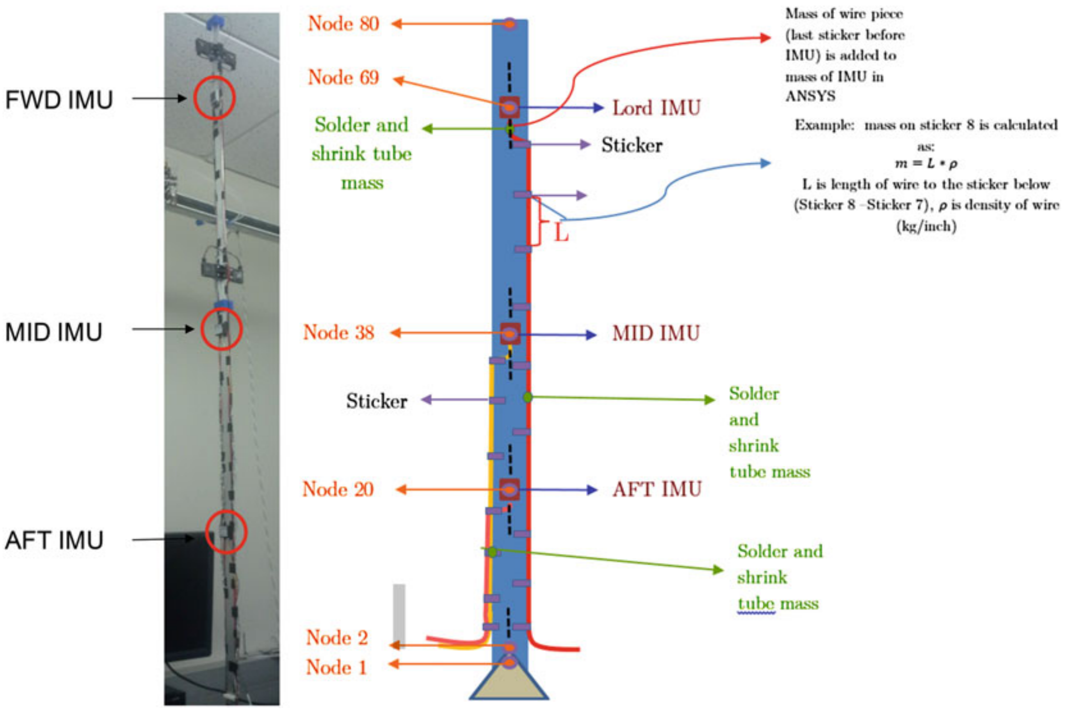

Fig. 2.4 Test article assembly and FEM node location on test article

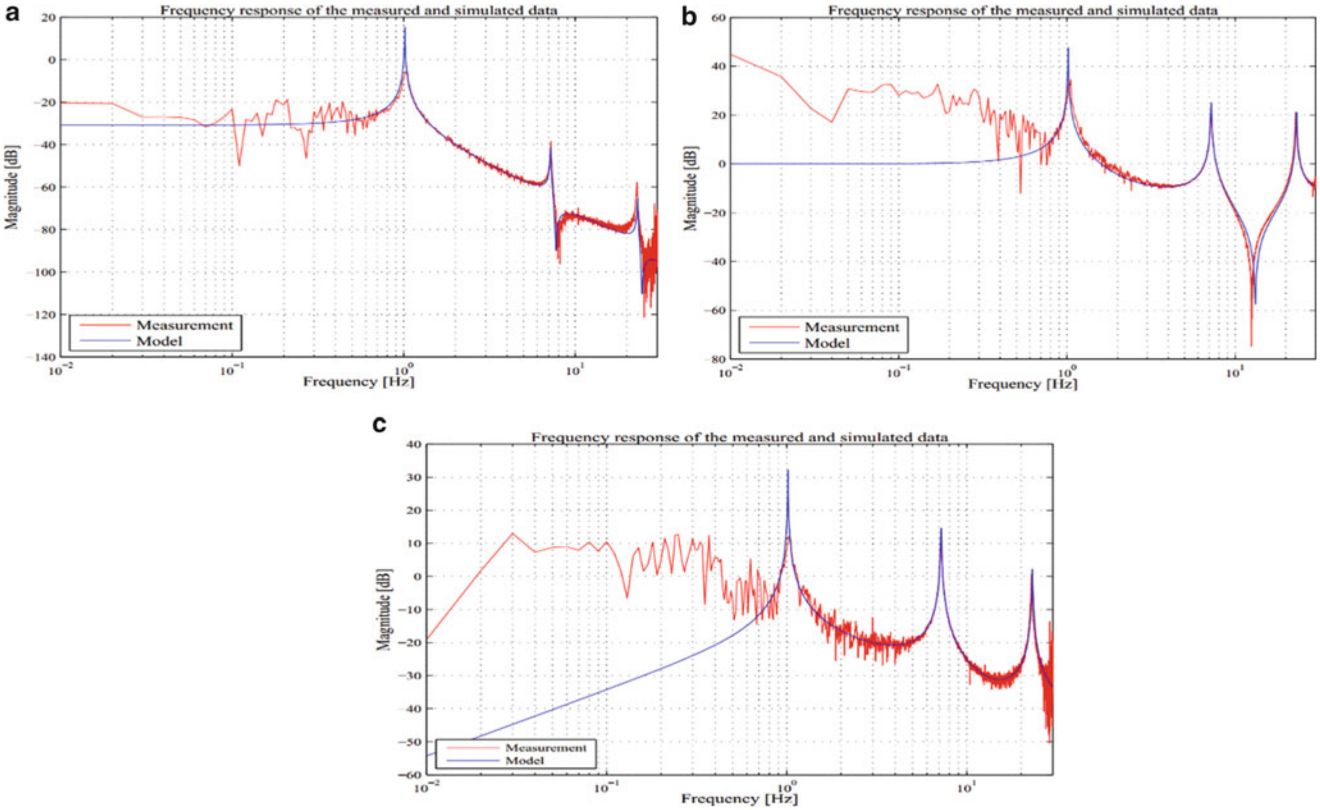

Fig. 2.5 Measured vs. predicted FRF, input base motion to output (**a**) deflection (**b**) rate of rotation (**c**) acceleration for node 69

2.4 Model Formulation

Two different novel modeling algorithm are discussed for developing FBG-IMU. Both take inputs from the FBG array and forward IMU time-domain data along with the launch vehicle's FEM (Finite Element Method) structural model and desired location(s) on launch vehicle, and output the estimated IMU data (Rate of rotation, acceleration) and deflection at any desired locations within the structure. While mode-shapes in the first method are calculated using $[M]$ and $[K]$ matrices the from finite element analysis of the test article, in the second method the mode-shapes are estimated by the use of Legendre polynomials.

2.5 FBG-IMU System Development (First Approach)

Consider a linear structure subject to a point force f, and a structural excitation given by a single axis base acceleration $\ddot{z}_{base}$ shown in Fig. 2.6. The system may be considered as placed on a fictitious shaking table excited by an (unknown) reaction force f_0 . Hamilton's principle shown in Eq. (2.5) states that the variational indicator vanishes for arbitrary virtual variations of the path between two instants t_1 and t_2 compatible with the kinematics, and such that the configuration is fixed at t_1 and t_2

$$\int_{t1}^{t2} (\delta L + \delta W_{nc})dt = \int_{t1}^{t2} [\delta(T - V) + \delta W_{nc}]dt = 0 \tag{2.5}$$

In (Eq. (2.5)) T is the kinetic energy, V the strain energy and δW_{nc} is the virtual work associated with the non-conservative forces (the external force f and the support reaction f_0 in this case). One can decomposes the global displacements Z (generalized displacements including translational as well as rotational degrees of freedom) into the rigid body mode and the flexible motion relative to the base as shown in Eq. (2.6).

Fig. 2.6 Flexible structure with sensor at point P, input force ***f*** and base acceleration $\ddot{z}_{base}$

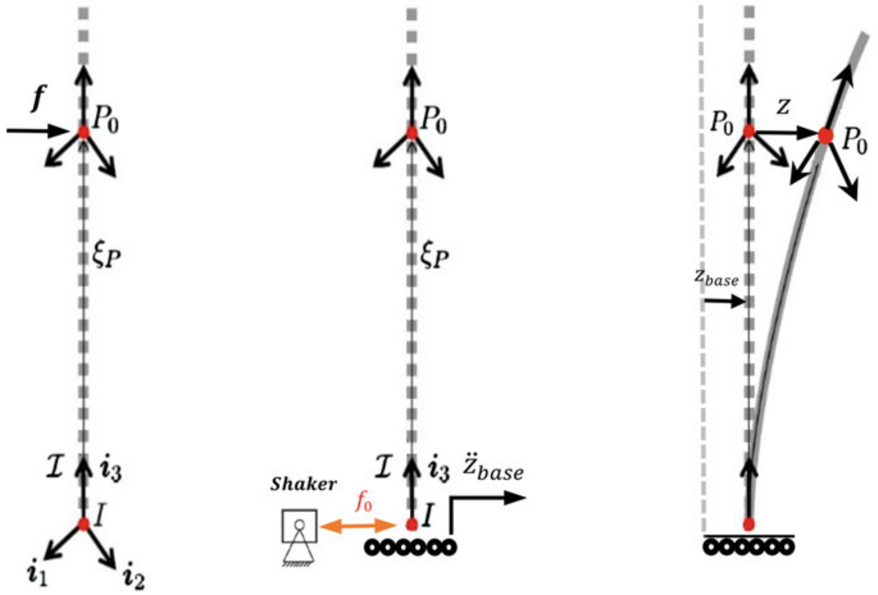

$$Z = 1z_0 + z \tag{2.6}$$

Where z_0 is the support motion, 1 is the unit rigid body mode (all translational d.o.f. along the axis of excitation are equal to 1 and the rotational d.o.f. are equal to 0). The virtual displacements satisfy Eq. (2.7).

$$\delta Z = 1\delta z_0 + \delta z \tag{2.7}$$

Where δz_0 is arbitrary and δz satisfies the clamped boundary conditions at the base. Let b be the influence vector of the external loading f (for a point force, b contains all 0 except 1 at the d.o.f. where the load is applied), so that $b^T Z$ is the generalized displacement of the d.o.f. where f is applied. The various energy terms involved in Hamilton's principle are:

$$T = \frac{1}{2}\dot{Z}^T M\dot{Z} \tag{2.8}$$

$$T = \frac{1}{2}z^T Mz \tag{2.9}$$

$$\delta W_{nc} = f_0\delta z_0 + fb^T\delta Z = \left(f_0 + fb^T\right)\delta z_0 + fb^T\delta z \tag{2.10}$$

One notices that the kinetic energy depends on the absolute velocity while the strain energy depends on the flexible motion alone that is the motion relative to the base. For a point force, $b^T 1 = 1$. Substituting into the variational indicator, one finds:

$$\int_{t1}^{t2}\left[\dot{Z}^T M\delta\dot{Z} - z^T K\delta z + \left(f_0 + fb^T\right)\delta z_0 + + fb^T\delta z\right]dt = 0 \tag{2.11}$$

And upon integrating the first term of Eq. (2.11) By parts and taking into account that $\delta Z(t_1) = \delta Z(t_1) = 0$, for arbitrary δx_0 and δy. It follows that:

$$M\ddot{Z} + Kz = bf \tag{2.12}$$

$$f_0 = 1^T M\ddot{Z} - f \tag{2.13}$$

The presence of *f* in the right side of this equation is necessary to achieve static equilibrium; it is often ignored in the formulation. Combining Eqs. (2.12) and (2.13), one can compute the classical equation expressed in rigid body coordinate frame:

$$M\ddot{z} + C\dot{z} + Ky = -M1\ddot{Z} + bf \tag{2.14}$$

$$f_0 = -1^T(Kz + C\dot{z}) \tag{2.15}$$

From now on, we will assume $f = 0$ to focus on the response to the support acceleration. Now let $\omega_1, \ldots, \omega_n$ and $\phi_z = (\varphi_{1z}, \varphi_{2z}, \ldots, \varphi_{nz})$ be natural frequencies and mode shapes of the structure, from mode superposition theory one can have:

$$\vec{z} = \phi_z \vec{q} \tag{2.16}$$

Equation (2.16) performs a change of variables from physical coordinates z (relative to rigid body frame) to modal coordinates q. Taking second derivative of Eq. (2.16) with respect to time results in [3]:

$$\ddot{\vec{z}} = \phi_z \ddot{\vec{q}} \tag{2.17}$$

$$\dot{\vec{q}} = \dot{\vec{q}} \tag{2.18}$$

To consider the relationship between strain, deflection and motion relative to the inertial frame, consider first the case of pure bending on the vertical plane. Notice that accelerometer readings, which are relative to the inertial frame but expressed on the flexible body frame (FBF), include rigid body rotation, rotation due to bending, and gravity. FBG sensors measure the motion of individual points in the structure relative to the rigid body frame (RBF). The FBG acceleration (second derivative of deflection at point P) is therefore the acceleration of P relative to the RBF. The vector of displacements in the RBF is calculated from the vector of strain measurements by the strain to deflection conversion [] which is shown in Eq. (2.19). One can rewrite Eqs. (2.17) and (2.18) in a state-space form, this is shown in Eqs. (2.20) and (2.21). $[C_{out}]$ and $[D_{out}]$ in Eq. (2.21) can be chosen differently depending on the desired output. one important point to notice is that as mentioned earlier The FEM model of the modified test article has 80 nodes and 79 mass elements. Since each element has 6 degrees of freedom, the mass $[M]$, stiffness $[K]$ and all d.o.f mode shape matrix $[\Phi]$ are 474 × 474 matrices. $[\Phi]$ matrix includes three deflection mode shape matrices : $[\phi_x]_{79\times 79}$, $[\phi_y]_{79\times 79}$ and $[\phi_z]_{79\times 79}$ and three rotation mode shape matrices: $[\theta_x]_{79\times 79}$, $[\theta_y]_{79\times 79}$ and $[\theta_z]_{79\times 79}$. The deflection and rotation mode shape matrix $[\phi_z]_{79\times 79}$ and $[\theta_y]_{79\times 79}$ are extracted from the 474 × 474 ANSYS modal matrix and are used in the both first and second FBG-IMU system modeling approaches (Fig. 2.7).

$$\vec{z}_{N_s\times 1} = \gamma[\phi_z]_{N_s\times N_m}\left([\Psi_z]^T_{N_m\times N_s}[\Psi_z]_{N_s\times N_M}\right)^{-1}[\Psi_z]^T_{N_m\times N_s}\,\vec{\in}_{N_s\times 1} \tag{2.19}$$

$$\begin{bmatrix} \dot{\vec{q}}_{N_m\times 1} \\ \ddot{\vec{q}}_{N_m\times 1} \end{bmatrix} = \begin{bmatrix} 0_{N_m\times N_m} & I_{N_m\times N_m} \\ 0_{N_m\times N_m} & 0_{N_m\times N_m} \end{bmatrix} \begin{bmatrix} \vec{q}_{N_m\times 1} \\ \dot{\vec{q}}_{N_m\times 1} \end{bmatrix} + \begin{bmatrix} 0_{N_m\times N_s} \\ \left(\phi_z^T\phi_z\right)^{-1}\phi_z^T N_m \times N_s \end{bmatrix} \left[\ddot{\vec{z}}_{N_s\times 1}\right] \tag{2.20}$$

$$y_{out} = [C_{out}] \begin{bmatrix} \dot{\vec{q}}_{N_m\times 1} \\ \ddot{\vec{q}}_{N_m\times 1} \end{bmatrix} + [D_{out}]\left[\ddot{\vec{z}}_{N_s\times 1}\right] \tag{2.21}$$

$$y_{out} \rightarrow Deflection \rightarrow [C_{out}] = \left[\phi_z\left(\zeta_p\right)_{1\times N_m} \quad 0_{1\times N_m}\right] \tag{2.22}$$

$$y_{out} \rightarrow rate\ of\ rotation \rightarrow [C_{out}] = \left[0_{1\times N_m} \quad \theta_y\left(\zeta_p\right)_{1\times N_m}\right] \tag{2.23}$$

$$y_{out} \rightarrow acceleration \rightarrow [C_{out}] = [0_{1\times 2N_m}],\ [D_{out}] = \left[\phi_z\left(\zeta_p\right)\phi_z^{+} 1 \times N_s\right] \tag{2.24}$$

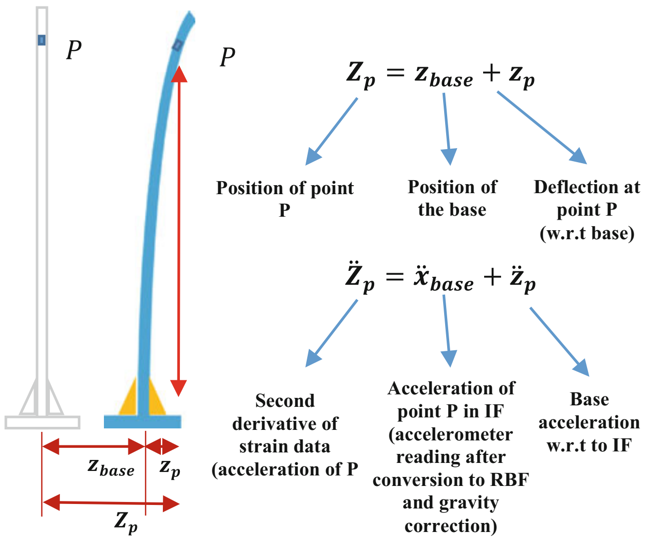

Fig. 2.7 Relationship between deflection and motion relative to the inertial frame

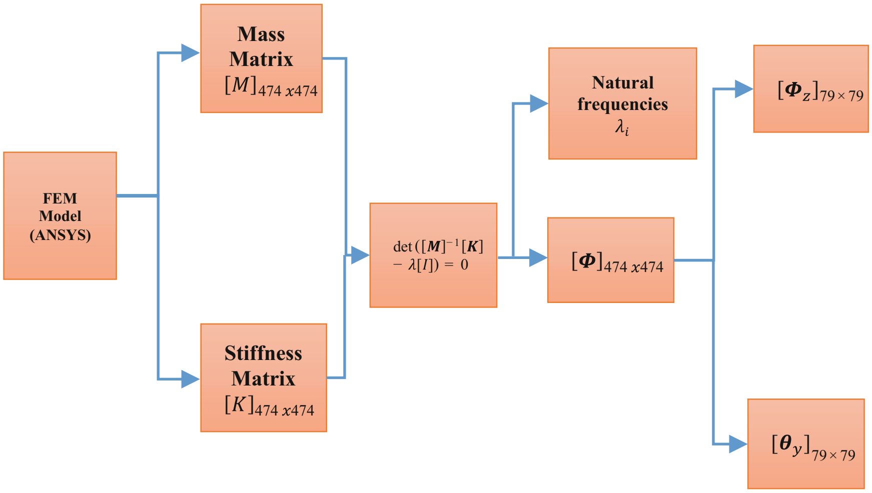

Fig. 2.8 Extraction of mode shape matrices from the ANSYS FEM Model

$[\phi_z]$ and $[\Psi_z]$ are matrix of deflection mode shape along z axis and matrix of strain mode shape both evaluated at N_s FBG sensor locations and for N_m number of modes; γ is a constant factor to convert strain from the beam's neutral axis to the beam's surface respectively. $\vec{z}_{N_s\times1}$ and $\vec{\in}_{N_s\times1}$ are vectors of deflection and strain at N_s FBG sensor locations along the beam. $\begin{bmatrix}\vec{q}_{N_m\times1}\\ \dot{\vec{q}}_{N_m\times1}\end{bmatrix}$ in Eq. (2.20) is a column vector of modal amplitudes and velocities and is the state vector of the state-space model. $\phi_z(\zeta_p)$ and $\theta_z(\zeta_p)$ In Eqs. (2.23) and (2.24) are row vectors generated by polynomial interpolation from N_m mode shapes at the desired output location (coordinate ζ along the beam) where one is interested to compute deflection, rate of ration or acceleration at that point. The displacement mode shape matrix in z bending plane $[\phi_z]$, and the rotation mode shape matrix in the axis perpendicular to the bending plane $[\theta_y]$ are 79×79 matrices and are extracted from the all D.O.F. mode shape matrix Φ computed by ANSYS. An outline of the extraction of model and modal matrices from the ANSYS FEM model is shown in Fig. 2.8.

2.6 Second Approach of FBG-IMU

The finite element (FE) model of the Euler-Bernoulli beam modeling is well established. The discrete FE equation of motion is:

$$[M]\ddot{\vec{u}} + [K]\{\vec{u}\} = \vec{Q} \tag{2.25}$$

Each node has a displacement (w_z) and a rotation (θ_y) degree of freedom, i.e.

$$\{u_i\} = \{w_{zi} \;\; \theta_{yi}\}^T \tag{2.26}$$

One of the major benefits of using a finite element is that the finite element method is compatible with both uniform and non-uniform beams. The finite element solution gives the nodal displacements w and rotations θ. The strain due to bending is given by Eq. (2.27).

$$\epsilon_x(x,t) = y_0 \frac{\partial^2 w_z(x,t)}{\partial x^2} \tag{2.27}$$

Where y_0 is the distance from the beam reference line to the location of the Fiber Optic Strain Sensor (FBG). The linear acceleration in lateral direction is given by Eq. (2.28):

$$a_z(x,t) = \ddot{w}_z(x,t) = \frac{\partial^2 w_z(x,t)}{\partial t^2} \tag{2.28}$$

The angular velocity can be derived from the rotation, i.e.

$$\omega_y(x,t) = \dot{\theta}_y(x,t) = \frac{\partial \theta_y(x,t)}{\partial t} \tag{2.29}$$

Since integration of Eq. (2.25) is not possible due to the unknown excitations $\vec{Q}$, a modal-based solution approach will be applied, i.e. the deformation of the beam is described as a linear combination of the mode shapes

$$w_z(x,t) = \sum_{i=1}^{\infty} \varphi_{iz}(x)\, q_i(t) \tag{2.30}$$

x is the normalized position along the beam, i.e. $x \in [0,1]$, which is a necessary condition for using the Legendre polynomials to estimate mode shapes. To approximate the solution the mode shapes are truncated by only selecting the N_m natural modes, i.e.

$$w_z(x,t) = \sum_{i=1}^{\infty} \varphi_{iz}(x)\, q_i(t) = \begin{bmatrix} \vdots & \vdots & \dots & \vdots \\ \varphi_{1z}(x) & \varphi_{2z}(x) & \dots & \varphi_{zN_m}(x) \\ \vdots & \vdots & \dots & \vdots \end{bmatrix} \begin{bmatrix} q_1(t) \\ q_2(t) \\ \vdots \\ q_{N_m}(t) \end{bmatrix} = \phi_z(x)\vec{q}(t) \tag{2.31}$$

Where $\varphi_{iz}(x)$ are the mode shapes of the beam evaluated at the normalized positions along the beam, $q_i(t)$ are the magnitudes of the corresponding modal deflection, N_n denotes the number of nodes in FEM model and $\phi_z \in \mathbb{R}^{N_n \times N_m}$ and $q \in \mathbb{R}^{N_n \times 1}$. The approximation of the strain is given by:

$$\vec{\epsilon}_x(x,t) = y_0 \sum_{i=1}^{\infty} \frac{\partial^2 \varphi_{iz}(x)}{\partial x^2} \vec{q}_i(t) = y_0 \frac{\partial}{\partial x^2} \begin{bmatrix} \vdots & \vdots & \dots & \vdots \\ \varphi_{1z}(x) & \varphi_{2z}(x) & \dots & \varphi_{zN_m}(x) \\ \vdots & \vdots & \dots & \vdots \end{bmatrix} \begin{bmatrix} q_1(t) \\ q_2(t) \\ \vdots \\ q_{N_m}(t) \end{bmatrix} = y_0 \frac{\partial^2 \phi_z(x)}{\partial x^2} \vec{q}(t) \tag{2.32}$$

Where $\vec{\epsilon}_x(x,t) \in \mathbb{R}^{N_n \times 1}$. The linear acceleration in the lateral direction z is obtained by

$$a_z(x,t) = \sum_{i=1}^{\infty} \varphi_{iz}(x)\, \ddot{q}_i(t) = \sum_{i=1}^{\infty} -\omega_i^2\, \varphi_{iz}(x)\, q_i(t) \tag{2.33}$$

In order to calculate the second spatial derivative of each mode $\frac{\partial^2 \phi_z(x)}{\partial x^2}$ as required in Eq. (2.32), an analytical expression for each mode is required. These expressions are found using the shifted Legendre polynomials, a set of complete and orthogonal polynomials which take input in the domain [0 1] and maps the output to the domain $[-1 \;\; 1]$. The general equations for the Legendre polynomial are given as

$$P_0(x) = 1 \tag{2.34}$$

$$P_1(x) = 2x - 1 \tag{2.35}$$

$$P_{i+1}(x) = \frac{(2i+1)(2x-1)P_i(x) - iP_{i-1}(x)}{i+1} \tag{2.36}$$

A discrete mode shape $\varphi_j(x)$ is approximated by using linear combinations of the shifted Legendre polynomials

$$\varphi_j(x) = a_{0j}P_0(x) + a_{1j}P_1(x) + \ldots + a_{Mj}P_M(x) \tag{2.37}$$

Where M is the number of Legendre polynomials. To solve for the coefficients a_{ij} the following matrix equality is solved

$$\begin{bmatrix} \vdots & \vdots & \ldots & \vdots \\ \varphi_{1z}(x) & \varphi_{2z}(x) & \ldots & \varphi_{zN_m}(x) \\ \vdots & \vdots & \ldots & \vdots \end{bmatrix} = \begin{bmatrix} \vdots & \vdots & \ldots & \vdots \\ P_0(x) & P_1(x) & \ldots & P_M(x) \\ \vdots & \vdots & \ldots & \vdots \end{bmatrix} \begin{bmatrix} a_{01} & a_{02} & \ldots & a_{0N} \\ a_{11} & a_{01} & \ldots & a_{1N} \\ a_{21} & a_{01} & \ldots & a_{2N} \\ \vdots & \vdots & \vdots & \vdots \\ a_{M1} & a_{M2} & \ldots & a_{MN} \end{bmatrix} \tag{2.38}$$

Which can be rewritten as

$$\phi_z = PA \tag{2.39}$$

Where $P \in \mathbb{R}^{N_n \times (M+1)}$ and $A \in \mathbb{R}^{(M+1) \times N}$. The coefficients matrix A can be solved as

$$A = P^{-1}\phi_z = \begin{bmatrix} \vdots & \vdots & \ldots & \vdots \\ P_0(x) & P_1(x) & \ldots & P_M(x) \\ \vdots & \vdots & \ldots & \vdots \end{bmatrix}^{-1} \begin{bmatrix} \vdots & \vdots & \ldots & \vdots \\ \varphi_{1z}(x) & \varphi_{2z}(x) & \ldots & \varphi_{zN_m}(x) \\ \vdots & \vdots & \ldots & \vdots \end{bmatrix} \tag{2.40}$$

Note that a pseudo-inverse of the P matrix is required in order to solve the previous equation. Now that the coefficients matrix A is known the first and second order spatial derivatives of the mode shape matrix are given by Eqs. (2.41) and (2.42)

$$\frac{d\phi_z(x)}{dx} = \frac{dP(x)}{dx}A \tag{2.41}$$

$$\frac{d^2\phi_z(x)}{dx^2} = \frac{d^2P(x)}{dx^2}A \tag{2.42}$$

Now let's define the number of FBG sensors as N_s and the number of IMU units as N_{IMU}. The locations of the normalized FOSS measurements along the beam are given by

$$\vec{x}_{FBG} = [x_{FBG,1} \;\; x_{FBG,2} \;\; \ldots \;\; x_{FBG,i} \;\; \ldots \;\; x_{FBG,N_s}]^T, \; x_{FBG,i} \in [0, 1] \tag{2.43}$$

The locations of the normalized IMU measurements along the beam are given by

$$\vec{x}_{IMU} = [x_{IMU,1} \;\; x_{IMU,2} \;\; \ldots \;\; x_{IMU,i} \;\; \ldots \;\; x_{IMU,N_{IMU}}]^T, \; x_{IMU,i} \in [0, 1] \tag{2.44}$$

The Legendre polynomial matrix and the mode shape matrix can now be evaluated at all the measurement points

$$P(\vec{x}_{FBG},\vec{x}_{IMU}) = \begin{bmatrix} \vdots & \vdots & \cdots & \vdots \\ P_0(\vec{x}_{FBG},\vec{x}_{IMU}) & P_1(\vec{x}_{FBG},\vec{x}_{IMU}) & \cdots & P_M(\vec{x}_{FBG},\vec{x}_{IMU}) \\ \vdots & \vdots & \cdots & \vdots \end{bmatrix} \tag{2.45}$$

$$\phi_z(\vec{x}_{FBG},\vec{x}_{IMU}) = \begin{bmatrix} \vdots & \vdots & \cdots & \vdots \\ \varphi_1(\vec{x}_{FBG},\vec{x}_{IMU}) & \varphi_2(\vec{x}_{FBG},\vec{x}_{IMU}) & \cdots & \varphi_N(\vec{x}_{FBG},\vec{x}_{IMU}) \\ \vdots & \vdots & \cdots & \vdots \end{bmatrix} \tag{2.46}$$

Where $P(\vec{x}_{FBG},\vec{x}_{IMU}) \in \mathbb{R}^{(N_{FBG}+N_{IMU})\times(M+1)}$ and $\phi_z(\vec{x}_{FBG},\vec{x}_{IMU}) \in \mathbb{R}^{(N_{FBG}+N_{IMU})\times(N)}$. Note that it is possible that $N_{FBG}+N_{IMU} \neq N_n$, i.e. the number of measurement points is not equal to the number of nodes from the finite element method or the positions corresponding to the nodes of the finite element model are not equal to the positions of the measurement points, if this is the case one should approximate the mode shapes at the desired measurement points. The coefficient matrix A is then given by

$$A = P(\vec{x}_{FBG},\vec{x}_{IMU})^{-1}\phi_z(\vec{x}_{FBG},\vec{x}_{IMU}) \tag{2.47}$$

Where $A \in \mathbb{R}^{(M+1)\times N}$. Now it's possible to solve for the modal solution, the strains are related to the modal deflections as follows:

$$\sum_{i=1}^{\infty} \frac{\partial^2 \varphi_{iz}(\vec{x}_{FBG})}{\partial x^2}\,\vec{q}_i(t) = \frac{\vec{\epsilon}_x(\vec{x}_{FBG},t)}{y_0} \tag{2.48}$$

The modes are approximated by using the second spatial derivative of the shifted Legendre polynomial

$$\frac{\partial^2 P(\vec{x}_{FBG})}{\partial x^2} A\,\vec{q}(t) = \frac{\vec{\epsilon}_x(\vec{x}_{FBG},t)}{y_0} \tag{2.49}$$

Which can be written as

$$B_1\vec{q}(t) = C_1 \tag{2.50}$$

Where $B_1 \in \mathbb{R}^{(N_{FBG})\times N}$ and $C_1 \in \mathbb{R}^{(N_{FBG})\times 1}$. The linear acceleration at IMU locations are given by:

$$\sum_{i=1}^{\infty} \varphi_{iz}(\vec{x}_{IMU})\,\ddot{q}_i(t) = \sum_{i=1}^{\infty} -\,\omega_i^2 \varphi_{iz}(\vec{x}_{IMU})\,q_i(t) = \vec{a}_y(\vec{x}_{IMU},t) \tag{2.51}$$

Which can be written as

$$B_2\vec{q}(t) = C_2 \tag{2.52}$$

Where $B_2 \in \mathbb{R}^{(N_{IMU})\times N}$ and $C_2 \in \mathbb{R}^{(N_{IMU})\times 1}$. The system can now be solved by stacking the matrices and vectors and solve for $\vec{q}(t)$, i.e.

$$\begin{bmatrix} B_1 \\ B_2 \end{bmatrix} \vec{q}(t) = \begin{bmatrix} C_1 \\ C_2 \end{bmatrix} \rightarrow B\vec{q}(t) = C \tag{2.53}$$

The solution for $\vec{q}(t)$ is then given by:

$$\vec{q}(t) = B^{-1}C \tag{2.54}$$

2.7 Results

Both FBG-IMU modeling approaches were implemented in MATLAB and benchmarked using both synthetic data and FOSS measured strain data. FBG-IMU prediction for synthetic data for deflection and the acceleration prediction are shown in Figs. 2.9 and 2.10. Figure 2.9 shows the result for 1st mode beam excitation and Fig. 2.10 shows the result for beam excitation consisted of a combination of 1st, 2nd and 3rd modes. Figures 2.11, 2.12 and 2.13 correspond to FBG-IMU Predictions with FOSS strain measurements as input to the model. Three experiments were done in which beam's base was excited with 1st, 2nd and frequency sweep excitations and then both modeling approaches were compared.

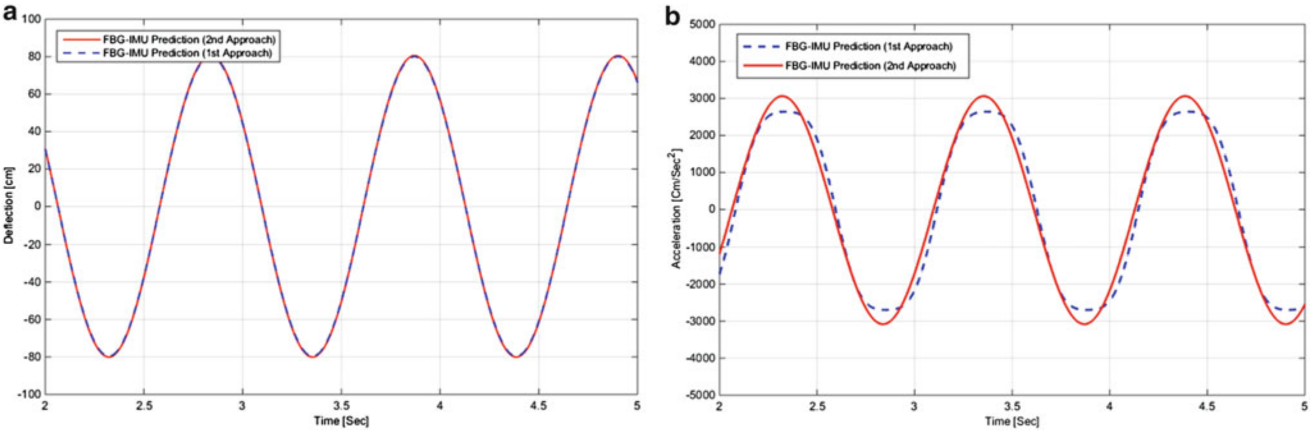

Fig. 2.9 FBG-IMU prediction, 1st approach vs. 2nd approach for deflection (*right*) and acceleration (*left*) using synthesized measurements at LORD IMU Location, 1st mode beam excitation

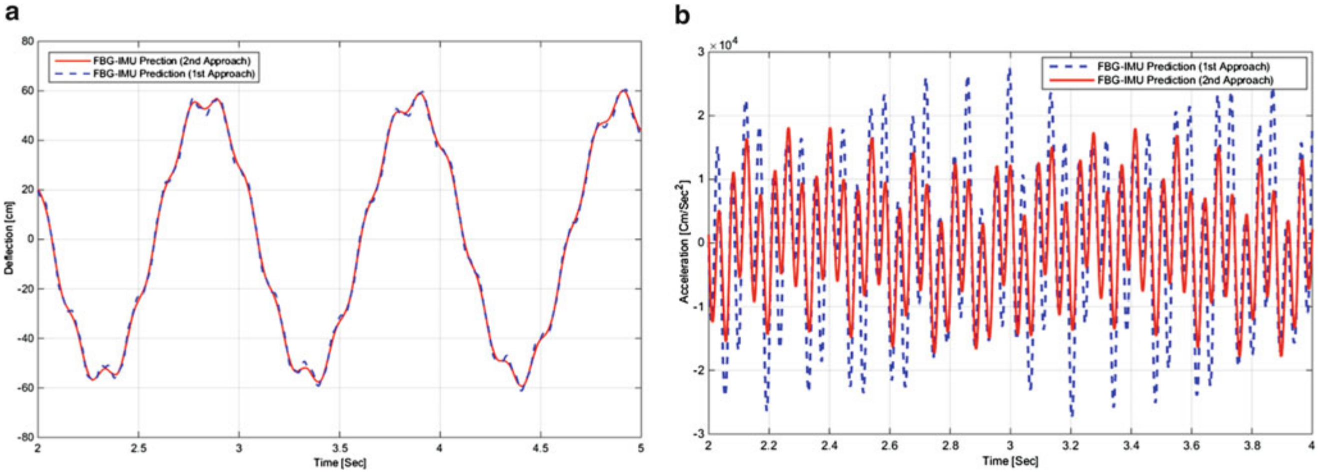

Fig. 2.10 FBG-IMU prediction for, 1st approach vs. 2nd approach for deflection (*right*) and acceleration (*left*) using synthesized measurements at LORD IMU location, beam excitation: combination of first three modes

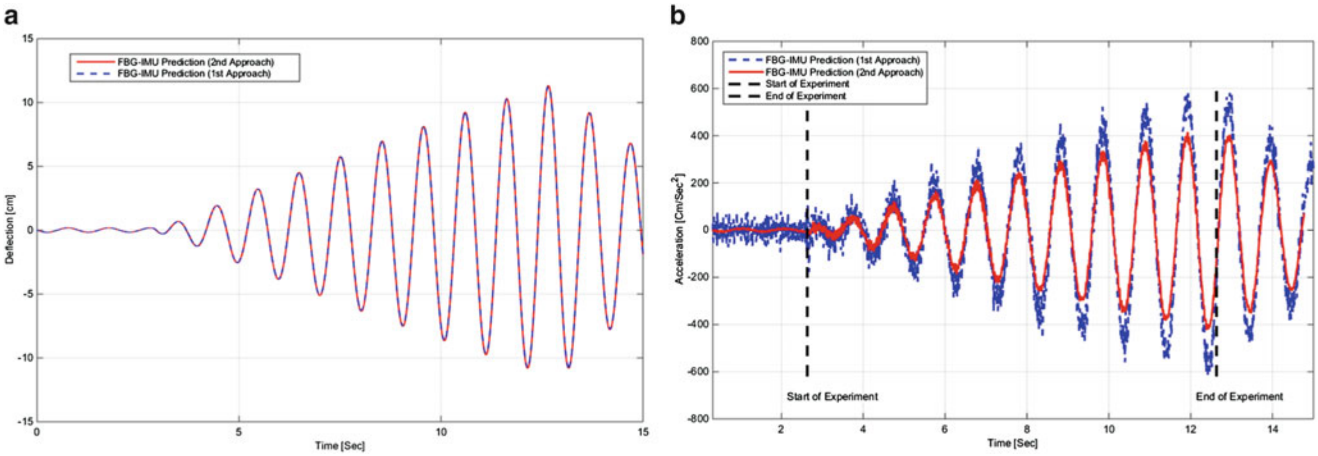

Fig. 2.11 FBG-IMU prediction for, 1st approach vs. 2nd approach for deflection (*right*) and acceleration (*left*) using FOSS measurements at LORD IMU location 1st mode base excitation

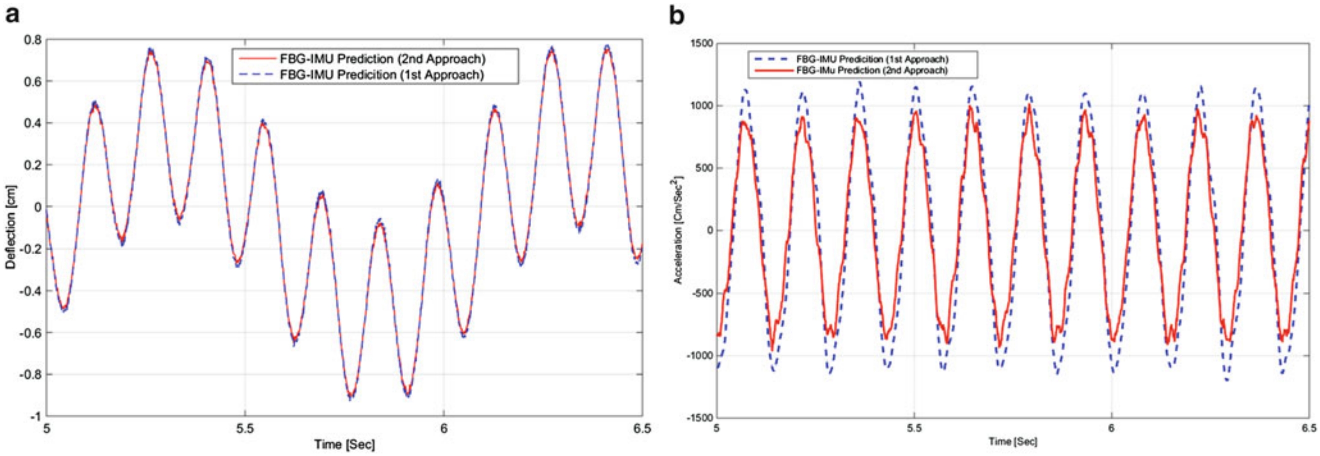

Fig. 2.12 FBG-IMU prediction for, 1st approach vs. 2nd approach for deflection (*right*) and acceleration (*left*) using FOSS measurements at LORD IMU location, 2nd mode base excitation

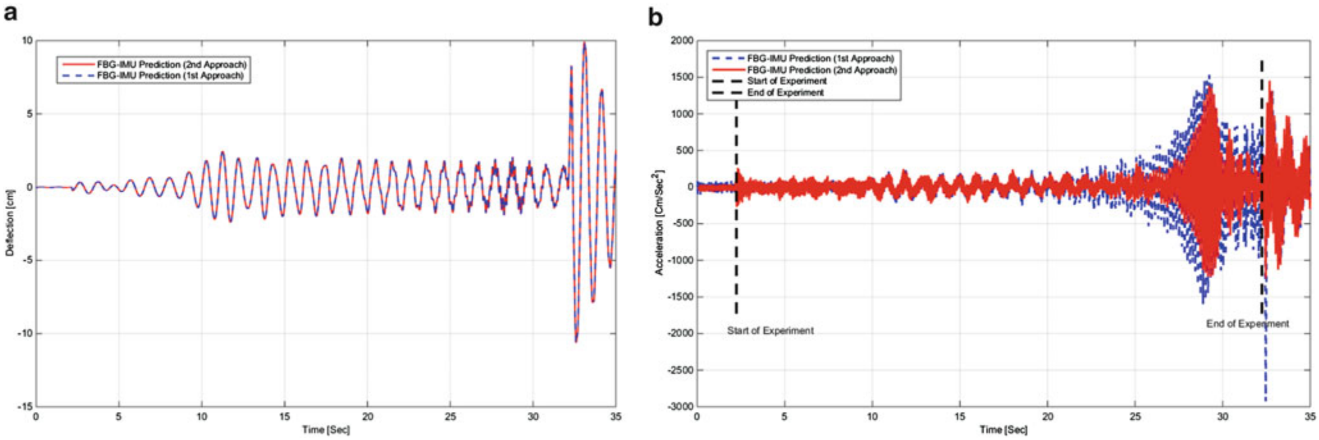

Fig. 2.13 FBG-IMU prediction for, 1st approach vs. 2nd approach for deflection (*right*) and acceleration (*left*) using FOSS measurements at LORD IMU location, frequency sweep sine (0.5–10 Hz) base excitation

2.8 Conclusions and Future Work

The FBG-IMU system is an innovative algorithm that enables accurate prediction of deflection, rate of rotation and acceleration at any point in a flexible structure relative to the rigid body frame. The FBG-IMU algorithm is based on modal matrices $\{[M], [k], [\Phi], [\Theta]\}$ that are calculated using only a finite element model of the structure. The FBG-IMU system uses an array of strain measurements at multiple points in the structure, which allows accurate estimation of the states of the flexible structure with no need of estimation of load forces or a damping matrix, or no need to assume that the damping is linear and viscous, as current structural models of flexible structures are forced to assume. The proposed algorithms are well suited for implementation on real-time, and have the potential to provide future tools for real-time estimation and control of the flexible dynamics of aerospace structures.

References

1. Jihang, H., Van Der Veek, B., Dolk, V., Kirk, D., Gutierrez, H.: Modal estimation by FBG for flexible structures attitude control. IEEE Trans. Aerosp. Electron. Syst. **50**(4), 2642–2653 (2014)
2. Jihang, H., Van Der Veek, B., Kirk, D., Gutierrez, H.: Real-time estimation of time-varying bending modes using fiber Bragg grating sensor arrays. AIAA J. **51**(1), 178–185 (2013)
3. Bottasso, C. L., Croce, A.: Cascading Kalman observers of structural flexible and wind states for wind turbine control. Scientific Report DIA-SR 09-02, Dipartimento di Ingegneria Aerospaziale, Politecnico di Milano (2009)

Chapter 3
On the Output-Only Vibration-Based Damage Detection of Frame Structures

Giacomo Bernagozzi, Luca Landi, and Pier Paolo Diotallevi

Abstract The present work aims at applying and comparing some methods for vibration-based damage detection of civil structures starting from ambient vibration data. The analyzed procedures are based on a dynamic identification of the modal parameters that is performed in output-only conditions; this is a typical situation that occurs when structural health monitoring strategies are applied to civil structures. The here investigated damage-sensitive features are the modal parameters, the modal flexibility matrix and the damage-induced deflection, due to unitary inspection loads, of the identified structure; possible variations in these parameters can be adopted in order to detect, localize and quantify the damage. A damaged condition is analytically simulated through a stiffness reduction in the elements of a RC shear-type plane frame. The output-only modal identification is performed through the Eigensystem Realization Algorithm, combined with the Random Decrement technique, on the simulated responses due to a white noise ground motion of both the undamaged and the damaged structures. At the end, the effectiveness of the different identified damage features is evaluated and the accuracy related to the identified modifications, due to damage, is determined through a comparison with the initially assumed variations in the structural model.

Keywords Output-only modal identification • Eigensystem realization algorithm • Structural health monitoring • Vibration-based damage detection • RC frame

3.1 Introduction

The knowledge of the mechanical parameters and the eventual damage state characterizing the existing civil structures in earthquake zones, especially the historical ones, is a very demanding priority for the reduction of the related seismic risk. Instead of performing local tests and due to the developments in the sensors technology, it is possible to adopt in situ non-destructive global approach procedures, which can be included in the so called vibration-based Structural Health Monitoring (SHM) [1–4]. Subsequently, a structural system identification [5] can be performed starting from the measured data obtained through the utilization of the dynamic monitoring system.

In the past, dynamic testings performed through artificial excitation were very common procedures for the investigation of the behavior of constructions but they are generally related to high economic costs and difficulties in producing and measuring “ad hoc” excitations, especially for large structures. Nowadays, natural excitation dynamic testings are more convenient as they can reduce the above disadvantages and the recordings can be performed while the structure is under operational conditions. Despite these benefits, some computational difficulties occur in the structural identification because, generally, ambient vibration inputs can not be measured and the process must be carried out in output-only conditions. The input–output identification, also known as experimental modal analysis (EMA), is replaced by operational modal analysis (OMA) [6], which performs successfully the identification even though the exciting inputs are unknown.

Damage is defined as a change between two different states in time of a generic construction, which negatively affects the structural behavior [2]. Damage detection can be carried out as the final step of an identification procedure where the modification of the identified structural parameters, such as the quantities related to both the modal and the spatial models, are evaluated between the baseline condition and the eventually damaged one [1].

The main purpose of this work is to compare different damage detection methods related to the vibration-based approach and to evaluate, within a simulated framework, their accuracy in the identification of the structural changes. The output-only modal identification is performed in the time domain adopting the Random Decrement technique [7–9] combined with the

---

G. Bernagozzi (✉) • L. Landi • P.P. Diotallevi
Department DICAM, University of Bologna, Viale Risorgimento 2, 40136 Bologna, Italy
e-mail: giacomo.bernagozzi2@unibo.it

A. Wicks, C. Niezrecki (eds.), *Structural Health Monitoring, Damage Detection & Mechatronics, Volume 7*,
Conference Proceedings of the Society for Experimental Mechanics Series, DOI 10.1007/978-3-319-29956-3_3

Eigensystem Realization Algorithm (ERA) [10–12]. The adopted damage detection methods are mainly based on the identification of the modal parameters and the modal flexibility matrices; these last can be derived, notwithstanding the output-only identification, through an estimation of the structural masses.

3.2 Output-Only Vibration-Based Damage Detection Methods

The damage detection methods are based on the comparison between, at least, two identified states at different time instants of a generic structure. In this way, it is possible to estimate the modifications of the system and the major task is to decide whether or not such changes are related to a structural damage [1]. The variation of the identified parameters can be investigated in order to obtain five different levels of damage detection achievements: they correspond, respectively from the first to the fourth, to the assessment of presence, location, classification and quantification of damage; the fifth one is related to the estimation of the remaining time life of the structure [4].

In the change-in-frequency method [1, 2, 4], damage is detected through the analysis of the variation of the natural frequencies; since damage in structures could be characterized by a stiffness reduction while the mass remains, in general, unchanged, it is clear that most damage conditions are related to a decrease in the natural frequencies. In the change-in-mode-shape method [1, 4], the variation of the mass-normalized mode shape amplitude is evaluated for each mode and each DOF of the structure. In literature, some other methods related to the mode shapes have been proposed: the Modal Assurance Criterion (MAC) [2, 4, 13] or the coordinate Modal Assurance Criterion (COMAC) [2, 4] can be evaluated between the mode shapes of two different identified models. Furthermore, it is possible to combine the modal parameters: the Yuen function [1, 4] evaluates the difference between the modal vectors after that they are scalarly divided by the respectively natural frequencies.

Passing from the modal to the spatial models, two common methods for damage detection are the change-in-flexibility [1, 2, 4, 14] and the change-in-stiffness [1, 2]. The first one is preferable in the experimentally based procedures since the estimation of the flexibility matrix starting from a limited number of identified modes is more accurate than the estimation of the stiffness matrix. By calculating the variations of the flexibility matrix components, the damage can be quantified and located: the damaged DOF is, indeed, the one related to the column of such matrix that exhibits the maximum variation. It is also possible to evaluate the deflections of the structure due to unitary inspection loads according to the Positive Shear Inspection Load (PSIL) method [15] starting from the identified flexibility matrices; in this approach, the investigated parameters are the damaged-induced displacements and the damage-induced interstory drifts.

3.3 Application: Identification and Damage Detection

The above-mentioned output-only damage detection methods are applied, within a simulated framework, to a RC plane frame, which is assumed as a test structure and considered in two different conditions: the first is the undamaged or baseline state and the second is the damaged one. The developed application is mainly composed by two parts: firstly, the output-only structural identification is applied and subsequently the damage-sensitive features are derived from the identified parameters.

The output-only modal identification is performed starting from the simulated responses of the test structure, which is excited by a white noise ground motion (Fig. 3.1). The obtained signals are processed according to the Random Decrement technique [7–9] in order to determine the Markov parameters of the system that are required for the application of the Eigensystem Realization Algorithm (ERA) [10–12]. Several procedures of simulation and identification are performed in order to obtain a statistically adequate sample of identified parameters. Finally, each identified model is compared to the initially assumed analytical one in order to evaluate the accuracy of the algorithm.

In order to detect the damage, the modifications of the identified parameters are evaluated with reference to the two different conditions of the test structure. Such changes are expressed as the mean values among the results of all the performed simulation/identification procedures. Finally, the accuracy in the determination of the damaged-induced changes is evaluated through the comparison between the identified and the initially assumed analytical values. The authors have implemented the computer code of the identification algorithm and of the damage detection methods in order to perform the computations.

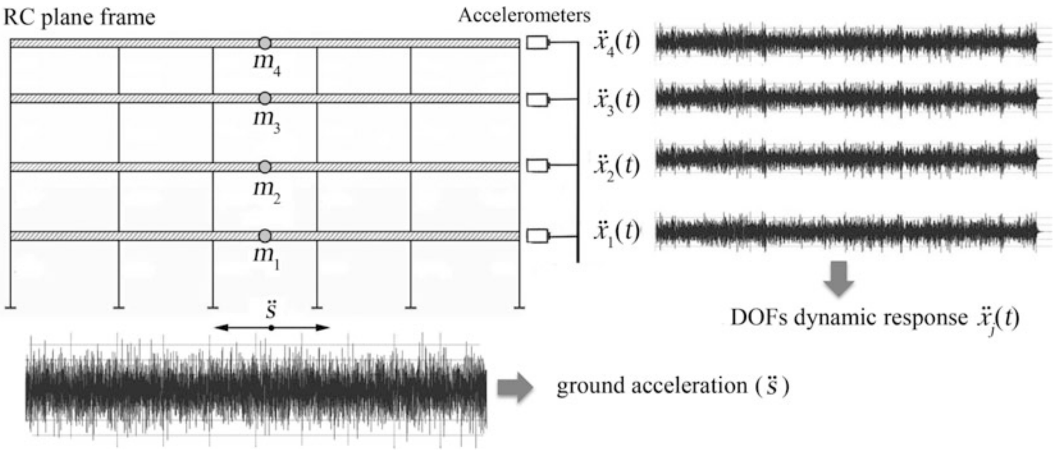

Fig. 3.1 RC plane frame and simulation of the dynamic response

Table 3.1 Geometric characterization of the RC plane frame

Story	Interstory height (m)	Column section (m)	Column moment of inertia J_{xG} (m^4)
4°	3.93	0.45 × 0.45	0.00342
3°	3.39	0.50 × 0.50	0.00521
2°	3.41	0.55 × 0.55	0.00762
1°	3.15	0.60 × 0.60	0.01080

3.3.1 Test Structure: Undamaged Condition

The test structure is a reinforced concrete (RC) plane frame formed by five spans and four stories (Fig. 3.1); the beams are supposed to be infinitely stiff in comparison to the columns and the structure is modelled as a shear type frame, which is completely described by four DOFs. The elastic modulus of the columns is assumed equal to 20000 N/mm^2 and the main geometric properties of the structure are summarized in Table 3.1.

The diagonal mass matrix $\boldsymbol{M}$ and the stiffness matrix $\boldsymbol{K}$ are computed and the modal damping ratio is assumed as $\zeta_i = 0.05$ for each mode.

$$\boldsymbol{M}=\begin{bmatrix}150.82 & 0 & 0 & 0\\ 0 & 221.97 & 0 & 0\\ 0 & 0 & 236.05 & 0\\ 0 & 0 & 0 & 331.29\end{bmatrix}\left({}^{\mathrm{kN\,s^2}}\!/_{\mathrm{m}}\right) \qquad \boldsymbol{K}=10^5\begin{bmatrix}0.811 & -0.811 & 0 & 0\\ -0.811 & 2.736 & -1.925 & 0\\ 0 & -1.925 & 4.694 & -2.769\\ 0 & 0 & -2.769 & 7.745\end{bmatrix}\left({}^{\mathrm{kN}}\!/_{\mathrm{m}}\right)$$

The natural circular frequencies and the mass-normalized modal matrix $\boldsymbol{\Phi}$ are obtained through the solution of the eigenvalue problem connected to the undamped free vibration analysis; in order to complete the model, the flexibility matrix $\boldsymbol{F}$ is reported.

$$\omega_1 = 13.18\ \mathrm{rad/s} \quad \omega_2 = 28.03\ \mathrm{rad/s} \quad \omega_3 = 42.53\ \mathrm{rad/s} \quad \omega_4 = 57.69\ \mathrm{rad/s}$$

$$\boldsymbol{\Phi}=\begin{bmatrix}0.0578 & 0.0540 & -0.0189 & 0.0036\\ 0.0391 & -0.0249 & 0.0447 & -0.0189\\ 0.0234 & -0.0356 & -0.0217 & 0.0441\\ 0.0090 & -0.0192 & -0.0344 & -0.0372\end{bmatrix} \qquad \boldsymbol{F}=10^{-4}\begin{bmatrix}0.2315 & 0.1082 & 0.0562 & 0.0201\\ 0.1082 & 0.1082 & 0.0562 & 0.0201\\ 0.0562 & 0.0562 & 0.0562 & 0.0201\\ 0.0201 & 0.0201 & 0.0201 & 0.0201\end{bmatrix}\left({}^{\mathrm{m}}\!/_{\mathrm{kN}}\right)$$

3.3.2 Test Structure: Damaged Condition

A reduction in the stiffness of the ground floor columns of the original structure is set up as ${k_{(1)}}^D = 0.5\ k_{(1)}$ in order to obtain a damaged state, where $k_{(1)}$ is the first story stiffness; the resultant stiffness matrix $\boldsymbol{K}^D$ is computed.

$$\boldsymbol{K}^D = 10^5 \begin{bmatrix} 0.811 & -0.811 & 0 & 0 \\ -0.811 & 2.736 & -1.925 & 0 \\ 0 & -1.925 & 4.694 & -2.769 \\ 0 & 0 & -2.769 & 5.257 \end{bmatrix} \left({}^{\mathrm{kN}}/_{\mathrm{m}}\right)$$

The mass matrix $\boldsymbol{M}$ and the modal damping ratios ζ_i are supposed to be unchanged in the analytical simulation of the damage. A modal analysis is performed on the undamped structure in order to determine the natural circular frequencies and the mass-normalized eigenvectors $\boldsymbol{\Phi}^{\mathrm{D}}$; the flexibility matrix $\boldsymbol{F}^{\boldsymbol{D}}$ is also computed.

$$\omega_1^D = 11.76\ \mathrm{rad/s} \quad \omega_2^D = 25.44\ \mathrm{rad/s} \quad \omega_3^D = 38.74\ \mathrm{rad/s} \quad \omega_4^D = 55.31\ \mathrm{rad/s}$$

$$\boldsymbol{\Phi}^{\mathrm{D}} = \begin{bmatrix} 0.0523 & 0.0563 & -0.0264 & 0.0053 \\ 0.0389 & -0.0115 & 0.0474 & -0.0248 \\ 0.0270 & -0.0315 & -0.0035 & 0.0501 \\ 0.0156 & -0.0280 & -0.0344 & -0.0284 \end{bmatrix} \quad \boldsymbol{F}^{\boldsymbol{D}} = 10^{-4} \begin{bmatrix} 0.2516 & 0.1283 & 0.0763 & 0.0402 \\ 0.1283 & 0.1283 & 0.0763 & 0.0402 \\ 0.0763 & 0.0763 & 0.0763 & 0.0402 \\ 0.0402 & 0.0402 & 0.0402 & 0.0402 \end{bmatrix} \left({}^{\mathrm{m}}/_{\mathrm{kN}}\right)$$

3.3.3 Simulation of the Structural Response

A stochastic ground acceleration $\ddot{s}$ is applied at the base of the frame structure, both for the undamaged case and for the damaged one, in order to generate the time-histories that are subsequently used for the output-only modal identification; the exciting input is assumed as a white noise signal (Fig. 3.1).

The dynamic response of the frame is calculated in the mass-normalized modal space through the convolution or Duhamel's integral between the ground acceleration $\ddot{s}$ and the impulse response function (IRF) of each mode of the structure. The displacement response in physical coordinates for the j-th DOF is determined starting from the response of each mode and the acceleration response $\ddot{x}_j(t)$ can be computed through a time double derivation of the displacement response.

The obtained signals are composed by two parts: the first one is the response of the model to the ground acceleration while the second one is related to the free damped vibrations that take back the structural DOFs to their rest positions. This second part of the signals is neglected in the subsequent identification procedure. A Fast Fourier Transform (FFT) is performed on the simulated signals in order to check their frequency content: the four peaks in the amplitude spectrum are directly related to the four natural frequencies of the frame, as shown in Fig. 3.2 for the undamaged case.

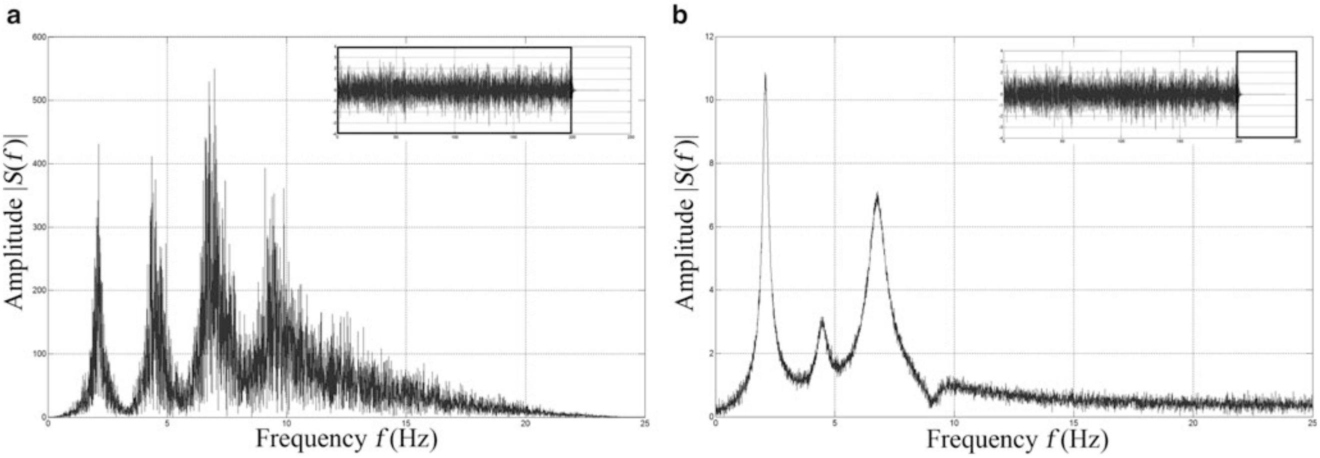

Fig. 3.2 Amplitude of the frequency spectrum via FFT—undamaged structure: (**a**) stochastic response (**b**) free damped response

3.4 Results and Discussion

3.4.1 *Output-Only Modal Identification*

The output-only modal identification through the RD-ERA method is applied to both the undamaged and the damaged structures, starting from the responses that are generated by the applied ground motion. The results of the identification is reported only for the undamaged structure for the sake of brevity. The Random Decrement functions are calculated (Fig. 3.3) and these sinusoidal decaying signals are assumed as the Impulse Response Functions (IRFs), or Markov parameters, that are needed for the application of the ERA method.

The raw output results of the RD-ERA contain both structural and computational modes. The first ones can be selected since they have the higher values of the Modal Amplitude Coherence (MAmC) and the Mode Singular Value (MSV) [11]; furthermore, the structural modes always occur in complex conjugate pairs and they must be characterized by reasonable values of the modal damping ratio. The identified modes for the first identification (#1) performed on the undamaged structure are reported in Table 3.2: they are ordered with respect to the MSV and only one of each complex conjugate modes pair is inserted in the table, for the sake of brevity.

In addition, the identification procedure is applied for each order of the state-space model, from the unitary one to the maximum value, in order to obtain the so-called stabilization diagram (as reported in Fig. 3.4): the natural frequencies of the true modes do not depend on the model order.

The complex value mode shapes obtained through RD-ERA are transformed to real values via the Standard technique [5]. The identified modal model in terms of natural circular frequencies, modal damping ratios and mode shapes (normalized to maximum values) for the first identification #1 procedure is expressed in Table 3.3.

Subsequently, the identified stiffness $\widehat{\boldsymbol{K}}$ and damping $\hat{C}$ matrices are obtained through the knowledge of the mass matrix $\boldsymbol{M}$, which leads to the mass-normalization of the mode shapes.

$$\widehat{\boldsymbol{K}} = 10^5 \begin{bmatrix} 0.790 & -0.777 & -0.029 & 0.020 \\ -0.777 & 2.584 & -1.723 & 0.040 \\ -0.029 & -1.723 & 4.432 & -3.028 \\ 0.020 & 0.040 & -3.028 & 8.748 \end{bmatrix} \left({}^{\mathrm{kN}}\!/_{\mathrm{m}}\right) \qquad \hat{C} = \begin{bmatrix} 279.53 & -119.23 & -22.56 & 13.48 \\ -119.23 & 625.11 & -245.58 & 36.99 \\ -22.56 & -245.58 & 864.02 & -427.36 \\ 13.48 & 36.99 & -427.36 & 1748.61 \end{bmatrix} \left({}^{\mathrm{kN\,s}}\!/_{\mathrm{m}}\right)$$

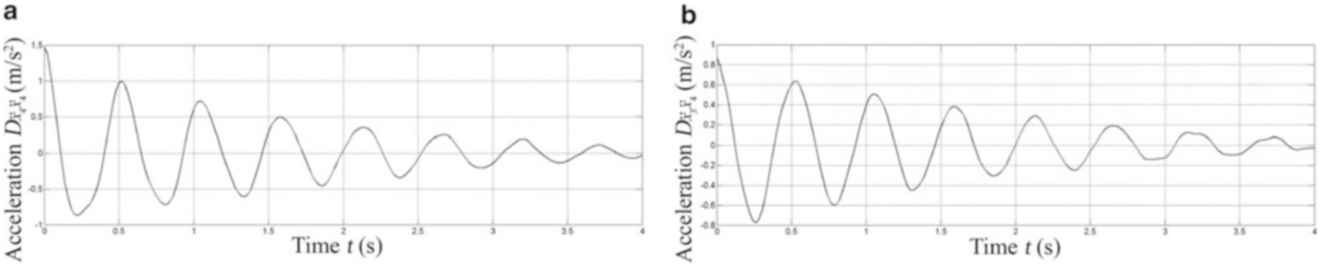

Fig. 3.3 RD functions: (**a**) auto RD function (node 4); (**b**) cross RD function (nodes 3 and 4)

Table 3.2 Raw output modes of the #1 identification (model order $N = 10$) with the true modes in bold type

Identified mode	$\widehat{\omega}_i$ (rad/s)	$\hat{\zeta}_i$ (/)	MAmC$_\mathrm{i}$	MSV$_\mathrm{i}$
1	**13.26**	**0.049**	**0.988**	**1.000**
2	**27.83**	**0.042**	**0.987**	**0.507**
3	**42.27**	**0.044**	**0.999**	**0.220**
4	74.93	1.000	0.961	0.145
5	**56.77**	**0.050**	**0.965**	**0.141**
6	65.95	0.325	0.400	0.041
7	75.39	0.117	0.295	0.036
8	117.79	0.199	0.492	0.019
9	107.05	0.114	0.434	0.018
10	158.31	0.125	0.192	0.003

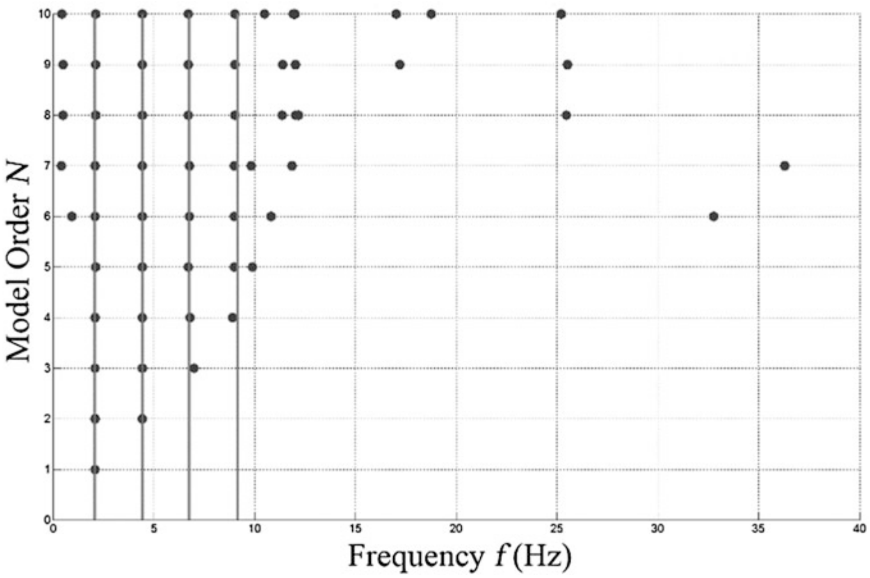

Fig. 3.4 Stabilization diagram for the #1 identification with *grey lines* referred to the analytical solution

Table 3.3 Output-only identified modal model of the #1 identification

Mode *i*	$\widehat{\omega}_i$ (rad/s)	$\hat{\zeta}_i$	$\hat{u}_{i4}$	$\hat{u}_{i3}$	$\hat{u}_{i2}$	$\hat{u}_{i1}$
I	13.26	0.0496	1.0000	0.6757	0.4036	0.1553
II	27.83	0.0420	1.0000	−0.4130	−0.6207	−0.3422
III	42.27	0.0442	−0.3811	1.0000	−0.4086	−0.7146
IV	56.77	0.0503	0.2006	−0.2884	1.0000	−0.5222

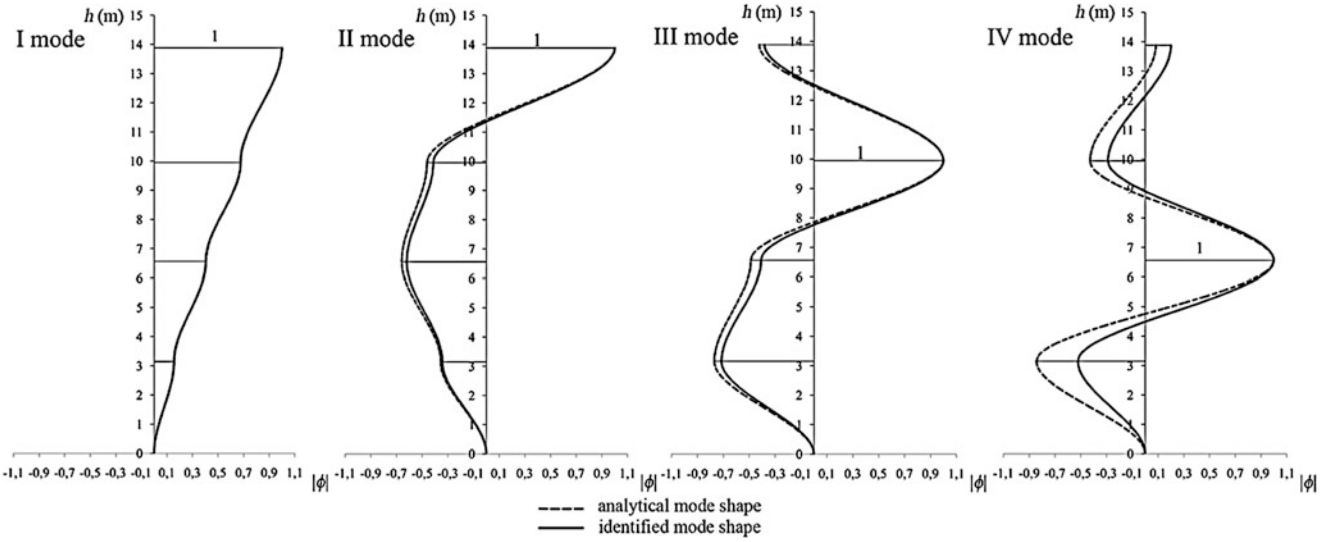

Fig. 3.5 Comparison between the mode shapes of the #1 identification and the analytical ones

The accuracy of the output only identification is graphically evaluated through the representation of the identified mode shapes (#1identification) and the analytical ones (Fig. 3.5).

The errors between the analytical and the identified models are calculated for all the performed identification procedures (from #1 to #4) and reported in Table 3.4 (for the modal model) and in Table 3.5 (for the spatial model). The final mean values between all the calculations performed, are also expressed and reported in the last row of these two tables. Referring to the identified stiffness matrix $\widehat{\boldsymbol{K}}$, the error is calculated with reference to the average value of all the components.

Table 3.4 Percentage errors in the RD-ERA identification of the modal model

	$\left|\text{Err }(\%)\ \hat{\omega}_i\right|$				$\left|\text{Err }(\%)\ \hat{\zeta}_i\right|$				$\left|\text{Err }(\%)\ \hat{\phi}_{ij}\right|$			
Mode *i*	I	II	III	IV	I	II	III	IV	I	II	III	IV
#1 Id.	0.61	0.70	0.63	1.60	0.74	16.1	11.5	0.66	0.35	4.97	8.25	52.5
#2 Id.	0.04	0.96	0.33	1.18	5.66	10.2	29.3	18.4	0.01	7.01	4.75	47.3
#3 Id.	1.01	0.35	0.65	0.08	10.8	11.1	30.8	14.6	0.50	2.56	8.74	8.78
#4 Id.	0.13	0.63	1.06	0.43	18.6	3.79	5.52	3.83	0.08	4.82	13.56	16.89
Average	**0.45**	**0.66**	**0.67**	**0.82**	**8.95**	**10.3**	**19.3**	**9.37**	**0.24**	**4.84**	**8.83**	**31.37**

Table 3.5 Percentage errors in the RD-ERA identification of the spatial model

	$\left|\text{Err }(\%)\ \hat{C}\right|$	$\left|\text{Err }(\%)\ \hat{K}\right|$
#1 Id.	12.15	7.24
#2 Id.	12.32	5.80
#3 Id.	14.92	1.75
#4 Id.	4.59	2.63
Average	**10.24**	**4.35**

Table 3.6 Analytical and identified changes of the natural circular frequencies

Mode *i*	I	II	III	IV
$\Delta\{\omega_i^D;\ \omega_i\}$ (rad/s)	−1.42	−2.59	−3.79	−2.38
$\Delta\{\ \omega_i^D;\ \omega_i\}$ (%)	−10.79	−9.24	−8.91	−4.13
$\hat{\Delta}\left\{\ \hat{\omega}_i^D;\ \hat{\omega}_i\right\}$ (rad/s)	−1.44	−2.45	−3.75	−2.20
$\hat{\Delta}\left\{\ \hat{\omega}_i^D;\ \hat{\omega}_i\right\}$ (%)	−10.90	−8.82	−8.78	−3.83
$\left|\text{Err. } \hat{\Delta}\,\Delta\ \omega_i\ (\%)\right|$	1.38	5.17	1.06	7.60

Referring to the identified damping matrix $\hat{C}$, which is obtained starting from the identified diagonal damping matrix in the modal space $\hat{C}_{(\omega,\zeta)}$, only the diagonal components are adequately identified and considered in the average while the off-diagonal elements are affected by much more uncertainties.

All the errors related to the identified modal parameters increase from the low-frequency to the high-frequency modes. As a matter of fact, the identified first mode shape overlaps the analytical one in Fig. 3.5 while more uncertainties occur in the identification of the high-frequency mode shapes, especially the fourth one. It is also worth noting that the major errors are related to both the modal damping ratios and the damping matrix components.

3.4.2 *Damage Detection*

Referring to each parameter, the difference between the analytical model of the undamaged structure and the damaged one is evaluated in order to choose the best damage features. In the case of analytical variations that are effectively related to the damage, these modifications are evaluated also for the results of the output-only modal identification: in this last case, the parameters are the mean values among all the performed identification procedures.

The changes of the natural circular frequencies are reported in Table 3.6: the presence of damage can be deduced from the reductions of the natural frequencies, especially for the first mode. The variations of these parameters are identified with an adequate precision through the output-only identification algorithm, as reported in the last row of Table 3.6; by averaging these values between the modes, the final mean error is estimated as equal to 3.80 %.

In the simulation of the damaged condition, the modal damping ratios are assumed as invariant and thus the modifications in the identified damping ratios (Table 3.7) are not expression of a damaged state but they are only caused by random errors related to the identification process.

The analytical changes in the maximum-value normalized mode shapes are plotted in Fig. 3.6: a general increase of the mode shape amplitude can be observed in the figure but this trend is not correlated with the location of the assumed damage. The same result is obtained by computing the absolute percentage variations of the mass-normalized mode shapes and the Yuen functions, as reported in the following matrices. It is worth noting one exceptional case: the percentage variations and

Table 3.7 Identified changes of the modal damping ratios

Mode i	I	II	III	IV
$\widehat{\Delta}\left\{\hat{\zeta}_i^D;\hat{\zeta}_i\right\}$ (/)	0.0022	0.0021	−0.0014	−0.0023
$\widehat{\Delta}\left\{\hat{\zeta}_i^D;\hat{\zeta}_i\right\}$ (%)	4.96	5.67	−1.74	−4.48

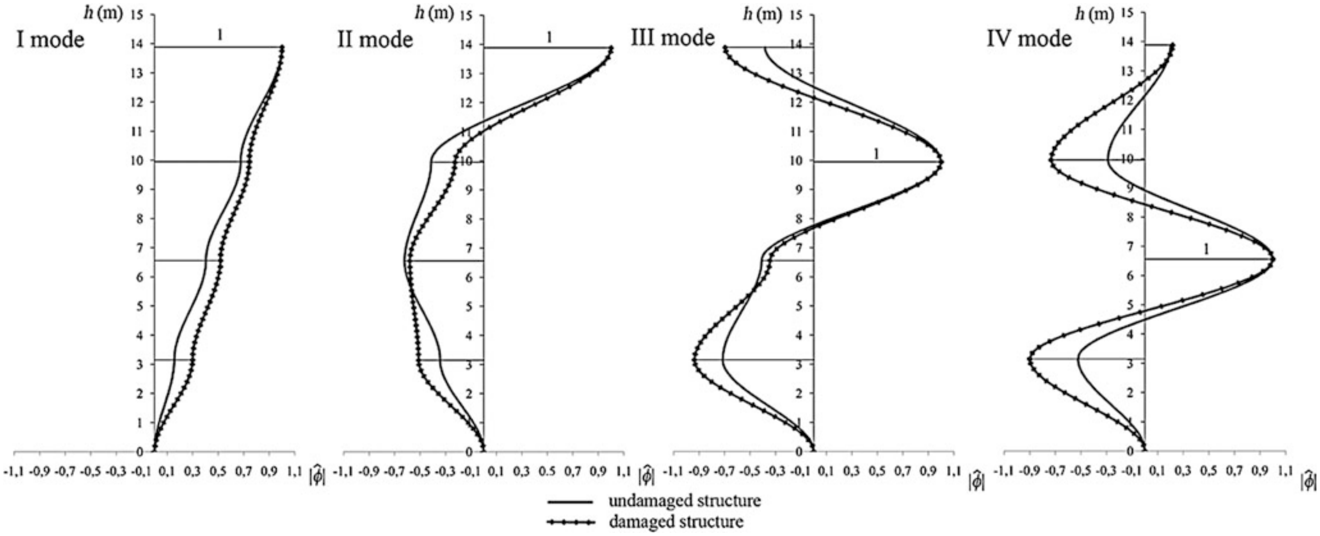

Fig. 3.6 Analytical changes in the maximum-value normalized mode shapes

Table 3.8 MAC and CoMAC between the analytical mode shapes for the undamaged structure and the damaged one

MAC						
Mode i	I	II	III	IV	DOF j	CoMAC
I	0.9848	0.1178	0.0002	0.0029	4	0.9857
II	0.0132	0.9460	0.1553	0.0054	3	0.9509
III	0.0067	0.0002	0.9054	0.1099	2	0.9085
IV	0.0002	0.0003	0.0012	0.9620	1	0.9355

the Yuen function of the first mode shape may be associated with the position of the damage since the highest variation occurs at the lowest DOF where the damage is assumed.

$$\left|\Delta\left\{\boldsymbol{\Phi}^{\mathbf{D}};\boldsymbol{\Phi}\right\}(\%)\right| = \begin{bmatrix} 9.50 & 4.14 & 40.07 & 45.41 \\ 0.69 & 53.96 & 6.13 & 31.40 \\ 15.25 & 11.68 & 83.73 & 13.46 \\ 72.18 & 45.89 & 0.13 & 23.68 \end{bmatrix} \quad \text{Yuen} = 10^{-3}\begin{bmatrix} 0.0633 & 0.2841 & 0.2387 & 0.0326 \\ 0.3363 & 0.4385 & -0.1734 & -0.1213 \\ 0.5190 & 0.0343 & -0.4200 & 0.1403 \\ 0.6386 & -0.4156 & 0.0803 & 0.1317 \end{bmatrix}$$

The Modal Assurance Criterion (MAC) matrix calculated between the mode shapes of the undamaged and the damaged structure is, as expected, not useful in the determination of the damage position since the spatial information are nullified by the correlation between modal vectors. Furthermore, also the CoMAC values, which are specifically calculated for each spatial DOF of the structure, do not express clear indications about the damage location (Table 3.8).

Referring to the analytical changes in the flexibility matrix, the individuation of the DOF where the damage is applied is not possible, for this frame and this simulated damage, through the determination of the column of the matrix, which has the maximum value, according to [14]. Notwithstanding that, due to the structure of the flexibility matrix for shear type frames, constant variations indicate, necessarily, that the damage is located at the first story. A quantification of the extension of the damage is also expressed by the flexibility changes. The accuracy of the change-in-flexibility method can be evaluated by calculating the errors between the analytical and the identified variations: the identified flexibility change matrix is characterized by a $\hat{\Delta}\,\Delta\,F_{ij}$ error estimated as 3.78 % by operating a mean among all the components.

$$\Delta\left\{\boldsymbol{F}^{\mathbf{D}};\boldsymbol{F}\right\} = 10^{-5}\begin{bmatrix} 0.201 & 0.201 & 0.201 & 0.201 \\ 0.201 & 0.201 & 0.201 & 0.201 \\ 0.201 & 0.201 & 0.201 & 0.201 \\ 0.201 & 0.201 & 0.201 & 0.201 \end{bmatrix}\left({}^{\mathrm{m}}\!/\!_{\mathrm{kN}}\right) \qquad \Delta\left\{\boldsymbol{F}^{\mathbf{D}};\boldsymbol{F}\right\}\% = \begin{bmatrix} 8.68 & 18.58 & 35.75 & 100.00 \\ 18.58 & 18.58 & 35.75 & 100.00 \\ 35.75 & 35.75 & 35.75 & 100.00 \\ 100.00 & 100.00 & 100.00 & 100.00 \end{bmatrix}$$

$$\Delta\left\{\widehat{\boldsymbol{F}}^{\mathbf{D}};\widehat{\boldsymbol{F}}\right\} = 10^{-5}\begin{bmatrix} 0.186 & 0.206 & 0.215 & 0.209 \\ 0.206 & 0.197 & 0.197 & 0.202 \\ 0.215 & 0.197 & 0.195 & 0.214 \\ 0.209 & 0.202 & 0.214 & 0.206 \end{bmatrix}\left({}^{\mathrm{m}}\!/\!_{\mathrm{kN}}\right) \qquad \Delta\left\{\widehat{\boldsymbol{F}}^{\mathbf{D}};\widehat{\boldsymbol{F}}\right\}\% = \begin{bmatrix} 7.94 & 19.12 & 38.71 & 110.80 \\ 19.12 & 18.61 & 36.04 & 104.26 \\ 38.71 & 36.04 & 34.42 & 105.98 \\ 110.80 & 104.26 & 105.98 & 106.19 \end{bmatrix}$$

The deflections due to constant loads (i.e., 100 kN at each story), according to the Positive Shear Inspection Load (PSIL) method, are evaluated for both the undamaged and the damaged analytical models of the structure. The absolute and the percentage variations of the displacements are reported in Table 3.9 while Table 3.10 refers to the interstory drifts. The PSIL displacements and interstory drifts for the undamaged and the damaged structures are evaluated after the application of the output-only identification, as reported in Tables 3.11 and 3.12. The highest percentage increments of these quantities localize the damage, as graphically shown in Fig. 3.7: these increments occur at the lowest DOF of the structure where, in fact, the stiffness reduction is initially stated in order to simulate the damage. It is worth noting that the interstory drift is a better indicator for the localization of the damage in comparison to the displacement.

The damage-induced deflection is identified with a very good accuracy since its related $\hat{\Delta}\,\Delta\,x_j$ error, with respect to the analytical values, is estimated as equal to 1.87 % among all the DOFs.

Table 3.9 Analytical variations in the displacements due to PSILs

j-th DOFs	x_j(m)	x_j^D(m)	$\Delta\{x_j^D;\ x_j\}\ 10^{-3}$ (m)	$\Delta\{x_j^D;\ x_j\}$(%)
4	0.0042	0.0050	0.804	19.33
3	0.0029	0.0037	0.804	27.47
2	0.0019	0.0027	0.804	42.60
1	0.0008	0.0016	0.804	100.00

Table 3.10 Analytical variations in the interstory drifts due to PSILs

j-th DOFs	id_j(m)	id_j^D(m)	$\Delta\{id_j^D;\ id_j\}\ 10^{-3}$(m)	$\Delta\{id_j^D;\ id_j\}$(%)
3-4	0.0012	0.0012	0.00	0.00
2-3	0.0010	0.0010	0.00	0.00
1-2	0.0011	0.0011	0.00	0.00
0-1	0.0008	0.0016	0.804	100.00

Table 3.11 Identified variations in the displacements due to PSILs

j-th DOFs	$\widehat{x}_j(m)$	$\widehat{x}_j{}^D(m)$	$\widehat{\Delta}\{\widehat{x}_j{}^D;\widehat{x}_j\}10^{-3}$ (m)	$\widehat{\Delta}\{\widehat{x}_j{}^D;\widehat{x}_j\}$(%)
4	0.0042	0.0050	0.816	19.62
3	0.0029	0.0037	0.802	27.91
2	0.0019	0.0027	0.822	43.89
1	0.0008	0.0016	0.832	106.77

Table 3.12 Identified variations in the interstory drifts due to PSILs

j-th DOFs	$\widehat{id}_j$(m)	$\widehat{id}_j{}^D$(m)	$\widehat{\Delta}\left\{\widehat{id}_j{}^D;\widehat{id}_j\right\}10^{-3}$(m)	$\widehat{\Delta}\left\{\widehat{id}_j{}^D;\widehat{id}_j\right\}$(%)
3-4	0.0013	0.0013	0.014	1.11
2-3	0.0010	0.0010	−0.020	−1.99
1-2	0.0011	0.0011	−0.010	−0.92
0-1	0.0008	0.0016	0.832	106.77

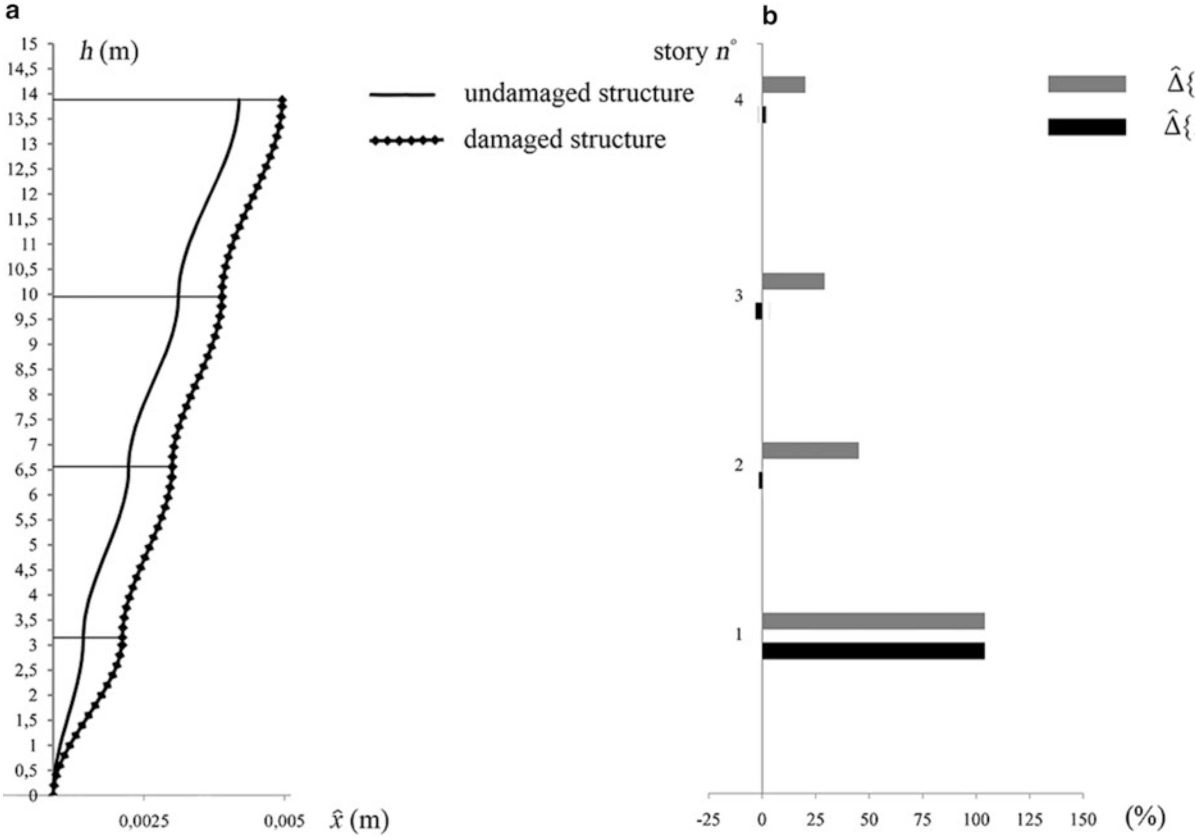

Fig. 3.7 Identified deflections due to PSILs: (**a**) graphical comparison between the undamaged state and the damaged one (**b**) percentage changes of the displacements and the interstory drifts

3.5 Conclusions

Some vibration-based damage detection methods have been applied, in output-only conditions and within a simulated framework, to a RC frame structure; a single-damage state has been simulated and subsequently identified through the RD technique and the Eigensystem Realization Algorithm starting from the dynamic responses of the structure, which is excited by a white noise ground motion.

Referring to the intermediate results of the output-only modal identification, the accuracy in the estimation of the modal parameters decreases passing from the low-frequency modes to the high-frequency ones; the major errors are related to the higher-order mode shapes and to all the identified modal damping ratios.

The damage has been detected by a natural frequency shift for each mode, especially for the first one. The changes in the mode shapes can not be systematically correlated to the localization of the damage, except for the first mode shape; it is worth noting that similar results have been obtained through the analysis of the Yuen functions. The damage can be quantified by the change-in-flexibility method even if, for this frame and for the assumed damage, an a priori knowledge of the structure of the flexibility matrix is required in order to localize the damage. This localization, by contrast, has been uniquely obtained through the damage-induced deflection of the structure due to some constant inspection loads, according to the PSIL method.

Future developments may be related to the analysis of more complex structures, such as spatial frames, and to the evaluation of the performance of the damage detection methods for multiple-damage conditions.

References

1. Doebling, S.W., Farrar, C.R., Prime, M.B., Shevitz, D.W.: Damage identification and health monitoring of structural and mechanical systems from changes in their vibration characteristics: a literature review. Technical report LA-13070-MS, UC-900, Los Alamos National Laboratory, New Mexico (1996)

2. Sohn, H., Farrar, C.R., Hemez, F.M., Shunk, D.D., Stinemates, S.W., Nadler, B.R., Czarnecki, J.J.: A review of structural health monitoring literature form 1996–2001, Los Alamos National Laboratory LA-13976-MS (2003)
3. Worden, K., Farrar, C.R., Manson, G., Park, G.: The fundamental axioms of structural health monitoring. Proc. R. Soc. London, Ser. A **463** (2082), 1639–1664 (2007)
4. Farrar, R., Worden, K.: Structural Health Monitoring – A Machine Learning Perspective. Wiley, Chichester (2013)
5. Alvin, F.K., Robertson, A.N., Reich, G.W., Park, K.C.: Structural system identification: from reality to model. Comput. Struct. **81**, 1149–1176 (2003)
6. Brincker, R., Ventura, C.: Introduction to Operational Modal Analysis. Wiley, Chichester (2015)
7. Cole, H.A.: On-line failure detection and damping measurements of aerospace structures by random decrement signature. Report NASA CR-2205 (1973)
8. Asmussen, J.C., Ibrahim, R., Brincker, R.: Random decrement: identification of structures subjected to ambient excitation. In: Proceedings of the 16th International Modal Analysis Conference, Santa Barbara (1998)
9. Rodrigues, J., Brincker, R.: Application of the random decrement technique in operational modal analysis. In: Proceedings of the 1st International Operational Modal Analysis Conference, Copenhagen, 26–27 April 2005
10. Juang, J.N., Pappa, R.S.: An eigensystem realization algorithm for modal parameter identification and model reduction. J. Guid. Control. Dyn. **8**(5), 620–627 (1985)
11. Juang, J.N.: Applied system identification. Prentice Hall, Englewood Cliffs (1994)
12. Juang, J.N., Phan, M.Q.: Identification and control of mechanical systems. Cambridge University Press, Cambridge (2001)
13. Wang, L., Chan, T.H.T.: Review of vibration-based damage detection and condition assessment of bridge structures using structural health monitoring. In: Proceedings of the Second Infrastructure Theme Postgraduate Conference: Rethinking Sustainable Development: Planning, Engineering, Design and Managing Urban Infrastructure, Queensland University, 26 March 2009
14. Pandey, A.K., Biswas, M.: Damage detection in structures using changes in flexibility. J. Sound Vib. **169**(1), 3 (1994)
15. Koo, K.Y., Sung, S.H., Park, J.W., Jung, H.J.: Damage detection of shear buildings using deflections obtained by modal flexibility. Smart Mater. Struct. **19**(11), 115026 (2010)

Chapter 4
On the Influence of Sample Length and Measurement Noise on the Stochastic Subspace Damage Detection Technique

Saeid Allahdadian, Michael Döhler, Carlos E. Ventura, and Laurent Mevel

Abstract In this paper the effects of measuring noise and number of samples is studied on the stochastic subspace damage detection (SSDD) technique. In this technique, i.e., SSDD, the need of evaluating the eigenstructure of the system is circumvented, making this approach capable of dealing with real-time measurements of structures. In previous studies, the effect of these practical parameters was examined on simulated measurements from a model of a real structure. In this study, these effects are formulated for the expected damage index evaluated from a Chi-square distributed value. Several theorems are proposed and proved. These theorems are used to develop a guideline to serve the user of the SSDD method to face these effects.

Keywords Damage detection • Subspace method • Health monitoring • Signal noise • Sampling • Stochastic subspace method

4.1 Introduction

Structural health monitoring is regarded as the main tool in assessing the functionality of existing structures. The importance of these techniques and researches becomes obvious by considering that failure of a structure can result in catastrophic loss. Existing civil structures deteriorate by aging and under different loading conditions imposed from natural phenomena such as earthquakes, typhoons, flood and etc. Therefore, it is imperative to investigate the safety of continuing using these structures, especially after occurring major demands on the structure from these phenomena.

Numerous researches can be found in the literature and different approaches are proposed to deal with this problem by detecting possible damages in a structure. Some of these tests include sampling of the structure, which may affect the functionality of structure. These tests are named destructive tests. However the other type of the tests, namely non-destructive tests, do not involve with any action that can damage the structure or affect its functionality. Due to the need of continuation of the serviceability of the structure, more researchers have been focusing on the latter approach.

Nondestructive damage detection techniques can be categorized into two groups based on their requirements [1, 2]: (1) local techniques, which need access to all parts of the structure or the location of damage if known, and (2) global damage techniques which use vibration data to evaluate global dynamic characteristics of the structure. Employing the local techniques may lead to interference in the operation of the structure and is not suitable for major structures. However, in the latter method there is no need to know or have access to the location of damage in priori.

The global techniques can be also categorized into two groups based on their approach to the problem. In the first category, the structural properties are identified and employed to assess the condition of the structure. The structural properties identified from these approaches include stiffness, damping, mass, load paths and boundary conditions (supports, connections, etc.). In the second category, the eigen-structure of the problem is employed to evaluate the safety condition of the structure. In these methods, modal properties such as natural frequencies, modal damping values and mode shapes are used to identify any changes in the structure. Any change in the structural properties leads to a change in the modal parameters of the structure. However generally, identifying the modal parameters in a structure is more practical and accurate than the structural properties.

S. Allahdadian (✉) • C.E. Ventura
University of British Columbia, Vancouver, BC, Canada
e-mail: saeid@civil.ubc.ca; ventura@civil.ubc.ca

M. Döhler • L. Mevel
Inria/IFSTTAR, I4S Campus de Beaulieu, 35042 Rennes, France
e-mail: michael.doehler@inria.fr; laurent.mevel@inria.fr

A. Wicks, C. Niezrecki (eds.), *Structural Health Monitoring, Damage Detection & Mechatronics, Volume 7*,
Conference Proceedings of the Society for Experimental Mechanics Series, DOI 10.1007/978-3-319-29956-3_4

In order to keep the structure in operation, shaking the structure artificially or using impact loads are not promising. Therefore by employing ambient vibration testing, the operation of the structure will not be interfered. In this case due to the fact that the input excitation to the structure, e.g. wind, traffic, earth vibration, cannot be measured practically, output-only damage detection techniques are of interest. Moreover, the process of evaluating and matching the modal parameters of a structure is also time consuming [3] and it usually cannot be employed in real-time monitoring of structures which are not well instrumented. In addition, local damage in a structure affects typically on higher frequency modes [2, 4] which are not usually identifiable to be used in damage detection due to their high modal density and low participation factors [5]. Evaluation of these modal characteristics can be avoided by using output-only statistical approaches e.g. Kalman filter technique [6], outlier analysis method [7] or the stochastic subspace damage detection technique (SSDD) [8, 9].

The SSDD technique evaluates the global condition of a structure by identifying changes in the eigen-structure of the system. The damage can be detected by comparing a statistical model from the possibly damaged structure to thresholds obtained from a reference state. A subspace based residual function between these states is defined and compared using a χ^2 test. The results from χ^2 test can be displayed and monitored in a chart, namely control chart [10]. Therefore, there is no need to estimate the natural frequencies and mode shapes, making this approach capable of being used in real-time monitoring of structures. In this way, the whole eigen-system of the measurements are included in the damage detection and the focus is not only on dominant frequencies. Including higher modes in this evaluation makes the damage detection approach more robust, considering that the main effect of local damages is on higher mode shapes.

Two main challenges in health monitoring of real structures are low number of sensors and existence of noise in the measurements. Statistical damage detection methods including SSDD have a robust architecture that can deal with sparsely instrumented structures, at least for the level one of damage detection, namely investigating the existence of damage. Moreover, these methods can also deal with noisy data due to their statistical approach to the problem and that the mean of the noise is usually zero in the time domain. However, this effect needs to be studied in detail for these damage detection techniques.

In this study we focus on the effect of measurement noise and number of samples, i.e. measurement length, on the SSDD technique. Existence of noise in experimental data is inevitable. There are different sources of the noise in measuring a structure [11] such as the change in excitation sources [12], noise of measuring instruments and human error. Moreover, the data quality (noise ratio) can affect significantly on the damage detection output (e.g. [13]). Therefore, investigating the effect of this inherent characteristic of the measurements on the SSDD technique is an important factor in assessing its functionality. It was demonstrated that SSDD technique can perform robustly under ambient excitations with changing statistics [11, 14]. In our previous studies, the effect of measurement noise ratio [15, 16], type of element damaged [17] and number of samples [16] were studied briefly by examining it for a model of real bridge, the S101 Bridge. It was shown that this technique can deal with even very high ratios of noise in the data.

In this paper the objective is to analyze the theory associated to the effects of the measurement noise and number of samples on this technique. This study helps in having a better understanding of the results from the SSDD approach and in creating some guidelines for using it.

This paper is organized as follows. In Sect. 4.2, the SSDD approach is recalled. In Sect. 4.3, a theoretical analysis of its properties regarding measurement noise and sample length is carried out. Section 4.4 contains a numerical validation of the theoretical results and concluding remarks are presented in Sect. 4.5.

4.2 Stochastic Subspace Damage Detection Technique

The theories and formulations of stochastic subspace damage detection (SSDD) stem from the subspace based system identification. In this section, models, parameters and formulations needed to derive the final residual used in assessing the condition of the system is presented based on studies in [8, 9].

4.2.1 Dynamic Equilibrium Equation in Discrete Time Domain

The state-space representation of a dynamic system is well known. Herein, the governing equation for the dynamic behaviour of a structural system is presented and then it is reformed to the state-space representation. The dynamic behaviour of a structure can be modeled with the following formulation

$$\begin{cases} M\ddot{u}(t) + C\dot{u}(t) + Ku(t) = p(t) \\ y(t) = L\ddot{u}(t) + e(t) \end{cases} \tag{4.1}$$

where M, C and K are mass, damping and stiffness matrices, respectively, and u represents the displacement vector in all degrees of freedom of the system. Vector p also shows the vector of forces and t denote continuous time. It should be noted that the external force p is unknown while it is assumed to be a non-stationary white noise. Vector y also contains the output responses measured from the structure. Based on the type of the sensor recording acceleration, velocity or displacement the second part of the equation changes; herein the type of the sensor is assumed as accelerometers. Matrix L states the location of the sensors in relation to the geometry of the degrees of freedom, and e represents the measurement noise.

The discrete time state-space form of model (4.1) can be written by performing sampling with time step τ as

$$\begin{cases} x_{k+1} = Fx_k + w_k \\ y_k = Hx_k + v_k \end{cases} \tag{4.2}$$

where, the state is represented by $x \in \mathbb{R}^n$ and the measured output is $y \in \mathbb{R}^r$. r is the number of sensors and n is the system order. The state transition matrix is represented by F, and H shows the observation matrix with dimensions $n \times n$ and $r \times n$, respectively. The state noise w_k and output noise ν_k are assumed to be white noise. The state x and the measured output, y, are related to the displacement vector with Eq. (4.3).

$$x_k = \begin{bmatrix} u(k\tau) \\ \dot{u}(k\tau) \end{bmatrix}, \, y_k = y(k\tau) \tag{4.3}$$

The modal parameters of the dynamic model (4.1), which are present in its eigenvalues μ, and mode shapes, $\boldsymbol{\Psi}$, can be related to the eigenvalues λ and eigenvectors ϕ of the state transition matrix, F:

$$\begin{cases} \lambda = e^{\mu\tau} \\ \varphi = \psi \end{cases} \quad \text{where } \varphi = H\phi \text{ and } \psi = L\Psi \tag{4.4}$$

The canonical parameterization of system (4.2) is formed by pairs (λ,φ) which is referred as the system eigenstructure and is employed as the system parameter $\theta \in \mathbb{C}^{n(r+1)}$ defined as

$$\theta = \begin{bmatrix} \Lambda \\ \mathrm{vec}(\Phi) \end{bmatrix}$$

in which Λ is the vector containing all the eigenvalues λ and $\boldsymbol{\Phi}$ is the matrix composed of all eigenvectors ϕ.

4.2.2 *Output-Only Covariance Based Subspace System Identification*

In order to compute a residual vector between the reference and the current states of the system, the output-only covariance based subspace system identification method [18] is employed. By defining the output covariance as $R_i = \mathbf{E}\left(y_k y_{k-i}^T\right)$, the block Hankel matrix $\mathbf{H}_p$ can be composed as

$$\mathbf{H}_p = \begin{bmatrix} R_1 & R_2 & \cdots & R_p \\ R_2 & R_3 & \cdots & R_{p+1} \\ \vdots & \vdots & \vdots & \vdots \\ R_{p+1} & R_{p+2} & \cdots & R_{2p} \end{bmatrix} = \mathrm{Hank}(R_i) \tag{4.5}$$

The output covariances satisfy $R_i = HF^{i-1}G$ [19], where $G = \mathbf{E}\left(x_{k+1} y_k^T\right)$ is the cross covariance between the states and the outputs, which leads to the well-known factorization property of

$$\mathbf{H}_p = O_p \mathrm{C}_p \tag{4.6}$$

where

$$O_p = \begin{bmatrix} H \\ HF \\ \vdots \\ HF^p \end{bmatrix}, \quad \mathrm{C}_p = \begin{bmatrix} G & FG & \cdots & F^{p-1}G \end{bmatrix}. \tag{4.7}$$

The observation matrix, H, state transition matrix, F, and subsequently the system parameters, θ, can be computed from the defined observability matrix, O_p. The residual employed in damage detection is directly linked to O_p and thus there is no need to identify the system matrices and parameters.

4.2.3 Residual Vector Formation

By assuming that the system parameter in reference state of the structure is θ_0 and in current state is θ, a residual function is defined between these states which reacts to the changes in the system due to, for instance, damage. In order to create such a residual, the left null-space of the observability matrix O_p, namely orthonormal matrix S, is computed from performing e.g. a singular value decomposition. The reference state $\theta = \theta_0$ is then characterized by

$$S^T(\theta_0)O_p(\theta_0) = 0 \tag{4.8}$$

Due to the factorization property (4.6), the left null-space of $\mathbf{H}_p$ is equal to $S(\theta_0)$ and hence (4.8) can be rewritten as

$$S^T(\theta_0)\mathbf{H}_p = 0 \tag{4.9}$$

With the interpretation that if the system is damaged the system parameter θ becomes changed, i.e. $\theta \neq \theta_0$, two hypotheses are defined as following.

$$\begin{cases} H_0: & \theta = \theta_0 \quad \therefore \quad \text{unchanged system} \\ H_1: & \theta \neq \theta_0 \quad \therefore \quad \text{changed system (damaged)} \end{cases} \tag{4.10}$$

To test these hypothesis, a residual function needs to be defined based on property (4.9) that holds if and only if $\mathbf{H}_p$ corresponds to the reference state. Since matrix $S(\theta_0)$ depends implicitly on parameter θ_0 (we are treating it as a function of θ_0[9]), a representation of the current state parameter of the structure, i.e. θ is needed. Therefore, by measuring data from the current state of the structure, an estimation of the block Hankel matrix, i.e. $\hat{\mathbf{H}}_p$, is computed from their covariances as

$$\hat{R}_i = \frac{1}{N}\sum_{k=1}^{N} y_k y_{k-i}^T, \quad \hat{\mathbf{H}}_p = \text{Hank}\left(\hat{R}_i\right). \tag{4.11}$$

In view of (4.9), this empirical block Hankel matrix is used to create residual function (4.12) which corresponds to the difference between θ and θ_0 [8, 9].

$$\zeta_N^e = \sqrt{N}\,\text{vec}\left(S(\theta_0)^T \hat{\mathbf{H}}_p\right) \tag{4.12}$$

The indexes N and e represent the number of samples and measurement noise level in the measured data, respectively. A change in the system parameter can be formulated based on the asymptotic local approach for change detection [20] as $\theta = \theta_0 + \delta\theta/\sqrt{N}$ where $\delta\theta$ is defined as the (unknown) parameter change vector normalized by $\sqrt{N}$. Using this basis, the asymptotical distribution of the residual function fulfills the Central Limit Theorem (CLT), and is for $N \to \infty$

$$\zeta_N^e \to \begin{cases} \mathcal{N}(0, \Sigma^e) & \text{under } H_0 \\ \mathcal{N}(J^e \delta\theta, \Sigma^e) & \text{under } H_1 \end{cases} \tag{4.13}$$

in which Σ^e is the asymptotic covariance and J^e is the asymptotic sensitivity of the residual. In order to test these hypothesis, a generalized likelihood ratio (GLR) test is employed [8], which will be presented in next section.

4.2.4 Hypothesis Test

4.2.4.1 Parametric Chi-Square Test

The GLR test for hypothesis (4.10) can be written as

$$GLR\left(\zeta_N^e\right) = -2 \log \frac{L\left(\zeta_N^e \middle| \theta_0\right)}{\sup_{\theta \in H_1} L\left(\zeta_N^e \middle| \theta\right)} \tag{4.14}$$

where $L(\bullet)$ represents the likelihood function. Plugging in the residual distributions from (4.13), it boils down to the test variable [8, 11]

$$\chi_N^2 = \left(\zeta_N^e\right)^T \left(\Sigma^e\right)^{-1} J^e \left(\left(J^e\right)^T \left(\Sigma^e\right)^{-1} J^e\right)^{-1} \left(J^e\right)^T \left(\Sigma^e\right)^{-1} \zeta_N^e. \tag{4.15}$$

which is asymptotically χ^2-distributed with $d = \text{rank}(J^e) = \dim(\theta)$ degrees of freedom. Its non-centrality parameter is 0 under H_0 and $\delta\theta^T \left(J^e\right)^T \left(\Sigma^e\right)^{-1} J^e \delta\theta$ under H_1.

The test variable in (4.15) is the parametric representation of a damage index and can be used to evaluate thresholds of safety, since its distribution shifts with the given non-centrality parameter under H_1. If the test value surpasses these thresholds, then it shows that the condition of the structure is being changed.

4.2.4.2 Non-parametric Chi-Square Test

By computing a null-space from a reference data set, a non-parametric residual is created for which there is no need to have a parametric model and to evaluate its parameters. Therefore, no system identification is needed. This null-space S_0 can be obtained by a singular value decomposition of the estimated Hankel matrix from the measurement data in reference state [21]. Similar to characterization in (4.8) and (4.9) it holds in the reference state:

$$S_0^T \hat{\mathbf{H}}_p^0 = 0. \tag{4.16}$$

S_0 and $\hat{\mathbf{H}}_p^0$ are, respectively, the estimated null-space and block Hankel matrix computed over a reference dataset. After measuring data from a possibly damaged structure, the block Hankel matrix is determined from the data and the residual is defined as

$$\zeta_N^e = \sqrt{N} \operatorname{vec}\left(S_0^T \hat{\mathbf{H}}_p\right). \tag{4.17}$$

Since no explicit system parameterization is used, we have $J^e = \mathbf{I}$ in the residual distribution in (4.13), where $\mathbf{I}$ is the identity matrix, and the CLT (4.13) can be expressed as

$$\zeta_N^e \to \begin{cases} \mathcal{N}(0, \Sigma^e) & \text{under } H_0 \\ \mathcal{N}(\delta, \Sigma^e) & \text{under } H_1 \end{cases} \tag{4.18}$$

where δ is now directly linked to the change in the residual vector (when normalized by $\sqrt{N}$). Then, the test variable simplifies to

$$\chi_N^2 = \left(\zeta_N^e\right)^T (\Sigma^e)^{-1} \zeta_N^e. \tag{4.19}$$

Analogously to the previous section, this variable is asymptotically χ^2-distributed with $d = \dim\left(\zeta_N^e\right)$ degrees of freedom. Its non-centrality parameter is 0 under H_0 and $\delta^T (\Sigma^e)^{-1} \delta$ under H_1.

For simplicity, this non-parametric test variable will be used in the following.

4.3 Investigating the Effect of Noise and Number of Samples

The residual ζ_N^e is a function of number of samples and the noise in the measured data. The dependence of this variable on the number of samples is explicit in Eq. (4.12). Moreover, analogous to the effect of change in the excitation properties [11], additional measurement noise superposed on the measured data will affect the cross covariance between the outputs, and therefore the estimated Hankel matrix. Thus, the evaluated residual (4.12) and its covariance Σ^e are a function of the superposed noise.

Hence, both the number of samples and measurement noise can change the residual and the final evaluated χ^2 value. In this section their effect on the non-parametric χ^2 test is studied for a constant damage.

It is always assumed that the residual covariance Σ^e is estimated once on healthy data from the reference state of the structure, where usually lots of data is available allowing for a good covariance estimate [11]. The covariance is never recalculated when testing a residual ζ_N^e for damage that is computed on new test data.

Before starting the analysis, we recall a basic property of the χ^2 distribution: let γ be a χ^2 distributed variable, d its number of degrees of freedom and n_c its non-centrality parameter. Then,

$$\mathbf{E}\gamma = d + n_c. \tag{4.20}$$

4.3.1 Effect of Number of Samples

The effect of number of samples can be seen in residual (4.17) both explicitly in terms of $\sqrt{N}$ and implicitly e.g. its variance and the change in the system parameter. The reason of pre-multiplying the square root of number of samples in the residual vector is that based on the Central Limit Theorem, the resultant product, i.e. (4.17), is distributed asymptotically normal as stated in (4.13) and (4.18), with its covariance being independent of the number of samples. Moreover, this framework allows for a trade-off between number of samples and damage size: the χ^2 test variable may have the same value either using a longer dataset with a smaller damage, or using a shorter dataset with a bigger damage. This also means that for constant (non-zero) damage the test variable grows with the number of samples. A detailed analysis is made in this section.

4.3.1.1 Effect on the Residual Covariance

Since the asymptotic residual covariance is the same in reference and damaged states (see Eqs. (4.13) and (4.18)), an estimate $\hat{\Sigma}^e$ of the covariance matrix Σ^e is more conveniently obtained from data in the reference state of the structure under the assumption of no changes in the noise properties of the system [11]. The computation of the covariance estimate is described in detail in [11]. Note that the asymptotic covariance Σ^e is independent of the number of samples N, which can also be seen in the CLT (4.13) and (4.18). Hence, the expected value of the covariance estimate $\hat{\Sigma}^e$ neither depends on the number of datasets nor their length used in the estimation. Of course, the quality of the estimate improves when using more data, and we assume that sufficient data has been used to achieve an accurate estimate.

4.3.1.2 Effect on the χ^2 Test Value

Due to the CLT (4.18), the residual is approximately Gaussian for any fixed number of samples N, and it holds

$$\zeta_N^e \approx \begin{cases} \mathcal{N}(0,\,\Sigma^e) & \text{under } H_0 \\ \mathcal{N}(\delta,\,\Sigma^e) & \text{under } H_1 \end{cases}, \tag{4.21}$$

where $\delta = \sqrt{N}\,\Upsilon^e$ with $\Upsilon^e = \mathbf{E}\big(\mathrm{vec}\big(S_0^T \hat{\mathbf{H}}_p\big)\big) = \mathrm{vec}\big(S_0^T \mathbf{H}_p\big)$.

Note that Υ^e depends on the expected value $\mathbf{H}_p$ of the Hankel matrix of the current system (which is independent of the number of samples N), and $\hat{\mathbf{H}}_p$ is a consistent estimate of matrix $\mathbf{H}_p$. Note also that $\Upsilon^e = 0$ if the system is in the reference state due to the definition of the null-space.

In the following, the influence of N on the expected value of the test variable χ_N^2 in (4.19) is investigated.

Theorem 1 *Under the undamaged state of the structure, i.e. H_0 is true, increase or decrease of the number of samples does not change the mean of the χ^2 value.*

Proof 1 Since $\zeta_N^e \approx \mathcal{N}(0,\Sigma^e)$ under H_0 (independently of the number of samples N), the non-centrality parameter of the resulting test variable χ_N^2 in (4.19) is 0, as stated in Sect. 4.3. From the property (4.20) of the χ^2 distribution it follows $\mathbf{E}\chi_N^2 = d$ where $d = \dim\big(\zeta_N^e\big)$ is the number of degrees of freedom of χ_N^2, independently of N.

Theorem 2 *If the structure is damaged, i.e. H_1 is true, change of the number of samples will result in a change (in the same direction) in the mean of the evaluated χ^2 test variable.*

Proof 2 Under H_1 the non-centrality parameter of χ_N^2 is $\delta^T(\Sigma^e)^{-1}\delta$. Since $\delta = \sqrt{N}\,\Upsilon^e$, the non-centrality parameter yields $N(\Upsilon^e)^T(\Sigma^e)^{-1}\Upsilon^e$, where both Υ^e and Σ^e are independent of N. From the property (4.20) of the non-central χ^2 distribution, it follows $\mathbf{E}\chi_N^2 = d + N(\Upsilon^e)^T(\Sigma^e)^{-1}\Upsilon^e$. Thus the mean of the test variable grows (or decreases) when the number of samples of the same damaged system grows (or decreases).

4.3.2 Effect of Measurement Noise

Effect of the amount of measurement noise is investigated in two settings. In the first one, the properties of the measurement noise are the same in the reference state and possibly damaged state, while in the second setting they are different. Each of these settings are investigated in the following sections.

First, some properties regarding the noise properties of the state space system (4.2) are recalled [19]. They are given by

$$\mathbf{E}\left[\begin{pmatrix} w_k \\ v_k \end{pmatrix}\begin{pmatrix} w_k^T & v_k^T \end{pmatrix}\right] = \begin{pmatrix} Q & S \\ S^T & R \end{pmatrix}$$

Only matrix R depends on the variance of the measurement noise. Note that the measurement noise is denoted as e in system (4.1), and the output noise term v_k is in fact a sum of the measurement noise and the excitation noise in the case of acceleration measurements. In this case matrix S only depends on the excitation noise, assuming that excitation and measurement noise are independent.

With these definitions, it can be seen that the expected value of the Hankel matrix does not depend on the measurement noise, since $R_i = \mathbf{E}\big(y_k y_{k-i}^T\big) = HF^{i-1}G$ for $i \geq 1$, where $G = FDH^T + S$ with D being the state covariance. None of these quantities depend on the measurement noise under the previous assumptions.

However, the residual covariance $\Sigma^e = \lim_N \mathbf{E}\Big(\big(\zeta_N^e - \mathbf{E}\zeta_N^e\big)\big(\zeta_N^e - \mathbf{E}\zeta_N^e\big)^T\Big)$ depends on the measurement noise, since squared terms like $\mathrm{vec}\big(\hat{R}_i\big)\mathrm{vec}\big(\hat{R}_i\big)^T$ appear within the expectation, and the expected value of data correlations without lag, $\mathbf{E}\big(y_k y_k^T\big) = HDH^T + R$, indeed depends on the measurement noise [19]. However, we will not make a detailed mathematical analysis of the relationship between residual covariance and measurement noise in this paper, but content ourselves with a qualitative analysis for simplicity and clarity.

For the analysis of the effect of changes in the measurement noise between noise properties e_1 and e_2, we denote $e_1 > e_2$ if the respective output noise covariance matrices satisfy $R^{e_1} \succ R^{e_2}$ (i.e. $R^{e_1} - R^{e_2}$ is positive definite). e_1 represents a higher measurement noise than e_1. This is the case if each of the measured signals in the first configuration have a lower signal to noise ratio than the respective signals in the second configuration (while the properties of the ambient excitation noise remain the same). A higher measurement noise leads to larger variations in the residual and thus to a bigger residual covariance. For our qualitative analysis, assume respectively $\Sigma^{e_1} = \alpha\Sigma^{e_2}$ with a scalar magnification factor $\alpha > 1$ to be able to study this effect in a closed form formulation. This magnification factor is in direct relation with the signal to noise ratio if the noise type is white. However, for colored noise this magnification factor is an approximate representation of the noise effect.

The effect of changes in the measurement noise is now investigated in two settings. In the first one, the noise properties between the reference state and possibly damaged state are constant, while in the second setting they are different.

4.3.2.1 Equal Noise Properties Between the Reference State and Possibly Damaged State

In this section, it is assumed that the measurement noise properties in data from reference state and possibly damaged state are equal. We compare different noise properties that are the equal in both states. Note that the residual covariance matrices Σ^{e_1} and Σ^{e_2} for different noise properties e_1 and e_2 are assumed to be obtained from reference datasets under the respective conditions.

Theorem 3 *If the structure is* ***undamaged*** *and the noise properties of both the reference state data and the current state data are equal, then an increase or decrease of the noise in both states does not change the expected* χ^2 *value. In other words,* $\mathbf{E}\left[\left(\zeta_N^{e_1}\right)^T\left(\Sigma^{e_1}\right)^{-1}\zeta_N^{e_1}\right] = \mathbf{E}\left[\left(\zeta_N^{e_2}\right)^T\left(\Sigma^{e_2}\right)^{-1}\zeta_N^{e_2}\right]$ *under* H_0.

Proof 3 From the property of the χ^2 distribution in (4.20) it follows that the expected value of the respective χ^2 values is $d = \dim\left(\zeta_N^{e_1}\right) = \dim\left(\zeta_N^{e_2}\right)$ under H_0, as in Proof 1, which is independent of the noise.

Theorem 4 *If the structure is* ***damaged*** *and the noise properties of both the reference state data and the current state data are equal, then an increase or decrease of the noise in both states results in a change (in inverse direction) in the expected* χ^2 *value for a constant damage. In other words, if* $e_1 > \mathrm{e}_2$ *then* $\mathbf{E}\left[\left(\zeta_N^{e_1}\right)^T\left(\Sigma^{e_1}\right)^{-1}\zeta_N^{e_1}\right] < \mathbf{E}\left[\left(\zeta_N^{e_2}\right)^T\left(\Sigma^{e_2}\right)^{-1}\zeta_N^{e_2}\right]$ *under* H_1.

Proof 4 As shown in the beginning of Sect. 4.4.2, the measurement noise does not influence the expected value of the respective Hankel matrices. Hence, $\delta = \mathbf{E}\zeta_N^{e_1} = \mathbf{E}\zeta_N^{e_2}$ is equal for both noise configurations (see also Eq. (4.21)), while the non-centrality parameters are $n_c^{e_1} = \delta^T\left(\Sigma^{e_1}\right)^{-1}\delta$ and $n_c^{e_2} = \delta^T\left(\Sigma^{e_2}\right)^{-1}\delta$, respectively. Due to assumption $\Sigma^{e_1} = \alpha\Sigma^{e_2}$ it follows $n_c^{e_1} = \frac{1}{\alpha}n_c^{e_2}$ with $\alpha > 1$, hence $n_c^{e_1} < n_c^{e_2}$. Then, the assertion follows from property (4.20) of the χ^2 distribution.

Theorem 4 is also intuitive in the sense that higher noise, i.e. a lower signal-to-noise ratio, decreases the quality of the data and makes it harder to detect damage, which is reflected in the lower χ^2 test value.

4.3.2.2 Different Noise Properties Between the Reference State and Possibly Damaged State

In this section it is assumed that the measurement noise will change in the test data irrespective to the noise in the reference data where the residual covariance was computed. Note that since the noise properties of the residual do not correspond to its covariance anymore, one would need to recompute the covariance matrix to accommodate noise changes in a correct test [11]. Moreover, the resulting χ^2 test value does not satisfy the stated parameters of the χ^2 distribution as in Sect. 4.3 anymore, which are shifted now. However, the numerical computation of the covariance is complex and impractical on each tested dataset in practice. Hence, the covariance is usually only computed once in the reference state, which is valid when the measurement noise properties are stable. In this section we investigate the consequence of different noise properties on the test results, violating the theoretical assumptions of the test.

First, the effect of changes in the measurement noise in the test data are investigated, while the noise level in the residual covariance remains constant. Second, different noise levels in the residual covariance are investigated, while the noise level in the test data remains constant.

Theorem 5 Change in the noise properties of the test data results in a change in the expected χ^2 value in the same direction, regardless to the state of the structure. In other words, if $\mathrm{e}_1 > \mathrm{e}_2$ then $\mathbf{E}\left[\left(\zeta_N^{e_1}\right)^T\left(\Sigma^{e_2}\right)^{-1}\zeta_N^{e_1}\right] > \mathbf{E}\left[\left(\zeta_N^{e_2}\right)^T\left(\Sigma^{e_1}\right)^{-1}\zeta_N^{e_2}\right]$ both under H_0 and H_1.

Proof 5 Analogous to Proof 4, if follows from the property (4.20) of the χ^2 distribution $\mathbf{E}\left[\left(\zeta_N^{e_1}\right)^T\left(\Sigma^{e_1}\right)^{-1}\zeta_N^{e_1}\right] = d + \delta^T\left(\Sigma^{e_1}\right)^{-1}\delta$. Using $\Sigma^{e_1} = \alpha\Sigma^{e_2}$ with $\alpha > 1$, it follows furthermore $\mathbf{E}\left[\left(\zeta_N^{e_2}\right)^T\left(\Sigma^{e_1}\right)^{-1}\zeta_N^{e_2}\right] = \frac{1}{\alpha}\mathbf{E}\left[\left(\zeta_N^{e_2}\right)^T\left(\Sigma^{e_2}\right)^{-1}\zeta_N^{e_2}\right]$. The right expectation corresponds now to a standard χ^2 distribution and hence

$$\begin{aligned}\mathbf{E}\left[\left(\zeta_N^{e_2}\right)^T\left(\Sigma^{e_1}\right)^{-1}\zeta_N^{e_2}\right] &= \frac{1}{\alpha}\left(d+\delta^T\left(\Sigma^{e_2}\right)^{-1}\delta\right) = \frac{1}{\alpha}\left(d+\delta^T\left[\alpha\left(\Sigma^{e_1}\right)^{-1}\right]\delta\right)\\ &= \frac{1}{\alpha}d+\delta^T\left(\Sigma^{e_1}\right)^{-1}\delta\end{aligned}$$

Comparing now with $\mathbf{E}\left[\left(\zeta_N^{e_1}\right)^T\left(\Sigma^{e_1}\right)^{-1}\zeta_N^{e_1}\right]$, the assertion follows both for H_0 (where $\delta = 0$) and for H_1, since $\alpha > 1$.

Theorem 5 may be somewhat counterintuitive as it states “less noise leads to a weaker reaction of the test”. However, this would not be the case if the appropriate covariance matrix had been used, which would be of lower magnitude and thus would normalize the residual correctly by dividing it with lower values.

Theorem 6 *Regardless of the state of the system, change in the noise properties of the reference data, on which the residual covariance is computed, results in a change in inverse direction in the expected* χ^2 *value. In other words, if* $e_1 > e_2$ *then* $\mathbf{E}\left[\left(\zeta_N^{e_1}\right)^T\left(\Sigma^{e_1}\right)^{-1}\zeta_N^{e_1}\right] < \mathbf{E}\left[\left(\zeta_N^{e_1}\right)^T\left(\Sigma^{e_2}\right)^{-1}\zeta_N^{e_1}\right]$ *both under* H_0 and H_1.

Proof 6 The proof is analogous to the Proof 5. We have $\mathbf{E}\left[\left(\zeta_N^{e_1}\right)^T\left(\Sigma^{e_1}\right)^{-1}\zeta_N^{e_1}\right] = d+\delta^T\left(\Sigma^{e_1}\right)^{-1}\delta$, and since $\Sigma^{e_1} = \alpha\Sigma^{e_2}$ with $\alpha > 1$, $\mathbf{E}\left[\left(\zeta_N^{e_1}\right)^T\left(\Sigma^{e_1}\right)^{-1}\zeta_N^{e_1}\right] = \alpha\mathbf{E}\left[\left(\zeta_N^{e_1}\right)^T\left(\Sigma^{e_1}\right)^{-1}\zeta_N^{e_1}\right] = \alpha d+\alpha\delta^T\left(\Sigma^{e_1}\right)^{-1}\delta$. Hence the assertion follows both for H_0 and for H_1.

4.4 Numerical Application

In this section the theorems stated at Sect. 4.4 are demonstrated for a simple mass-spring system. This system is composed of six degrees of freedom associated to six masses connected with springs as shown in Fig. 4.1. There is a damping ratio of 2 % associated to all modes. Damage is modeled as a stiffness reduction of 5 % of the second spring, i.e. k_2. The excitation is simulated as Gaussian white noise and the resulting acceleration measurements are acquired from three sensors located on the masses at a sampling rate of 50 Hz. In order to illustrate the effects in the theorems, three case studies are performed. The first one is related to Theorems 1–2, second one is related to Theorems 3–4, and the last one is related to Theorems 5–6.

4.4.1 Cases Study 1, Effect of Number of Samples

For this case, the number of samples is changed from 1000, 2000, . . ., to 10000 in 10 steps for both undamaged and damaged cases. In each step, 100 repetitions are made to calculate the mean, representing the expected value of the χ_N^2. The measurement noise ratio in all cases is 5 %. It can be seen from the results in Fig. 4.2, that as stated in Theorem 1, when the model is not damaged, the expected χ_N^2 is not changed. However, when the model is damaged, it can be seen that this value grows linearly with the number of samples, which confirms the (linear) factor N in the non-centrality parameter as shown in the proof of Theorem 2.

4.4.2 Case Study 2, Effect of Noise with Equal Properties

In here, the number of samples is kept constant at 10000. However, the measurement noise, which has equal properties in reference and testing state, is changed. This noise ratio is changed from 5 to 125 % in 25 steps for damaged and undamaged

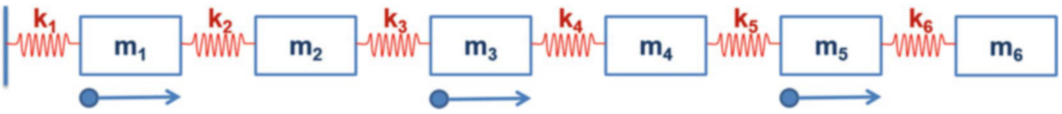

Fig. 4.1 The mass-spring model and the sensor locations

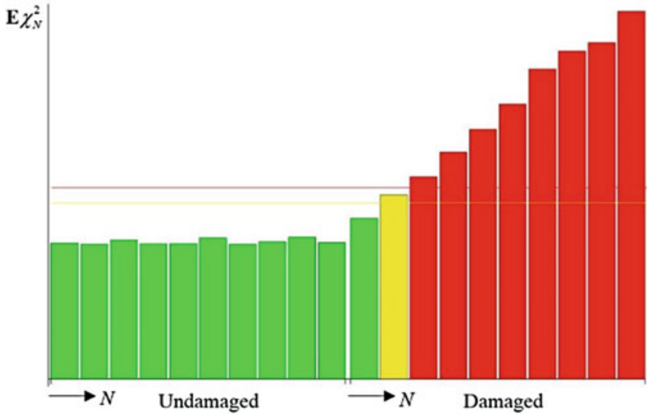

Fig. 4.2 Expected χ_N^2 value evaluated for different number of samples in damaged and undamaged conditions (*red line*: 99 percentile, *yellow line*: 95 percentile)

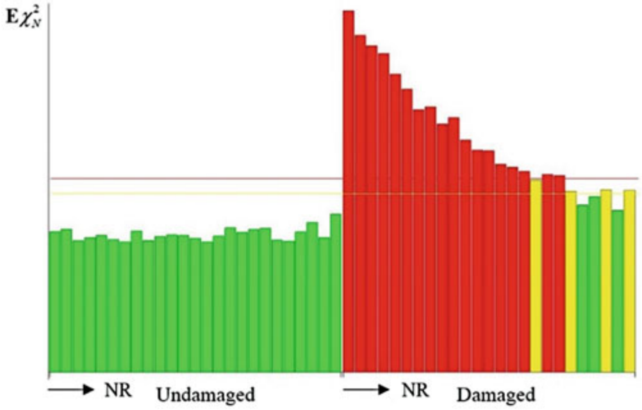

Fig. 4.3 Expected χ_N^2 value evaluated for different noise ratios with equal properties in damaged and undamaged conditions (*red line*: 99 percentile, *yellow line*: 95 percentile)

conditions. Again in each step the repetition is 100 times. The results are presented in Fig. 4.3. The test values in the undamaged state are constant and independent of the noise ratio, confirming Theorem 3. The test values in the damaged state decrease when the noise ratio increases, as shown in Theorem 4. From Fig. 4.3 it can be observed that the test values decrease approximately quadratically with increasing noise, thus the factor α in Sect. 4.3.2 seems to be quadratic in the measurement noise level.

4.4.3 Case Study 3, Effect of Noise with Unequal Properties

In this case study, the noise properties are not equal in the reference and test states as mentioned in Sect. 4.4.2. For this purpose, same as previous case study, the number of samples is constantly equal to 10000. The noise is being increased in 25 steps from 5 to 125 % with 100 repetitions in each step. This is also investigated for damaged and undamaged conditions. In Fig. 4.4 the results are shown when the measurement noise is changed only for the testing state (both in undamaged and damaged conditions, respectively). The measurement noise in the reference state that was used to set up the residual covariance is constant at 5 %. It can be seen that both in undamaged and damaged states the test value increases when the noise level increases, confirming Theorem 5. Again, the increase rate seems to be quadratic.

In Fig. 4.5, the same study is done for the changing of measurement noise in the residual covariance computed in the reference state while the measurement noise in the test data is kept constant at 5 %. It can be seen that by increasing the measurement noise in the reference data, the expected χ_N^2 value is being decreased for both undamaged and damaged conditions, as stated in Theorem 6.

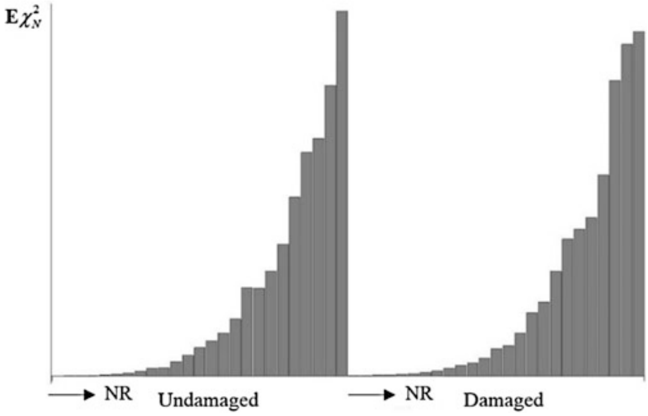

Fig. 4.4 Expected χ_N^2 value evaluated for different noise ratios only in the test data, in damaged and undamaged conditions

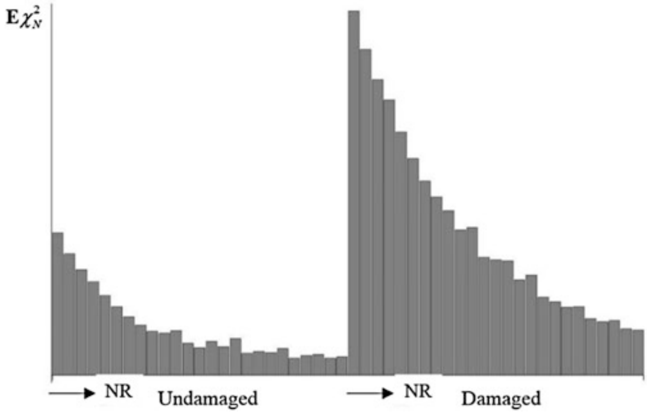

Fig. 4.5 Expected χ_N^2 value evaluated for different noise ratios only in the reference data, in damaged and undamaged conditions

4.5 Discussion and Conclusion

In this paper, several theorems are proposed and proved on the effect of noise and number of samples on SSDD technique. From these theorems some conclusions can be inferred that will serve the user of SSDD technique as a guideline in dealing with these effects.

1. Considering Theorems 1 and 2, data duration does not affect the expected χ^2 value in the reference state. This is an advantage of this approach that will help in identifying a unique threshold in the reference state which can be compared to the χ^2 value acquired from the test data. However, when the structure is damaged, by increasing the data length the χ^2 value will be increased. In other words, if there is more data the damage state becomes more distinct and identifiable. Therefore, the more samples we have, the better results we get to detect the damage, and if there is not enough data, the damage state may not be identifiable.
2. Different noise levels in the system (each time both for reference and test data) lead to changes in the resulting χ^2 values acquired from damaged structure changes in inverse direction (Theorems 3 and 4). Therefore, an increase of measurement noise in the system results in decreasing the χ^2 value for damaged state, making the damage possibly undetectable. Note that this can be compensated by longer datasets (see previous point). The amount of measurement noise in the system should not be too high.
3. It can be inferred from Theorem 5 that by having higher noise in the test or validation data, while the residual covariance is not re-evaluated, their χ^2 value becomes higher. This can affect the damage detection process in two ways. Firstly, if the safety thresholds are evaluated from a low noise reference data, then a high noise test data from undamaged structure can be identified as being damaged leading to a false alarm. Secondly, if the safety thresholds are evaluated from a high noise reference data and the noise in test data of damaged structure is very low, then the damaged structure might not be detected. These two suggests that the measurement noise in the reference and test data should be about the same. The sensitivity of the threshold was studied in [15].

4. Based on Theorem 6, increasing noise in the reference data results in a decrease of the χ^2 value for both undamaged and damaged test data. Nevertheless, the effect of damage for the same noise level is still visible.

It should be mentioned that, in all of these cases it is assumed that the reference data is not corrupted with too high noise and that the left null-space ${S_0}^T$ and the residual covariance matrix Σ^e are evaluated properly.

References

1. Fan, W., Pizhong, Q.: Vibration-based damage identification methods: a review and comparative study. Struct. Health Monit. **10**(1), 83–111 (2011)
2. Doebling, S.W., Farrar, C.R., Prime, M.B.: A summary review of vibration-based damage identification methods. Shock and Vibration Digest **30**(2), 91–105 (1998)
3. Salawu, O.S.: Detection of structural damage through changes in frequency: a review. Eng. Struct. **19**(9), 718–723 (1997)
4. Worden, K., Farrar, C.R., Manson, G., Park, G.: The fundamental axioms of structural health monitoring. In: Proceedings of the Royal Society of London A: Mathematical, Physical and Engineering Sciences, 463.2082, The Royal Society (2007)
5. Farrar, C.R., Doebling, S.W., Nix, D.A.: Vibration–based structural damage identification. Philos. Trans. R. Soc. Lond. A **359**(1778), 131–149 (2001)
6. Yan, A.M., De Boe, P., Golinval, J.C.: Structural damage diagnosis by Kalman model based on stochastic subspace identification. Struct. Health Monit. **3**(2), 103–119 (2004)
7. Worden, K., Manson, G., Fieller, N.R.J.: Damage detection using outlier analysis. J. Sound Vib. **229**(3), 647–667 (2000)
8. Basseville, M., Abdelghani, M., Benveniste, A.: Subspace-based fault detection algorithms for vibration monitoring. Automatica **36**(1), 101–109 (2000)
9. Basseville, M., Mevel, L., Goursat, M.: Statistical model-based damage detection and localization: subspace-based residuals and damage-to-noise sensitivity ratios. J. Sound Vib. **275**(3), 769–794 (2004)
10. Carden, E.P., Fanning, P.: Vibration based condition monitoring: a review. Struct. Health Monit. **3**(4), 355–377 (2004)
11. Döhler, M., Mevel, L., Hille, F.: Subspace-based damage detection under changes in the ambient excitation statistics. Mech. Syst. Signal Process. **45**(1), 207–224 (2014)
12. Döhler, M., Hille, F.: Subspace-based damage detection on steel frame structure under changing excitation. Structural Health Monitoring, vol. 5, pp. 167–174. Springer International Publishing, (2014)
13. Alvandi, A., Cremona, C.: Assessment of vibration-based damage identification techniques. J. Sound Vib. **292**(1), 179–202 (2006)
14. Döhler, M., Mevel, L.: Subspace-based fault detection robust to changes in the noise covariances. Automatica **49**(9), 2734–2743 (2013)
15. Allahdadian, S., Ventura, C., Andersen, P., Mevel, L., Döhler, M.: Investigation on the sensitivity of subspace based damage detection technique to damage and noise levels. In: IOMAC-International Operational Modal Analysis Conference, Gijon, Spain. (2015)
16. Allahdadian, S., Ventura, C., Andersen, P., Mevel, L., Döhler, M.: Subspace based damage detection technique: investigation on the effect of number of samples. In: CCEE-Canadian Conference on Earthquake Engineering, Victoria, Canada. (2015)
17. Allahdadian, S., Ventura, C., Andersen, P., Mevel, L., Döhler, M.: Sensitivity evaluation of subspace-based damage detection method to different types of damage. Structural Health Monitoring and Damage Detection, vol. 7, pp. 11–18. Springer International Publishing, Florida, USA. (2015)
18. Basseville, M., Benveniste, A., Goursat, M., Hermans, L., Mevel, L., Van der Auweraer, H.: Output-only subspace-based structural identification: from theory to industrial testing practice. J. Dyn. Syst. Meas. Control **123**(4), 668–676 (2001)
19. Van Overschee, P., De Moor, B.: Subspace Identification for Linear Systems: Theory, Implementation, Applications. Kluwer, Dordecht (1996)
20. Benveniste, A., Basseville, M., Moustakides, G.: The asymptotic local approach to change detection and model validation. IEEE Trans. Autom. Control **32**(7), 583–592 (1987)
21. Balmès, E., Basseville, M., Bourquin, F., Mevel, L., Nasser, H., Treyssède, F.: Merging sensor data from multiple temperature scenarios for vibration-based monitoring of civil structures. Struct. Health Monit. **7**(2), 129–142 (2008)

Chapter 5
Quantification of Structural Damage with Self-Organizing Maps

Osama Abdeljaber, Onur Avci, Ngoan Tien Do, Mustafa Gul, Ozan Celik, and F. Necati Catbas

Abstract One of the main tasks in structural health monitoring process is to create reliable algorithms that are capable of translating the measured response into meaningful information reflecting the actual condition of the monitored structure. The authors have recently introduced a novel unsupervised vibration-based damage detection algorithm that utilizes self-organizing maps to quantify structural damage and assess the overall condition of structures. Previously, this algorithm had been tested using the experimental data of Phase II Experimental Benchmark Problem of Structural Health Monitoring, introduced by the IASC (International Association for Structural Control) and ASCE (American Society of Civil Engineers). In this paper, the ability of this algorithm to quantify structural damage is tested analytically using an experimentally validated finite element model of a laboratory structure constructed at Qatar University.

Keywords Self organizing maps • Damage detection • Damage identification • Structural health monitoring • Modal testing

5.1 Introduction

Engineering structures are subjected to environmental and human-induced factors that reduce reliability and life cycle performance regardless of their design quality. Structural damage due to deterioration, fatigue, corrosion, creep, shrinkage and scour are commonly encountered especially in countries with extreme climate. The traditional approaches of damage assessment which basically rely on visual inspection and human judgment are no longer effective due to economical and practical reasons. Therefore, it is of utmost importance to develop automated and smart structural damage detection systems with the ability to assess the structural condition in the real-time.

In general, damage detection techniques are classified into local and global methods. Local damage detection methods are developed to detect and quantify damage in a relatively small scale, whereas global techniques are implemented to track the overall behavior of structures. Due to the large size and complexity of civil infrastructures, local damage assessment methods are not sufficient for health monitoring of such structures. Consequently, local damage detection techniques should be incorporated with global techniques (i.e., vibration-based techniques) to develop an efficient structural health monitoring system that provides a complete understanding of the structural condition. Vibration-based damage assessment methods use the vibration response of the structure measured by a relatively small set of accelerometers for damage identification and quantification. Vibration-based damage assessment approaches are divided into parametric and nonparametric methods. Parametric methods use structural system identification algorithms to identify the modal parameters of the monitored structure, such as modal frequencies and damping ratios, according to the measured vibration response. Nonparametric methods employ statistical approaches to process raw acceleration signals and extract damage indicators. Nonparametric algorithms demonstrate damage features that cannot be easily attributed to physical changes of the monitored structure [1]. Therefore, nonparametric methods have attracted the attention of researchers in the field of structural health monitoring [2].

O. Abdeljaber • O. Avci (✉)
Department of Civil and Architectural Engineering, College of Engineering, Qatar University, P.O. Box 2713, Doha, Qatar
e-mail: onur.avci@qu.edu.qa

N.T. Do • M. Gul
Department of Civil and Environmental Engineering, University of Alberta, 7-203 Donadeo Innovation Centre for Engineering,
9211-116 Street NW, Edmonton, AB, Canada, T6G 2R3

O. Celik • F.N. Catbas
Department of Civil, Environmental and Construction Engineering, University of Central Florida, Central Florida Blvd, Orlando,
FL 32816-2450, USA

A. Wicks, C. Niezrecki (eds.), *Structural Health Monitoring, Damage Detection & Mechatronics, Volume 7*,
Conference Proceedings of the Society for Experimental Mechanics Series, DOI 10.1007/978-3-319-29956-3_5

Artificial neural networks (ANNs) have been used by several researchers in an attempt to develop nonparametric damage detection algorithms. Many types ANNs have been implemented for this purpose such as nonlinear autoregressive with exogenous inputs (NARX) neural networks [3], probabilistic resource allocation networks [4], pattern recognition neural networks [5], and Bayesian neural networks [6].

Self-organizing maps (SOMs) are another important type of neural networks that can be used to generate a two-dimensional map that describes the topology of the input data. In other words, SOMs are utilized to cluster high-dimensional data set into a number of groups. SOMs are trained using unsupervised learning rules, which means that the training process of SOMs relies only on the internal properties between the inputs and does not require input–output samples [7].

Recently, the authors have introduced a novel nonparametric damage detection algorithm that relies on SOMs to extract damage indices from the acceleration data in the time domain measured under random excitation. In a previous study [8], the authors have demonstrated the ability of this algorithm to quantify structural damage under five damage scenarios included in Phase II Experimental Benchmark Problem of Structural Health Monitoring [9]. These scenarios include removing braces and/or loosening bolts of an experimental four-story steel frame. The results have shown that this algorithm is accurate, robust, and reliable for damage quantification.

In the study presented herein, the SOM-based damage detection algorithm is tested analytically on a finite element model of a recently constructed lab structure. As will be explained in Sect. 5.2, this lab structure represents the first phase of the construction of a grandstand simulator at Qatar University (QU). The accuracy of the finite element model used in this study has been experimentally validated by comparing the finite element modal properties to the actual properties of the lab structure which were measured using experimental modal testing. The five damage cases considered in this study are created analytically either by introducing damage to a number of connections or by slightly reducing the stiffness of particular beams.

5.2 Qatar University Grandstand Simulator

The authors are currently conducting comprehensive analytical and laboratory studies related to structural health monitoring and vibrations serviceability of stadia. These studies aim at developing new structural damage detection methods optimized for monitoring of modern stadia as well as investigating the effects of human-environment-structure interaction on the dynamic response of such structures. A grandstand simulator is currently under construction at Qatar University to serve as a test bed for the aforementioned studies.

QU grandstand simulator is still in the initial phase of construction. So far, as shown in Fig. 5.1, only the main steel frame has been constructed. Non-structural elements such as the risers, treads, handrails, and seats will be installed in the next stage of construction. However, before proceeding with the construction of the complete structure, the authors have decided to utilize the test structure in its current form to conduct a series of studies related to modal testing and structural damage detection.

Fig. 5.1 QU grandstand simulator under construction

The main steel frame of QU grandstand simulator consists of 8 main beams and 25 filler beams supported on 4 columns. The eight main beams are 4.6 m long, while the length of the five filler beams in the lower portion is about 1 m and the length of the remaining filler beams is 77 cm. The main girders as well as the secondary beams were assigned by slender steel sections (IPE120). The 25 filler beams are removable and interchangeable which makes this test structure ideal for damage detection studies since many damage scenarios can be simulated either by loosening the bolts at beams to girder connections or by replacing some of the filler beams with damaged ones.

5.3 Verification of the Finite Element Model

Based on the design calculation and CAD drawings, a detailed three-dimensional finite element model of the main steel frame of QU grandstand was created using Abaqus 6-14 [10]. This FE model is shown in Fig. 5.2. All members within the steel deck were modeled as C3D20R elements (20-node quadratic brick, reduced integration). A very fine mesh was used to model the members in order to enhance the accuracy of the FE model. The connections between the main and secondary beams were modeled in Abaqus as tie constraints. The steel deck was assumed to be pin-supported over the locations of the four columns. All elements in the FE model were assigned by 210 GPa Young's modulus, 0.3125 Poisson's ratio, and 7850 Kg/m^3 density. Lanczos eigensolver was used to identify the natural frequencies and the mode shapes of the first four bending modes of the FE model. The results of this numerical modal analysis are provided in Fig. 5.3 and Table 5.1.

Dynamic impact test was carried out in order to experimentally measure the actual natural frequency, mode shapes, and damping ratios of the steel frame. In order to verify the accuracy of the finite element model, a comparison between the finite element and experimental modal frequencies is presented in Table 5.1. This comparison indicates an excellent agreement between the actual frequencies measured experimentally by impact testing and those predicted analytically by finite element analysis especially for the first two bending modes. Therefore, it can be concluded that the finite element model represents the fundamental modes of the structure accurately even without applying finite element model updating techniques.

5.4 The SOM-Based Damage Detection Algorithm

As previously mentioned, the authors have recently developed and tested an SOM-based nonparametric damage detection algorithm [8]. In this algorithm, SOMs are utilized to process the signals acquired by the accelerometers in the time domain measured under random excitation in order to generate a topology map for the random response at each node. The topology maps generated for the undamaged structure are considered as the structural signature. The algorithm requires dividing the accelerometers into groups of two. For each group, a self-organized map is trained and used to extract features from the relative response between its two accelerometers for the undamaged structure. These features (in the form of two-dimensional maps) constitute the baseline of the proposed damage assessment technique. When damage assessment is conducted, the same feature extraction procedure is applied. By comparing the baseline and the measured two-dimensional maps, damage can be quantified by measuring the extent to which the relative response between the two accelerometers in each group has changed with respect to the undamaged condition. The training and implementation processes of the SOM-based damage detection algorithm are explained in the following two subsections.

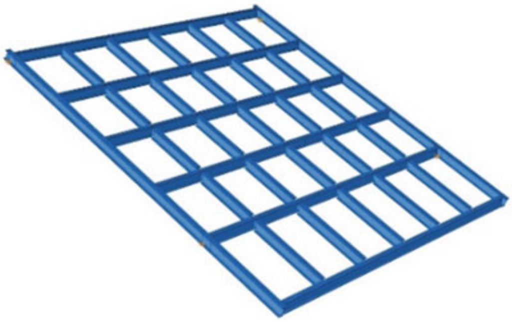

Fig. 5.2 Abaqus finite element model of the test structure

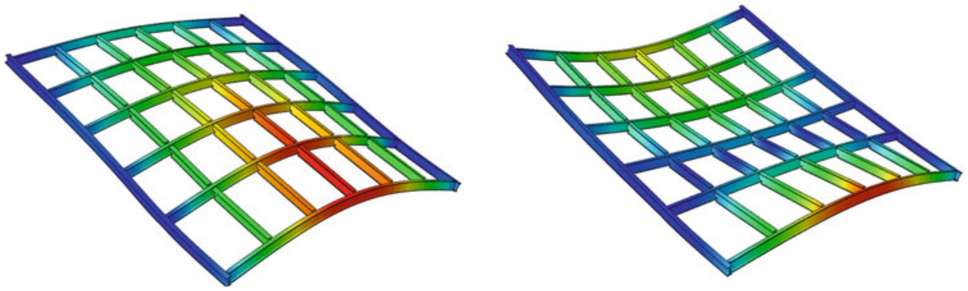

1st Bending Mode 2nd Bending Mode

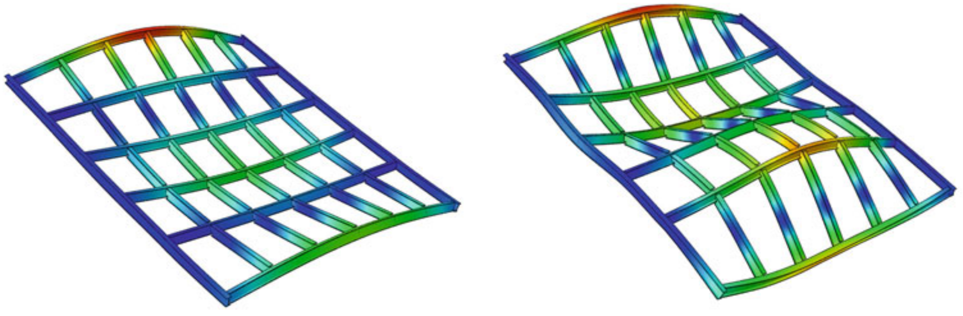

3rd Bending Mode 4th Bending Mode

Fig. 5.3 The first four bending modes of the test structure

Table 5.1 Comparison between the finite element and the experimental natural frequencies

Bending mode	Finite element frequency (Hz)	Experimental frequency (Hz)	Error (%)
1	16.00	15.7	1.91
2	16.58	16.4	1.10
3	24.48	25.2	−2.86
4	48.34	50.6	−4.47

5.4.1 *Training of the SOMs*

Training of the SOMs is conducted according to the following steps:

Step 1: The vibration response of the undamaged structure under random excitation signal is measured for *n* time steps using a set of accelerometers.

Step 2: The accelerometers are divided into *k* groups $\left(G^{i=1}, G^{i=2}, \ldots, G^{i=k}\right)$. Each group is assigned by two accelerometers G_1^i and G_2^i.

Step 3: The relative acceleration signal between the two accelerometers in each group *i* is computed as

$$S^i = G_2^i - G_1^i \tag{5.1}$$

Step 4: For each relative acceleration signal S^i, at each time step *t*, the acceleration value at this time step as well as the values at *d* time steps behind $\left(S_{t-d}^i, S_{t-d+1}^i, \ldots, S_{t-1}^i\right)$ are stored in a vector $\boldsymbol{V}_t^i = \left[S_{t-d}^i \; S_{t-d+1}^i \; \ldots \; S_{t-1}^i \; S_t^i\right]$. Therefore, at the end of this step a total of *n* vectors are stored for each acceleration signal. This process is illustrated in Fig. 5.4.

Step 5: All vectors generated in the previous step are normalized by dividing each one by its maximum absolute value according to the following equation.

$$\boldsymbol{VN}_t^i = \frac{\boldsymbol{V}_t^i}{\max\left|\boldsymbol{V}_t^i\right|} \tag{5.2}$$

Fig. 5.4 Signals processing and computation of vectors

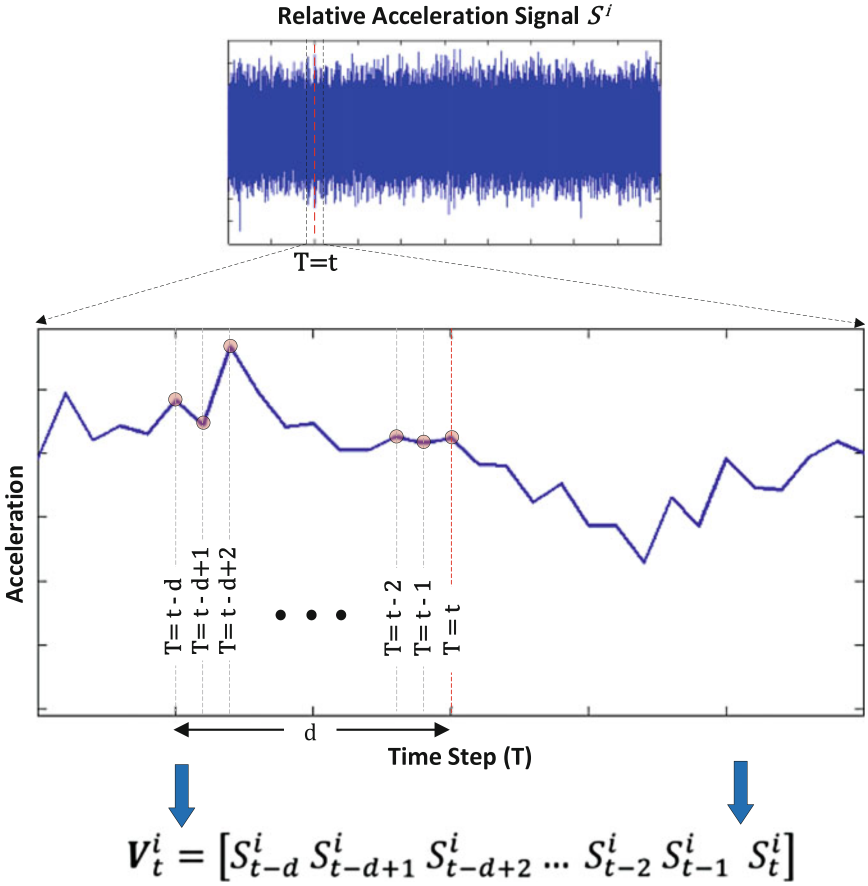

Step 6: The normalized vectors corresponding to each relative accelerometer signal S^i are arranged in a matrix $\boldsymbol{M}^i = \left[\boldsymbol{VN}_{t=1}^i \; \boldsymbol{VN}_{t=2}^i \dots \; \boldsymbol{VN}_{t=n}^i\right]^{\mathrm{t}}$. The number of matrices generated in this step equals to the total number of groups k.

Step 7: A self-organizing map SOM^i is trained to cluster the normalized vectors in each matrix $\boldsymbol{M}^i$ corresponding to the relative acceleration signal S^i into a two dimensional topology map $\boldsymbol{T}_u{}^i$ with a dimension of $(l \times l)$. In other words, the self-organizing map SOM^i is trained to classify the n normalized vectors in the matrix $\boldsymbol{M}^i$ into $(l \times l)$ groups according to the similarity between the vectors. Therefore, each element in the topology map generated after the training of SOM^i will be assigned by an integer which describes how many vectors in the matrix $\boldsymbol{M}^i$ are assigned to the group represented by this element. The training of the SOMs is carried out using batch unsupervised weight/bias training algorithm. At the end of this step, a total of k SOMs corresponding to the total number of accelerometers groups are trained. Also, a total of k topology maps are obtained. The trained SOMs are stored in order to be used for damage assessment. The procedure described in this step is explained in Fig. 5.5.

Step 8: The topology maps for the undamaged case generated by each SOM $\left(\boldsymbol{T}_u^{i=1}, \; \boldsymbol{T}_u^{i=2}, \; \dots, \boldsymbol{T}_u^{i=k}\right)$ are normalized by dividing each map by the total number of normalized vectors in the corresponding matrix $\boldsymbol{M}^i$ (i.e. the number of time steps n in the recorded acceleration signals).

$$\boldsymbol{TN}_u^i = \frac{\boldsymbol{T}_u^i}{n} \tag{5.3}$$

Step 9: The normalized topology maps for the undamaged case $\left(\boldsymbol{TN}_u^{i=1}, \; \boldsymbol{TN}_u^{i=2}, \; \dots, \boldsymbol{TN}_u^{i=k}\right)$ are stored in order to be used for damage assessment.

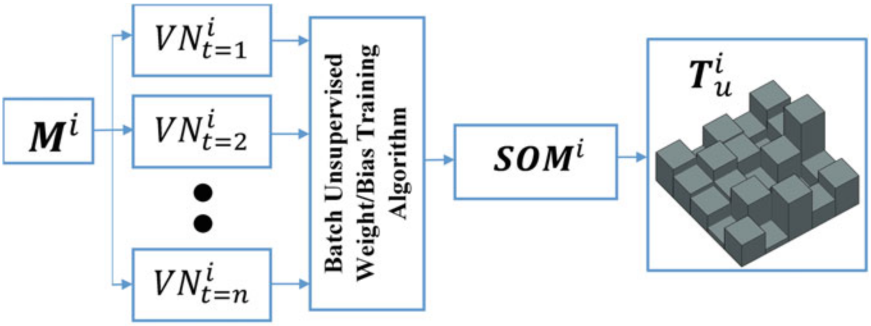

Fig. 5.5 Training of self-organizing maps and generation of topology maps

5.4.2 *Structural Damage Assessment*

Here, the SOMs as well as the normalized topology maps for the undamaged case obtained by the previous procedure are used to evaluate the condition of the monitored structure by comparing the measured topology maps to the topology maps generated for the undamaged case (i.e. the structural signature). This is explained in the following steps.

Step 1: The response of the monitored structure under random excitation is measured for n time steps using a set of accelerometers.

Step 2: The steps 2–6 explained in the previous section are followed in order to create the matrices $\left(\boldsymbol{M}^{i=1},\ \boldsymbol{M}^{i=2},\ \ldots,\ \boldsymbol{M}^{i=k}\right)$ that contain the normalized vectors for each relative accelerometer signal.

Step 3: For each relative accelerometer signal S^i, the corresponding self-organizing map SOM^i trained according to the undamaged response in the previous section is used to generate a topology map $\boldsymbol{T}_m{}^i$. At the end of this step, a total of k topology maps are generated.

Step 4: The measured topology maps for the current case $\left(\boldsymbol{T}_m^{i=1},\ \boldsymbol{T}_m^{i=2},\ \ldots,\ \boldsymbol{T}_m^{i=k}\right)$ are normalized by dividing each map by the total number of normalized vectors in the corresponding matrix $\boldsymbol{M}^i$ (i.e. the number of time steps n in the recorded acceleration signals).

$$\boldsymbol{TN}_m^i = \frac{\boldsymbol{T}_m^i}{n} \tag{5.4}$$

Step 5: Each measured normalized topology map $\boldsymbol{TN}_m{}^i$ is compared to the corresponding undamaged normalized topology map $\boldsymbol{TN}_u{}^i$ generated in the previous section. This is done by computing the root mean square (rms) value of the difference between the measured and the undamaged maps according Eq. (5.5). The computed value is called the damage index for the accelerometer group i. At the end of this step, the damage indices at each node are computed $(DI_{i=1},\ DI_{i=2}\ ,\ \ldots,\ DI_{i=k})$. The damage indices can be scaled by a constant C. Steps 3, 4 and 5 are illustrated in Fig. 5.6.

$$DI^i = C \times \mathrm{rms}\left(\boldsymbol{TN}_u^i - \boldsymbol{TN}_m^i\right) \tag{5.5}$$

Step 6: The damage indices are summed to evaluate the overall condition of the structure according to the following equation.

$$\boldsymbol{D} = \sum_{i=1}^{k} DI^i \tag{5.6}$$

High values of $\boldsymbol{D}$ indicate a considerable change in the structural signature, which can be used to evaluate the severity of damage. On the other hand, low values of $\boldsymbol{D}$ (closer to zeros) indicate that the monitored structure is undamaged.

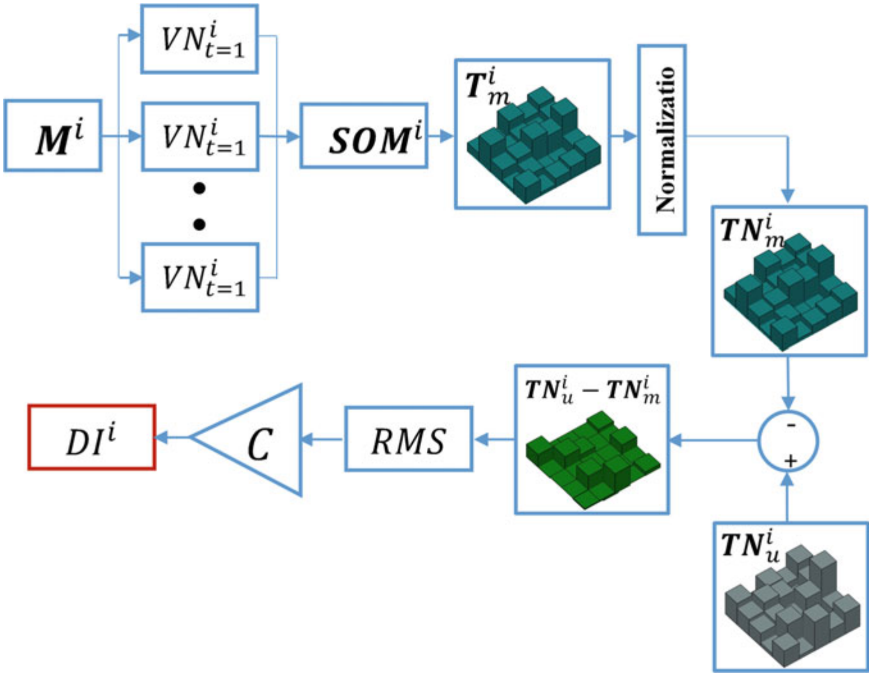

Fig. 5.6 Computation of damage indices

5.5 Numerical Demonstration of the Damage Detection Algorithm

In this section, the finite element model of the lab structure created and verified in Sect. 5.3 is utilized to demonstrate the ability of the damage detection algorithm to assess the overall structural condition. As shown in Fig. 5.7, the structure is assumed to be equipped with a total of 15 accelerometers. The accelerometers are grouped in 10 groups as explained in Table 5.2. The five damage cases illustrated in Figs. 5.8 and 5.9 are considered in this study. For the first four cases, damage is simulated by reducing the stiffness at a number of beam-beam connections by 50 %. For the Case 5, further damage is introduced by slightly reducing the stiffness of a main girder (by 10 %). The five damage scenarios are arranged to the damage severity, from almost undamaged to (Case 1) to extremely damaged (Case 5).

The procedure explained in Sect. 5.4.1 was followed to train the SOMs required for damage detection. Abaqus software was used to simulate the response of the undamaged structure under a randomly-generated white noise base excitation. The dynamic response was computed for 20 s at a time increment of 0.001 s. This analysis resulted in 15 acceleration signals, each consisting of 15×10^3 time steps. Based on these signals, a total of 10 SOMs (corresponding to the number of accelerometers groups) were generated and trained. Also, the resulting topology maps were stored in order to be used damage assessment. A Matlab [11] code has been written to carry out the SOM training process. This code employs the batch unsupervised weight/bias training algorithm available in Matlab Neural Network Toolbox under “trainbu” subroutine. The parameters of the damage detection algorithm were selected based on trial-and-error. The size of SOMs was selected as $l \times l = 12 \times 12$, and the number of past acceleration values in vectors $\boldsymbol{V}_t^i$ was taken as $d = 20$.

Similarly, the acceleration response of the structure under the five damage cases was simulated using Abaqus for the same duration and time increment. Again, the responses were computed under randomly-generated white noise excitation signals. The damage assessment process described in Sect. 5.4.2 was programmed using Matlab and applied to compute the 10 damage indices and the overall damage index under each damage case. The results of this process are given in Table 5.3. Also, the total damage values for the five cases are graphically presented in Fig. 5.10.

Fig. 5.7 Accelerometers distribution and IDs

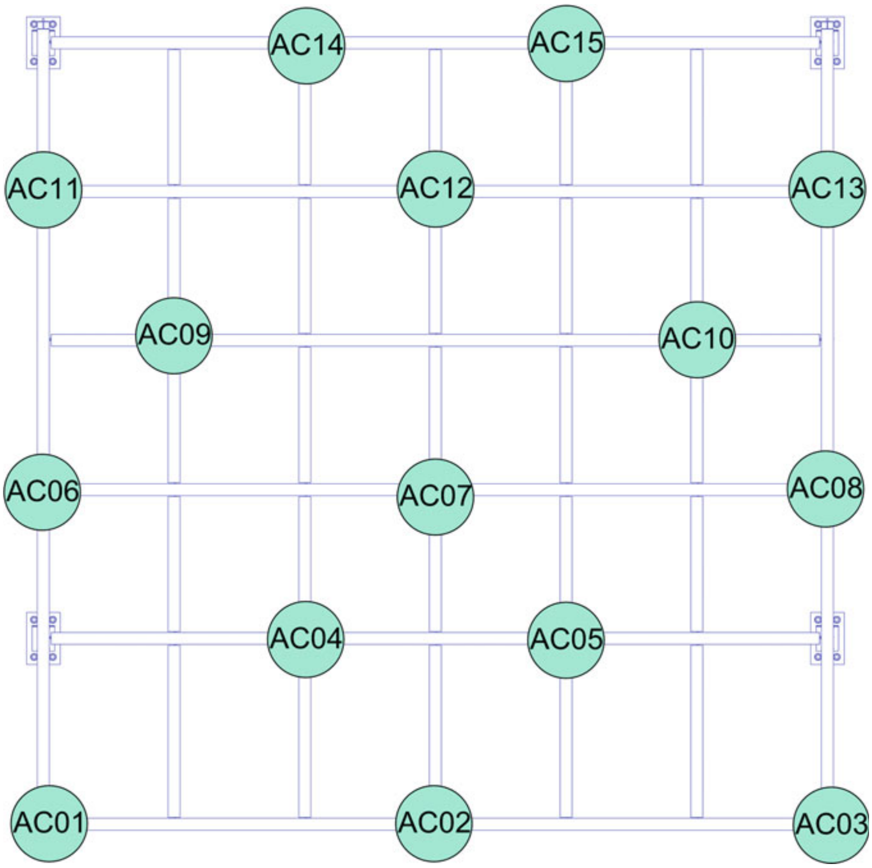

Table 5.2 Accelerometers groups

Group number	First accelerometer	Second accelerometer
1	AC01	AC06
2	AC02	AC07
3	AC03	AC08
4	AC04	AC09
5	AC05	AC10
6	AC06	AC11
7	AC07	AC12
8	AC08	AC13
9	AC09	AC14
10	AC10	AC15

5.6 Discussion

The damage assessment results shown in Table 5.3 demonstrate the ability of the damage detection algorithm to quantify structural damage. Starting from the slightest damage case (i.e. Case 1), damaging one connection only has resulted in a relatively low overall damage value of 15.4. When further damage is introduced in Case 2 by damaging two more critical connections, the total damage value computed by the algorithm has increased dramatically to 105.3 (by about 580 % compared to Case 1). For Case 3, two additional beam-beam connections were damaged, however, the total damage amount increased by only 35 % to a value of 142.7. This is totally expected since the two additional connections damaged in Case 3 correspond to a non-critical filler beam. Therefore, introducing damage to these connections didn't affect the structural

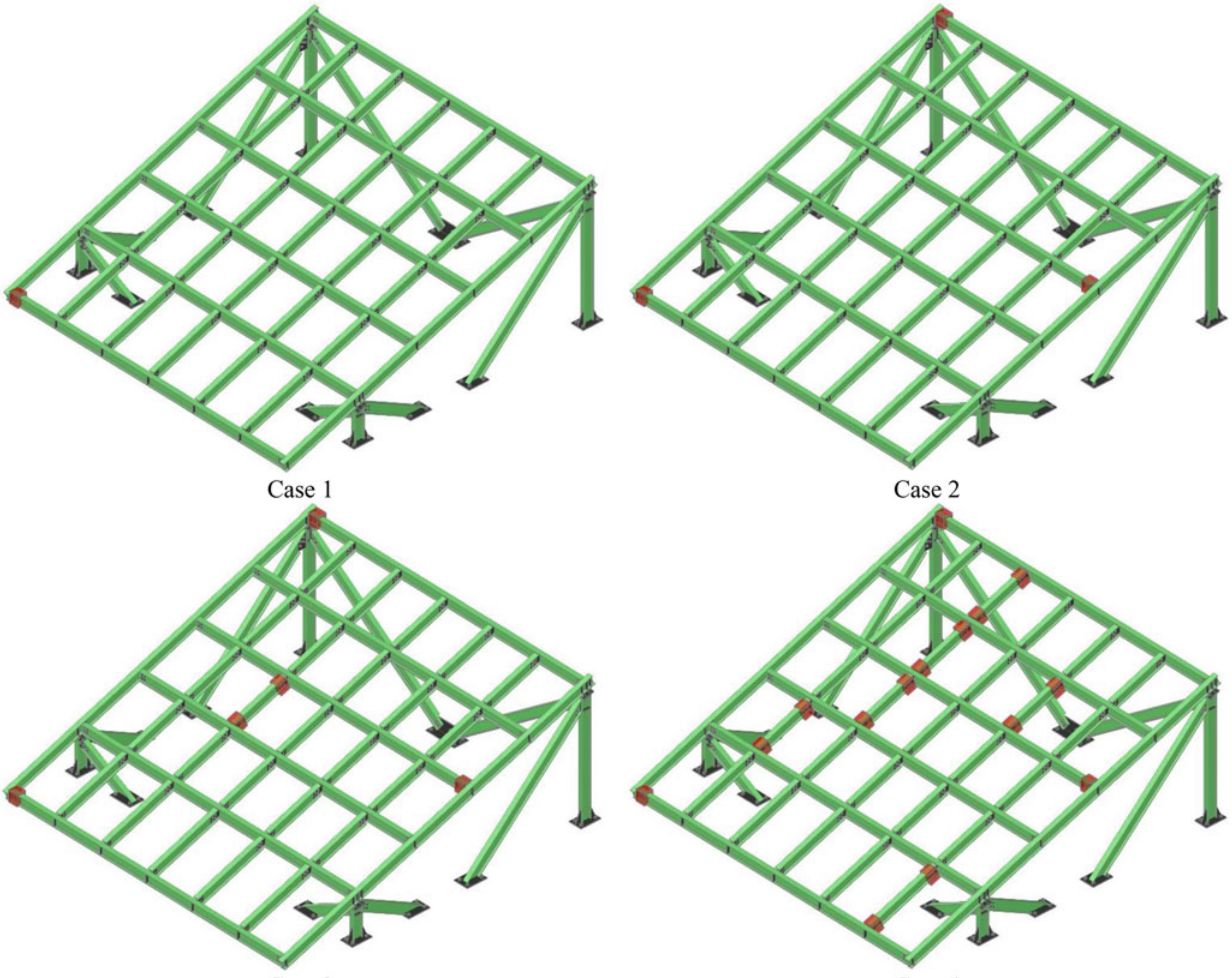

Case 1

Case 2

Case 3

Case 4

Fig. 5.8 Damage cases 1–4 (*highlighted connections* represent damaged connections)

Fig. 5.9 Damage case 5 (*highlighted connections* represent damaged connections, and *red beam* represents a damaged beam)

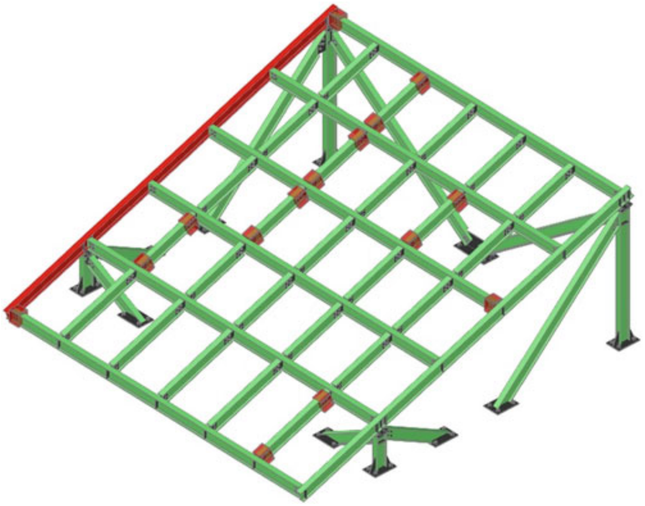

Table 5.3 Damage indices computed for the five damage cases

Damage case	DI^1	DI^2	DI^3	DI^4	DI^5	DI^6	DI^7	DI^8	DI^9	DI^{10}	Total damage
1	1.56	1.21	1.52	1.78	1.84	1.81	1.57	2.19	0.75	1.19	15.41
2	4.64	17.71	4.23	4.42	12.74	5.41	10.34	11.71	13.31	16.74	105.27
3	6.01	23.23	5.45	5.43	19.63	6.33	15.16	15.11	23.04	23.32	142.72
4	12.68	19.98	12.92	12.85	32.33	11.06	30.93	31.42	19.66	19.73	203.58
5	16.62	17.35	26.50	26.23	56.21	17.00	25.65	67.66	25.23	27.61	306.07

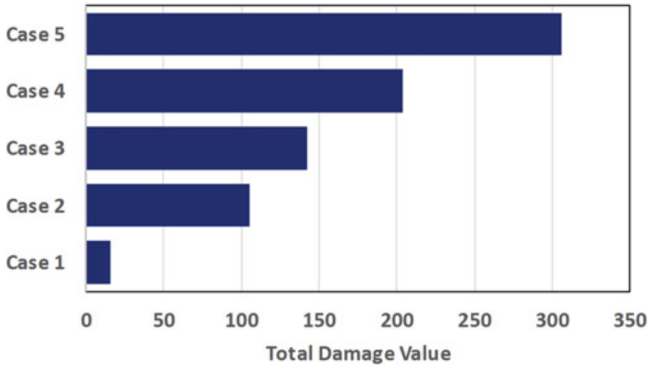

Fig. 5.10 Total damage values of the five damage cases

performance significantly. Again, damaging several additional non-critical connections in Case 4 increased the total damage only by 43 % to a value of 203.6. In Case 5, the algorithm is tested against another damage scenario in which one of the stiffness of one of the main beam is slightly reduced (by 10 %) in addition to the connections damaged in the previous four cases. The total damage for this case increased by 50 % with respect to the previous damage case which shows that the algorithm is able to detect and quantify damage due to slight loss of stiffness. Overall, the algorithm has shown great sensitivity to damage. Additionally, the total damage value ***D*** computed for each damage case is found to be proportional to the actual damage amount.

5.7 Conclusion

A novel nonparametric vibration-based damage detection algorithm has been previously introduced by the authors. In the study presented in this paper, the ability of this algorithm to assess the overall structural condition was numerically demonstrated. A detailed three-dimensional finite element model of a test structure was utilized for this purpose. The accuracy of the FE model was verified experimentally by comparing the FE modal characteristics to the actual properties measured experimentally. The performance of the algorithm was tested against five simulated damage cases. It was concluded that the algorithm is sensitive to structural damage. Moreover, the total damage value computed using the proposed algorithm is representative the actual amount of damage in each damage scenario. Therefore, this algorithm is useful as an indicator to the overall structural health.

It is highly recommended to conduct further studies to understand the relationship between the distribution of the damage indices and the location of damage. Such studies will allow the algorithm to identify the location of damaged members/ connections. Additionally, it is recommended to conduct extensive experimental studies in order to verify the findings of the numerical analysis presented in this paper.

Acknowledgements The financial support for this research was provided by Qatar National Research Fund, QNRF (a member of Qatar Foundation) via the National Priorities Research Program (NPRP), Project Number: NPRP 6-526-2-218. The statements made herein are solely the responsibility of the authors.

References

1. Catbas, F.N., Kijewski-Correa, T., Aktan, A.E.: Structural Identification of Constructed Systems: Approaches, Methods, and Technologies for Effective Proactive of Structural Identification. American Society of Civil Engineers (ASCE) Structural Engineering Institute (SEI), Reston (2013)
2. Gul, M., Catbas, F.N.: Damage assessment with ambient vibration data using a novel time series analysis methodology. J. Struct. Eng. **137**, 1518–1526 (2011)
3. Yan, L., Elgamal, A., Cottrell, G.W.: Substructure vibration NARX neural network approach for statistical damage inference. J. Eng. Mech. **139**, 737–747 (2013)
4. Yeung, W.T., Smith, J.W.: Damage detection in bridges using neural networks for pattern recognition of vibration signatures. Eng. Struct. **27**, 685–698 (2005)
5. Rhim, J., Lee, S.W.: A neural network approach for damage detection and identification of structures. Comput. Mech. **16**, 437–443 (1995)
6. Arangio, S., Beck, J.L.: Bayesian neural networks for bridge integrity assessment. Struct. Control Health Monit. **19**, 3–21 (2012)
7. Kohonen, T.: Self-Organizing Maps. Springer, Berlin (2001)
8. Avci, O., Abdeljaber, O.: Self-organizing maps for structural damage detection: a novel unsupervised vibration-based algorithm. ASCE J. Perform. Constr. Facil. 04015043 (2015). doi: 10.1061/(ASCE)CF.1943-5509.0000801
9. Dyke SJ, Bernal D, Beck J, Ventura C. Phase II experimental structural health monitoring benchmark problem. ASCE Engineering Mechanics Conference. WA, (2003)
10. Abaqus/CAE version 6.12-1. Providence, Rhode Island, Dassault Systèmes, (2012)
11. MATLAB version 8.1.0.604. MathWorks, Natick

Chapter 6
Accuracy Enhancement of a Device for Automated Underbridge Inspections

Hermes Giberti, Marco Tarabini, Federico Cheli, and Marco Garozzo

Abstract The inspection and maintenance of bridge decks is a procedure that requires objectivity and systematic steps; great benefits would derive from the adoption of automated techniques minimizing the human intervention. From this point of view, the laser scanner technology can provide excellent results; in order to reconstruct the geometry of the underbridge, the scanning head can be mounted on a motorized cart travelling on a walkway moved by a truck. The motion of the laser scanning head must be compensated in post-processing in order to obtain a reliable reconstruction of the underbridge geometry; the accuracy of the reconstruction depends on the accuracy of the trajectory itself. This paper describes the actions undertaken to improve a measurement system based on noncontact techniques (laser distance meters and vision systems) aimed to reconstruct the scanning head trajectory with respect to a reference system integral to the bridge deck. The measurement uncertainty of the proposed system was evaluated by numerical simulations and then experimentally verified. At first, the developed mathematical model was validated through a comparison with an ideal system simulated in SimMechanics. Experiments performed in a controlled environment proved the validity of the proposed approach.

Keywords Bridge inspection • Measurement techniques • Uncertainty • Monte Carlo simulation

6.1 Introduction

The automation of methodologies for bridge inspections is the focal point of several studies [1–7]; the interest in this field is motivated by the obsolescence of several existing highway bridges (built in the 60s [1]) associated with the costs of the inspection procedures [2]. To date, the inspection of concrete bridges is performed visually by trained subjects, which observe the underbridge from a slow moving platform mounted at the end of a multi-link arm moved by a truck. This procedure has several limits, which derive from the discretional margins in the identification of the concrete defects and from the limited stability of the platform.

The state of the art in the inspection of steel bridges was summarized by McCrea et al. in 2002 [3]; the inspection of metallic structures is usually based on non-destructive techniques, while the inspection of concrete bridges is still performed with visual analyses. The recent attempts to create automated inspection systems still have accuracy limitations generated by the difficulty of detecting defects of a few millimetres on constructions of hundreds of meters. The potentiality of vision systems for the inspection of concrete structures has been addressed by Yu et al. [7], but the acquisition of images has to be associated with the measurements of the position where the images were taken. Many works [8–10] proposed methods for managing large quantity of image data, but the mere image-based methods do not provide any geometrical information about the bridge.

Recently, the idea of using a moving laser scanner to reconstruct the underbridge geometry has been proposed [2] together with its mathematical model [1]. The main limitation of the method is the limited accuracy of the reconstruction, with average geometrical error close to 20 mm and typical values comprised in the ±40 mm range. The main source of error was the large uncertainty in the reconstruction of the scanning head trajectory and orientation.

In this work, we describe a novel measurement approach for identification of the position of the scanning head for the automated underbridge inspection. The measurement chain has been optimized using the uncertainty as a figure of merit for the validation of the design choices, similarly to what was done in [11]: the measurement model obtained from the

H. Giberti (✉) • M. Tarabini • F. Cheli
Department of Mechanical Engineering, Politecnico di Milano, Via La Masa 1, 20156 Milano (MI), Italy
e-mail: hermes.giberti@polimi.it

M. Garozzo
SINECO S.p.A., Via Felice Casati, 1/A 20124 Milano (MI), Italy

A. Wicks, C. Niezrecki (eds.), *Structural Health Monitoring, Damage Detection & Mechatronics, Volume 7*,
Conference Proceedings of the Society for Experimental Mechanics Series, DOI 10.1007/978-3-319-29956-3_6

geometrical characteristics of the system has been initially validated through a comparison with an ideal SimMechanics model. This step was necessary in order to identify the consistency of the small rotations hypothesis, which would allow obtaining transformation matrices that are independent from the rotation order. The model was then used to identify the expected measurement uncertainty as per ISO GUM annex 1 [12, 13] and to identify the minimal transducers characteristics in order to obtain an accuracy lower than 10 mm. Once that the measurement chain elements were selected, the manufacturers' declared accuracies were verified with a metrological calibration; the probability density functions of the errors were used to compute the expected uncertainty with the Monte Carlo method. Results were eventually verified with tests performed in controlled conditions.

This paper is structured as follows: the measurement model is presented in the Sect. 6.2. The results of the numerical simulations and of the experiments are presented in the Sect. 6.3, which are discussed in the Sect. 6.4.

6.2 Method

The truck used for the underbridge inspection is the same one described in references [1, 2]; the hypotheses that probably lead to errors (±40 mm) larger than expected were:

- small rotations between the reference systems (i.e. rotation matrix linearization);
- no slippage between the cart and the by-bridge;
- null tilt of the vertical support of the by-bridge
- null pitch of the cart on the by-bridge.

The importance of these hypotheses was verified by implementing a SimMechanics model, which was used as a reference to verify the effect of the small tilt and pitch motion of joints on the position of a point measured by the scanning head. The physical by-bridge model and the SimMechanics model are shown in Fig. 6.1.

The position of the scanning head has been identified applying roto-translations starting from the position of the truck:

$$M_{ON} = M_{01}M_{12}M_{23}\ldots M_{(N-1)N}$$

Where

$$[M_{01}] = \begin{bmatrix} R_{01} & T_{01} \\ 0 & 1 \end{bmatrix}$$

R_{01} and T_{01} are respectively the rotation matrix (3 × 3) and the translation vector (3 × 1) which describe the position of a reference system with respect to the previous one. Under the hypothesis of small rotation, the rotation matrix R (whose complete expression can be found in many robotics textbooks) can be linearized as follows:

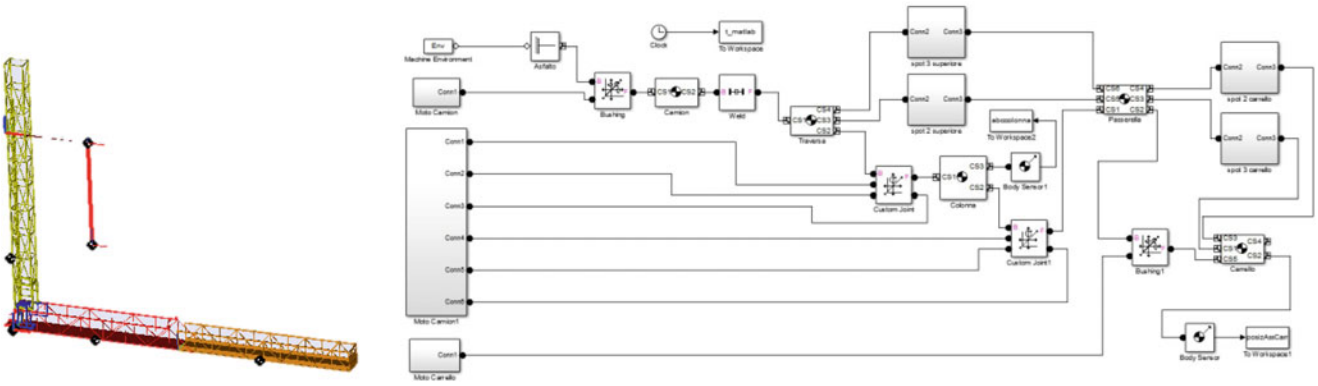

Fig. 6.1 Physical model of the by-bridge (*left*) and SimMechanics model (*right*)

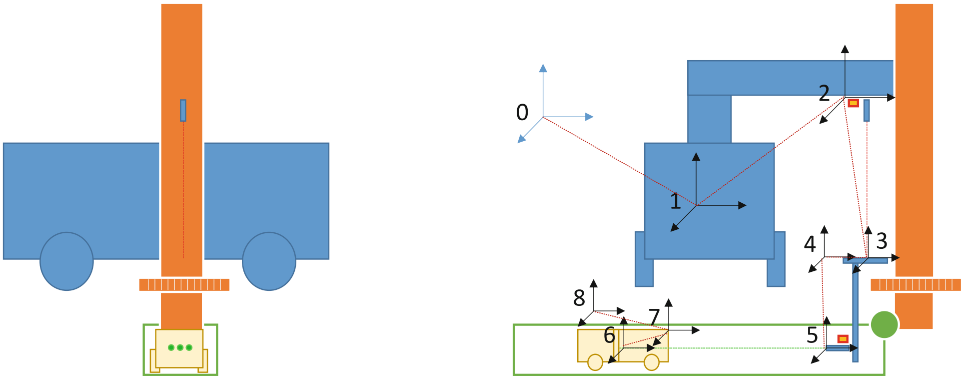

Fig. 6.2 Reference systems used to track the position of the scanning head with respect to the truck

$$R_{01} = \begin{bmatrix} 1 & -\gamma & \beta \\ \gamma & 1 & -\alpha \\ -\beta & \alpha & 1 \end{bmatrix}$$

The great advantage of the adoption of the small rotations hypothesis is that each rotation can be measured separately from the others. Measurements performed in the previous study [1, 2] have been also refined by considering all the possible relative motions between the elements, thus requiring the adoption of the eight Cartesian reference systems shown in Fig. 6.2.

The eight Cartesian coordinate systems are:

0	Absolute reference system (fixed with respect to the bridge)
1	Truck reference system, which is coincident with the bridge reference system when the measurement starts
2	Upper crosspiece reference system, which can only rotate around the vertical axis of the truck; the distance from the reference number 1 is supposed to be constant (measured before the tests)
3	Vertical laser—spot reference system, identified by the intersection between the laser beams defining the axes of the reference system 2 and a horizontal plane. Axes are parallel to those of the horizontal plane reference system (number 4)
4	Horizontal plane reference system, fixed to the frame below the lower fifth wheel. The origin is located on the camera used for the image analyses
5	Lower laser reference system, whose distance from reference system number 4 is constant (identified before the tests)
6	Cart spot reference system; as for the reference system number 3, the origin is the intersection between the laser emitted from reference 5 and a vertical plane located on the cart. The axes are parallel to those of the reference system 7
7	Cart reference system, fixed to the cart, with the origin located on the camera used for the image analyses
8	3D laser scanner reference system; is located on the FARO scanning head; the distance from the reference system number 7 is constant and has been identified before the measurements.

The errors introduced by the linearization of rotation matrixes was quantified by computing the difference between M_{08} computed from the first equation of this paper and the actual position computed from the SimMechanics model. Simulated measurements were performed under the hypothesis of scanning a flat horizontal surface located 3 m above the scanning head; the truck was supposed to move at a constant speed over the bridge and the cart has a uniform acceleration on the by-bridge. The laser scanner is supposed to work in helix mode and the different joints move with harmonic motions with the following amplitudes (identified from preliminary tests):

- 2° of roll, pitch and yaw of the cart
- 3° of rotation of the footbridge along the z axis and 2° around the x and y axes;
- 1° of roll of the truck, 0.5° truck pitch.

The truck and cart speeds were also identified from the results of preliminary experiments. Errors deriving from the linearization of rotation matrices are shown in Fig. 6.3. The plots show that the position error along the x-axis is the largest one and that its magnitude increases at the end of the platform (maximum error close to 30 mm). y and z axes errors are lower than 5 mm. The tilt errors are lower than 0.2° and the largest one is the error of rotation around the x axis (alpha angle).

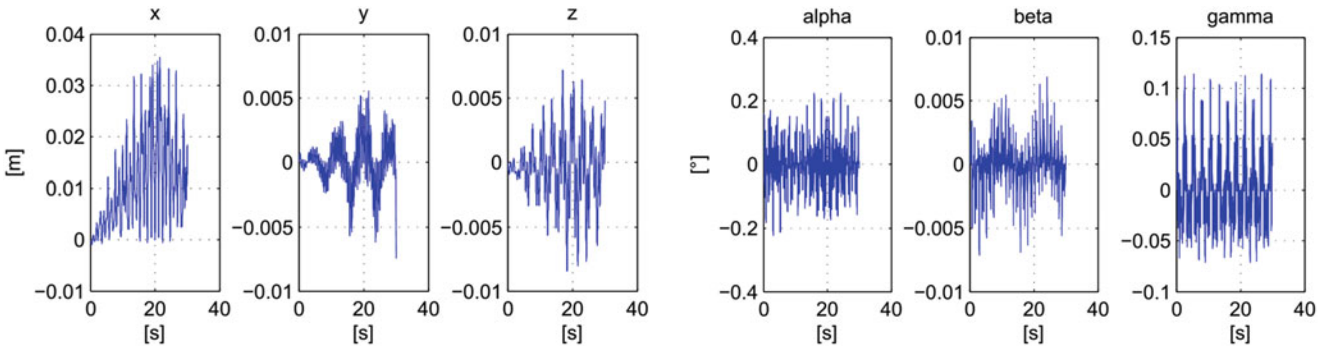

Fig. 6.3 Rotation and position errors deriving from the linearization of rotation matrices

Table 6.1 Characteristics of the distributions used in the Monte Carlo method

Quantity	Type of distribution	Distribution characteristics
Distance (laser disto)	Uniform	Maximum error 0.5 mm
Spot position	Uniform	Maximum error 0.5 pixel
Distance (Odometer)	Gaussian	Standard deviation 0.1 mm
Tilt (inclinometers)	Gaussian	Standard deviation 0.01°
Tilt (vision)	Gaussian	Standard deviation 0.01°

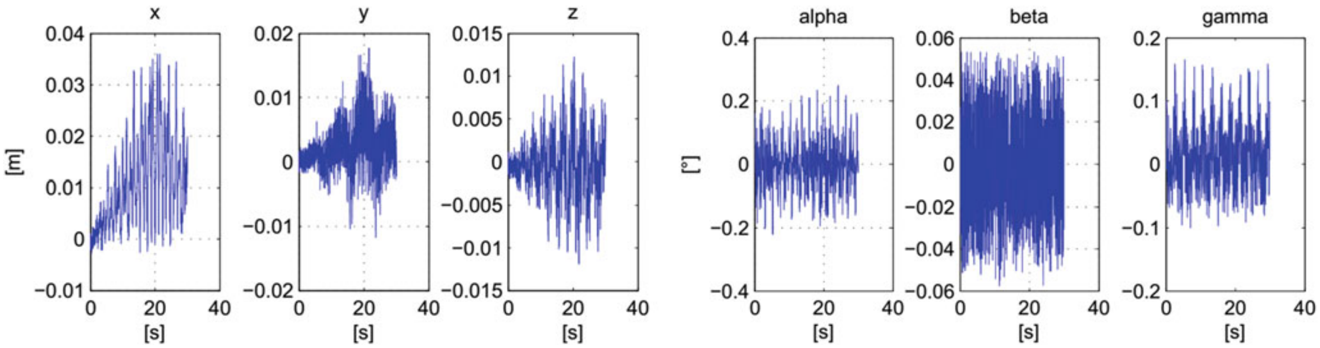

Fig. 6.4 Rotation and position errors deriving from the linearization of the rotation matrices and the uncertainty of the sensors

The errors deriving from the non-ideal instrument characteristics have been evaluated with the Monte Carlo method, i.e. by imposing, in addition to the aforementioned errors, errors sampled from populations with probability density functions (PDF) identified starting from manufacturers' catalogues. The errors' PDF are summarized in Table 6.1.

The evaluation of the simultaneous effects of instrumental and linearization error allow deriving the instrumental effects from a comparison with data presented in Fig. 6.3; in this way, errors are not computed in a single position. Results are shown in Fig. 6.4.

The comparison between Figs. 6.3 and 6.4 demonstrates that the instrumental effects on x and z axes are small in comparison to those on the y axis (the maximum y error increases from 5 to 15 mm). The effect on the alpha and gamma angles is also trivial, while the beta error increases of approximately one order of magnitude (from 0.005° to 0.05°). Further analyses were performed to identify the effect of systematic tilt/shift errors non-compensated by the preliminary calibration (for instance, a tilt between the cart reference systems and the cart itself, or an offset of the inclinometers used to measure the coordinate system number 2 and number 5). The effect of these errors is quite complex, given that a tilt error in one of the coordinate systems causes a non-planar distortion of the measured surface. For instance, the presence of simultaneous time-dependent errors on the inclinometers, the flat surface is reconstructed with a curved one, as in Fig. 6.5.

Fig. 6.5 Effect of simultaneous tilt errors on the inclinometers

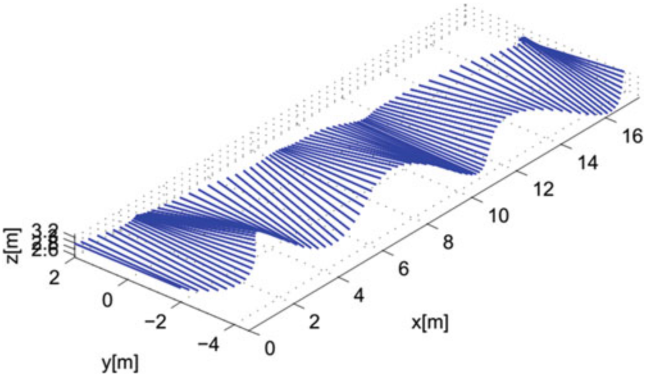

Other analyses (not described in this work) were performed to analyze the point density; results evidenced that the parameters that allows obtaining the desired point density are a cart velocity of 0.9 m/s and a distance of 2 m between the head and the scanned surface. The best configuration is the one in which the laser head has a tilt of 45° with respect to the cart direction, in order to scan correctly the vertical surfaces.

After these analyses, the following sensors were chosen:

- Laser distance meter FAE LAS 121 FA (range 100 m, digital output, resolution 0.1 mm) to measure the distances between reference systems 2–3 and 5–6;
- Laser με IDL1400-100 for the detection of the rotation of reference system 2 with respect to 1;
- Inclinometers SEIKA SBG2U with measurement range ±10° and linearity deviation lower than 0.01° to measure the rotations around the vertical axis of reference systems 2 and 5;
- Cameras for cart tilt detection (observing lines on the by-bridge frame): model IDS UI 5240CP-M-GC with resolution of 1.3 Mpixel;
- Smart cameras for the identification of the laser spots NI 1772.

6.3 Results

The accuracy benefits deriving from the use of the full (nonlinear) rotation matrixes and from the metrological characterization of the system were assessed by analysing the planarity error of the façade of a building; the cart was travelling over a non-flat terrain simulating the by-bridge. The measurement chain was set-up as follows:

- the cart fore-and-aft motion was measured by the FAE laser distance meter;
- the cart lateral and vertical motion were measured by the displacement of the spots of two fixed lasers pointing on the cart, as described in [14].
- the cart roll was measured by the tilting of the line connecting the two aforementioned spots; and
- the cart pitch and yaw were measured by cameras observing linear guides located on the ground and on the lateral railing, as shown in the next figure;

A pictorial view of the measurement system and of the building used for the method validation is shown in Fig. 6.6.

The coordinates of the cart measured with the setup described in this paper are shown in Fig. 6.7.

The geometry of the façade reconstructed by a 3D laser scanner located on the moving cart is shown in Fig. 6.8. Preliminary results evidenced the importance of the misalignments between the laser rays, which resulted in a twisted façade, as shown in Fig. 6.8a. After de-trending the cart roll (Fig. 6.8b), the planarity error of the façade was lower than 6 mm, thus evidencing the validity of the proposed approach. As in the previous works, the planarity error was evaluated as the RMS of the distance between the points' coordinates and the best fitting vertical plane.

Fig. 6.6 Pictures of the experimental setup (**a** and **b**) and of the façade used for the method validation (**c**)

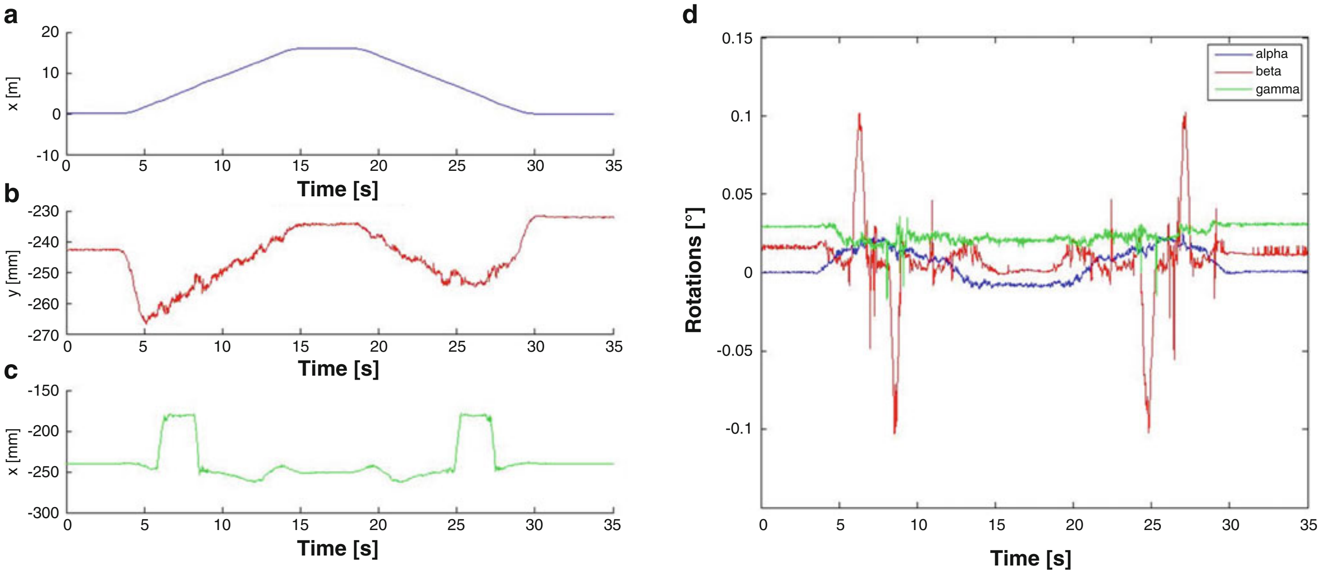

Fig. 6.7 Translation and rotations of the cart during the test; *left plots* shows the x, y and z coordinates (**a**, **b** and **c** plots). The *right plot* (**d**) shows the roll, pitch and yaw angles

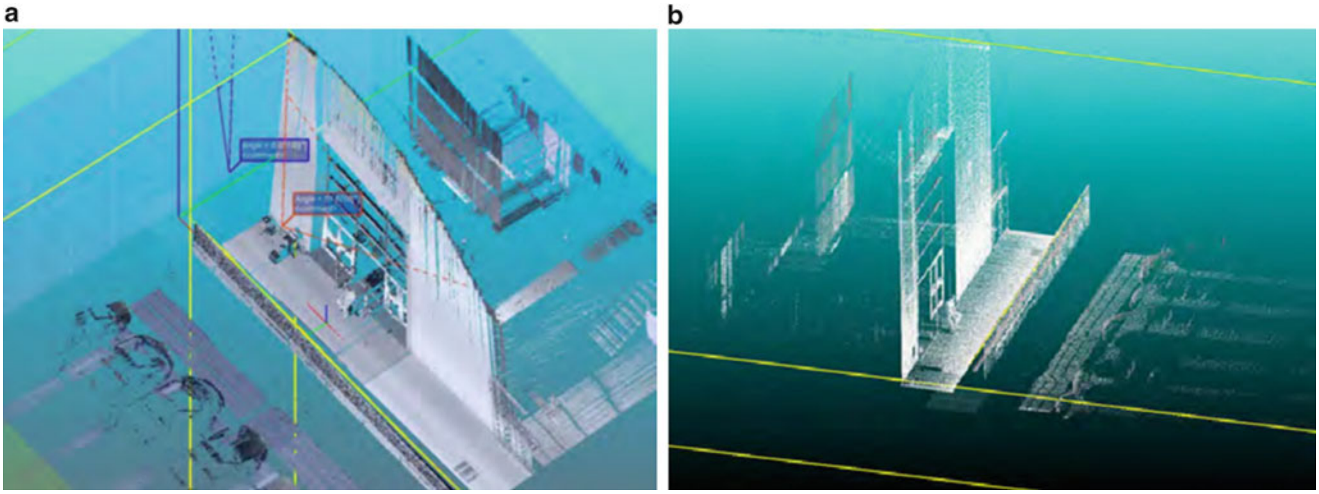

Fig. 6.8 3D map of the façade acquired during the tests without misalignment compensation (**a**) and with compensation (**b**)

6.4 Concluding Remarks

In this work, we have proposed and validated a mathematical model that allows identifying the position of a cart moving on a truck-driven platform for the underbridges inspection. Results of simulations evidenced the necessity of considering also the nonlinear terms in the rotation matrices, given that the linearization-induced errors were close to 20 mm. Errors deriving from the uncertainties of selected instruments have been analysed as well; the effects of the tilt uncertainties were generally larger than those of uncertainties in distance measurements. Experiments performed in a simulated environment allowed validating the entire measurement procedure, which involved also the conversion of raw data acquired by the Faro 3D scanning head into a cloud of points. The RMS of the planarity error was 6 mm, a value three times smaller than that obtained with the previous configuration. Tests performed on the by-bridge in the actual working conditions (not described in this paper) outlined planarity errors lower than 9 mm and a measurement density of 50,000 points/m^2; the combination between the geometrical information and of the images allowed the precise localization of the bridge surface features.

References

1. Zanoni, A., Maninetti, G., Cheli, F., Garozzo, M.: Development of a computer vision tracking system for automated 3D reconstruction of concrete bridges. In: ASME 2014 12th Biennial Conference on Engineering Systems Design and Analysis, pp. V003T15A012-V003T15A012 (2014)
2. Giberti, H., Zanoni, A., Mauri, M., Gamminom, M.: Preliminary study on automated concrete bridge inspection. In: ASME 2014 12th Biennial Conference on Engineering Systems Design and Analysis, pp. V003T15A011-V003T15A011 (2014)
3. McCrea, A., Chamberlain, D., Navon, R.: Automated inspection and restoration of steel bridges—a critical review of methods and enabling technologies. Autom. Constr. **11**, 351–373 (2002)
4. Hugenschmidt, J.: Concrete bridge inspection with a mobile GPR system. Constr. Build. Mater. **16**, 147–154 (2002)
5. Adhikari, R., Moselhi, O., Bagchi, A.: Image-based retrieval of concrete crack properties for bridge inspection. Autom. Constr. **39**, 180–194 (2014)
6. Busca, G., Cigada, A., Mazzoleni, P., Tarabini, M., Zappa, E.: Static and dynamic monitoring of bridges by means of vision-based measuring system. In: Conference Proceedings of the Society for Experimental Mechanics Series, pp. 83–92 (2013)
7. Yu, S., Jang, J., Han, C.: Auto inspection system using a mobile robot for detecting concrete cracks in a tunnel. Autom. Constr. **16**, 255–261 (2007)
8. Brilakis, I., Fathi, H., Rashidi, A.: Progressive 3D reconstruction of infrastructure with videogrammetry. Autom. Constr. **20**, 884–895 (2011)
9. Zhu, Z., German, S., Brilakis, I.: Detection of large-scale concrete columns for automated bridge inspection. Autom. Constr. **19**, 1047–1055 (2010)
10. Abudayyeh, O., Al Bataineh, M., Abdel-Qader, I.: An imaging data model for concrete bridge inspection. Adv. Eng. Softw. **35**, 473–480 (2004)

11. Moschioni, G., Saggin, B., Tarabini, M., Hald, J., Morkholt, J.: Use of design of experiments and Monte Carlo method for instruments optimal design. Measurement **46**, 976–984 (2013)
12. ISO GUIDE 98 part 3: Guide to expression of uncertainty in measurements (GUM 1995). International Organization for Standardization (2008)
13. Cox, M.G., Siebert, B.R.L.: The use of a Monte Carlo method for evaluating uncertainty and expanded uncertainty. Metrologia **43**, S178 (2006)
14. Giancola, S., Giberti, H., Sala, R., Tarabini, M., Cheli, F., Garozzo, M.: A non-contact optical technique for vehicle tracking along bounded trajectories. J. Phys. Conf. Ser. **658**(1), 012010 (2015). IOP Publishing

Chapter 7
A Brief Overview of Mechatronics

A.L.Wicks

Abstract Mechatronics is a rapidly evolving technology that links mechanics, electronics and computer science to realize complex systems that improves our lives. The focal point for these systems is the microcontroller that links the digital/analog world to the mechanical. Inputs are provided by sensors and the output is typically actuation in some form. An overview of how these tools combine to form mechatronic systems is discussed. Sensing tools, actuation devices, bus structures for communicating with the microcontroller are discussed. To complement the hardware, is a wide variety of software programs that enhances the design process by minimizing the need for extensive bread boarding and prototyping.

Keywords Mechatronics • Microcontrollers • Sensors • Actuators • Bus structures

7.1 Introduction

Mechatronics is the fusion of electronics, mechanics, controls, sensing and computers to generate sophisticated, adaptive and intelligent systems for commercial products. Although it may appear to be the combination of mechanics and electronics, the real catalyst has been the development of the microcontroller coupled with the support software. The ability to have distributed intelligence, reduced power and high speed buses opens the door to many of the applications of mechatronics we utilize today. An often overlooked aspect of these developments/technologies is the rate of change that this technology is undergoing. The increase of clock speeds, RAM and memory access time is well documented, but a significant change has been realized in size and power requirements, coupled with expanded capability. This evolution has created new design paradigms that transition our dynamic systems on a yearly basis.

This paper attempts to review the growth and potential of mechatronics, discussing the technology and the use of these tools in the design of systems. Topics such as actuation, sensing, computation and data fusing, battery technology, bus structures and wireless applications will be discussed. Before the technology is discussed, a historical perspective is deserving.

7.2 Background

The bases for mechatronic systems, originally named by the Japanese in 1969, revolves around the microprocessor. A mechanical system containing actuators and sensors, analog and/or digital, can be controlled through the use of a microprocessor. Earlier attempts to automate process was originated by Ford in the 1940s. Subassemblies were positioned at sequential stations to add components. With the development of the microprocessor, these concepts exploded into the technologies we employ today to create 'smart' systems.

Mechatronic systems are the intersection of a variety of technologies. Sensors and actuators provides the inputs and responses for the system. Physical models, be it fluids, thermal, mechanical or electrical represents the 'plant', the model that the input and output data will react with. Lastly, the software, logic systems, computers and the DSP/controls theory that represents the 'glue' to hold the system together.

A.L. Wicks (✉)
Department of Mechanical Engineering, Virginia Tech, Blacksburg, VA, USA
e-mail: awicks@vt.edu

A. Wicks, C. Niezrecki (eds.), *Structural Health Monitoring, Damage Detection & Mechatronics, Volume 7*,
Conference Proceedings of the Society for Experimental Mechanics Series, DOI 10.1007/978-3-319-29956-3_7

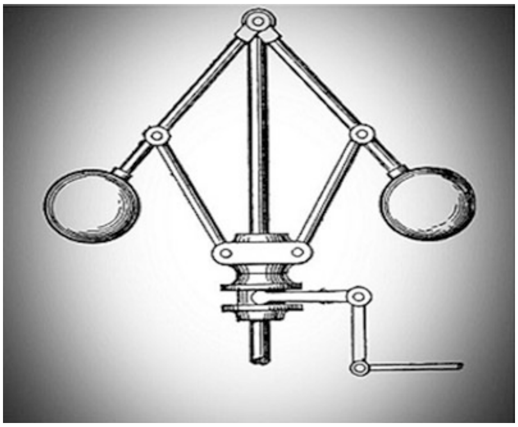

Fig. 7.1 Simple centrifugal governor

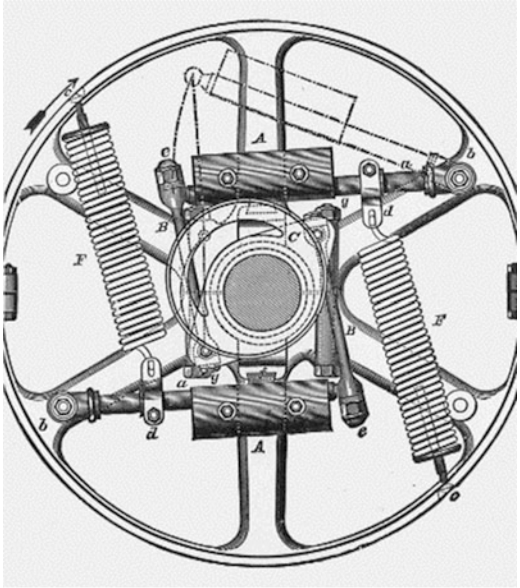

Fig. 7.2 Buckeye automatic governor

The origins of control are centuries old, advanced civilizations developed complex irrigation solutions providing water in a controlled manner to their fields. The Romans and the Greeks developed complex mechanisms for controls, many related to military applications. Mechanical control systems for steam engines revolutionized transportation and manufacturing, and earned the label of the industrial revolution. Figure 7.1 shows the mechanical governor control (flyball) associated with steam technologies. The twentieth century version of this control system can be seen in Fig. 7.2. The fly wheel version was a common attachment to the output pulley of steam engine systems for industrial application.

The electrical link to mechatronics got its start in the 1800s. The invention of the electric motor and the broad spectrum of electrical/ magnetic components such as contactors, relays and selenoids were also realized throughout the mid 1800s. The actual explosion of these devices into the industrial applications we would identify as mechatronics did not happen until the early twentieth century with the widespread electrification of Europe and the United States. These systems, the combination of mechancial/electrical control , was implemented in the automobile industry, power generation industry and even agriculture (Fig. 7.3).

The next significant leap in technology that defines what we currently consider mechatronics is the invention of the transistor and thryistor in the 1940s. The ‘pn’ junction defines the basics of the electrical digital components we use today. The 1950s and 1960s saw the development of the digital computer, the combination of the analog computer to control applications. Software capable of real time operation was beginning to find applications in control schemes. The next big leap was the miniaturization of the electronics with the development of the microcontroller and microprocessor.

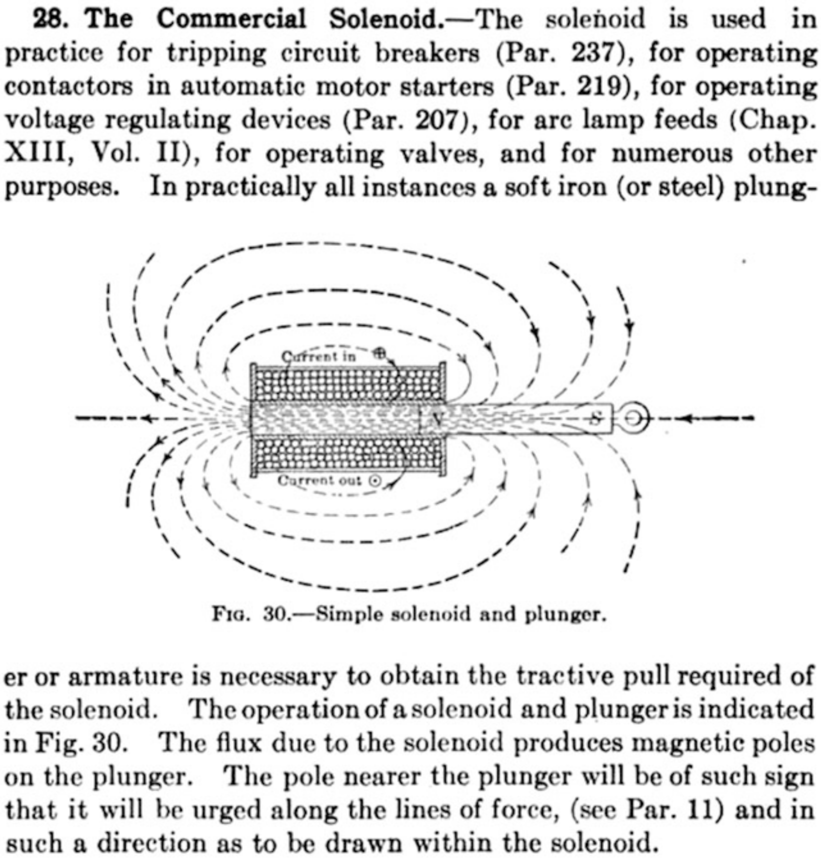

Fig. 7.3 Advertisement for a solenoid circa 1920

28. The Commercial Solenoid.—The solenoid is used in practice for tripping circuit breakers (Par. 237), for operating contactors in automatic motor starters (Par. 219), for operating voltage regulating devices (Par. 207), for arc lamp feeds (Chap. XIII, Vol. II), for operating valves, and for numerous other purposes. In practically all instances a soft iron (or steel) plunger or armature is necessary to obtain the tractive pull required of the solenoid. The operation of a solenoid and plunger is indicated in Fig. 30. The flux due to the solenoid produces magnetic poles on the plunger. The pole nearer the plunger will be of such sign that it will be urged along the lines of force, (see Par. 11) and in such a direction as to be drawn within the solenoid.

Fig. 30.—Simple solenoid and plunger.

The microcontroller was invented at Texas Instruments in the early 1970s, around the same time as the first microprocessor was invented at Intel. The Intel 8008 was introduced in 1973, about the same time as the PL/M software to support processor programming. The first true microprocessor, the 8080 was introduced in 1974. Its this processor that launched the PC. The 8080 found many applications as a controller for systems such as traffic lights and cash registers. Early microcontrollers were simply microprocessors with built-in memory such as RAM and ROM such as Intel's 8048 and 8051. Later, microcontrollers evolved into devices tailored for specific embedded applications in products such as cars, wireless phones and household appliances. Specialized microcontrollers are now being produced for areas such as automotive, lighting, communications, low-power consumer devices and a broad range of hobby applications. Microcontrollers have also become smaller and more powerful. As previously mentioned, the evolution of the microcontroller, both in speed, memory and low power requirements coupled with MEMs sensors has fueled an explosion in mechatronics systems.

7.3 Basic Microcontroller

The basic microcontroller consists of a central processing unit (CPU) supported with multiple input/ output ports, analog to digital conversion, RAM , ROM and some basic bus support. In the Fig. 7.4, the diagram shows a serial bus, but USB, CAN and Ethernet are also common. The multiple I/O ports serve to sense inputs as well as output control signals to any actuators that may be part of the system. One of the attributes of these available microcontrollers is the low power requirements. For example, the Texas Instruments MSP 432P401x Mixed-Signal Microcontroller operates on a supply voltage between 1.62 and 3.7 V and only draws 90 μA when operating at 128 KHz. This power requirement makes possible the GPS watches that runners wear, sensor fusion for complex medical measurements as well as the broad spectrum of portable commercial products for supporting and managing wireless links.

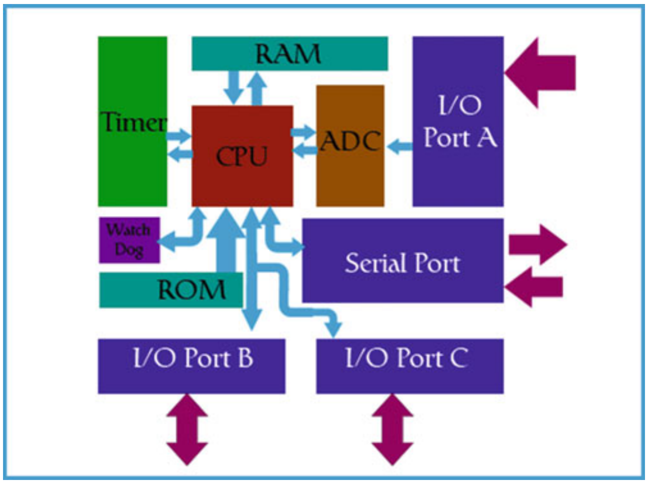

Fig. 7.4 Block diagram for a typical microcontroller

Much as computers have found their way into our daily lives, with systems designed to be used by children of all ages with games and educational applications, microcontrollers have been designed to be used by the non-technical hobbyist. Microcontrollers such as the Arduino, Raspberry pi or the Beaglebone are easily programmed and can be used for many hobby level projects. These tools are popular STEM assets that supports robotic projects and other high school technical programs.

7.4 Actuation

Actuation generally is broken down into three topics, hydraulic/pneumatic, mechanical and electrical. Hydraulic actuation is common where large forces and displacements are required. Earthmoving equipment, agricultural equipment and automotive applications have utilized these technologies for many years. Pneumatic actuation is popular where authority is required and compressed air is available. The ever popular air braking system is still used on large trucks. Mechanical components related to actuation includes four-bar linkages, cams, belts and chains, gears and rack and pinions. These tools are well understood and can easily be included in design.

The significant growth in actuation tools is in the electrical area. Simple elements in electronics has teamed with the families of microprocessors and microcontrollers to contribute to the mechatronic success. Bipolar transistors can be used as switches to replaces relays and contactors. MOSFETs has taken solid state switching to new levels providing switching speeds measured in nanoseconds and resistive losses measure in milliohms. This technology has led to efficient, chip size DC-DC converters and active rectification. The improvement in power control has been coupled with motor technology to improve efficiency and control of motors for actuation. Brushless DC motors, Universal motors, stepper motors and servos are available, many with control packages augmented with feedback from sensors in the motor and coupled with high speed switching power supplies to limit current and control motor speed and torque. These ‘smart’ motors are available and easily integrated into a microcontroller driven system with off the shelf components (Figs. 7.5 and 7.6).

Rotating machinery has been configured through gearing to create linear motion, so linear actuators with significant authority are readily available. In addition, there is a broad selection of linear motors to provide linear motion with precision control for use in mechatronic applications. As shown in the figure, these actuators have feedback from built-in encoders.

7.5 Sensors

Sensing represents one of the parts of the mechatronic triad, sensing, computation, and actuation. As a result, we sense with the use of transducers. This data is then processed by the microcontroller in the mechatronic system to provide suitable signals to the actuation activity.

Transducers are required to supply information to make decisions in any system. We measure strain to relate stresses for failure prediction. We measure body temperature to make health evaluations. We use displacement measurements to provide feedback for locating printing heads in 3-D printers. The broad spectrum of sensing tools is briefly discussed as it relates to mechatronics.

Fig. 7.5 An example of a smart motor

Fig. 7.6 Linear actuator

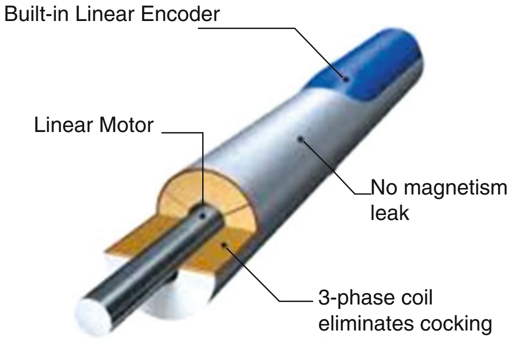

One group of sensors relies on the basic elements in electronics, resistance, capacitance and inductance. Strain gages have been available for more than 100 years and can be used to measure strain by utilizing a linear relationship between strain and resistance change. This simple tool, coupled with circuitry to sense the small resistance changes, translates into force transducers, accelerometers, microphones and many other transducers that measures a force. Inductive sensing is used to measure large displacements in LVDTs, linear variable differential transformers to give one example. The development of MEMs has capitalized on the capacitance measurement. MEMs accelerometers as well as gyroscopes are popular transducers used in cell phones, gaming sensors and a plethora of other mechatronic systems. The basic measurement is the change of capacitance in response to forces applied to the transducer. The attractive attribute for these sensors is the lower power requirements. Unlike resistive elements the capacitive approach does not consume power thus does not generate significant heat that impacts accuracy and stability of the sensor. This family of sensors can be used to measure force, motion, and pressure (Figs. 7.7 and 7.8).

Piezoelectric sensors are a technology that detects the change in charge of materials in response to a load. The load can be tensile/compressive or shear. This group of sensors measure the dynamic loads, meaning the load has to be time varying as opposed to steady. For example, accelerometers using piezo-based sensing cannot measure gravity acceleration since it is constant. The attractive attribute for these transducers is the frequency response which can be as high as 75 KHz.

Another group of sensors is based on detecting changes in magnetic fields. Magnetic sensing is important for several different applications. Magnetic fields are linked to current flow. These sensors are used to measure the Earth's magnetic field as part of inertial measurement systems for navigation. In addition, due to the sensitivity and size, this technology can be used in encoders for feedback in rotating applications.

Optical sensing is a growing area that takes advantage CCD, charge couple device, or CMOS sensors and their derivatives to acquire unique information. An example of this are LIDARs, sensors that measure range, distance to a target by the time of flight, TOF. These devices or sensors are fundamental to autonomous systems and robots where perceiving the environment is necessary for navigation. In addition to TOF measurements, optical sensors can measure the Doppler shift resulting from interacting a laser with a moving object.

Fig. 7.7 Magnetoresistive material

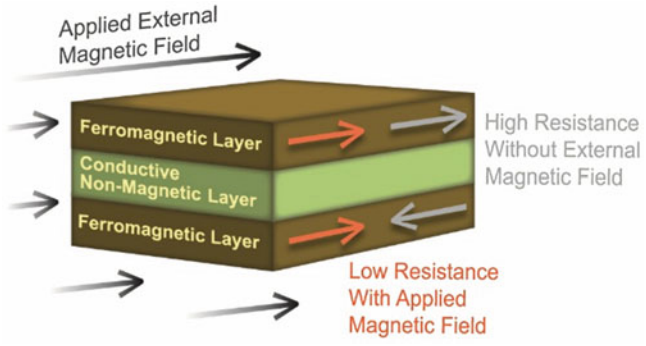

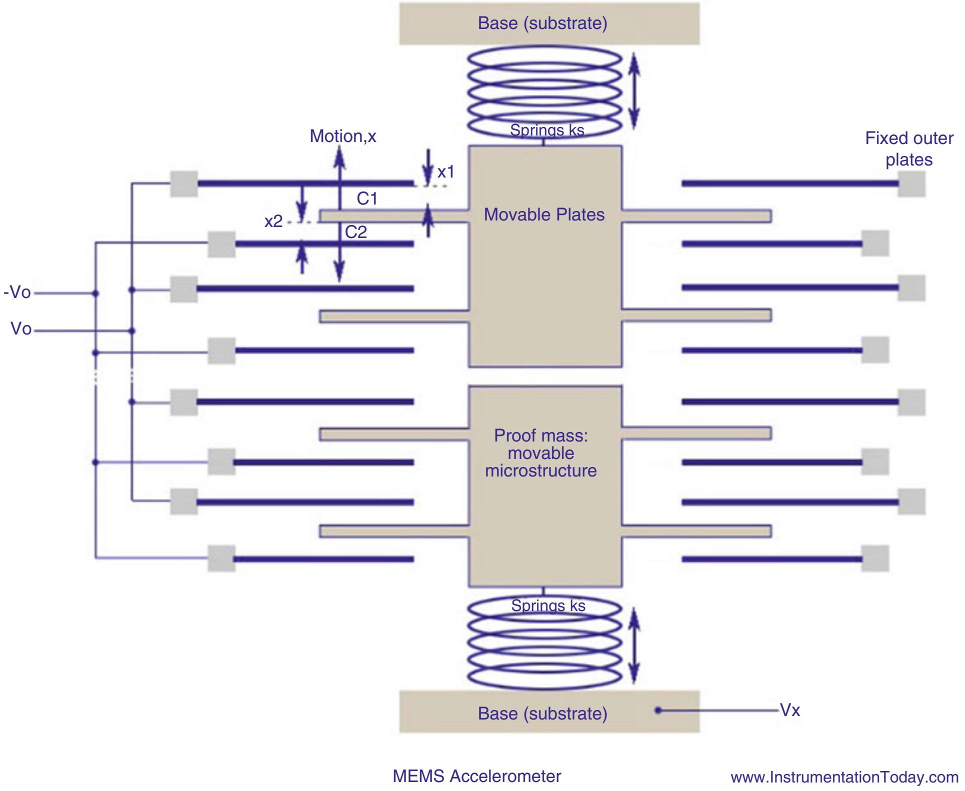

Fig. 7.8 MEMs accelerometer sensing element

7.6 Modeling/Simulation

A key set of design tools that has contributed to the explosion in mechatronic based systems are the modeling programs available to the engineer. Spice models used to simulate analog electronics have proven to have the fidelity to permit the designer to skip the breadboard stage. Software optimizes routing for PC board layout, and programs like Simulink validates control design.

High fidelity models of many hardware components are also available to include in the system simulation. Models for the response of motors and linear actuators can be integrated into the system simulator to prove performance prior to prototype construction.

7.7 Bus Structures

A key component of the mechatronics system is the bus structure, the linking between the actuators, sensors and the microcontroller. The bus structure typically comes in two flavors, the bus on the PC board interfacing the various on board components and the external bus that links the board to the actuators, sensors and other computer systems. Included as part of the discussion on buses is the use of wireless links, a popular tool for transferring data.

The on board bus structure is typically either Serial Peripheral Interface (SPI) or I2C. SPI, developed by Motorola, is a full duplex bus operating in a master–slave configuration. A single master forms the frames for reading and writing to multiple slaves that are selected through individual lines. SPI is simple to implement, is high speed and is low power. It does require extra pins on the IC chips and there is no error checking capability (Figs. 7.9 and 7.10).

Inter Integrated Circuit Communication, I2C, pronounced I squared C, is the other common onboard bus structure. I2C was developed by Philips is slower than SPI but is often used to transfer data from ADCs and DACs to the controller. I2C suffers a bit from limited addressing and can cause problems with certain components. Most microcontrollers support both on board communication protocols with many devices supporting multiple bus of each so that different speeds can be used to communicate with the various slaves. For example, data acquisition would typically require a much higher data rate than say power control where updates can be 10 s of milliseconds.

Bus structures for off board communications tend fall into the familiar areas of Control Area Network (CAN), Universal Serial Bus (USB) or Ethernet.

The CAN bus is of particular interest because of its breath of applications. Developed by Bosch, and officially released in 1986, this bus structure is generally associated with the automobile industry. With the growth in robotics and other complex systems, CAN is finding an expanded application. CAN is has two speeds, a low speed used for applications where latency is not an issue and a high speed configuration used for control. The typical automobile now contains 100 or more microcontrollers. These systems do the sensing and control from sophisticated engine control units, ECUs, to simple applications like controlling the interior lighting. Unlike the more common USB or Ethernet structures, CAN does not send large packets of data from point to point. Instead, each node in the system sends small amounts of data, for example engine temperature, on the bus making it available to any of the other nodes on the bus. Data rates for these buses can be 1 Mbit/sec.

USB and Ethernet are also popular bus structures used in mechatronics applications to interface the microcontroller system to more complex computer units. Power over USB or Ethernet is also useful since the power requirements for many of these applications are easily handle with the power available on these buses.

Wireless links are a popular option for mechatronic systems. The use of low power Bluetooth or Zigbee is supported by many microcontrollers. In many applications, these devices can replace slip ring configurations to link system on rotating machinery. Transducers can be designed to store data, gigabytes at a time and then download when a Bluetooth is established

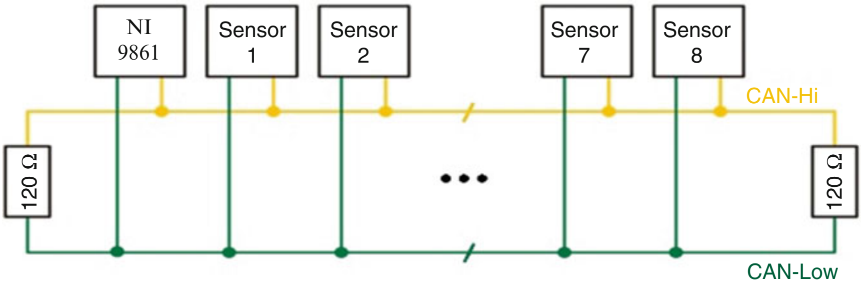

Fig. 7.9 CAN bus topology

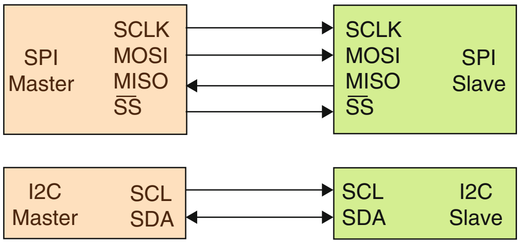

Fig. 7.10 Diagram of SPI and I2C topology for on board bus

with a configured receiver. Sports watches and other devices allow athletes to participate in an event and then download inertial measurement data, GPS information as well as variety of vital signs, all time stamped for post processing. The data device, sports watch for example is simply brought in proximity to the receiver and the data is downloaded.

7.8 Batteries

Normally in a discussion about mechatronic systems, batteries would not be part of the discussion. However, with the low power requirements of these microcontrollers coupled with MEMs sensor technology and low power wireless or micro SD card storage, makes battery selection an important component in mechatronic design.

Three basic chemistries will be discussed here although battery technology is a rapidly evolving science, particularly for hybrid/electric vehicles. The three chemistries are lead-acid (Pb-acid), Nickle metal hydride (Ni-MH) and Lithium Ion, (Li-ion). One of the important measures is specific energy in units of watt-hr/kg. These values are 35, 75, 150 for Pb-acid, Ni-MH and Li-ion respectively. Li-ion wins most of these comparisons but suffered from charging issues that caused fires. These issues have been mitigated using intelligent charging schemes, using microcontroller based chargers by the way. Charging, cycle limits, current draw and battery balancing are important considerations for selection of a system battery pack. Most manufacturers will provide definitive information on their batteries to assist in the design process.

7.9 Conclusions

Mechatronics is a rapidly evolving technology that links sensing tools with microcontrollers and actuators. Complex systems can be realized, designed and tested with minimal prototyping and initial hardware. Simulation programs such as Spice models captures many of the real world properties that produces valid models for design. The rapid development of downloadable hardware models enhances the design process allowing a designer to test and validate sensor inputs, actuation of properties as well as the embedded software.

The significant characteristics of many of these systems is the ultra- low power usage. Unlike the power needs just a few years ago where +/−15 V were standard, many components operate on voltage ranges from 1.6 to 3.3 V.

The transition to lower power more compact systems will continue to evolve, increasing the importance of the microcontroller and the supporting tools.

References

1. Bolton, W.: Mechatronics. Pearson-Prentice Hall, New York, NY (2008). ISBN 978-0-273-71298-5
2. Bishop, R.H.: The Mechatronics Handbook. CRC Press, New York, New York (2002)
3. Petruzella, F.D.: Electric Motors and Control Systems’. McGraw Hill, New York, New York (2010). ISBN 978-0-07-352182-4
4. Regtien, Paul P.L.: Sensors for Mechatronics. Elsevier, London, England (2012). ISBN 978-0-12-391497-2
5. Islam, N.: Microelectromechanical Systems and Devices. InTech, Rijeka, Croatia (2012). ISBN 978-953-51-0306-6
6. DeSilva, Clarence W.: Mechatronics: An Integrated Approach. CRC Press, New York, New York. ISBN 978-020-36-116-47

Chapter 8
Enhanced Vibration Damping by Means of a Negative Capacitance

Marta Berardengo, Riccardo Bonsignori, Alfredo Cigada, and Stefano Manzoni

Abstract The use of shunted piezoelectric transducers to damp mechanical vibrations is an interesting approach thanks to its low cost and the light weight of the actuators used. Among the different ways to build the shunt impedance, the use of negative capacitances is very attractive because it allows for high damping performances with low power required by the control system. Negative capacitances do not exist as physical components but they can be designed and built using circuits based on operational amplifiers. The use of shunt circuits based on a negative capacitance coupled to a resistance allows to have a broadband control. This paper explains how to increase the bandwidth of this controller by adding to such a shunt circuit an inductance. The dynamics of the controlled system is solved analytically and the reason why the introduction of the inductance is able to give the mentioned improvement is made clear also using numerical simulations. Furthermore, this improvement also allows to increase the attenuation performance in a certain frequency band. The conditions necessary to assure the stability of the electro-mechanical system are found and explained.

Keywords Piezoelectric shunt • Broadband vibration control • Negative capacitance • Damping • Smart materials

8.1 Introduction

This paper deals with vibration reduction by means of piezoelectric benders shunted with an electric impedance. This approach is very attractive when dealing with light structures. Indeed, this control method requires no, or few, power and it is based on lightweight actuators so that low load effects occur. Furthermore, no feedback signals and digital controllers are needed. Hence, such a control method is very cheap if compared to traditional active damping.

The electric impedance connected to the piezoelectric actuator can be realised with different layouts, depending on the kind of control required: mono-modal, multi-modal and broadband. This paper focuses on broadband control. The simplest way to build such a kind of controller is to connect the actuator to a resistance. Despite Hagood and von Flotow [1] proved that a proper choice of the resistance allows to focus the damping action on a given mode of the structure, this control technique is effective also on the other modes of the structure, even if the control action is lower than that acting on the mode on which the resistance has been tuned. Moreover, this control strategy is passive because the added element (i.e. the resistance) is passive and thus no power is fed to the system. The consequence is that this control is always stable, whatever resistance value is chosen.

A big issue related to this control technique is that the control action results very limited and thus the attenuation provided by this shunt impedance is often poor and unsatisfactory, even in the case in which the mode on which the resistance is tuned is considered [2].

One way to enhance the attenuation provided by this kind of shunt is the addition of a second element into the shunt Impedance: a negative capacitance. This element does not exist in nature but it can be realised by employing an operational amplifier (OP-AMP). The increase of the vibration attenuation allowed by this further element was already evidenced in different works in literature [3–5]. The main issue related to this technique is the stability of the whole electro-mechanical system (EMS) (i.e. vibrating structure + piezoelectric bender + shunt impedance) because the OP-AMP introduces energy into the system and thus stability must be checked. If a value of the negative capacitance which guarantees the stability of the EMS is chosen, a great benefit in terms of vibration reduction is observed.

M. Berardengo • R. Bonsignori • A. Cigada • S. Manzoni (✉)
Department of Mechanical Engineering, Politecnico di Milano, Via La Masa 34, 20156 Milan, Italy
e-mail: stefano.manzoni@polimi.it

A. Wicks, C. Niezrecki (eds.), *Structural Health Monitoring, Damage Detection & Mechatronics, Volume 7*,
Conference Proceedings of the Society for Experimental Mechanics Series, DOI 10.1007/978-3-319-29956-3_8

This paper proposes a new shunt impedance made up of a the resistance, a negative capacitance and an inductance. The use of an inductance coupled to a resistance (LR) is already considered in literature but usually this circuit is used for mono-harmonic attenuation [1]. Indeed, the circuit composed by the resistance and the inductance, together with the capacitance of the piezoelectric patch (C_p, see the Sect. 8.2), and eventually the added negative capacitance, behaves like a resonant system. Therefore, this circuit can be seen as the electric equivalent of the tuned mass damper [6, 7].

The aim of this paper is to demonstrate that an inductance in the shunt circuit can be used also for broadband control when coupled to a resistance and properly tuned. Moreover, guidelines to choose the value of the shunt parameters will be given.

The paper is structured as follows: Sect. 8.2 introduces the model employed to describe the EMS, while Sect. 8.3 explains how to fix the values of the resistance, the negative capacitance and the inductance for broadband damping and explains the driving idea of this paper. Furthermore, this section shows some numerical simulations to highlight the benefits provided by the addition of the inductance in the shunt circuit. Finally, Sect. 8.4 focuses on the stability of the EMS.

8.2 Analytical Model of the Electro-Mechanical System

The model employed to describe the behaviour of the EMS is the one presented by Thomas et al. in [2].

A generic elastic structure is considered, with one piezoelectric patch bonded on it (see Fig. 8.1). U is the displacement of any point x of the structure at time t. A shunt impedance Z is connected to the piezoelectric actuator and V is the voltage between the electrodes of the piezoelectric patch, which is also the shunt terminal voltage. Q is the electric charge in one of the electrodes and, considering the convention of sign for V in Fig. 8.1, Q is the charge in the upper electrode.

A reduced order model of the EMS is obtained by expressing the displacement U in modal coordinates and considering N eigenmodes:

$$U(\boldsymbol{x},t) = \sum_{i=1}^{N} \phi_i(\boldsymbol{x}) q_i \tag{8.1}$$

where q_i is the ith modal coordinate and ϕ_i is the ith eigenmode of the structure. The modal coordinates q_i are solutions of the problem [2]:

$$\ddot{q}_i + 2\xi_i\omega_i\dot{q}_i + \omega_i^2 q_i - \chi_i V = F_i \quad \forall i \in 1, \ldots, N \tag{8.2a}$$

$$C_p V - Q + \sum_{j=1}^{N} \chi_j q_j = 0 \tag{8.2b}$$

Therefore, the motion of the EMS is described by N modal equations, corresponding to the balance law of mechanical forces (Eq. (8.2a)). Since the model describes the whole electro-mechanical behaviour of the system, the dynamics of the structure

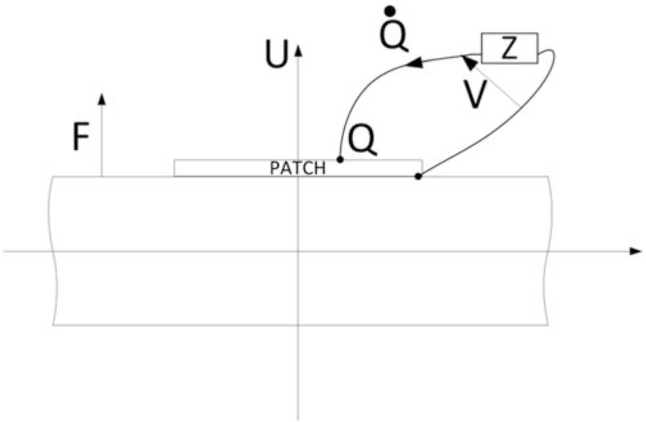

Fig. 8.1 A piezoelectric patch bonded on a structure and shunted with an impedance Z. F is an external force exciting the structure

is coupled to the electric behaviour of the piezoelectric actuator and the shunt impedance (described by Eq. (8.2b)) by the term χ_i. Particularly, Eq. (8.2b) describes the balance of electric charges on the piezoelectric electrodes. ω_i is the ith eigenfrequency of the mechanical structure and ξ_i is the associated non-dimensional damping ratio. Here, ϕ_i, ξ_i and ω_i are related to the situation with the piezoelectric patch short circuited (i.e. $V = 0$). χ_i is a modal coupling coefficient, which is related to the energy transfer between the ith mode shape and the piezoelectric actuator. The χ_i coefficients can be computed by either a finite element model of the structure [8] or by an analytical approach [9]. Finally, C_p is the blocked electric capacitance of the patch (i.e. with $U(x,t) = 0\ \forall\, x \Rightarrow q_i = 0\ \forall i$).

It is possible to demonstrate [5] that under a single degree of freedom approximation (under the hypothesis of low modal density), the Frequency Response Function (FRF) of the controlled system between a disturbance force and the response of the system around the ith mode considered can be expressed in the Laplace domain as:

$$H_i = \phi_i(x_f)\phi_i(x_m)\frac{ZC_{p,i}s + 1}{ZC_{p,i}s^3 + \left(1 + 2\xi_i\omega_i ZC_{p,i}\right)s^2 + \left(2\xi_i\omega_i + \omega_i^2 ZC_{p,i} + \omega_i^2 C_{p,i}k_i^2 Z\right)s + \omega_i^2} \tag{8.3}$$

Where $C_{p,i}$ is the capacitance of the piezoelectric patch between the ith and the (i + 1)th mode [5], and Z is the shunt impedance (see Fig. 8.1). x_m is the point where the response of the structure is measured and x_f is the point where the disturbance force is applied. k_i is the modal electro-mechanical coupling factor, which is expressed as $k_i = \chi_i/\left(\omega_i\sqrt{C_{p,i}}\right)$ and it is a very good approximation of the ith effective coupling factor [2] $k_{eff,i} = \sqrt{\left(\omega_{OC,i}^2 - \omega_i^2\right)/\omega_i^2}$ (where $\omega_{OC,i}$ is the ith eigenfrequency of the EMS when the piezoelectric patch is in open-circuit).

8.3 Structure of the Electric Impedance

As stated in Sect. 8.1, this paper proposes a new shunt impedance Z with the aim of improving the performances of the traditional broadband controller made up of the series of a NC and a resistance (R-NC, Fig. 8.2a). This new impedance considers the addition of an inductance in series to the R-NC shunt (RL-NC, Fig. 8.2b).

In order to better understand the working principle of this new circuit, it is worth analysing at first the behaviour of the simple R-NC impedance (Fig. 8.2a). This impedance consists of a resistance (R) in series to a negative capacitance (NC). The effect of adding a NC in a generic shunt impedance is to enhance the control performances of the piezoelectric actuator with respect to the traditional shunts (e.g. R, RL) [5, 10]. The use of a NC can be interpreted as a way to improve the characteristics of the piezoelectric actuator, making it more performing in terms of control action given to the structure [10, 11]. This effect depends on the value taken by the negative capacitance $-C_n$ compared to the one of the piezo-actuator: the closer C_n is to $C_{p,i}$, the higher the attenuation provided by the shunt is [5].

If we look at the FRF of the EMS, the effect of the NC, connected in series to the piezo-actuator, is to move each short circuit natural frequency of the EMS to lower values [3], and the closer C_n is to $C_{p,i}$ the higher the shift is. The new value of each short circuit eigenfrequency can be expressed as:

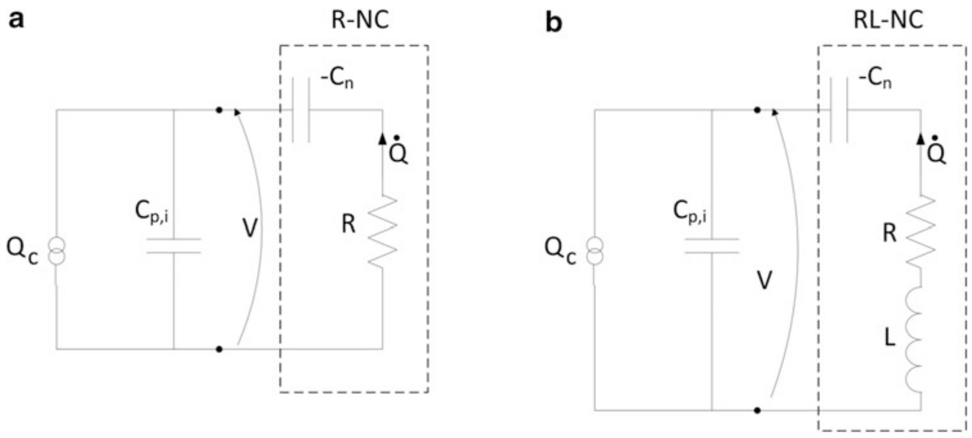

Fig. 8.2 Shunt impedance layout: R-NC (**a**) and RL-NC (**b**)

$$\omega_i^n = \sqrt{\omega_i^2 - \frac{\chi_i^2}{C_n - C_{p,i}}} \tag{8.4}$$

This aspect is of great importance because it will be used to fix the optimal inductance value, as explained in the following.

It is worth highlighting that the value of C_n cannot be chosen arbitrarily close to $C_{p,i}$ to increase the performances, since stability problems can occur. There exists in fact a threshold on the value of C_n to assure the EMS stability, and it will be calculated in Sect. 8.4.

As for the resistance R, it can be considered the electrical equivalent of a mechanical damper. The optimal value for the resistance, $R_{i,opt}$, can be chosen in order to focus the control action on a specific mode; in this way the vibration attenuation is maximised on the mode considered. This value can be found by minimising H_i^{max}, the maximum of the module of the FRF H_i (see Eq. (8.3)) in correspondence of the mode considered.

Once fixed the value $R_{i,opt}$ for the resistance, the modes other than the ith result damped as well, but the vibration attenuation achieved will be lower than that achievable with their optimal tuning. The control action is indeed focused on the ith mode.

This can be deduced also by looking at Fig. 8.3. Figure 8.3 shows the modulus and phase of the FRF between Q_c and V (see Fig. 8.4). This FRF called H_c can be seen as the FRF of the EMS controller [7, 10]. It is possible to notice that the controller acts in a frequency band that depends on the value of the resistance. The higher the resistance is, the lower the frequency band of the controller is. The effect of the controller, indeed, tends to decrease after a frequency equal to the one on which the resistance is tuned.

In order to increase the bandwidth of the controller, and therefore to improve the damping of the modes other than the one on which the resistance is tuned, an inductance L can be added in series to the R-NC circuit (see Fig. 8.2b). This new circuit made up by a resistance R, an inductance L and an equivalent capacitance (due to the presence of $C_{p,i}$ and $-C_n$ [5]) represents a resonant circuit and has its natural frequency at ω_e:

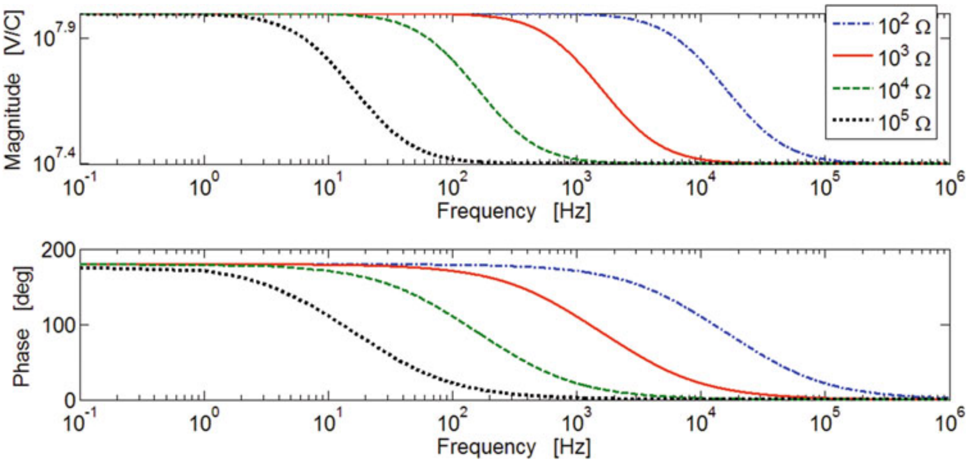

Fig. 8.3 FRF $\boldsymbol{V/Q_c}$ (see Fig. 8.4) for different values of $\boldsymbol{R}$. Here$C_{p,i}$ = 40 nF and C_n = 50 nF

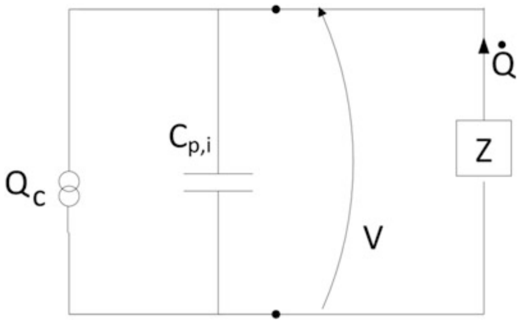

Fig. 8.4 Electrical scheme of the shunt system; the piezoelectric patch is composed by the parallel of the capacitance and the strain-induced charge source

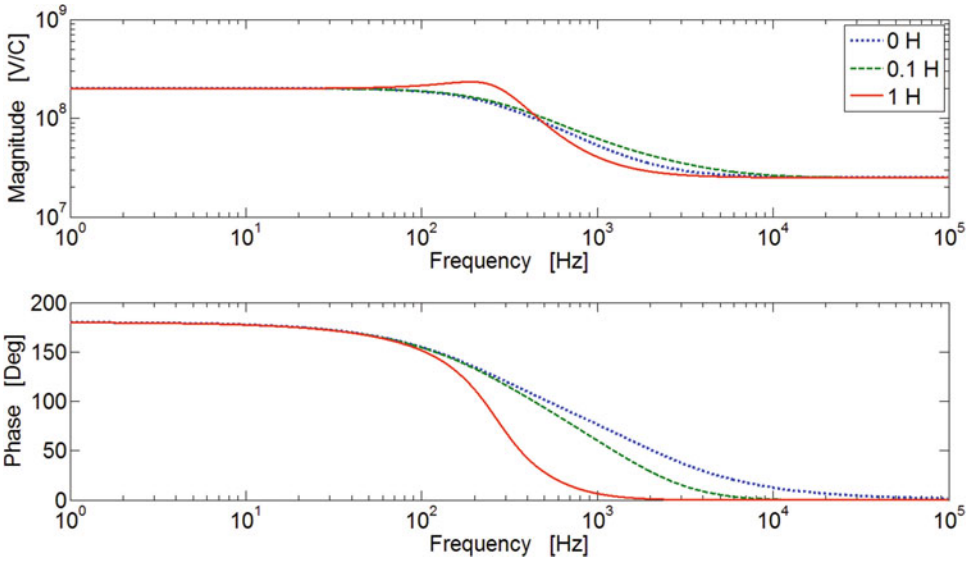

Fig. 8.5 FRF $\boldsymbol{V/Q_c}$ (see Fig. 8.4) for different values of L. Here $C_{p,i} = 40$ nF and $C_n = 45$ nF, $R = 1.8$ kΩ

$$\omega_e = \frac{1}{\sqrt{LC_{eq,i}}} \tag{8.5}$$

Where $C_{eq,i} = C_n C_{p,i} / (C_n - C_{p,i})$.

Figure 8.5 shows the FRF of the controller, H_c, for this RL-NC circuit, when the inductance assumes different values. It is easy to notice that H_c shows a peak in correspondence of its eigenfrequency ω_e but its shape is the same as the one of H_c for R-NC circuits for frequency below ω_e. The effect of the controller tend instead to vanish for the frequency band above ω_e.

Thanks to this behaviour it is easy to see that it is possible to increase the performances of the R-NC controller in a certain frequency band around a fixed frequency ω_k, by properly tuning the inductance value to have $\omega_e = \omega_k$.

In order to better explain the effect of the RL-NC controller, let us suppose to consider a system with four modes and to be interested in damping the first three modes. Then the C_n value must be chosen in order to satisfy the stability condition (see Sect. 8.4) and as close as possible to $C_{p,i}$ to maximise the performance. Then the value of R is fixed as $R_{i,opt}$, where i is the mode on which the control action must be focused, for example the second. Finally the value of L must be decided in order to increase the performance on the modes lower than the fourth. As mentioned before the RL-NC circuit allows to increase the performances in a frequency band around ω_e. Therefore, to increase the control action on the modes lower than the fourth, ω_e must be fixed equal to the third natural frequency of the EMS. At this point it is important to notice that, as explained before, the use of the NC decreases the short circuit natural frequencies of the system (see Eq. (8.4)), therefore ω_e must be set equal to ω_3^n, the new third eigenfrequency.

In order to quantify the improvements achievable with this new kind of shunt circuit, in terms of vibration attenuation, it is convenient to define the index $A_{r,i}$:

$$A_{r,i} = A_i(L = 0,\ R = R_{4,opt}) - A_i\ (L \neq 0,\ R = R_{4,opt}) \tag{8.6}$$

Where A_i is the attenuation of the ith mode in decibel.

This index represents the attenuation improvements obtained with the impedance RL-NC with respect to the case in which the simple R-NC circuit is used. Figure 8.6 shows $A_{r,i}$ for the modes of the system in Table 8.1 when a value $R = R_{4,opt}$ is chosen (in this example the goal is to control all the four modes, not just the first three as in the previous case) and ω_e is fixed equal to the eigenfrequency of the fourth mode. It is possible to see in this case that the addition of the inductance is able to increase the attenuation on all the modes until a value of $L < 2$ H is chosen. It is worth noticing that, the closer an eigenfrequency ω_i^n is to ω_e, the higher the attenuation improvement provided by the addition of the inductance is.

One could notice that the structure of this RL-NC impedance is the same as the one used for mono-modal control. For this reason, it is worth highlighting that the value of R employed in the RL-NC circuit used here is much higher than the optimal

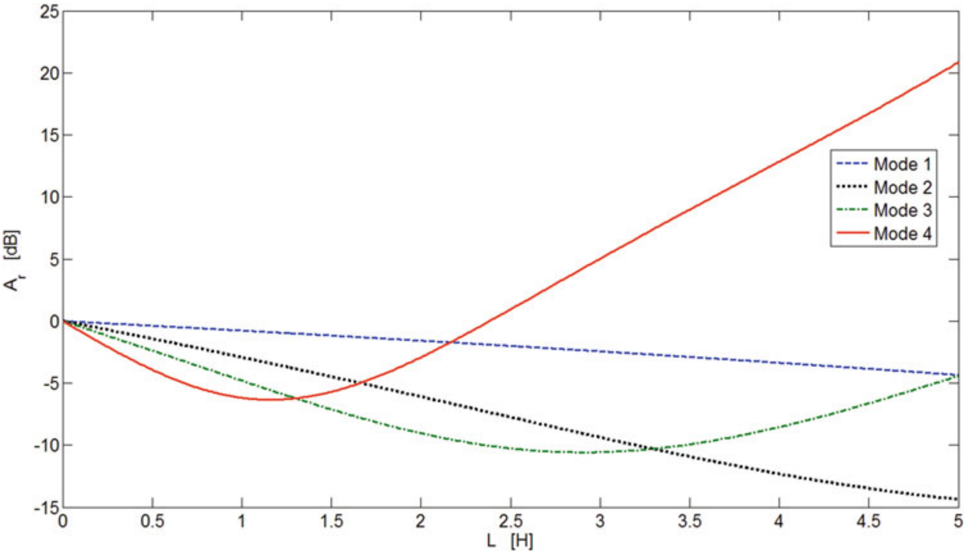

Fig. 8.6 $\boldsymbol{A_r}$ as a function of L for the modes of the system in Table 8.1. Here $C_{p,4} = 40$ nF and $C_n = 45$ nF, $R = 1.8$ kΩ (very close to $\boldsymbol{R_{4,opt}}$)

Table 8.1 Modal data of a four degree-of-freedom system

Mode	ω_i [rad/s]	ξ_i [%]	k_i
1	2π40	0.2	0.20
2	2π100	0.2	0.10
3	2π150	0.1	0.08
4	2π200	0.2	0.10

value which should be used for a mono-modal resonant control [12] (indeed the value of R has been chosen with a criterion different from that used for classical LR impedances). This high value of R allows to have a broad peak in correspondence of ω_e for the FRF H_c (see Fig. 8.5) and thus the control action is increased in the frequency range around ω_e.

8.4 Stability of the Electro-Mechanical System

As mentioned in Sect. 8.2, the use of a negative capacitance poses some critical issues related to EMS stability. Therefore, stability conditions were derived by applying the Routh-Hurwitz criterion to the denominator of H_i (see Eq. (8.3)). The value of the NC which guarantees stability is:

$$C_n > C_{p,i}\left(1 + k_i^2\right) \tag{8.7}$$

This condition should be satisfied for each mode of the EMS, therefore the strictest one is that related to the first mode [5]. Consequently, the stability condition for the whole EMS becomes:

$$C_n > C_0 = C_{p,1}\left(1 + k_1^2\right) \tag{8.8}$$

Where C_0 is the capacitance of the piezoelectric patch at the null frequency. It is worth noticing that $C_0 > C_{p,i}$ (for all the modes) and therefore the value of C_n cannot be chosen as close as desired to $C_{p,i}$ in order to increase as much as possible the performances (as already mentioned in Sect. 8.3) but the threshold of Eq. (8.8) must be always fulfilled.

This poses some limitations to the maximum obtainable performance with this control strategy.

8.5 Conclusion

This paper has dealt with vibration attenuation by means of piezoelectric patches shunted with electric impedances based on negative capacitances. A negative capacitance is able indeed to increase a lot the attenuation performance of a pure resistive shunt. This paper explains how to further increase its performance by adding an inductance into the shunt impedance layout. This added element is able to increase the broad-band attenuation. The condition for the stability of the electro-mechanical system is provided as well. The next step is the experimental validation of the strategy proposed.

References

1. Hagood, N., von Flotow, A.: Damping of structural vibrations with piezoelectric materials and passive electrical networks. J. Sound Vib. **146**, 243–268 (1991)
2. Thomas, O., Ducarne, J., Deü, J.-F.: Performance of piezoelectric shunts for vibration reduction. Smart Mater. Struct. **21**, 015008 (2012)
3. de Marneffe, B., Preumont, A.: Vibration damping with negative capacitance shunts: theory and experiment. Smart Mater. Struct. **17**, 035015 (2008)
4. Behrens, S., Fleming, A.J., Moheimani, S.O.R.: A broadband controller for shunt piezoelectric damping of structural vibration. Smart Mater. Struct. **18**, 18–28 (2003)
5. Berardengo, M., Thomas, O., Giraud-Audine, C., Manzoni, S.: Improved resistive shunt by means of negative capacitance: new circuit, performances and multi mode control. Smart Mater. Struct. Under review (2015)
6. Preumont, A.: Mechatronics - Dynamics of Electromechanical and Piezoelectric Systems. Springer, Dordrecht (2006)
7. Moheimani, S., Fleming, A.: Piezoelectric Transducers for Vibration Control and Damping. Springer, London (2006)
8. Thomas, O., Deü, J., Ducarne, J.: Vibrations of an elastic structure with shunted piezoelectric patches: efficient finite element formulation and electromechanical coupling coefficients. Int. J. Numer. Methods Eng. **80**, 235–268 (2009)
9. Ducarne, J., Thomas, O., Deü, J.-F.: Placement and dimension optimization of shunted piezoelectric patches for vibration reduction. J. Sound Vib. **331**, 3286–3303 (2012)
10. Berardengo, M., Manzoni, S., Thomas, O., Giraud-Audine, C.: A new electrical circuit with negative capacitances to enhance resistive shunt damping. In: Proceedings of the ASME 2015 Conference on Smart Materials, Adaptive Structures and Intelligent Systems - SMASIS 2015, Colorado Springs, p. 8836 (2015)
11. Moheimani, S.O.R., Fleming, A.J., Behrens, S.: On the feedback structure of wideband piezoelectric shunt damping systems. Smart Mater. Struct. **12**, 49–56 (2003)
12. Berardengo, M., Cigada, A., Manzoni, S., Vanali, M.: Vibration control by means of piezoelectric actuators shunted with LR impedances: performance and robustness analysis. Shock. Vib. **2015**, 704265 (2015)

Chapter 9
Vehicle Tracking for Bridge Load Dynamics Using Vision Techniques

Ryan Brown and Al Wicks

Abstract Structural health monitoring for bridges is an important field that is growing in necessity in the United States with the aging of the interstate and highway system. Most health monitoring systems rely on detecting the motion of the bridge through strain gauges, accelerometers and GPS units. These sensors are very good at measuring the output motion of the bridge, but do not take into account the input signal from the vehicles. Adding the ability to directly measure the location of the input forces on the bridge would improve the ability to model the bridge dynamics. In this paper we propose a system that can identify a vehicle on a bridge and track its location through multiple video frames. Previous work in vehicle tracking has focused on traffic pattern research but has not been adequately translated into a sensing application for structural dynamics. The algorithm was tested and the results show that vehicles are able to be tracked along a bridge with acceptable error in the location output. This method allows a researcher to provide a dynamic input load to his model, rather than estimating or using some load distribution. Combining this with the structural sensing on the bridge will allow for more accurate modeling of the bridge dynamics.

Keywords Mechatronics • Computer vision • Dynamic structural loads • Vehicle tracking • Background segmentation

9.1 Introduction

The field of structural health monitoring is rapidly growing in both publications and necessity. A cursory keyword search of 'Structural Health Monitoring' shows an exponential growth in the number of publications containing the phrase since 1985 [1]. The current state of the art in bridge health monitoring focuses on measuring the vibrations and displacements in the bridge structure typically using accelerometers, GPS units, temperature sensors and strain gauges [2–4]. These sensor are well studied and can be arranged in a multitude of ways to gather precise and useful data. However, none of these sensors measure solely the input forces on the bridge. All of their measurements are of bridge vibration due to the input forces from vehicles. The ability to know the location of the input force on the bridge, especially in real world conditions with multiple vehicles at multiple speeds, is not feasible with the listed sensing packages.

Our system allows for the measurement of the location of multiple vehicles moving at multiple speeds and directions on the bridge. With this information, the measured vibrations and displacements of the bridge can be linked with a known input, which can lead to better modeling and more accurate monitoring of the bridge.

9.2 Vehicle Tracking Algorithm

9.2.1 Types of Vehicle Detection Schemes

Tracking a vehicle on a roadway has been studied and accomplished using a variety of techniques. The techniques fall into two main categories: Shape detection/Template matching or Background-foreground segmentation. Shape Detection or Template Matching is the process of attempting to search for car-like shapes in an image and track those shapes. Template matching is typically used in scenarios where the type of vehicle is important information [5, 6]. The basic process is to generate a library of vehicle templates and then convolve them with the image. The higher the response of the convolution at

---

R. Brown (✉) • A. Wicks
Department of Mechanical Engineering, Virginia Tech, 445 Goodwin Hall, 635 Prices Fork Road, Blacksburg, VA 24061, USA
e-mail: brownrc@vt.edu

A. Wicks, C. Niezrecki (eds.), *Structural Health Monitoring, Damage Detection & Mechatronics, Volume 7*,
Conference Proceedings of the Society for Experimental Mechanics Series, DOI 10.1007/978-3-319-29956-3_9

a particular point, the more likely that particular vehicle exists at that point. The main drawback of a template matching scheme is the necessary processing time to convolve several different template across each video frame.

Background-Foreground Segmentation is the process of detecting the statistical properties of pixels in an image over time to create a model of what the background of that image should be [7, 8]. This allows the detection of deviations from that model and can be used to segment the image into a foreground-background set. This method is faster than the template matching method, but it does not detect the type of vehicle, nor if the motion is actually a vehicle. It merely detection deviations from an iteratively updating background model. However, in the context of roadways, most background deviations will be vehicles so this limitation is not significant. Another limitation is that the viewed scene needs to remain mostly static across multiple frames as the background model is iteratively built and updated. As the target use for this algorithm is a stationary camera over a roadway, this limitation is also not an issue. Based on the features of these two methods, we chose to use a background-foreground segmentation to identify the vehicles in the roadway

9.2.2 *Overview of Vehicle Location Algorithm*

The proposed vehicle location algorithm has two main components. First, the bridge image is marked by the researcher with a region of interest (ROI) and the width and length of that region is provided. This information is used to create a projective transformation between the bridge image and the defined ROI. This transformation is used to project the locations of the detected vehicles to coordinates inside the rectangular ROI. This is discussed in more detail in Sect. 9.2.3.

Once the transformation has been found, the frames are processed one by one with the background subtraction method to identify the vehicles in the image. The vehicle contours are found using a binary image contour method and then their centroids are calculated to find the location of the vehicle in the original image. Once these locations are found, the transformation from the previous step is used to project the points into the new bridge coordinates. These coordinates can be viewed and/or saved for later analysis. Figure 9.1 shows the flow of the algorithm. The algorithm was written using C++ and the OpenCV library [9].

9.2.3 *Bridge Projective Transformation*

To appropriately transform the perspective bridge images to a rectangular image, a projective transformation matrix must be created. This is a 3×3 matrix that transforms a set of points in one plane to another plane. First, eight points defining two arbitrary quadrangles are chosen. These points are used to find the transformation from one quadrangle to another. The points must be converted to homogenous coordinates, where

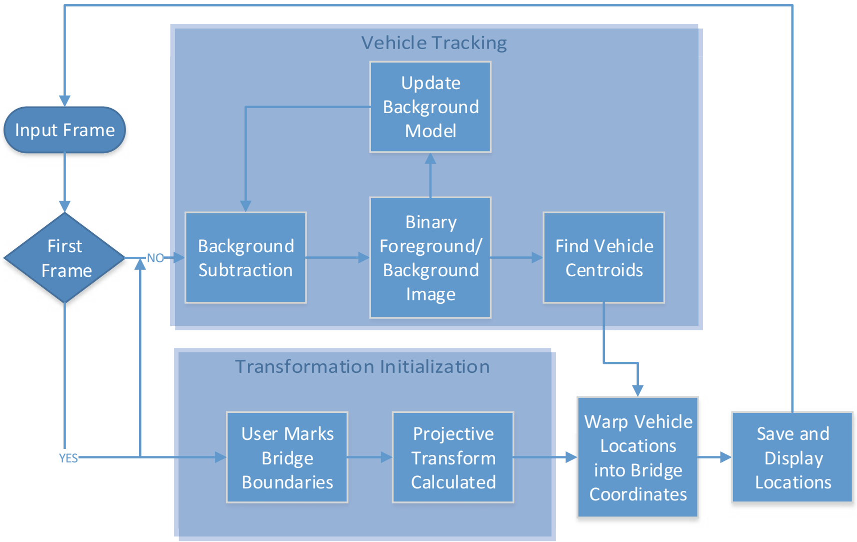

Fig. 9.1 Vehicle tracking algorithm flowchart

$$\begin{pmatrix} x \\ y \end{pmatrix} \rightarrow \begin{pmatrix} x \\ y \\ 1 \end{pmatrix}$$

Once the location points have been converted, a set of linear equations can be solved that will result in a 3×3 transformation matrix. This matrix can be used to transform one homogenous coordinate to its corresponding point in the other quadrangle.

$$A = \begin{pmatrix} a_{11} & a_{12} & a_{13} \\ a_{21} & a_{22} & a_{23} \\ a_{31} & a_{32} & a_{33} \end{pmatrix}$$

$$\begin{pmatrix} a_{11} & a_{12} & a_{13} \\ a_{21} & a_{22} & a_{23} \\ a_{31} & a_{32} & a_{33} \end{pmatrix} \begin{pmatrix} x \\ y \\ 1 \end{pmatrix} = \begin{pmatrix} wx' \\ wy' \\ w \end{pmatrix} \rightarrow \begin{pmatrix} x' \\ y' \end{pmatrix}$$

In the above equation, A is the transformation matrix, $(x,\ y)$ are the original coordinates to be transformed and $(x',\ y')$ are the resulting transformed coordinates. This transformation is generated from the bridge image once and the same transformation is applied to each vehicle location to warp it onto the bridge coordinates.

Some limitations that this transformation method imposes on the system are:

1. The bridge must not curve inside the ROI
2. The bridge must not significantly change height inside the ROI

The method will not work on bridges that fail either of these two conditions. Methods of removing these limitations are discussed below in Sect. 9.5.

9.2.4 *Background Subtraction and Vehicle Tracking*

The particular background subtraction method chosen is a Mixture of Gaussians method. This method assumes that each pixel's intensity can be modeled by Gaussian mixture model. This model is updated with each frame to account for changes in the background scene. Some assumptions made by this model are that there is more background visible than foreground, and that the modes of the background intensity values do not have very high variance [10]. The original version of this background segmentation method was developed by Stauffer and Grimson [11], and has been expanded and refined since. The particular method used in this experiment was developed by KaewTraKulPong and Bowen and includes a refinement in the accuracy and the ability to detect shadows from foregrounds objects and omit them from the detected foreground [12].

The method assumes that the probability of a certain pixel having a certain value at some time is a mixture of N Gaussian distributions. These distributions are controlled by previous values of that pixel. If the predicted pixel value differs by some threshold from the detected pixel value, then the pixel is marked as foreground. The value is then incorporated into the background model. This process is repeated for each pixel and the models updated with each frame.

9.3 Experiments

To evaluate the performance of the algorithm, simulated road data was created in software using computer generated roadway and vehicle images. This data allowed a comparison of the algorithm generated locations against ground truth locations. This was not possible using real data, as there was no access to the necessary information using a real bridge or roadway. The images from road cameras were already in perspective, so there was no ability to generate ground truth vehicle locations on the bridge from that data. In Sect. 9.5, methods of testing this algorithm with real data are discussed. Figure 9.2 shows a transposed sample frame from the simulated data. For all the simulated data, consider the X coordinate to be the width of the bridge from left to right in the image and the Y coordinate to be the length of the bridge from the top of the image to the bottom, shown in the arrows on Fig. 9.2.

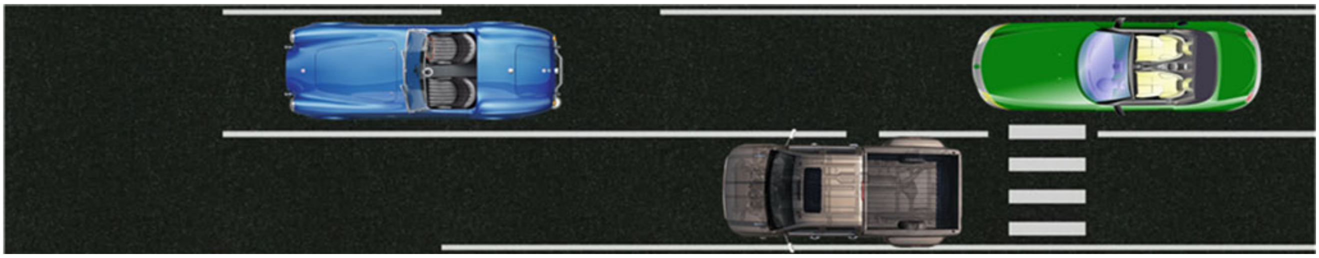

Fig. 9.2 Simulated road data

9.3.1 *Simulated Data Creation*

The simulated data was created using the OpenCV C++ library. The vehicles were moved along the simulated roadway at different speeds and the image was warped to different shapes to simulate different camera positions. Some of the different camera angles are shown in Fig. 9.3. These different simulated camera angles were used to verify the performance of the algorithm and determine if there was growth in error relative to any of the particular camera orientation variables. Five thousand frames were analyzed for each of the different camera angles were created with multiple vehicles in most frames moving at different speeds.

9.3.2 *Experiments on Simulated Data*

Each simulated data set of 5000 frames was used in tests with different ROIs on the bridge. The ROIs were generated at different starting and ending locations along the bridge. Markings at even increments were used to identify the length of each ROI. The projective transformations were calculated and the X-Y location errors were stored for the runs. As part of each experiment, to determine the length along the bridge that the vehicles have moved, the width of the lower part of the ROI was calculated in pixels. The width of the actual bridge is known and can be used to create a pixel per foot value for each ROI width. This value is used to scale the calculated X-Y locations onto the ground truth X-Y locations.

9.4 Results of Experiments

The most important result of the experiments is the overall error in the X-Y location. The width of each bridge is set at 28 ft. The error in the X direction was negligible, less than ±0.5 ft. across 28 ft. The error in the Y direction is more pronounced. This is discussed further below.

9.4.1 *Accuracy of Location*

Focusing on the error in the Y direction, histograms for all runs on the three bridges shown above in Fig. 9.3 are shown below in Fig. 9.4.

The histograms are shown with lines at the standard deviation and twice the standard deviation of the data distribution. Most of the mass of the histogram is within the first standard deviation, and most of the mass of the histogram is within ±5 ft of error. Based on the length of a typical mid-size sedan, the Toyota Camry, which is 15.8 ft., the majority of the error in the Y dimension is confined to within the bounding box of a typical vehicle. There is mass in the histograms outside the ±8 ft. that would keep the error within the vehicle bounding box, but the probability of that occurring is much smaller than the alternative.

The standard deviation in the Bridge 3 dataset is altered based on some mass appearing in the -20 to -10 error range. This mass is caused by errors in the background subtraction method and vehicle contours appearing in areas that they are not,

Fig. 9.3 Examples of warped simulated data (bridge 1, 2 3 from *left* to *right*)

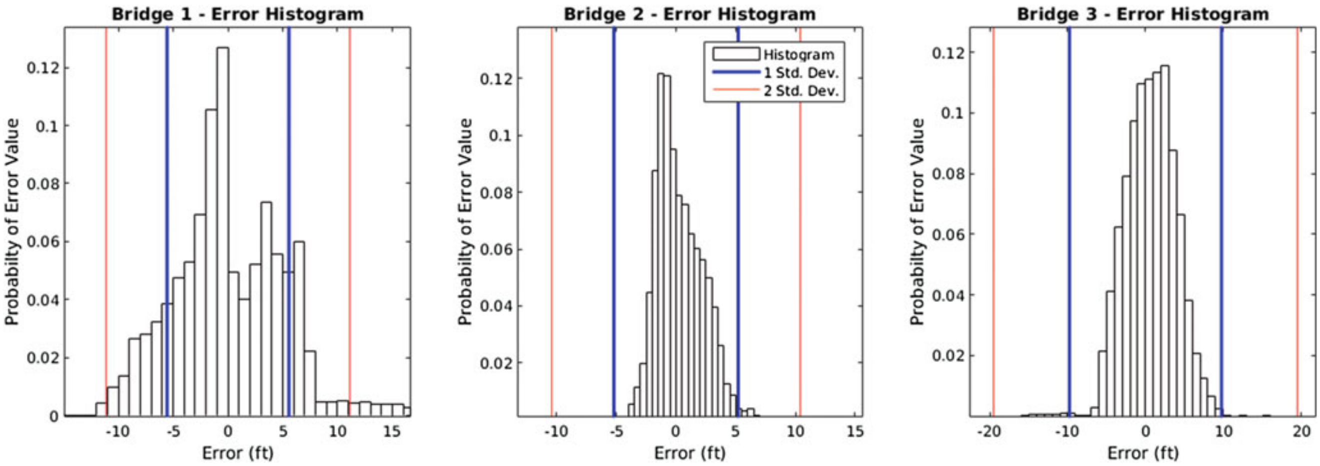

Fig. 9.4 Histograms of Y error normalized for probability

or contours being split into two separate blobs. Either way, the probability of that error is much smaller than the probability of the typical distribution of error that all exists within the ±10 ft. range. To eliminate these errors is a feature for future work and is discussed below in Sect. 9.5.

9.4.2 *Types of Error and Potential Causes*

Figure 9.4 shows a good overview of the errors that exist in the system, but looking closer at individual data runs gives more insight into the type of error that occurs. Figure 9.5 shows a set of data runs where single vehicle tracks are easily seen and separated. The error is not randomly distributed around the desired value, but instead has a relationship with the distance the vehicle has traveled down the simulated bridge. As the vehicle travels down the bridge, the error first decreases and then increases. This distribution of error has to do with the length of the bridge, the location of the ROI on the bridge and the accuracy of the user input. Figure 9.6 shows the same information as Fig. 9.5, but for multiple ROI on the same bridge. Different ROI cause different amounts of error. The slope of each vehicle "error line" scales with the maximum and minimum error in that ROI.

Fig. 9.5 Single vehicle data runs and associated error

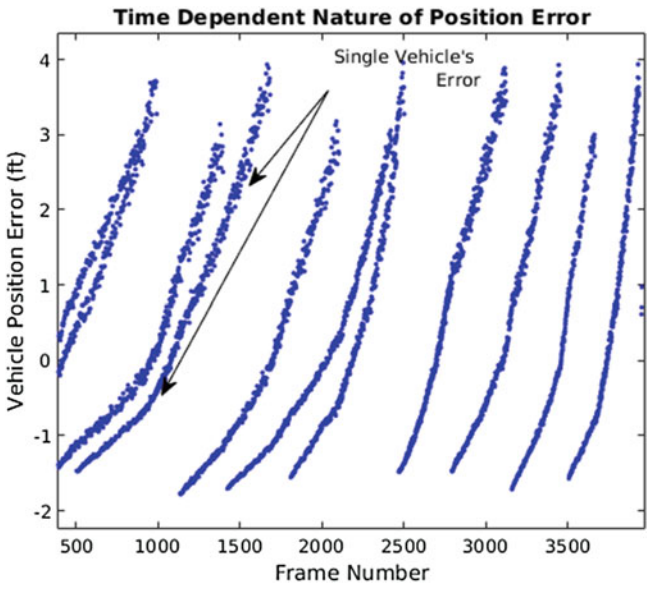

Fig. 9.6 Multiple data runs with different ROI

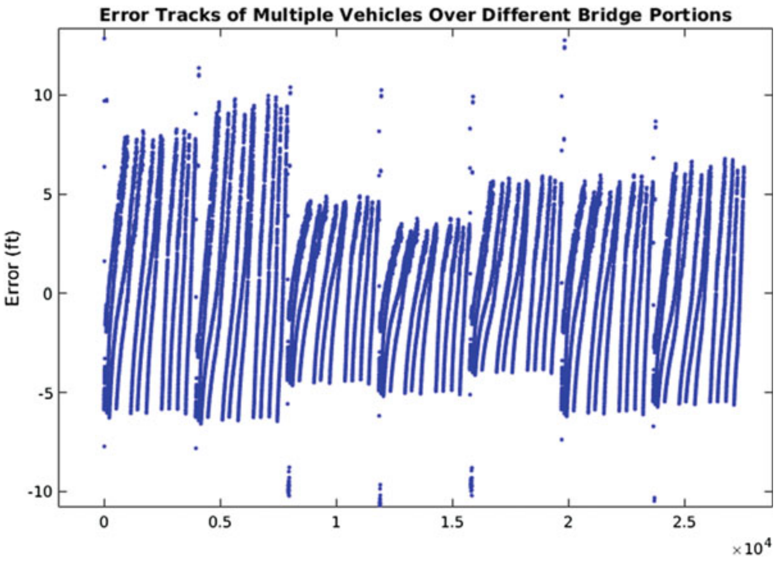

To determine the cause of the error, the traits of the ROIs were compared against the error to see if there was any correlation between them. The length of the ROI did not correlate to the error in the vehicle location, but the pixels per foot value calculated from the lower width of the ROI had a higher degree of correlation. These two values are plotted in Fig. 9.7. The decreasing trend in pixels per foot as error increases is noticeable, but not extreme. However, this finding makes sense based on the operation of the algorithm. The pixels per foot value is used to translate the pixel location of the X-Y coordinate to a location in feet. If this value is off, the location has a higher degree of error. With a smaller pixel per foot value, a single pixel deviation from the actual value can cause more error, as it is a higher percentage of the overall value. This leads to more error in the ROIs that are further from the base of the image.

9.5 Conclusions and Future Work

The information from Sect. 9.4.2 leads us to say that the best usage case for this method is a system where the ROI is near the bottom of the image, and the camera is aligned closer to the centerline of the roadway, but the errors present in the cases where this is not true are still not so great as to prevent the system from being useful for data collection. The largest limitation

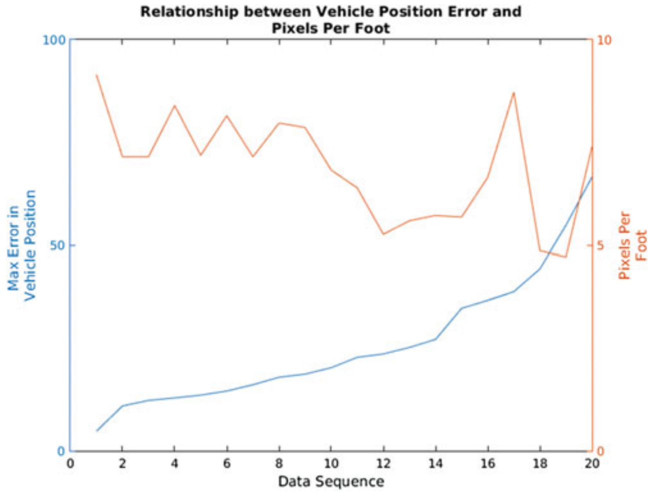

Fig. 9.7 Pixels per foot and vehicle location error

in the current state of the system is the inability to work with non-rectangular bridges. The system as it is currently cannot handle more than minimal curvature in the roadway. Also, it assumes that the bridge height does not significantly change over the ROI. These assumptions prevent the algorithm from analyzing a significant portion of highway bridges.

The curvature limitation can be overcome by calculating the transformation based on the camera location instead of an ROI on the bridge. If the camera location is known relative to a known point on the bridge, a projective transformation can be calculated that will perform the same transformation as the ROI method discussed above. This is not an unrealistic expectation to know the camera position, and in a real data scenario this would be the transformation generation method of choice.

The height limitation is harder to overcome. The camera has a much more difficult time distinguishing the height of an object from its distance from the camera. This could be accomplished using some relationships between the angles of the two edges of the bridge, but the relationships would need to be researched before they could be implemented.

This system can be tested using real road data if there was a way to identify the ground truth location of the vehicles on the road. Attaching GPS monitoring devices to vehicles driving over an instrumented bridge would allow for real world testing of the algorithm. This would be a "plug-and-play" style testing, as the same algorithm as used on the simulated data could be used without any changes on the real world data.

Eliminating the errors in the background segmentation is not a high priority item, as they contribute very small percentages of the overall error in the system. However, a region growing step would prevent the vehicle contours from separating and creating false vehicle blobs in the image. The effects of this on the accuracy of the detected locations would need to be studied.

In the cases where it is not limited by assumptions, the system performs well and is able to resolve the locations of the simulated vehicles to within ±5 in most cases and ±10 ft at worst. This error is within the bounding box of most vehicles that would be detected on the highway, apart from very small vehicles like Smart Cars or motorcycles. As these are the minority on the road, for most situations, this error is acceptable.

References

1. Google Books N-gram Viewer [Online]. http://books.google.com/ngrams. Accessed 01 Jan 2015
2. Hu, X., Wang, B., Ji, H.: A wireless sensor network-based structural health monitoring system for highway bridges. Comp. Aid. Civil Infrastruct. **28**(3), 193–209 (2013). Retrieved from http://onlinelibrary.wiley.com/doi/10.1111/j.1467-8667.2012.00781.x/full
3. Hackmann, G., Guo, W., Yan, G., Sun, Z., Lu, C., Dyke, S.: Cyber-physical codesign of distributed structural health monitoring with wireless sensor networks. IEEE Trans. Parallel. Distrib. Syst. **25**(1), 63–72 (2014). http://doi.org/10.1109/TPDS.2013.30
4. Magalhães, F., Cunha, A., Caetano, E.: Vibration based structural health monitoring of an arch bridge: from automated OMA to damage detection. Mech. Syst. Signal Process. **28**, 212–228 (2012). http://doi.org/10.1016/j.ymssp.2011.06.011
5. Li, T., Li, D.M., Dou, Y.M.: A novel vehicle type recognition based on template matching. Adv. Mater. Res. **945–949**, 1856–1860 (2014). http://doi.org/10.4028/www.scientific.net/AMR.945-949.1856

6. Thiang, A., Lim, R.: Type of vehicle recognition using template matching method of the International Conference on Electrical. (2001). Retrieved from http://faculty.petra.ac.id/thiang/download/paper/Pengenalan_Mobil_P017.pdf
7. Yao, L., Ling, M.: An improved mixture-of-Gaussians background model with frame difference and blob tracking in video stream. Sci. World J. **2014**, 1–9 (2014). http://doi.org/10.1155/2014/424050
8. Oh, J.-S.: Improved MOG algorithm based on adaptive threshold for effective background classification. TECHART **1**(4), 54 (2014). http://doi.org/10.15323/techart.2014.11.1.4.54
9. Bradski, G.: OpenCV. Dr. Dobb's journal of software tools (2000)
10. Power, P., Schoonees, J.: Understanding background mixture models for foreground segmentation. Proceedings of Image and Vision, pp. 267–271 (2002). Retrieved from http://kauri.auck.irl.cri.nz/~johanns/publications/MOG-fg-seg-ivcnz02-preprint.pdf
11. Stauffer, C., Grimson, W.: Adaptive background mixture models for real-time tracking. Proceedings of the 1999 IEEE Computer Society Conference on Computer Vision and Pattern Recognition (Cat. No PR00149), pp. 246–252 (1999). IEEE Comput. Soc. http://doi.org/10.1109/CVPR.1999.784637
12. KaewTraKulPong, P., Bowden, R.: An improved adaptive background mixture model for real-time tracking with shadow detection. In: Video-Based Surveillance Systems, pp. 135–144. Springer US, Boston, MA (2002). http://doi.org/10.1007/978-1-4615-0913-4_11

Chapter 10
Model Based System Testing: Bringing Testing and Simulation Close Together

Fábio Luis Marques dos Santos, Roland Pastorino, Bart Peeters, Cassio Faria, Wim Desmet, Luiz Carlos Sandoval Góes, and Herman Van Der Auweraer

Abstract Experimental modal analysis is commonly associated with the use of simulation models for validation, correlation and model updating. However, this interaction between simulation and test is constantly evolving, not in the least because it can be applied to model-based design engineering in the broad sense. Over time, new simulation methods have emerged and consequently, new approaches combining experimental and numerical methodologies are needed and possible. Model Based System Testing (MBST) is an innovative paradigm that allows to structure this process and, in particular, to investigate how the well-established modal testing and analysis procedures and ways of working can be adopted to the multiphysical nature of mechatronic systems. As a result, many possibilities arise: test data can be used to validate multiphysical models, models help gaining insights into test conditions, hybrid approaches allow combining testing and simulation on hardware-in-the-loop and system-in-the-loop test benches, where physical systems can be combined with simulation models to apply loads and more realistic test conditions, as well as the use of data coming from feedback control system information for testing purposes. In this paper, the context and concepts of MBST will be introduced, and application examples will be shown, highlighting the advantages of such a methodology.

Keywords Testing • Model Based System Testing • Model based systems engineering • Multiphysics • Hybrid testing

10.1 Introduction

Modal testing or experimental modal analysis (EMA) is a well known and established procedure in both academia [1–3] and industry [4–6]. It has historically been a common means of estimating and identifying the modal parameters of a system for structural dynamics and vibro-acoustics applications, be it under laboratory conditions, in operational testing or for fatigue and lifecycle estimation. These tests are customarily used in conjunction with structural acoustic finite element (FE) models, for the correlation [7] and updating [8] of these models, with the purpose of improving their prediction capability. These practices are commonly used in mechanical applications, such as in the automotive [9], aerospace [10], civil engineering [11] and wind turbine [12] industries.

F.L.M. dos Santos (✉)
Siemens Industry Software, Interleuvenlaan 68, 3001 Leuven, Belgium

KU Leuven, Division PMA, Celestijnenlaan 300B, 3001 Heverlee, Belgium

Instituto Tecnológico de Aeronáutica (ITA), Praça Marechal Eduardo Gomes, 50 - Vila das Acácias,
CEP 12.228-900, São José dos Campos, SP, Brazil
e-mail: fabio.m.santos@siemens.com

R. Pastorino • B. Peeters • C. Faria
Siemens Industry Software, Interleuvenlaan 68, 3001 Leuven, Belgium

W. Desmet
KU Leuven, Division PMA, Celestijnenlaan 300B, 3001 Heverlee, Belgium

L.C. Sandoval Góes
Instituto Tecnológico de Aeronáutica (ITA), Praça Marechal Eduardo Gomes, 50 - Vila das Acácias,
CEP 12.228-900, São José dos Campos, SP, Brazil

H. Van Der Auweraer
Siemens Industry Software, Interleuvenlaan 68, 3001 Leuven, Belgium

KU Leuven, Division PMA, Celestijnenlaan 300B, 3001 Heverlee, Belgium

A. Wicks, C. Niezrecki (eds.), *Structural Health Monitoring, Damage Detection & Mechatronics, Volume 7*,
Conference Proceedings of the Society for Experimental Mechanics Series, DOI 10.1007/978-3-319-29956-3_10

Over time, these experimental methodologies have evolved beyond the boundaries of purely mechanical systems, and their applications have expanded to other fields, such as electrical motor testing [13, 14], electromechanical systems [15], multiphysical analyses [16] and mechatronic applications [17]. Additionally, EMA is no longer solely related to troubleshooting analysis, and the modal parameters and models are also being used to estimate forces and loads acting on their systems, the so-called virtual sensing applications. In [18], modal parameters obtained experimentally are used to obtain an augmented Kalman Filter to estimate forces acting on a structure and similarly, [19] further investigates the use of such a filter for force estimation, while [20] uses the approach to estimate modal loads acting on a system.

The challenges that arise with respect to physical testing are related to the growing complexity and multiphysical nature of these new systems and applications. In turn, this leads not only to new ways of carrying out the tests (and a more diverse type of measurement quantities), but also to new types of numerical models to be validated, such as multibody and 1D multiphysical simulation models [21]. In this way, test data can be used on one hand to validate these models, and on the other hand for more complex and realistic interactions, combining these multiphysical models with experimental data into hybrid approaches, where a system can be tested in a system-in-the-loop (SyiL) configuration, in which part of the system is physical, and part of it is simulated.

In this context, the Model Based System Testing (MBST) is defined as the discipline combining physical testing and simulation models with the aim to study, identify, validate and improve the behavior of multiphysical and mechatronic systems. It deals not only with structural tests and/or 3D simulation models, but also with multiphysical systems and 1D simulation models. MBST can be divided into three categories: "Testing for Simulation", "Simulation for Testing" and "Testing with Simulation", with the first two being cases where test and simulation are decoupled, and in the latter, test and simulation are tightly coupled. The first category is an expansion of one of the main roles in modal analysis—obtaining test parameters to create and/or improve simulation models, but in this case also including multiphysics systems. It also involves the use of test post-processing tools with simulation data. The "Simulation for Testing" category is related to the use of simulation models to improve or accelerate the testing process—this includes well known procedures, such as optimal sensor and excitation placement, but contains also more recent methodologies, such as virtual testing or human-in-the-loop applications. Finally, the last category contains the cases in which test and simulation are tightly coupled. Such is the case with hardware-in-the-loop, system-in-the-loop, virtual sensing and hybrid testing, mostly involving real-time processing capabilities. Figure 10.1 shows the MBST tree diagram with all the categories.

This paper will present some application cases that represent each branch of the Model Based System Testing application tree. In the "Testing for Simulation" case, it will be shown how parameters obtained from test can be directly used in a multiphysical model of an electric vehicle and its drivetrain. Then, the use of simulation models to provide insight into the testing of an electric power steering system will be presented, representing the "Simulation for Testing" branch. Finally, the "Testing with Simulation" branch of the application tree will be demonstrated with a model-based high fidelity steering wheel feedback system. In this case, a real-time simulation is coupled with a steering wheel force feedback system to provide realistic force feedback coming from the steering system.

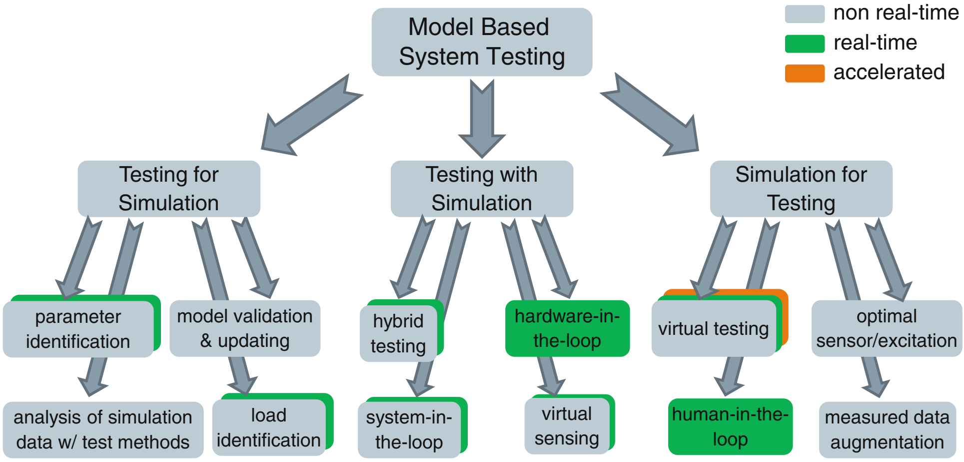

Fig. 10.1 Model Based System Testing application tree

10.2 Testing for Simulation: Simulation of Switched Reluctance Motors

The electrification of road vehicles poses new design challenges regarding the design process of electric drivetrain and vehicle efficiency. There are many new components present in electric motor drives and its subsystems, such as the battery and ECU. Moreover, electric motor losses and acoustic performance have to be accounted for in this process. With this new vehicle design paradigm, it becomes important to investigate how parameter changes affect subsystems individually (such as noise or thermal distribution in the motor) and how they affect the global system, (e.g. efficiency and vehicle autonomy). Therefore it is critical to understand the interaction between these subsystems and their global effect. All of these simulation systems and subsystems require validation and parameters that are obtained from tests.

The following examples are taken from [22] and [16], where an electric vehicle model using a switched reluctance motor as the drivetrain was investigated. This model is composed of many complex subsystems that can be used to compute the energy flow in the vehicle. Figure 10.2 shows such a model with the subsystem divisions.

Many of the subsystems from the electric vehicle require realistic parameters that can be used in the simulation. For example, losses on the battery are estimated with a model that takes into account the internal resistance of the battery, as well as the open circuit voltage, using look-up tables that are obtained experimentally. Similarly, the thermal model of the switched reluctance motor (SRM) uses a thermal resistance network representing the different motor components and thermal losses, which are parameters that are usually hard to estimate and that can be updated using test results.

A more detailed model of the switched reluctance motor was also used for vibro-acoustic prediction purposes. In this case, the process can be divided in many steps (shown in Fig. 10.3): magnetic simulation, 1D simulation, magnetic forces prediction and acoustic simulation. To obtain valid simulation results, the models in some parts of the process need to be validated. An important validation step can be carried out in the 1D simulation, where phase currents obtained in simulation can be correlated with test. If necessary, the characteristics of the motor can be updated based on experimental results. The modal parameters of the stator can also be correlated and updated in the acoustic prediction step.

The overall objective of using these models is to aid in the design of the electric vehicle, allowing for prediction of thermal, energetic and acoustic efficiency, without the need of having a fully built vehicle. Nonetheless, these models and subcomponents still use parameters mostly obtained from experiments at component level.

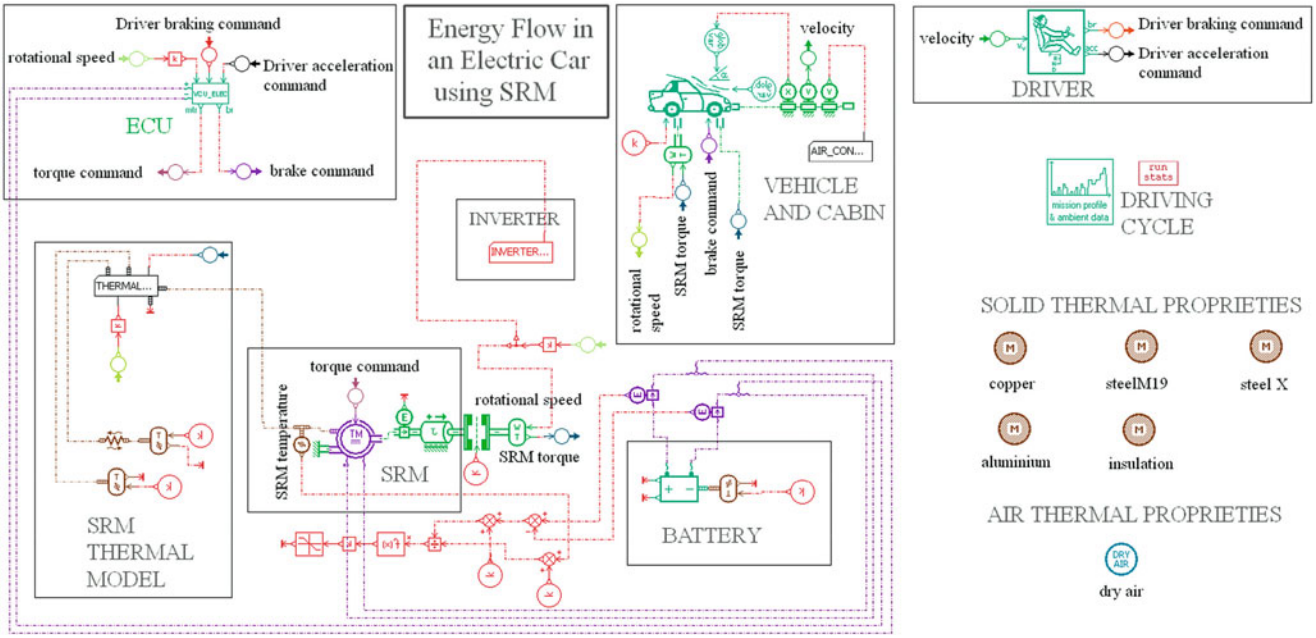

Fig. 10.2 Model of an electric vehicle with energy flow management

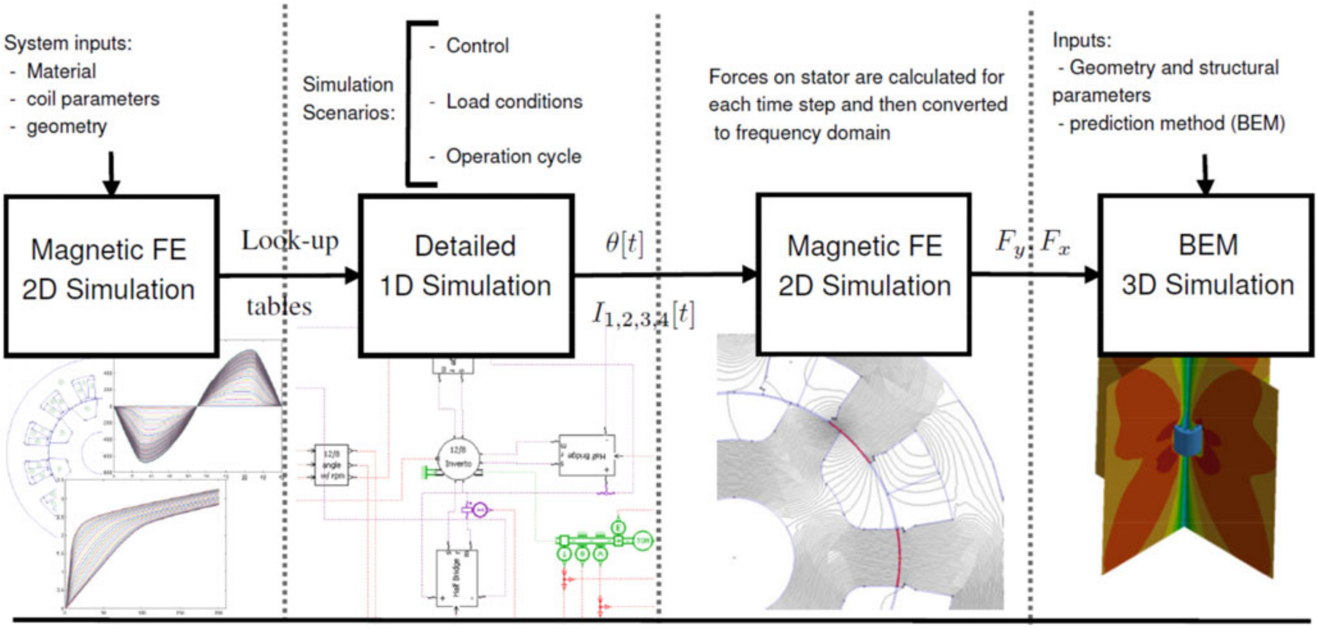

Fig. 10.3 Switched reluctance motor acoustic simulation diagram

10.3 Simulation for Testing: Electric Power Steering

Electrical power steering (EPS) has several advantages when compared to its concurrent technology in power steering (hydraulic actuation): compactness, higher efficiency, easier maintenance and higher reliable. However, depending on the control strategy used to alleviate the driver's required torque these EPS system can create undesired behaviors to the driver, such as, isolate the driver's torque feedback (driving feeling) from the road and provide poor isolation of road disturbances (noise and vibration). The first issue has serious impact on the driver's notion of the vehicle handling and could lead to unsafe driving conditions (e.g. abrupt transition to vehicle side-slipping).

Model-based control strategies often prove to be an appropriate solution for EPS systems but they heavily rely on high fidelity models of the steering system which is by nature a complex, nonlinear, multiphysical. Nonlinearities such as friction and backlash are common characteristic of the rack-pinion gear pair and also for the worm gear, some basic elements of the EPS system (see illustration Fig. 10.4a). A good model must include these physics to improve its prediction capabilities (e.g. such as the one implemented in LMS.IMAGINE AMESim on Fig. 10.4) and allow for the model-based controller to properly drive the system.

A major portion of the mismatch between model and system behaviors arises from the poor characterization of the nonlinear component parameters. Experience from engineering projects within Siemens Industry Software dictates that the nonlinear behavior of the individual components is not the same as the behavior observed when they are interconnected. Therefore the parameters needed for the model needs to be identified at a system testing and not by a series of isolated measurements. This measurement campaign of an entire electromechanical system poses several challenges, in particular to isolate and determine the influence of individual parameter on the overall system behavior.

At this point, since the architecture of the model is available prior to the beginning of the test campaign, this virtual representation can be used to provide significant insight on the influence of the model parameters in the overall system response. This approach can identify sensitive points in the system to a particular nonlinear parameter and allows for the evaluation of a large number of testing configuration, scenarios and procedures at a very low cost and fast implementation.

For the EPS system the instrumentation on different parts of the system without changing the original system behavior is quite challenging, therefore just a few parameters of the system is measured (e.g. driver's torque, rack displacement and steering rod force). One example of such application is to investigate what is the effect of one specific parameter on the driver's torque, Fig. 10.5 shows the impact predicted by the model of different levels of the friction properties on the worm gear (dynamic and static friction coefficients) for a 90° cornering maneuver at low speed.

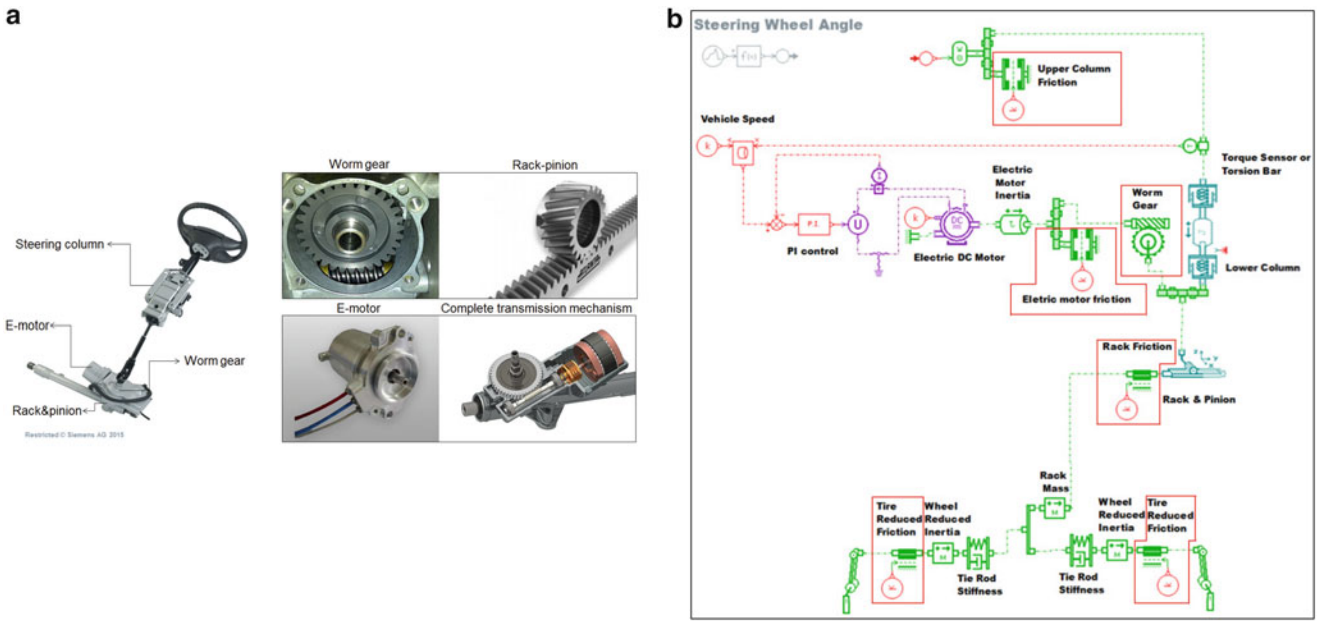

Fig. 10.4 (**a**) EPS components and (**b**) EPS model in LMS.Imagine AMESim

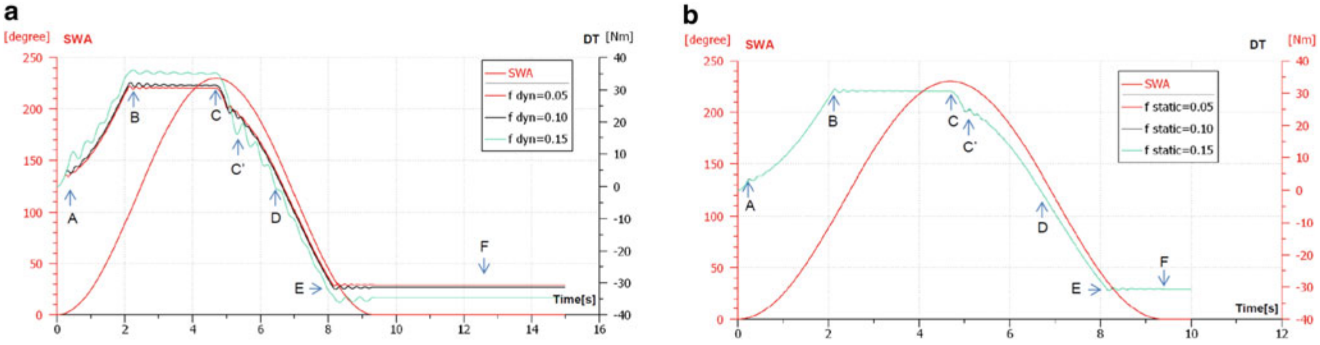

Fig. 10.5 Influence of the dynamic (**a**) and static (**b**) friction coefficient parameters of the worm gear

It is clear that the driver's torque is not sensitive to changes in the static friction in the worm gear and therefore should not be used later in the model identification process to define the static friction values for the worm gear. This simulation exercise suggests that another measurement have to be added to the system such that this model parameter can be later identified.

Following such a strategy multiple maneuvers can be tested to identify the most suitable ones to be carried out during the experiments and also components can be easily disconnected or added to reproduce different test configurations, e.g. electric motor connected but disabled, etc. This approach maximizes the output of relevant results from the test campaign and focus testing efforts to scenarios that will later facilitate and improve the matching between model and the physical system. This planning stage (pre-test) reduces experimental costs, accelerate testing time and maximize the quality of test output data.

10.4 Testing with Simulation: Model-Based High Fidelity Steering Wheel Force Feedback

A steering wheel force feedback system coupled to a real-time simulation is a key element in advanced Human-In-The-Loop driving simulators and Steer-by-Wire systems [23]. It provides accurate and realistic force feedback from the tires, the road and the vehicle to the driver. This is of particular interest for: (1) early evaluation of the steering feel during vehicle or

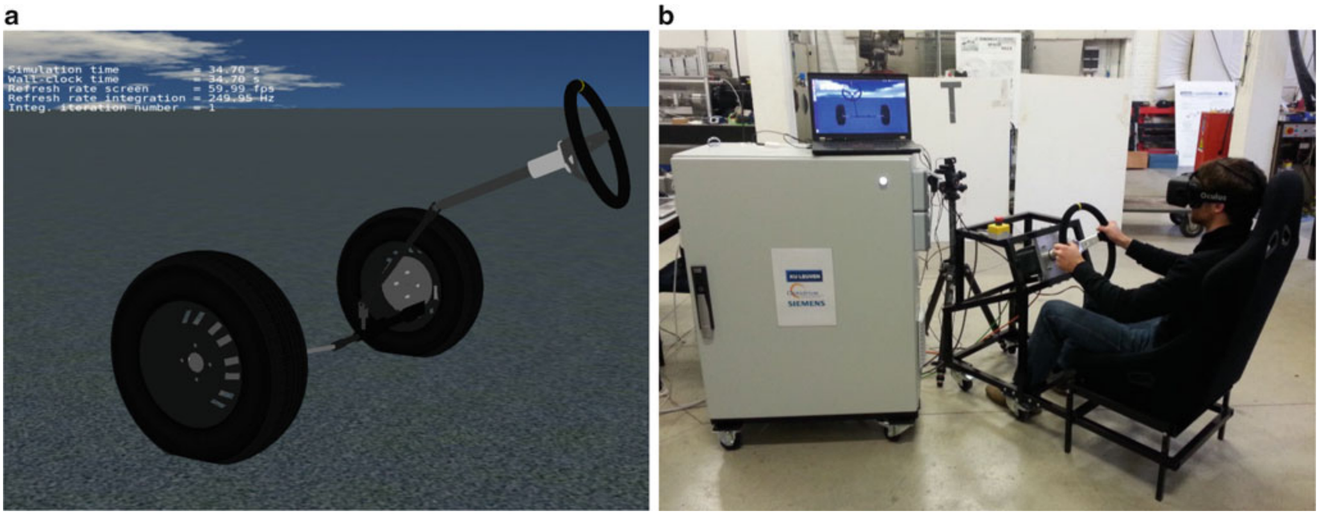

Fig. 10.6 (**a**) 3D steering mechanism. (**b**) Driving simulator

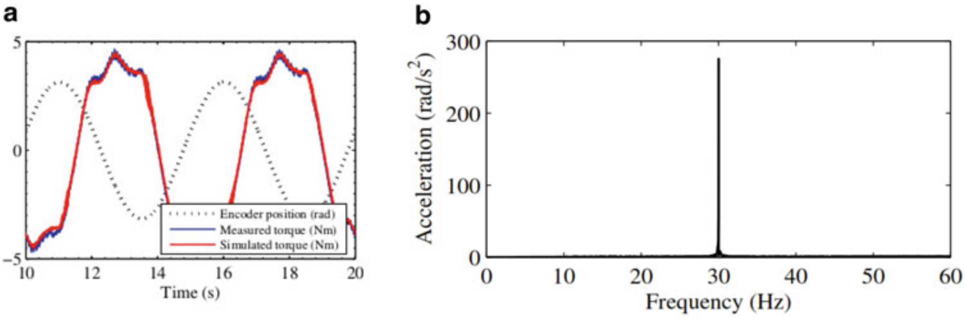

Fig. 10.7 (**a**) Comparison of simulated and measured steering wheel torque (**b**) measured frequency response function in the steering wheel

steering system design, (2) accurate steering feel for enhanced immersion in a driving simulator, (3) steering system ECU calibration for optimal performance, NVH characteristics, etc. The models of the steering system can be analytical as well as based on multibody models [23–25].

In practice, such a feedback system has to be carefully designed in order to guarantee accurate driver haptic feedback. For this, It is necessary to tightly couple the real-time simulation of the vehicle and/or the steering system to actuators and sensors. In [26], a driving simulator with steering wheel force feedback has been designed, built and validated (see Fig. 10.6a).

It consists of a steering wheel equipped with an AC permanent magnet synchronous direct-drive motor, its corresponding electric drive, a real-time control target, an Ethernet-based fieldbus connecting the target to the electric drive, a chassis, a seat and a virtual-reality headset (see Fig. 10.6b).

The feedback system has been designed and validated to faithfully reproduce steering torque inputs up to 30 Hz. Figure 10.7a shows an angle sine input given by a driving robot to the steering wheel, the steering wheel torque calculated by the simulation as well as its measured counterpart. The overlap of the simulated and measured torques demonstrates that the driver feedback is accurate and does not suffer any delays. Figure 10.7b shows the frequency measured at the steering wheel when applying, in simulation, a 30 Hz input torque to one of the tires. Again it demonstrates that the driver feedback is accurate up to 30 Hz.

10.5 Conclusions

In this paper, the underlying concepts of Model Based System Testing were presented. MBST represents the combination of test and simulation methodologies with the objective of obtaining more precise engineering models to be used in the design stage of such systems and frontloading test activities in the product development cycle. MBST extends modal testing and 3D simulation to multiphysical measurements and 1D simulations, be it for the improvement of simulation models ("Testing for Simulation"), to obtain more insight into test configurations ("Simulation for Testing") or to perform tests under realistic conditions in early stages of product design ("Testing with Simulation"). In order to better illustrate the MBST concept, an example from each of the three cases has been presented: simulation of switched reluctance motors for "Testing for Simulation", electric power steering for "Simulation for Testing" and model-based high fidelity steering wheel feedback for "Testing with Simulation".

References

1. Heylen, W., Lammens, S., Sas, P.: Modal Analysis Theory and Testing. Katholieke Universteit Leuven, Departement Werktuigkunde, Heverlee (2006)
2. Ewins, D.J.: Modal Testing: Theory and Practice. Wiley, New York (1995)
3. Manuel Mendes Maia, N., Martins Montalvão e Silva, J.: Theoretical and Experimental Modal Analysis. Research Studies Press, Taunton (1997)
4. Peeters, B., Van der Auweraer, H., Guillaume, P., Leuridan, J.: The polymax frequency-domain method: a new standard for modal parameter estimation? Shock Vib. **11**, 395–409 (2004)
5. Hermans, L., Van der Auweraer, H.: Modal testing and analysis of structures under operational conditions: industrial applications. Mech. Syst. Signal Process. **13**(2), 193–216 (1999)
6. Wyckaert, K., Van der Auweraer, H.: Operational analysis, transfer path analysis, modal analysis: tools to understand road noise problems in cars. Technical report, SAE Technical Paper (1995)
7. Allemang, R.J., Brown, D.L.: A correlation coefficient for modal vector analysis. In: Proceedings of the 1st International Modal Analysis Conference, vol. 1, pp. 110–116. SEM, Orlando (1982)
8. Mottershead, J.E., Friswell, M.I.: Model updating in structural dynamics: a survey. J. Sound Vib. **167**(2), 347–375 (1993)
9. Storck, H., Sumali, H., Pu, Y.: Experimental modal analysis of automotive exhaust structures. Technical report, SAE Technical Paper (2001)
10. Kehoe, M.W.: Aircraft ground vibration testing at NASA Ames-Dryden flight research facility. NASA Technical Memorandum 88272, National Aeronautics and Space Administration, Ames Research Center, Dryden Flight Research Facility, July 1987
11. Sampaio, R.P.C., Maia, N.M.M., Silva, J.M.M.: Damage detection using the frequency-response-function curvature method. J. Sound Vib. **226** (5), 1029–1042 (1999)
12. Manzato, S., White, J.R., LeBlanc, B., Peeters, B., Janssens, K.: Advanced identification techniques for operational wind turbine data. In: Topics in Modal Analysis, vol. 7, pp. 195–209. Springer, Heidelberg (2014)
13. Cai, W., Pillay, P., Tang, Z., Omekanda, A.M.: Low-vibration design of switched reluctance motors for automotive applications using modal analysis. IEEE Trans. Ind. Appl. **39**(4), 971–977. Monte, Carlo (2003)
14. Chauvicourt, F., Faria, C., Dziechciarz, A., Martis, C.: Influence of rotor geometry on NVH behavior of synchronous reluctance machine. In: Tenth International Conference on Ecological Vehicles and Renewable Energies (EVER), pp. 1–6. IEEE, Monte, Carlo (2015)
15. Burak Ozdoganlar, O., Hansche, B.D., Carne, T.G.: Experimental modal analysis for microelectromechanical systems. Exp. Mech. **45**(6), 498–506 (2005)
16. dos Santos, F.L.M., Anthonis, J., Naclerio, F., Gyselinck, J.J.C., Van der Auweraer, H., Goes, L.: Multiphysics NVH modeling: simulation of a switched reluctance motor for an electric vehicle. IEEE Trans. Ind. Electron. **61**(1), 469–476 (2014)
17. Samin, J.-C., Brüls, O., Collard, J.-F., Sass, L., Fisette, P.: Multiphysics modeling and optimization of mechatronic multibody systems. Multibody Syst. Dyn. **18**(3), 345–373 (2007)
18. Lourens, E., Reynders, E., De Roeck, G., Degrande, G., Lombaert, G.: An augmented Kalman filter for force identification in structural dynamics. Mech. Syst. Signal Process. **27**, 446–460 (2012)
19. Naets, F., Cuadrado, J., Desmet, W.: Stable force identification in structural dynamics using kalman filtering and dummy-measurements. Mech. Syst. Signal Process. **50**, 235–248 (2015)
20. Hwang, J.-S., Kareem, A., Kim, W.-J.: Estimation of modal loads using structural response. J. Sound Vib. **326**(3), 522–539 (2009)
21. Van der Auweraer, H., Anthonis, J., De Bruyne, S., Leuridan, J.: Virtual engineering at work: the challenges for designing mechatronic products. Eng. Comput. **29**(3), 389–408. Springer, London (2013)
22. dos Santos, F.L.M., Anthonis, J., Van der Auweraer, H.: Multiphysics thermal and NVH modeling: integrated simulation of a switched reluctance motor drivetrain for an electric vehicle. In: 2012 I.E. International Electric Vehicle Conference (IEVC), pp. 1–7. IEEE (2012)
23. Bajcinca, N., Cortesao, R., Hauschild, M., Bals, J., Hirzinger, G.: Haptic control for steer-by-wire systems. In: Proceedings of the IEEE/RSJ International Conference on Intelligent Robots and Systems (IROS 2003), October 2003
24. Hoskins, A.H., El-Gindy, M.: Technical report: literature survey on driving simulator validation studies. Int. J. Heavy Veh. Syst. **13**(3), 241–252 (2006)
25. Iyasere, E., Black, J., Kinstle, M., Post, B., Wagner, J., Dawson, D.: A real time re-configurable steering simulator for system design studies. In: Proceedings of the 2007 American Control Conference, vol. 113, New York, July 2007, pp. 3760–3766
26. Pastorino, R., Desloovere, M., Vanneste, F., Degezelle, P., Desmet, W.: Development, implementation and validation of a hard real-time multibody simulation for high-fidelity steering wheel force feedback. In: Proceedings of the ECCOMAS Thematic Conference on Multibody Dynamics, Barcelona, Spain (2015)

Chapter 11
Time-Varying System Identification Using a Hybrid Blind Source Separation Method

F. Musafere, A. Sadhu, and K. Liu

Abstract System identification and damage detection are one of the major building blocks of structural health monitoring for critical infrastructure. Using measured vibration response of structure, the unknown structural parameters can be extracted by any traditional system identification approach. However when there is a damage, these parameters vary with time which makes the signal nonstationary. In this paper, a simple yet effective method is proposed under the framework of blind source separation (BSS) method to identify the instant and severity of damage. Several time-frequency decompositions including Hilbert transform and time-varying auto-regressive modeling are explored to improve source separation capability of the BSS method.

Keywords Damage detection • SHM • SOBI • Auto-regressive time-series model • Hilbert transform

11.1 Introduction

Failures of large-scale infrastructure have significant societal and human consequence. Deteriorations of structures primarily occur due to varying environmental conditions, man-made excitations or natural hazards. Early detection of damage under operational or in-service condition is of paramount importance to avoid further risks in life safety and economic losses. Many researchers proposed sophisticated damage detection methods for structural health monitoring (SHM) applications [1–3]. In this paper blind source separation (BSS) [4, 5], a new and powerful signal processing method for modal identification, is explored as a possible candidate for robust damage detection algorithm.

Vibration-based damage detection algorithms are mainly divided into two types; parametric and non-parametric. The parametric damage detection methods estimate the system parameters of the structure using frequency response functions [6], the auto-regressive models [7–9], statistical information [10–12], and genetic algorithms [13]. Moreover, these parameters are then compared with those from the finite element (FE) model [11] in order to identify instant and severity of damage. Nevertheless, the drawbacks of parametric methods are the requirement of an accurate FE model and the related computational cost and modeling error limiting their applications towards damage detection algorithms.

On the other hand, non-parametric methods utilize advanced signal processing techniques over the vibration measurements in order to extract modal parameters such as natural frequency, mode shape, and damping ratio. This category of methods exploits classical time-frequency analysis including the wavelet transform [10, 14–16], Empirical mode decomposition (EMD) and Hilbert Huang transform [17–20], and synchro-squeezed transform [21]. These methods utilize the modal parameters to identify damage. Recently, a promising method called Blind Source Separation (BSS) has gained significant popularity in the field of ambient modal identification [4, 22–25]. In this work, BSS has been expanded further to develop a damage detection method.

In previous studies Independent Component Analysis (ICA), a variant of higher-order BSS, was employed towards structural damage detection [25, 26]. Principal component analysis (PCA) was further explored as a fault detection method with the aid of wavelet transform [15, 27]. Successively, using auto-correlation functions, second-order blind identification (SOBI) was undertaken to conduct damage detection [28, 29]. In [28], the SOBI method was implemented in multiple

F. Musafere (✉) • K. Liu
Department of Mechanical Engineering, Lakehead University, Thunder Bay, ON, Canada, P7B 5E1,

A. Sadhu
Department of Civil Engineering, Lakehead University, Thunder Bay, ON, Canada, P7B 5E1,
e-mail: asadhu@lakeheadu.ca

A. Wicks, C. Niezrecki (eds.), *Structural Health Monitoring, Damage Detection & Mechatronics, Volume 7*,
Conference Proceedings of the Society for Experimental Mechanics Series, DOI 10.1007/978-3-319-29956-3_11

windows of incoming vibration data to delineate the effect of damage. However such multiple windowing operations in the SOBI make it computationally expensive and insensitive to the lower level of damage. In this paper, Hilbert transform and time-varying autoregressive models are integrated with BSS to identify time-varying modal parameters of structures.

11.2 Hybrid BSS Method

Consider a linear, proportionally damped and lumped-parameter structural system with n_s degrees of freedom subjected to a broad-band random input force, $\mathbf{F}(t)$:

$$\mathbf{M}\ddot{x}(t) + \mathbf{C}\dot{x}(t) + \mathbf{K}x(t) = \mathbf{F}(t) \tag{11.1}$$

where, $\mathbf{x}(t)$ is a vector of displacement coordinates at the degrees of freedom. $\mathbf{M}$, $\mathbf{C}$, and $\mathbf{K}$ are the mass, damping and stiffness matrices of the system respectively. The solution to Eq. (11.1) can be written in terms of superposition of vibration modes with the following matrix form:

$$\mathbf{x}(n) = \mathbf{A}s(n) \tag{11.2}$$

where, $\mathbf{x} \in n_m \times N$ is the measurement matrix composed of the sampled components of $\mathbf{x}$ and $\mathbf{A}_{n_m \times n_s}$ is the mode shape matrix and N is the number of data points of the measurements. The SOBI algorithm is utilized in order to estimate $\mathbf{A}$ matrix that removes the spatial and temporal correlation between the modal responses (i.e., $\mathbf{s}$). The SOBI method formulates two covariance matrices $\mathbf{R}_x(0)$ and $\mathbf{R}_x(p)$ evaluated at the time lag zero and p from the observed measurements, then simultaneously diagonalize them in order to find the unknown mixing matrix, $\mathbf{A}$. In this way, the proposed damage detection method takes advantage of the SOBI method in separating the modal responses containing both damaged and undamaged states of the structure.

$$\begin{aligned} \mathbf{R}_x(0) &= \mathbb{E}[\mathbf{x}(n)\mathbf{x}^T(n)] = \mathbf{A}\mathbf{R}_s(0)\mathbf{A}^T \\ \mathbf{R}_x(p) &= \mathbb{E}[\mathbf{x}(n)\mathbf{x}^T(n-p)] = \mathbf{A}\mathbf{R}_s(p)\mathbf{A}^T \end{aligned} \tag{11.3}$$

There are three main steps of the SOBI algorithm: whitening, orthogonalization and unitary transformation [30]. In the whitening process, the covariance matrix $\mathbf{R}_x(0)$ is decomposed using the singular value decomposition method in order to obtain the whitened data $\overline{\mathbf{x}}$. The reason for whitening is to remove the correlation between the measured responses $\mathbf{x}$. Next, the whitened data is used to formulate whitened covariance matrices $\mathbf{R}_{\overline{x}}(p)$ with many lags. Then, the SOBI utilizes the joint approximate diagonalization (JAD) method to find an unitary matrix that diagonalizes these whitened covariance matrices. Using many time-delayed whitened covariance matrices, the SOBI is able to further reduce the presence of additive noise in the modal responses. Consequently, through unitary transformation the mixing matrix can be obtained. Then using the mixing matrix we can estimate the sources (i.e., modal responses) by the equation below.

$$\hat{\mathbf{s}}(n) = \mathbf{A}^{-1}\mathbf{x}(n) \tag{11.4}$$

In this study, the vibration data contains discrete damage event. Therefore, each modal response $\hat{\mathbf{s}}(n)$ obtained from the SOBI method contains both undamaged and damaged states. This phenomena is called as mixed modal response (MMR) in this paper. In order to separate them, the time-varying auto regressive (TVAR) models of modal responses are used:

$$y(n) = \sum_{k=1}^{p} a_k(n)y(n-k) + v(n) \tag{11.5}$$

where p represents the model order of the TVAR model. Once the TVAR modeling is performed over the modal responses, it reveals that the TVAR coefficients represent the discrete changes in system in a better way than the Hilbert transform method. In this study, the Kalman filter is adopted to estimate these TVAR coefficients.

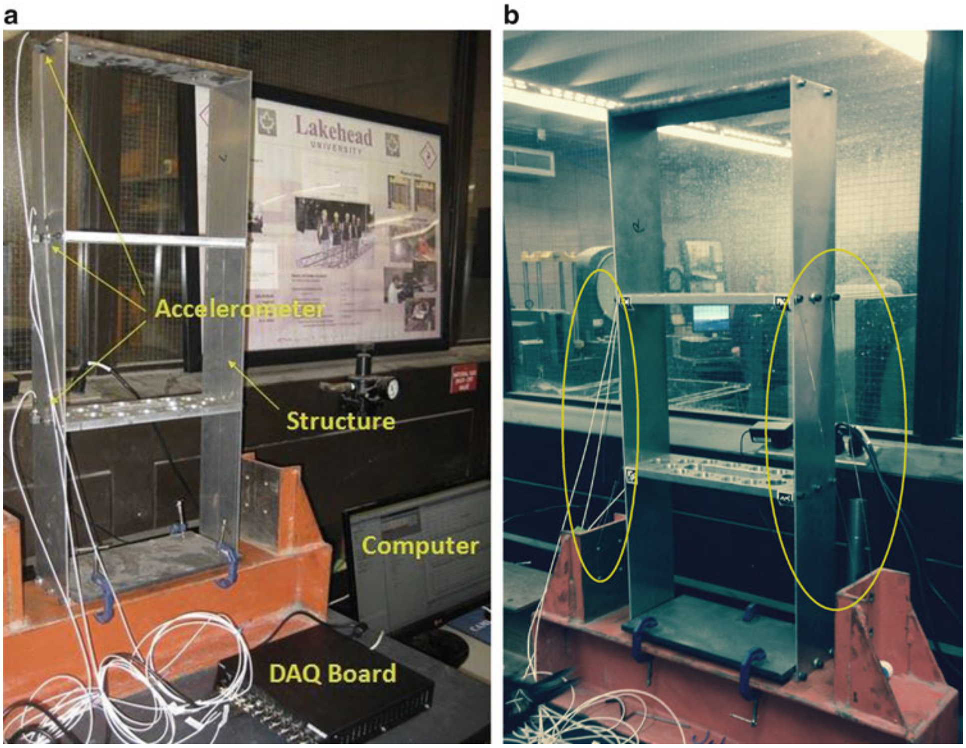

Fig. 11.1 (**a**) Experimental setup and (**b**) the initiation of damage by stiffening the model using steel wire (*circled*)

Fig. 11.2 Fourier spectra of (**a**) the observed signals (**b**) and the MMRs of the experimental model

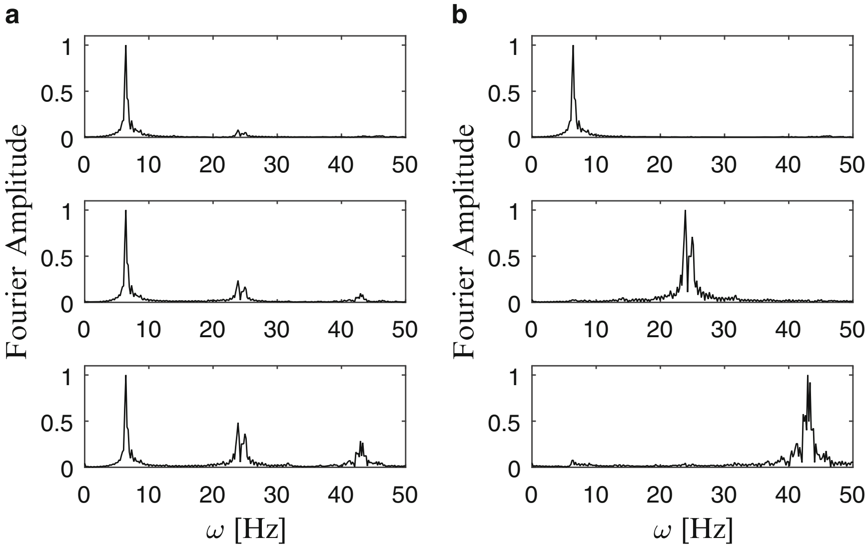

11.3 Experimental Study

An experimental model is constructed to validate the proposed damage detection method. Figure 11.3 shows a three-storey experimental building model used in this study. In Fig. 11.3 shows the 3-DOF structure model is stiffened by additional steel wire bracing connected to the second floor. During its vibration, these steel wires were cut suddenly and thereby, inducing damage into the structure. This case is similar to a practical situation where the columns of a civil engineering structure get damaged due to earthquake or blast event. Three accelerometers are used to measure the vibration at each floor level.

In Fig. 11.3 shows the FFT spectra of the measured signals which reveal that there are three pairs of frequencies corresponding to the individual modes of the undamaged and damaged states. First, the SOBI is employed to extract the

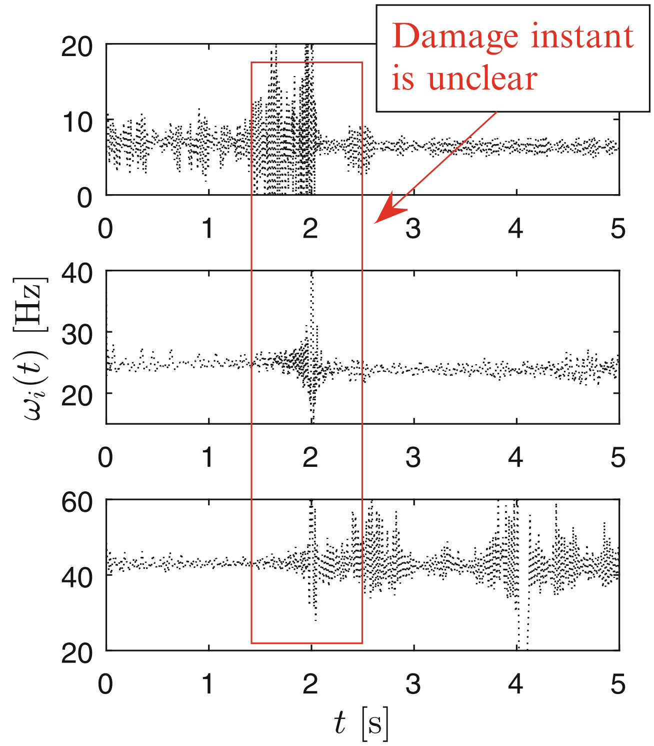

Fig. 11.3 Hilbert transform applied to all the MMRs of 3-DOF structure

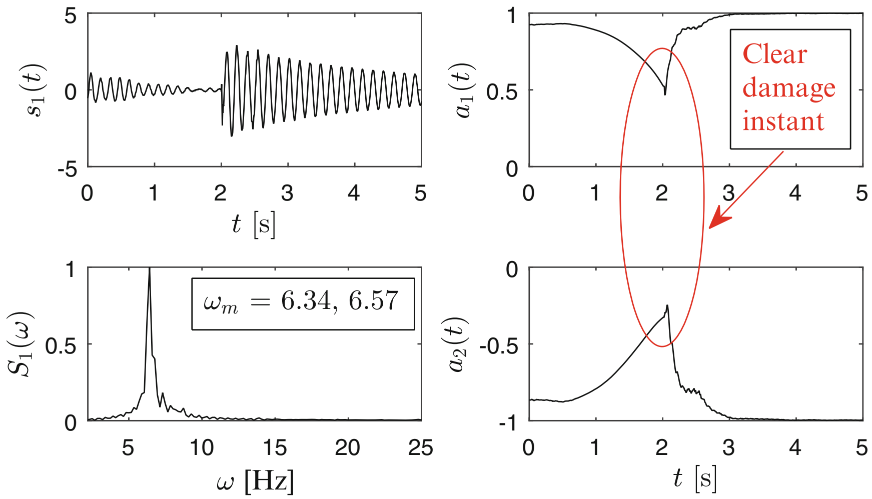

Fig. 11.4 TVAR modeling of the first MMR of the structure

modal responses of the structure. The FFT spectra of the resulting modal responses are shown in Fig. 11.3. It should be noted that the data contains a total of six modes, whereas only three measurements are used in the SOBI method resulting an *underdetermined modal identification* problem where the number of measurements is less than the number of target modes of interest. Therefore, it is expected that the SOBI method alone cannot separate individual undamaged and damaged frequencies (i.e. six frequencies).

The Hilbert transform is employed as an initial attempt to identify the damage instant due to its well-known time-frequency decomposition capability. The HT is applied to individual mixed modal responses. The results are shown in Fig. 11.3 which reveals that it is somewhat difficult to accurately identify the damage instant. Moreover, the end effects of the HT bring further difficulties to this problem [17, 18]. Now, the TVAR method is utilized to detect damage instant. Each MMR is estimated with a low model order p, considering the mono-component nature of MMRs. Figure 11.4 shows that by processing the 1^{st} MMR through the TVAR method; the time-dependent coefficients of the TVAR reveal an accurate damage instant at $t_d = 2$ seconds. Based on this observation, it can be conclusively reported that the combination of the

Table 11.1 Identified ω and ξ of $s_{ud}(t)$ and $s_d(t)$ of the 3-DOF experimental model

Mode #	ω_{ud} (Hz)	ξ_{ud} (%)	ω_d (Hz)	ξ_d (%)	Severity of damage (%)
1	6.57	4.46	6.34	3.67	19.83
2	24.94	1.28	23.87	1.13	4.48
3	43.08	0.79	42.62	0.49	0.59

SOBI and the TVAR method confirms the suitability of this method towards damage identification. In this way, the proposed method addresses the limitation of the SOBI method. It should also be noted that proper selection of model order for the TVAR modeling is a mathematically intensive exercise. However, by employing the SOBI method first for delineating the sources (i.e., MMRs), a low model order should be sufficient enough to properly estimate each MMR.

Using the information of damage instant, the MMRs are separated and the undamaged s_{ud} and damaged s_d modal responses are extracted to get the accurate natural frequencies, ω_{ud} and ω_d. The modal parameters for both the damaged and undamaged responses are tabulated in Table 11.1 along with the percentage difference in the frequencies which represents the severity of damage.

11.4 Conclusions

A novel damage detection method is developed for the SHM application. The proposed technique uses second-order BSS method integrated with the time-varying auto-regressive (i.e., TVAR) modeling to delineate the damaged state from the undamaged state. First, the SOBI method is utilized to obtain the mixed modal responses (i.e., MMR) of the structure. Then, the TVAR modeling is employed to approximate the MMR responses from which the time-varying coefficients are estimated and a more precise estimation of damage instant t_d can be obtained. Moreover, using t_d, the undamaged and damaged states of the structure can be separated out to get the modal frequencies ω_{ud} and ω_d. The purposed method is successfully validated using a 3-DOF lab-scale structure.

References

1. Doebling, S., Farrar, C., Prime, M., Shevitz, D.: Damage identification and health monitoring of structural and mechanical systems from changes in their vibration characteristics: a literature review. Technical Report LA-13070-MS, Los Alamos National Laboratory, Los Alamos, NM (1996)
2. Carden, E.P., Fanning, P.: Vibration based condition monitoring: a review. Struct. Health Monit. **3**(4), 355–377 (2004)
3. Chao, S., Loh, C., Tseng, M.: Structural damage assessment using output-only measurement: localization and quantification. J. Intell. Mater. Syst. Struct. **25**(7), 1097–1106 (2014)
4. Antoni, J.: Blind separation of vibration components: principles and demonstrations. Mech. Syst. Signal Process. **19**(6), 1166–1180 (2005)
5. Sadhu, A.: Decentralized ambient modal identification of structures, pp. 1–180. PhD thesis (2013)
6. Feng, L., Yi, X., Zhu, D., Xie, X., Wang, Y.: Damage detection of metro tunnel structure through transmissibility function and cross correlation analysis using local excitation and measurement. Mech. Syst. Signal Process. **60**, 59–74 (2015)
7. Bodeux, J.B., Golinval, J.C.: Application of ARMAV models to the identification and damage detection of mechanical and civil engineering structures. Smart Mater. Struct. **10**, 479–489 (2001)
8. Nair, K.K., Kiremidjian, A.S., Law, K.H.: Time series-based damage detection and localization algorithm with application to the ASCE benchmark structure. J. Sound Vib. **291**, 349–368 (2006)
9. Yao, R., Pakzad, S.N.: Autoregressive statistical pattern recognition algorithms for damage detection in civil structures. Mech. Syst. Signal Process. **31**, 355–368 (2012)
10. Kuwabara, M., Yoshitomi, S., Takewaki, I.: A new approach to system identification and damage detection of high-rise buildings. Struct. Control Health Monit. **20**(5), 703–727 (2013)
11. Bao, C., Hao, H., Li, Z.: Multi-stage identification scheme for detecting damage in structures under ambient excitations. Smart Mater. Struct. **22** (2013)
12. Garcia, D., Trendafilova, I.: A multivariate data analysis approach towards vibration analysis and vibration-based damage assessment: application for delamination detection in a composite beam. J. Sound Vib. **333**, 7036–7050 (2014)
13. Chen, B., Nagarajaiah, S.: Observer-based structural damage detection using genetic algorithm. Struct. Control Health Monit. **20**(4), 520–531 (2013)
14. Yun, G.J., Lee, S.-G., Carletta, J., Nagayama, T.: Decentralized damage identification using wavelet signal analysis embedded on wireless smart sensors. Eng. Struct. **33**(7), 2162 – 2172 (2011)

15. Kesavan, K.N., Kiremidjian, A.S.: A wavelet based damage diagnosis algorithm using principal component analysis. Struct. Control Health Monit. **19**(8), 672–685 (2012)
16. Dziedziech, K., Staszewski, W., Basu, B., Uhl, T.: Wavelet-based detection of abrupt changes in natural frequencies of time-variant systems (2015)
17. Xu, Y., Chen, J.: Structural damage detection using empirical mode decomposition: experimental investigation. J. Eng. Mech. **130**, 1279–1288 (2004)
18. Yang, J., Lei, Y., Wu, Z., Huang, N.: Hilbert-Huang based approach for structural damage detection. J. Eng. Mech. **130**(1), 85–95 (2004)
19. Lin, S., Yang, J., Zhou, L.: Damage identification of a benchmark building for structural health monitoring. Smart Mater. Struct. **14**, 162–169 (2005)
20. Kunwar, A., Jha, R., Whelan, M., Janoyan, K.: Damage detection in an experimental bridge model using Hilbert-Huang transform of transient vibrations. Struct. Control Health Monit. **20** (2013)
21. Amezquita-Sanchez, J., Adeli, H.: Synchrosqueezed wavelet transform-fractality model for locating, detecting, and quantifying damage in smart highrise building structures. Smart Mater. Struct. (2014)
22. Poncelet, F., Kerschen, G., Golinval, J.C., Verhelst, D.: Output-only modal analysis using blind source separation technique. Mech. Syst. Signal Process. **21**(6), 2335–2358 (2007)
23. Sadhu, A., Hazra, B., Narasimhan, S.: Decentralized modal identification of structures using parallel factor decomposition and sparse blind source separation. Mech. Syst. Signal Process. **41**(1–2), 396–419 (2013)
24. Sadhu, A., Narasimhan, S., Goldack, A.: Decentralized modal identification of a pony truss pedestrian bridge using wireless sensors. J. Bridge Eng. **19**(6), 04014013 (2014)
25. Yang, Y., Nagarajaiah, S.: Blind identification of damage in time-varying system using independent component analysis with wavelet transform. Mech. Syst. Signal Process. **47**(1–2), 3–20 (2014)
26. Zang, C., Friswell, M.I., Imregun, M.: Structural damage detection using independent component analysis. Struct. Health Monit. **3**(1), 69–83 (2004)
27. Tibaduiza, D.A., Mujica, L., Rodellar, J., Guemes, A.: Structural damage detection using principal component analysis and damage indices. J. Intell. Mater. Syst. Struct. 1–16 (2015)
28. Sadhu, A., Hazra, B.: A novel damage detection algorithm using time-series analysis-based blind source separation. Shock Vib. **20**(3), 423–438 (2013)
29. Spiridonakos, M., Yadav, N., Chatzi, E.: Identification and damage detection of a shear frame model based on a blind source separation method. In: 7th European Workshop on Structural Health Monitoring, pp. 2167–2174 (2014)
30. Belouchrani, A., Abed-Meraim, K., Cardoso, J., Moulines, E.: A blind source separation technique using second-order statistics. IEEE Trans. Signal Process. **45**(2), 434–444 (1997)

Chapter 12
An Energy Measure for Mode Localization

Michael I. Friswell, Arun Chandrashaker, and Sondipon Adhikari

Abstract The vibration characteristics of periodic structures are highly sensitive to its mass distribution, stiffness distribution and geometrical properties. Parametric uncertainties in structures that arise due to material defects, structural damage or variations in material properties can break the symmetry of periodic structures. This often leads to mode localization, where the deformation in a mode is concentrated in a small region of the structure. Localization can be directly detected by visually inspecting animated mode shapes given by finite element software. Although a visual approach is physically intuitive, for complex geometries the identification of mode localization can be subjective and may not be obvious. Hence this paper presents a reliable method to measure the degree of mode localization based on the distribution of energy within the modes of the finite element model. The properties of this measure are demonstrated by examples. Such a measure will be of great value in optimization studies where it can be included directly in objective functions or constraints.

Keywords Mode veering • Mistuning • Localization • Uncertainty • Periodic structure

12.1 Introduction

Turbine blades, ship hulls, aircraft fuselages and oil pipelines with periodic supports are examples of structures with uniform periodic spacing and repeated geometry. The vibration characteristics of these periodic structures are highly sensitive to its mass distribution, stiffness distribution and geometrical properties. Parametric uncertainties in structures which arise due to material defects, structural damage or variations in material properties can break the symmetry of periodic structures. This often leads to mode localization, where the deformation in a mode is concentrated in a small region of the structure [1, 2]. Severe mode localization can cause failure due to high cycle fatigue in periodic structures such as turbine blades. Localization can be directly detected by visually inspecting animated mode shapes or energy distributions given by finite element software. Although a visual approach is physically intuitive, in some cases (e.g. complex geometry) the identification of mode localization can be subjective and may not be obvious. Hence this paper presents a reliable method to measure the degree of mode localization based on the distribution of energy within the modes of the finite element model.

Numerous examples of linearly and rotationally periodic structures exist. Excitation of the localized vibration modes can lead to High Cycle Fatigue (HCF) which contributes to premature failure of the structure [3, 4]. HCF in turbine blades has been identified as the major cause of aircraft engine failures [4]. Perfect periodic structures are idealized cases; in reality most structures are only nearly periodic due to parametric uncertainties such as material imperfections or structural damage. As structures are never perfectly periodic, various authors have introduced intentional mistuning to reduce the effects of localization in turbine blades. Castanier and Pierre [3] discussed the importance of preventing HCF and summarized the design strategies used thus far to prevent extreme localization. Nikolic [4] gave further details about intentional mistuning and the reduction of the forced response of bladed disks. Slater and Blair [5] proposed disk modifications to find the configuration that would give the best mistuning pattern using the finite element method.

Energy measures based on the element kinetic and strain energy have been used for many years to visualize the spatial distribution of energy in modes [6–9]. Indeed the element energies are already calculated within many finite element codes such as NASTRAN, and some ranking of the energy densities obtained. This paper extends these approaches by proposing a numerical quantity to determine the localization of a given mode.

M.I. Friswell (✉) • A. Chandrashaker • S. Adhikari
College of Engineering, Swansea University, Bay Campus, Fabian Way, Crymlyn Burrows, Swansea SA1 8EN, UK
e-mail: m.i.friswell@swansea.ac.uk

A. Wicks, C. Niezrecki (eds.), *Structural Health Monitoring, Damage Detection & Mechatronics, Volume 7*,
Conference Proceedings of the Society for Experimental Mechanics Series, DOI 10.1007/978-3-319-29956-3_12

12.2 The Measure of Mode Localization

Mode localization occurs when the mode shape displacement is concentrated in a small region of the structure. Here we assume that the structure has been modeled with finite element analysis and the mode shapes are available at every degree of freedom. Defining a localization measure based on displacements directly is difficult because the generalized displacements can be translations or rotations, which have very different ranges. Also there is no obvious volume weighting measure to assign each displacement. Hence we will use the energy within each element to derive a measure of localization. Either the strain or kinetic energy may be used, which will give slightly different results.

Assume that a finite element model of the structure exists. The procedure is then as follows:

- Calculate the natural frequencies and mode shapes of the model.
- For each mode of interest calculate the strain energy or the kinetic energy of every element for each mode.
- Calculate a volume (or mass) measure for each element. For 3D brick elements this is the actual volume. For plate and shell elements this is the product of the area and thickness. For beam elements this is the product of length and cross sectional area. For discrete mass and spring elements the volume assignment is more difficult and has to be based on engineering judgment. Note that only a relative volume measure is required.
- Normalize the energy measure for each mode and the volume measure by the total energy and total volume respectively so that both are in the range [0, 1].
- Sort the elements by energy density (element energy / element volume), with the highest density first.
- Based on the elements sorted by energy density, find the cumulative energy function and the cumulative volume function.
- Calculate a suitable localization measure. For example this might be the percentage volume which accounts for 90 % of the energy of the mode, denoted by V_{90}. It is an open question whether capturing 90 % of the energy is a good measure and other percentages could be tried. Indeed the optimum percentage is likely to depend on the application.

The element strain energy, U_e, is easily obtained from the element stiffness matrix, $\mathbf{K}_e$, and the i th mode shape vector, $\boldsymbol{\phi}_i$, as

$$U_e = \frac{1}{2}\boldsymbol{\phi}_i^T \mathbf{H}_e^T \mathbf{K}_e \mathbf{H}_e \boldsymbol{\phi}_i \tag{12.1}$$

where $\mathbf{H}_e$ is a matrix that picks out the element degrees of freedom (in the right order for the element definition) from the global set of degrees of freedom. The normalization of the mode shapes is not important as the spatial energy distribution for the mode is required.

Similarly the element kinetic energy, T_e, is based on the element mass matrix, $\mathbf{M}_e$, and is given by

$$T_e = \frac{1}{2}\omega_i^2 \boldsymbol{\phi}_i^T \mathbf{H}_e^T \mathbf{M}_e \mathbf{H}_e \boldsymbol{\phi}_i \tag{12.2}$$

where ω_i is the i th natural frequency. Since the energy distribution of each mode is considered in turn, the factor of ω_i^2 in Eq. (12.2) makes no difference to the normalized energy values.

This procedure is best illustrated by a simple example.

12.3 A Simple Mass-Spring Example

Consider the discrete mass-spring chain example shown in Fig. 12.1. Coupling springs are placed between each adjacent mass, and also between the end masses and ground. Each mass also has grounded spring between the mass and ground. In the baseline system each mass is 1 kg, each grounded spring is 1 N/m, and each coupling spring is 0.01 N/m.

As an example a 30 degrees of freedom system is modeled, and Fig. 12.2 shows the first four modes. Other modes could be investigated but these modes are sufficient to illustrate the localization measure. Figure 12.3 shows the cumulative kinetic energy, where the dotted horizontal line denotes the 90 % energy level, which is used as an example here. None of the modes are localized; indeed for all modes, the kinetic energy of 19 masses (63 %) are required to capture 90 % of the energy.

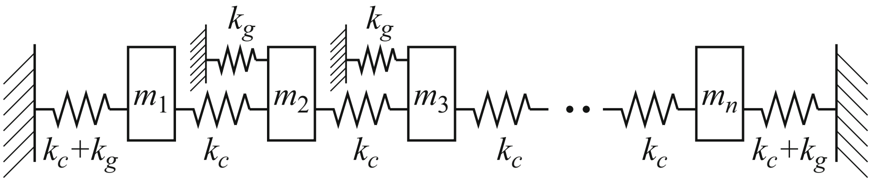

Fig. 12.1 The *n* degree of freedom discrete mass-spring example

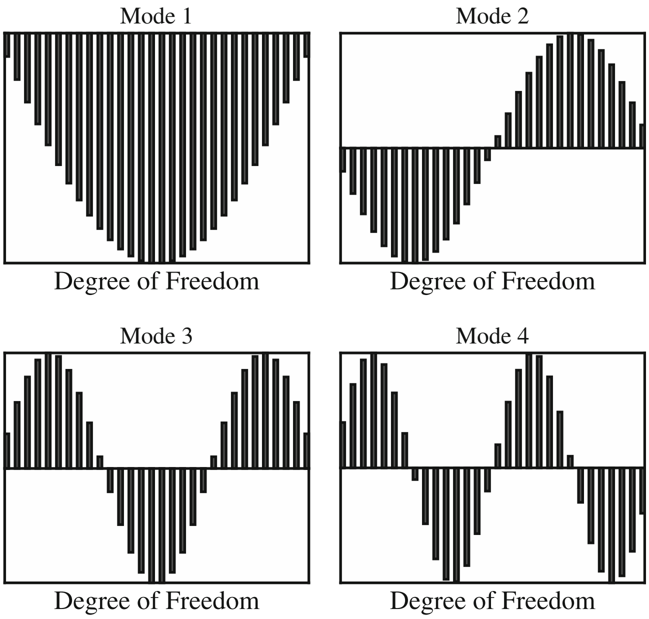

Fig. 12.2 Modes of the baseline discrete mass-spring example

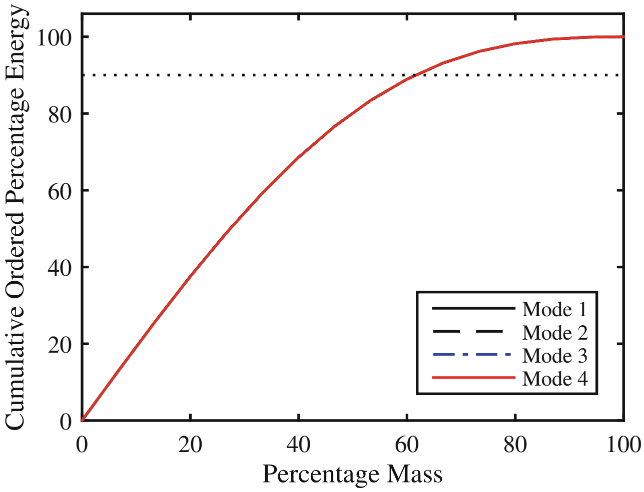

Fig. 12.3 The energy localization for the baseline discrete mass-spring example

Now assume that mass 9 is increased to 1.2 kg. Figure 12.4 shows the corresponding modes and highlights that localization occurs, particularly for mode 1. The cumulative kinetic energy is shown in Fig. 12.5, as a function of the cumulative mass, where the dotted horizontal line denotes the 90 % energy level, which is used as an example here. Thus only one mass (mass 9), i.e. 3.3 % of the total mass, is required to capture 90 % of the kinetic energy in mode 1. For mode 4 only 6 masses (i.e. 20 % of the total mass) are required to capture 90 % of the energy, and for modes 2 and 3 14 masses (47 %) are required. From a visual inspection of the modes, the percentage of mass required to capture 90 % of the kinetic energy is a good measure of the localization of the modes.

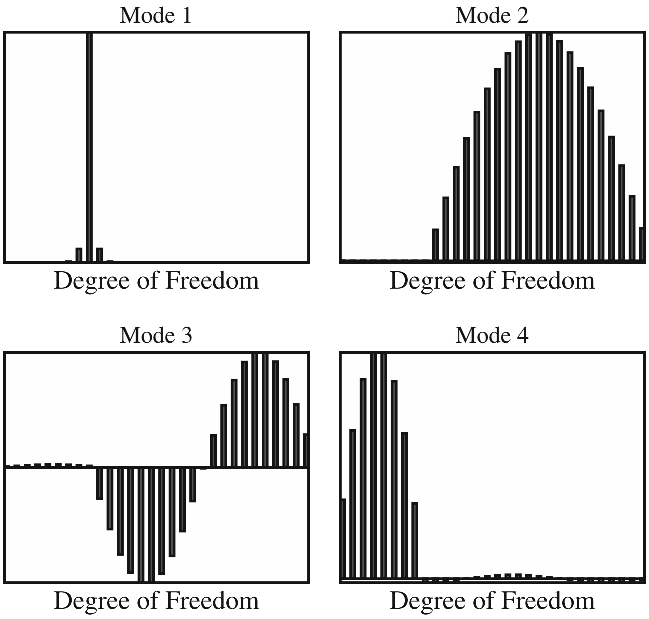

Fig. 12.4 Modes of the perturbed discrete mass-spring example

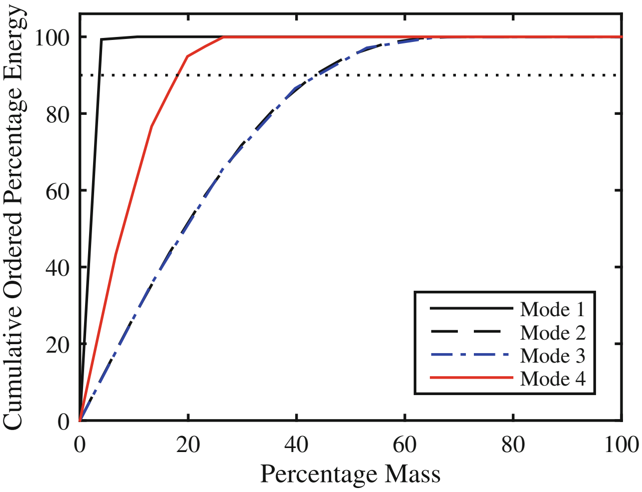

Fig. 12.5 The energy localization for the perturbed discrete mass-spring example

12.4 An Idealized Bladed Disk Example

To demonstrate the localization measure on a more complex and practical example, a finite element model of an idealized bladed disk was developed. The bladed disk has 12 sectors with 12 blades, and is constructed from a constant thickness plate. The model was build in ANSYS and uses 1296 8-noded solid brick elements, shown in Fig. 12.6, which gives a model size of 1836 degrees of freedom. The bladed disk was modeled free-free and the first 20 modes were calculated.

The modes were calculated for perfectly uniform material properties and also when the mass density of one blade is increased by 10, 20 and 30 %. The strain energy in every element for every mode was calculated for the baseline model, and the models with the perturbed mass. The volume of every element was also extracted from ANSYS. Only the results for the 10 % mass perturbation are shown as the results for the 20 and 30 % are very similar.

Figure 12.7 shows the V_{90} localization measure, i.e. the percentage volume that captures 90 % of the strain energy for each mode. Modes 1–3 are shown separately because the volumes required are very high, indicating that these modes are global. Mode 11 with the 10 % mass perturbation is the most localized, where only 2.3 % of the bladed disk volume is required to capture 90 % of the strain energy. This mode also shows the most localization due to the mass perturbation. Figure 12.8 shows a selection of these modes to demonstrate that the localization measure results correspond to the

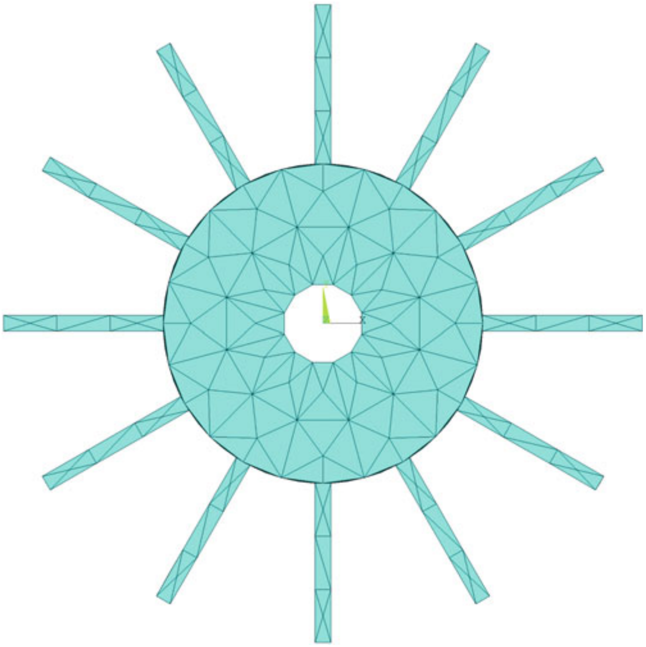

Fig. 12.6 The finite element mesh for the idealized bladed disk

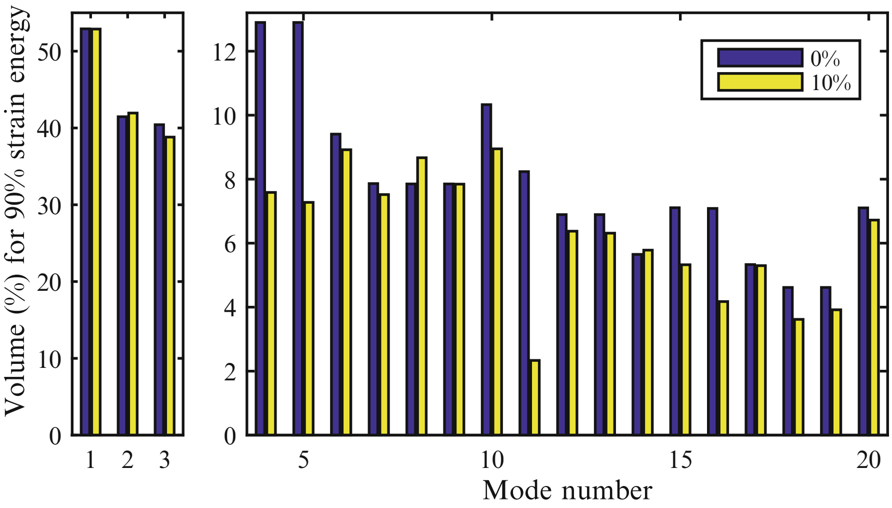

Fig. 12.7 The percentage volume that captures 90 % of the strain energy in the first 20 modes of the bladed disk

conclusions from a visual inspection of the modes. Mode 1 is a global mode that is insensitive to the mass perturbation. Mode 4 is moderately localized by the perturbation, in that the response is localized to alternate blades. Mode 11 is severely localized, with the significant response mainly limited to a single blade in the perturbed case.

12.5 Conclusions

This paper has presented a measure of mode shape localization based on the predicted strain or kinetic energy within a structure. A visual inspection of the modes of example systems and structures shows that the measure does reliably predict localization. Such a measure will be of great value in optimization studies where it can be included directly in objective functions or constraints, possibly to reduce susceptibility to high cycle fatigue during the design process.

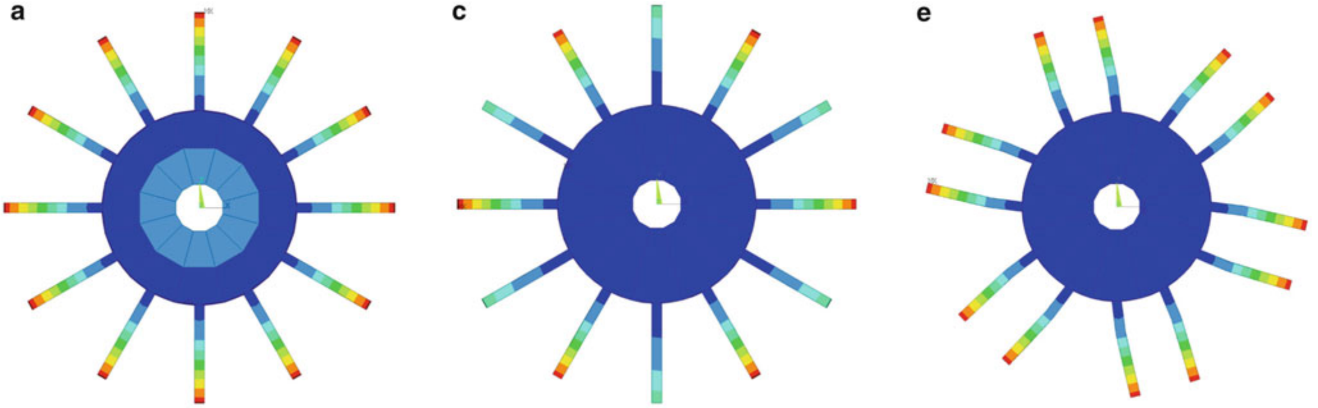

Mode 1, 0%   Mode 4, 0%   Mode 11, 0%

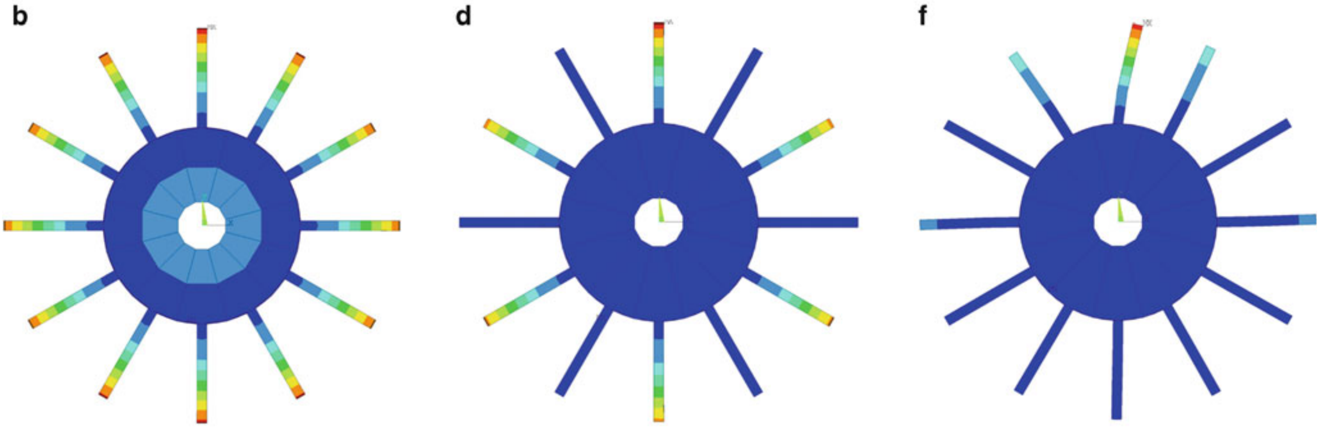

Mode 1, 10%   Mode 4, 10%   Mode 11, 10%

Fig. 12.8 Typical modes of the bladed disk for the uniform mass density (0 %) or with a 10 % mass perturbation to one blade. *Red* is large displacement and blue is small displacement. (**a**) Mode 1, 0 %, (**b**) Mode 1, 10 %, (**c**) Mode 4, 0 %, (**d**) Mode 4, 10 %, (**e**) Mode 11, 0 %, (**f**) Mode 11, 10 %

References

1. Ewins, D.J.: Vibration characteristics of bladed disc assemblies. J. Mech. Eng. Sci. **15**(3), 165–186 (1973)
2. Pierre, C., Murthy, D.V.: Aeroelastic modal characteristics of mistuned blade assemblies - mode localization and loss of eigenstructure. AIAA J. **30**(10), 2483–2496 (1992)
3. Castanier, M.P., Pierre, C.: Modeling and analysis of mistuned bladed disk vibration: status and emerging directions. J. Propul. Power **22**(2), 384–396 (2006)
4. Nikolic, M.: New insights into the blade mistuning problem. Ph.D. thesis, Imperial College (2006)
5. Slater, J.C., Blair, A.J.: Minimizing sensitivity of bladed disks to mistuning. In: Proceedings 16th IMAC Conference, Society of Experimental Mechanics, Santa Barbara, pp. 284–290 (1998)
6. Parker, G.R., Brown, J.J.: Kinetic energy DMAP for mode identification. In: Proceedings of the MSC/NASTRAN Users Conference, Pasadena (1982)
7. Parker, G.R., Rose, T.L., Brown, J.J.: Kinetic energy calculation as an aid to instrumentation location in modal testing. In: Proceedings of the MSC World Users Conference, Los Angeles (1990)
8. Chung, Y.T., Kahre, L.L.: A general procedure for finite element model check and model identification. In: Proceedings of the MSC World Users Conference, Universal City, California (1995)
9. Nehad, B.I., Fiorelli, K.J., Le, A.D., Leuer, J.P., Wright, D.R.: A quantitative approach to target mode selection for component-level modal survey. In: Proceedings of IMAC XVI, Santa Barbara, pp. 1401–1408 (1998)

Chapter 13
Vibration Control on a Space Flexible Structure with a PZT Stack Actuator Using Strain and MPPF Control

Oscar Alejandro Garcia-Perez, Gerardo Silva-Navarro, and Juan Fernando Peza-Solis

Abstract This works deals with the vibration control problem on a space frame flexible structure mounted on a rigid revolute servomechanism, which is actuated and controlled with a dc motor as a flexible-like robotic system. For active vibration control is synthesized a combined control scheme, by using a PD with direct strain feedback control for regulation and trajectory tracking tasks, via the rigid joint, and a Multiple Positive Position Feedback (MPPF) control by means of a PZT stack actuator mounted into the structure. Therefore, the endogenous and exogenous vibrations on the overall structure are simultaneously attenuated by the combined controller. The MPPF controller is computed to attenuate the two first dominant (bending) modes, using information obtained from strain gages, to improve the regulation and trajectory tracking of the tip position of the overall structure. The modal parameters of the structure are estimated using experimental modal analysis techniques. Finally, the overall dynamic performance is evaluated and validated by numerical and experimental results.

Keywords Active vibration control • Direct strain feedback • Flexible frame structure • Modal parameters • Positive position feedback

13.1 Introduction

Cranes and robotic manipulators are widely used on industrial applications. Most of these systems are designed and built in such a way, as to maximize stiffness in an attempt to minimize the vibration in order to achieve a good end-effector position accuracy. Thus, in order to improve the industrial productivity of light-weight structures, higher operational speeds and larger work volume have been a desirable objective to accomplish. Because of this, space-frame mechanical structures cannot be treated under the rigid body assumption. Hence, it is necessary to address them from a flexible structure point of view. Since the greatest disadvantage of these manipulators is the residual vibration problem due to low stiffness as the result of their low weight and large spans.

In the last few decades, many researchers have focused their work on dynamics and control of flexible manipulators in order to minimize the vibration problem in flexible robot arms and flexible structures. Most of these researches have mainly modeled and controlled single flexible robot arms, using the well-known Euler-Bernoulli beam, but most of the industrial robots and cranes have more complicated and sophisticated structures.

Many researches have focused their works on modeling and controlling of flexible structures, trying to improve their dynamical performance using the latest technological available solutions. In this regard, the new developments in materials, known as smart materials, have allowed both, sensors and actuators, to change some of their physical characteristics (e.g., stiffness, damping) in order to enhance their dynamical response in presence of a wide variety of disturbances. Piezoelectric materials, electrostrictive materials, magneto -or electrorheological fluids and shape memory alloys, just to mention a few, can be used to design smart structures which require to apply control forces to compensate inherent disturbances into the system motions and thus, minimize the resulting vibrations on the structure [1, 2]. Some researchers have also used piezoelectric materials to change, either damping, or stiffness in the structure. Most of these works have been applied on civil structures, like building frames, spatial structures and bridges. Vibration control of a scaled space truss tower controlled by two PZT struts, applying an integral force feedback controller has been reported in [3]. By using PZT actuators it is

---

O.A. Garcia-Perez (✉) • G. Silva-Navarro • J.F. Peza-Solis
Centro de Investigación y de Estudios Avanzados del I.P.N., Departamento de Ingeniería Eléctrica, Sección de Mecatrónica,
Av. Instituto Politécnico Nacional No. 2508, San Pedro Zacatenco, 07360 México Distrito Federal, México
e-mail: ogarciap@cinvestav.mx; gsilva@cinvestav.mx; jpeza@cinvestav.mx

A. Wicks, C. Niezrecki (eds.), *Structural Health Monitoring, Damage Detection & Mechatronics, Volume 7*,
Conference Proceedings of the Society for Experimental Mechanics Series, DOI 10.1007/978-3-319-29956-3_13

possible to add damping to the system and minimize its vibration amplitudes. Hence, lowering the settling time of the frame structure and, thus, contributing to the enhancement of quality and productivity.

A challenging problem on the control of flexible manipulators is the one concerning the regulation and trajectory tracking of the end effector position, mainly because most of conventional controllers tend to excite the vibration modes, which are due to the flexible nature of these mechanical systems and do very little, or no action at all, to suppress such vibrations. Direct Strain Feedback (DSF) has been used to control vibration of flexible arms, this control allows the adding of a damping term into the equation governing the dynamics of flexible arms.

In this work, a rotatory arm crane-like space flexible structure is analyzed with the final goal to minimize the overall undesired vibrations by using a PZT stack actuator. This work is organized as follows: In the second section a mathematical model is derived for the flexible structure using Finite Element Methods (FEM). The modal parameter identification of the structure for finite element model validation is performed using Experimental Modal Analysis (EMA) techniques. On the third section the vibration absorption scheme and the trajectory tracking problem is formulated. Finally, some simulations and experimental results are reported to validate the dynamic performance and robustness of the proposed scheme.

13.2 Modeling of Flexible Frame Structure with a PZT Stack Actuator

In this section, a mathematical model of a flexible frame structure is presented, where one end of flexible structure is attached to a rigid revolute servomechanism, actuated and controlled by a dc motor, which delivers a torque $\tau(t)$ and the other end is free as shown in Fig. 13.1. The flexible structure moves around the motor shaft in the horizontal plane, where the angular displacement is denoted by $\theta(t)$. The flexible structure is made of aluminum bars alloy type 6061-T5, in which one of them has been replaced by a mechanical arrangement including a PZT stack actuator. The PZT stack actuator can be used for vibration control or some other purposes as well. The PZT stack actuator position is selected by using an approach given in [5], which consist in evaluating the norm H_2 or H_∞, whilst each one of the elements of structure is replaced by a PZT stack actuator (see [4]).

The mathematical model for a passive flexible structure is obtained by using the Finite Element Method (FEM). This flexible structure is discretized in 190 frame elements and 67 nodes, where each node has 6 DOF, being three of them of the translational kind and the other three of the rotational kind. The overall flexible structure motion is given by

$$M\ddot{q} + D\dot{q} + Kq = Bu_{PZT}(t) + B_a\ddot{\theta}(t), \qquad q,\ B,\ B_a \in R^{396};\ \ u_{PZT}, \ddot{\theta} \in R \tag{13.1}$$

where q, B_{PZT} and B_a are the displacement vector, influence vector of PZT stack actuator and the influence vector of the acceleration on the flexible structure, respectively. Moreover, M, D, K are the global mass, global damping and global stiffness matrices, addressed in the order they appear. For modeling purposes is considered proportional (Rayleigh) damping as follows

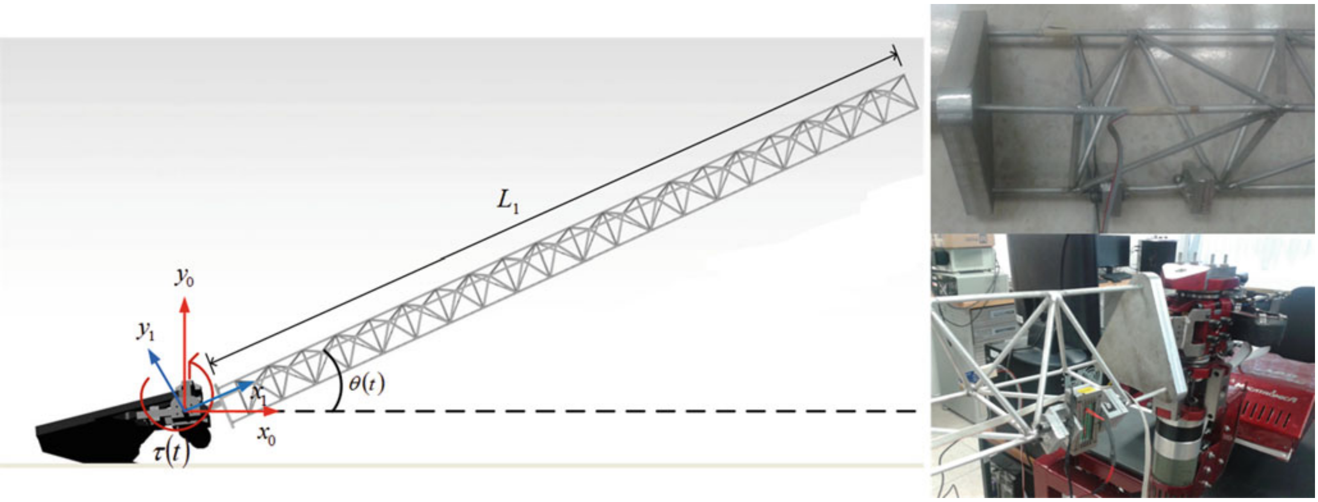

Fig. 13.1 Schematic of the flexible space frame structure

$$D = \alpha_1 K + \alpha_2 M, \qquad \alpha_1, \alpha_2 \in R \tag{13.2}$$

The influence vector B is considered to be $B^T = [\cdots, \quad 1, \quad 0, \quad \cdots, \quad 1, \quad 0, \quad \cdots]$, where the non-zeros components represent the degrees of freedom of nodes where the ends of the PZTs are attached into the flexible structure. Hence, the dynamics of the flexible structure is modified by the influence of PZT stack actuator whose extensions or contractions are represented by δ, which is proportional to the applied voltage in amount and sign, as shown in the next expression

$$\delta(t) = d_{33} n V(t) = g_a V(t) \tag{13.3}$$

Here, g_a is the gain of the actuator. When the PZT stack actuator is placed on a space frame structure, its effect on the structure can be represented by corresponding equivalent piezoelectric loads actuating on the passive structure [6]. Piezoelectric loads applied axially to both ends of the element of the structure have magnitudes equal to the product of the stiffness of the PZT stack and piezoelectric displacement δ as follows

$$u_{PZT}(t) = K_a \delta(t) \tag{13.4}$$

Using the following linear transformation

$$q = \Phi q_m \tag{13.5}$$

Thus, assuming modal damping, Eq. (13.1) can be transformed into a set of differential equations

$$\begin{gathered} \ddot{q}_m + 2Z\Omega\dot{q}_m + \Omega^2 q_m = B_m u_{\ddot{\theta}}(t) + B_{mc} u_{PZT}(t), \quad y = C_m q_m, \\ B_m = {M_m}^{-1}\Phi^T B_a, \quad B_{mc} = {M_m}^{-1}\Phi^T B, \quad M_m = \Phi^T M \Phi, \quad C_m = C_{oq}\Phi \end{gathered} \tag{13.6}$$

where $\Phi = [\phi_1 \quad \phi_2 \quad \ldots \quad \phi_n]$ is the modal matrix obtained from the solution of an undamped eigenvalue problem

$$K\phi_i = {\omega_i}^2 M\phi_i, \qquad i = 1, \ldots, n \tag{13.7}$$

The frequency ω_i is called the i-th natural frequency and, therefore, the n natural frequencies are in the vector

$$\Omega = diag[\omega_1 \quad \omega_2 \quad \ldots \quad \omega_n] \tag{13.8}$$

Using the mechanical parameters of the flexible structure given in Table 13.1, the modal shapes and natural frequencies are numerically computed. These results are shown in Fig. 13.2 and Table 13.2, respectively.

In order to validate the theoretical results obtained by using FEM and, with the goal to find the natural frequencies and damping ratios of the overall structure, an Impact Hammer Test (IHT) and Peak Picking (PP) techniques are used. The signals are obtained from accelerometers installed on the flexible structure. In Fig. 13.3 the free decaying in time and the resulting Frequency Response Function (FRF) of the structure are shown, taking into account that the structure was hit on

Table 13.1 System parameters of the flexible structure

Systems parameters	Nomenclature	Magnitude	Unit
Equivalent joint shaft inertia	I_{eq}	1.701	$Kg \cdot m^2$
Structure length	L_1	2.05	m
Density	ρ	2710	Kg/m^3
Elasticity modulus	E	6.89×10^{10}	Pa
Shear modulus	G	2.6×10^{10}	Pa
Diameter	D	4.7625×10^{-3}	m
Cross sectional area	A	1.78×10^{-5}	m^2
Moment of inertia	I_{yy}	2.53×10^{-11}	m^4
Moment of inertia	I_{zz}	2.53×10^{-11}	m^4
Polar moment of inertia	J	5.05×10^{-11}	m^4

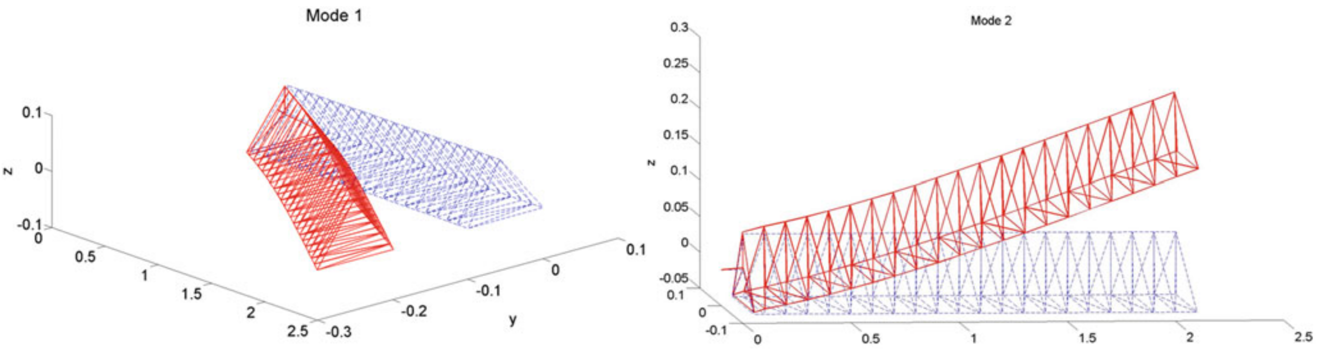

Fig. 13.2 Two first modal shapes of the flexible frame structure

Table 13.2 First four numerical natural frequencies

Mode	Frequency ω_i [Hz] (FEM)
1	6.3383
2	10.7098
3	58.5109
4	70.0353

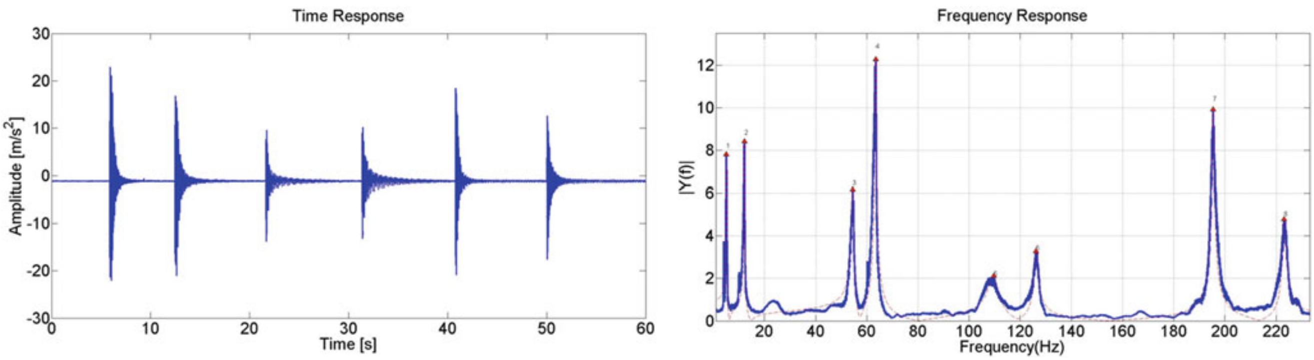

Fig. 13.3 Time domain and FRF of the structure

Table 13.3 Natural frequencies and modal damping of the first four modes of the flexible structure

Mode	Frequency ω_i [Hz] (peak picking)	Modal dampingζ_i (peak picking)
1	6.0121	0.0114
2	9.7964	0.0095
3	54.49	0.0081
4	63.47	0.0055

different nodes. The natural frequencies ω_i and damping ratios ζ_i are identified by using Peak Picking techniques. These modal parameters identification process is summarized in Table 13.3.

With the aim to obtain a signal for applying active vibration controls, two strain gauges were mounted on the elements where bending stresses are higher for the first two vibration modes. But, it is necessary to verify that strain gauges are able to measure these two modes. Figure 13.4 describes the signal on time domain and FRF of the flexible structure, obtained using a strain gauge, when the structure is hit.

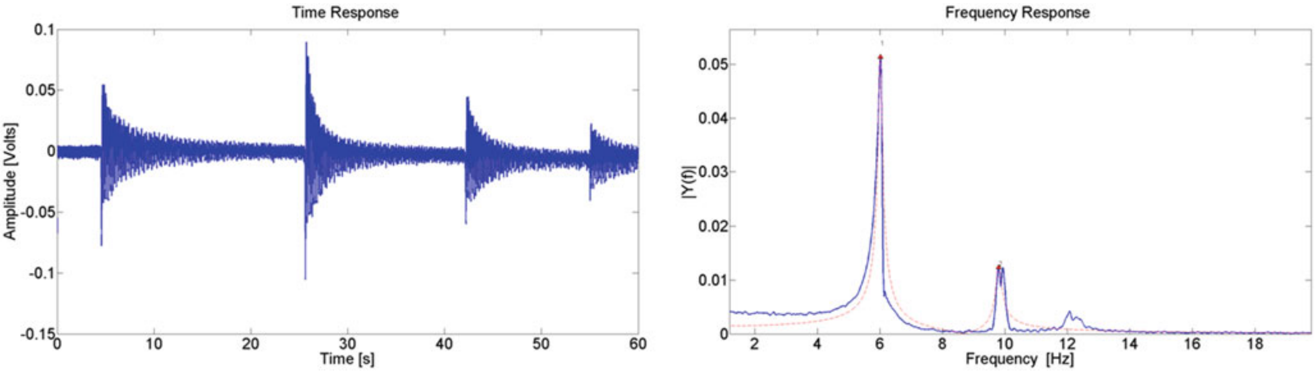

Fig. 13.4 Time domain and FRF of the structure using a strain gauge

13.3 Vibration Control Using MPPF and Direct Strain Feedback

Direct Strain Feedback (DSF) was proposed for stabilization and regulation tasks on flexible-link robot arms [7, 8]. This strategy injects damping to the governing equation of flexible arms. DSF controller is also used to improve the dynamic performance of a simple PD controller. The controller is given by

$$\tau = -k_p[\theta(t) - \theta_d] - k_v\dot{\theta}(t) - k_f\omega''(x_s, t)\int_0^t \dot{\theta}(s)\omega''(x_s, t)ds \tag{13.9}$$

where k_p, k_v are positive constants and $k_f \geq 0$, and ω'' (x_s, t) is the strain gauge signal that is attached on one element of the flexible structure close to the clamped end of the flexible structure.

Using DSF and PD control schemes, numerical simulations are made in order to know how the system dynamics is improved. The results are described in Fig. 13.5.

13.3.1 Application of Multiple Positive Position Feedback (MPPF)

The Positive Position Feedback is a second order filter, which is forced positively by position measurements on the flexible structure [9]. Because the flexible structure is submitted to angular motion, several of its vibration modes can be excited. In order to simultaneously attenuate the first two dominant vibration modes, a MPPF control scheme is applied as follows

$$\begin{aligned}
&\ddot{\eta}_1 + 2\zeta_1\omega_{f_1}\dot{\eta}_1 + {\omega_f}^2 = g_1{\omega_{f_1}}^2 y\\
&\ddot{\eta}_2 + 2\zeta_2\omega_{f_2}\dot{\eta}_2 + {\omega_f}^2 = g_2{\omega_{f_2}}^2 y\\
&u_{PZT} = \sum_{i=1}^{2} g_i{\omega_{f_i}}^2\eta_i, \qquad y = C_{mg}q_m
\end{aligned} \tag{13.10}$$

where $\omega_{f_i}, \zeta_{f_i}$ and g_i are design parameters denoting natural frequency, damping ratio and gain of the filter, respectively. Typically, the frequency ω_{f_i} is selected equal or close to the resonance frequency (mode) to be compensated.

Considering the system dynamics given in Eq. (13.6) and assuming only the first three vibration modes, a reduced order model can be obtained:

$$\begin{aligned}
&M_r\ddot{q}_m + D_r\dot{q}_m + K_r q_m = B_{m_r}u_{\ddot{\theta}}(t) + B_{mc_r}u_{PZT}(t)\\
&D_r = diag[2\zeta_1\omega_1, 2\zeta_2\omega_2], \quad K_r = diag[{\omega_1}^2, {\omega_2}^2]
\end{aligned} \tag{13.11}$$

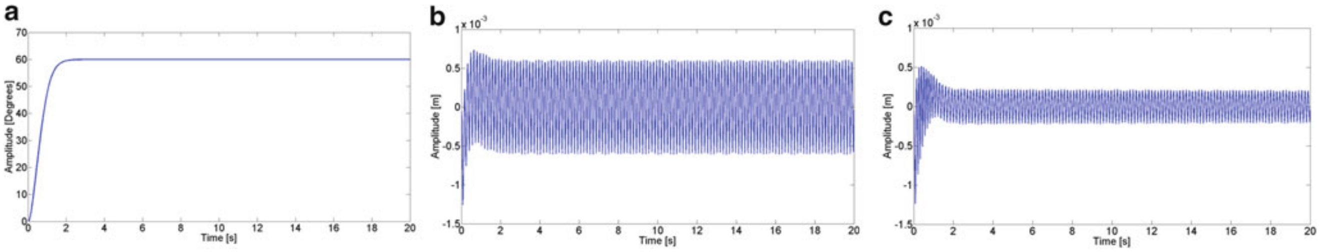

Fig. 13.5 Numerical results using DSF for position regulation. (**a**) Position, (**b**) Vibration amplitude measured at the base of the structure without DSF, (**c**) Vibration amplitude measured at the base of the structure with DSF

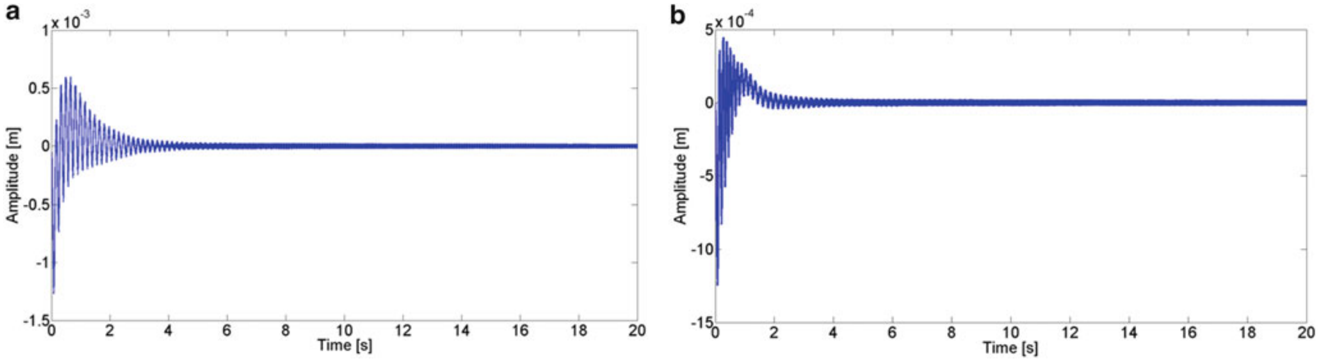

Fig. 13.6 Numerical results using MPPF and DSF control schemes. (**a**) Using MPPF, (**b**) Using MPPF and DSF

where M_r, D_r, K_r are an identity (mass), damping and stiffness matrices of the reduced order model associated to the flexible structure, respectively. The closed-loop flexible systems dynamics Eq. (13.11) and Eq. (13.10) is described by

$$\begin{bmatrix} M_r & 0 \\ 0 & I \end{bmatrix}\begin{bmatrix} \ddot{q}_{m_r} \\ \ddot{\eta} \end{bmatrix} + \begin{bmatrix} D_r & 0 \\ 0 & 2Z_f W_f \end{bmatrix}\begin{bmatrix} \dot{q}_{m_r} \\ \dot{\eta} \end{bmatrix} + \begin{bmatrix} K_r & -B_{mc_r} G^T {W_f}^2 \\ -{W_f}^2 G B^T{}_{mc_r} & {W_f}^2 \end{bmatrix}\begin{bmatrix} q_{m_r} \\ \eta \end{bmatrix} = \begin{bmatrix} B_{mr} \\ 0 \end{bmatrix} u_{\ddot{\theta}}(t)$$
$$Z_f = diag\left[\zeta_{f_1}, \zeta_{f_2}\right], \quad W_f = \left[\omega_{f_1}, \omega_{f_2}\right], \quad G = \left[g_1 \quad g_2\right]^T \tag{13.12}$$

In Fig. 13.6 some numerical results using MPPF and MPPF+DSF are described, respectively. One can observe that the dynamic performance of the flexible structure results slightly better with MPPF+DSF.

13.4 Experimental Vibration Control Using MPPF and MPPF+DSF

In order to verify the effectiveness of the proposed control schemes, a flexible frame structure was constructed attached on a rigid revolute servomechanism as shown in Fig. 13.7. In addition, a PZT stack actuator and two strain gauges are mounted for monitoring and control purposes of the undesirable vibrations on the overall structure.

A fast processing data acquisition system based on a PCI board (Sensoray 626) into a PC running under *Windows/XP*® and *Matlab/Simulink*® platforms is used to get measurements from strain gauges, optical encoders and provide the analog outputs to implement the controllers. The PZT stack actuator is driven by a power amplifier, which transforms the low amplitude analog signal provided by the acquisition system with the required high voltage signal for the PZT effect on the actuator.

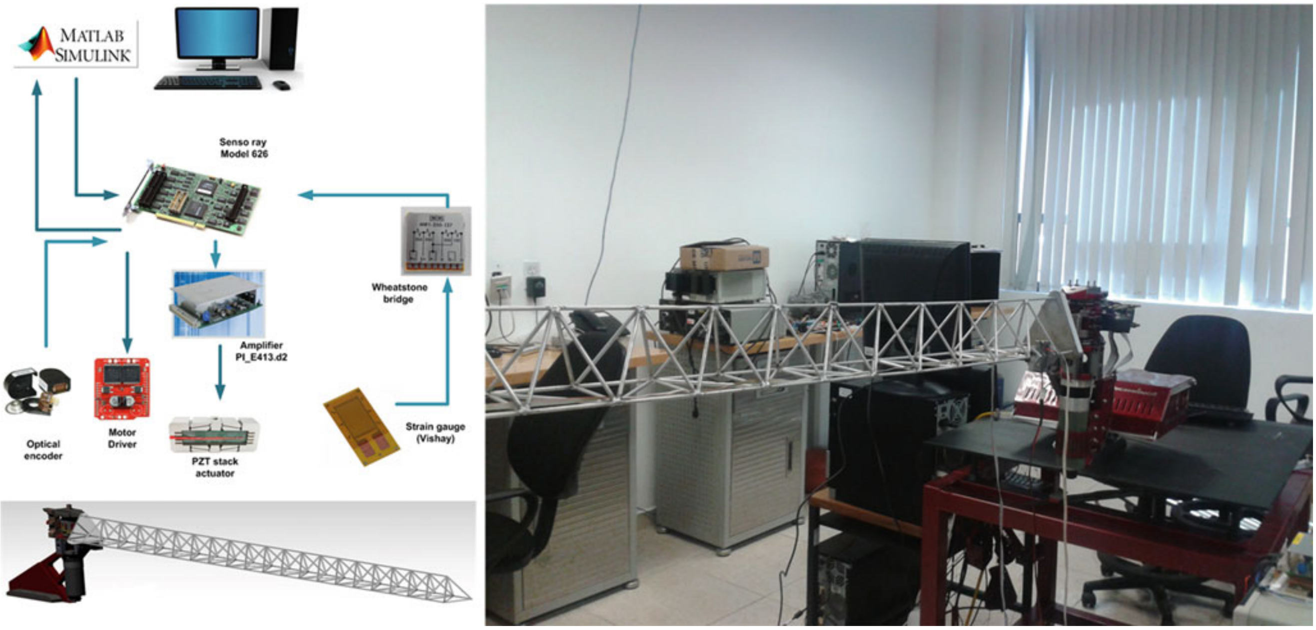

Fig. 13.7 Schematic diagram of the integrated system and experimental setup

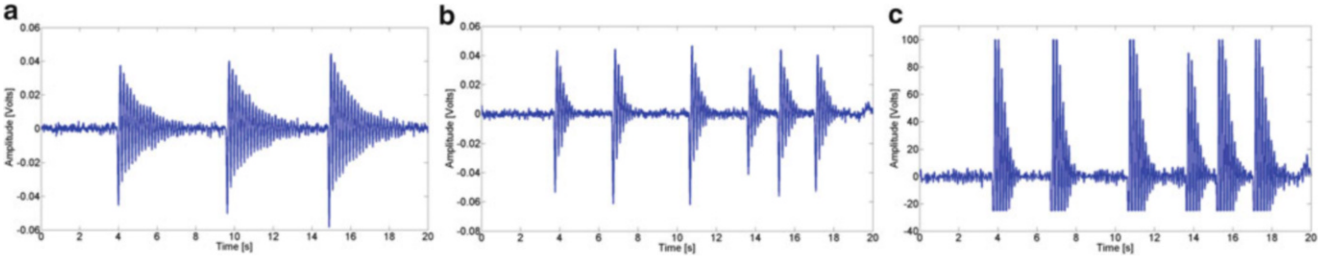

Fig. 13.8 Experimental results. (**a**) Without MPPF control. (**b**) With MPPF control, (**c**) Control effort for PZT stack actuator

13.4.1 *Some Experimental Results*

Performance of proposed control are evaluate using experimental setups show in Fig. 13.7. The experimental results obtained using PZT stack as actuator where input signal control for PZT stack was computed by applying MPPF control scheme using the signal measured by the strain gauge which are show in Fig. 13.8, where we can see that undesirable vibration are attenuated faster when MPPF is applied.

After verifying that the dynamics of the structure has been improved, by the application of MPPF control schemes, then such a MPPF tuning is combined with DSF in order to minimize the vibration amplitude on two principal tasks in any manipulator, which are regulation position and trajectory tracking. Some experimental results, when the desired angle is 60° on the motor shaft, are shown in Fig. 13.9. Note how the flexible structure is excited. In Fig. 13.9b is shown a comparison when MPFF and DSF are used to minimize the vibration amplitude on the overall structure.

Some trajectory tracking tasks where also carried on, in order to verify the robustness of the control schemes presented in this work. In this regard, some satisfactory experimental results are shown in Fig. 13.10, where it can be observed that, the strains amplitude measurements are kept lower when both schemes, MPPF and DSF, are applied together (see Fig. 13.10b).

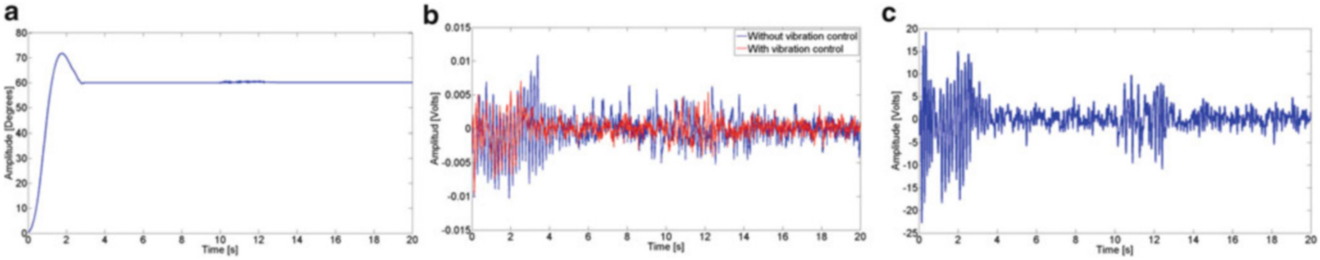

Fig. 13.9 Position regulation and vibration control using MPPF and DSF. (**a**) Hub angle, (**b**) Stress measurement by strain gauge, (**c**) Control effort for PZT stack actuator

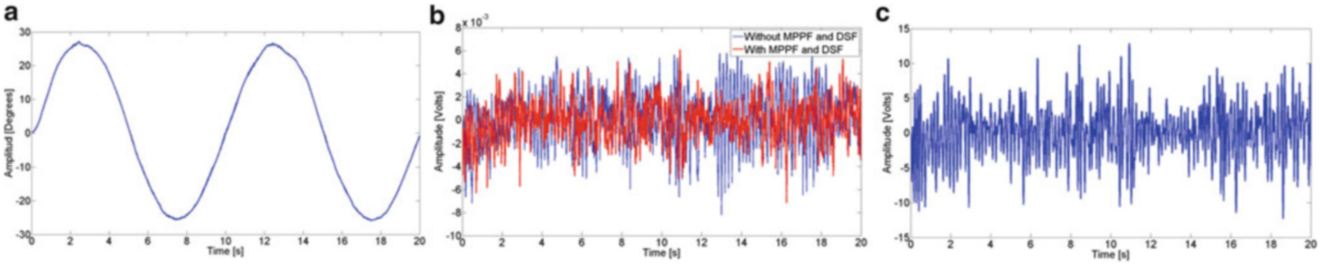

Fig. 13.10 Trajectory tracking and vibration control using MPPF and DSF. (**a**) Hub angle, (**b**) Stress measurement by strain gauge, (**c**) Control effort for PZT stack actuator

13.5 Conclusions

In this paper, theoretical and experimental results using DSF and MPPF control schemes, to improve the dynamic performance for regulation and trajectory tracking of the end tip position of a flexible structure, mounted on a rigid revolute servomechanism, are shown. Both control schemes are used in order to minimize de vibration amplitude, which remains as a part of the dynamic response of the inherent system motion. Finite element methods and modal analysis allow to evaluate numerically how the dynamics of the structures is modified with two different control schemes. MPFF control schemes allow to inject additional damping to the flexible frame structure. MPPF control was tuned up to the first two natural frequencies of the flexible structure, resulting in vibration attenuation up to 50 % with respect to the open-loop response. DSF was applied as a complementary part of the MPPF control scheme, and it was found that DSF contribution to effectively suppress structural vibrations, turned out to be less than that expected, since the flexible frame structure nature has many 3D degrees of freedom, containing among some which cannot be controlled by the planar rotation of the servomechanism. Flexible frame structures are naturally designed in such a way to maximize their stiffness, thus, rendering the strain gages measurements less significant on the overall control process. However, the PZT stack actuator does have influence to control the first two vibration modes, regardless of the 3D plane they belong to. Therefore, it was possible to introduce controlled forces, which are opposed to the structural vibrations, so as to effectively damp them out. This fact was observed into the experimental results as a faster decay of the vibratory effects.

References

1. Preumont, A., Seto, K.: Active Control of Structures. Wiley, Cornwall (2008)
2. Hurlebaus, S., Gaul, L.: Review: smart structure dynamics. Mech. Syst. Signal Process. **20**, 255–281 (2006)
3. Preumont, A., de Marneffe, B., Deraemaeker, A., Bossen, F.: The damping of a struss structure with a piezoelectric transducer. Comput. Struct. **86**, 227–239 (2008)
4. García-Pérez, O.A., Silva-Navarro, G., Peza-SolísJ.F. and Trujillo-Franco L. G.: Trajectory tracking and vibration control in a space frame flexible structure with a PZT stack actuator. Proc. SPIE 9431, Active and Passive Smart Structures and Integrated Systems 2015, p. 943136 (April 2, 2015). doi:10.1117/12.2084478

5. Gawrosnki, Q.K.: Advanced Structural Dynamics and Active Control of Structures. Springer, New York (2004)
6. Preumont, A.: Vibration Control of Active Structures, 2nd edn. Kluwer, Dordrecht (2002)
7. Luo, Z.: Direct strain feedback control of flexible robot arms: new theoretical and experimental results. IEEE Trans. Autom. Control **38**(11), 1610–1622 (1993)
8. Ge, S.S., Lee, T.H., Zhu, G.: Improving regulation of a single-link flexible manipulator with strain feedback. IEEE Trans. Robot. Autom. **14**(1), 179–184 (1998)
9. Friswell, M.I., Inman, D.J.: The relationship between positive position feedback and output feedback controllers. Smart Mater. Struct. **8**, 285–291 (1999)

Chapter 14
Multi-Reference Time-Frequency Active Control of Vehicle Interior Road Noise

Tao Feng, Guohua Sun, Mingfeng Li, and Teik C. Lim

Abstract Active noise control (ANC) technique has been successfully implemented by various automotive manufacturers to interior powertrain noise cancellation and/or sound management. For the powertrain noise control, the ANC system only requires one reference signal (typically using tachometer signal) due to the fact that the powertrain response is functionally related to the engine rotational speed. Instead, the multi-reference ANC system is often required for the road noise control since the multiple-coherence between the reference accelerometer signals and the target noise must be guaranteed to yield an acceptable control performance. However, the adoption of traditional multi-reference filtered-x least mean square (FXLMS) algorithm for road noise ANC often leads to a large computational burden and slow convergence rate due to the long length of adaptive filter and a huge dynamic range of the filtered reference signal. To address these problems, road noise ANC systems configured with the time-frequency domain FXLMS (TF-FXLMS) algorithm and subband FXLMS (SFXLMS) algorithm are developed, where the adaptive algorithm either calculates the gradient estimate and filtered reference signal in the frequency domain or subband frequency domain to reduce the computational requirement and also updates the control signals in the time domain to avoid delay in the reference path. Then, a comprehensive computational complexity analysis is conducted to exhibit the computational cost for different algorithms. The effectiveness of the different algorithms will be demonstrated through an ANC system with eight accelerometers, one secondary loudspeaker, and one error microphone in the driver side to control actual road noise.

Keywords Active noise control • Road noise • FXLMS algorithm • Time-frequency FXLMS algorithm • Subband FXLMS algorithm

14.1 Introductions

In recent years, lightweight design is a primary and crucial way to achieve energy saving and gas economy for a greener vehicle. However, the lightweight deign will increase structural vibration and consequent interior noise, especially at low frequencies (60–400 Hz). Meanwhile, passive noise control is not ideal because it tends to add more weight and cost into the vehicle [1]. To solve these problems, active noise control (ANC) technology has been developed by using the audio system as the secondary speaker to control the powertrain noise and road noise in automobile industry [2–11].

ANC is based on the principle of linear superposition; the unwanted primary noise is cancelled by a secondary noise of equal amplitude and opposite phase [12]. Generally, the road noise is the dominant source when the vehicle runs at middle and high speed. Hence, there have been many research works devoted to develop a feasible ANC system to control the road noise in the last three decades. For instance, in 1990, Elliott et al. [7] showed a feasible way to control the road noise using the ANC system. Later, Sutton et al. [8] developed a multi-channel ANC system by utilizing the conventional filtered-x least mean square (FXLMS) algorithm to control the road noise. Also, this paper presented the guideline for the selection of reference accelerometers and secondary speaker. Then, in 2001, Sano et al. [9] first proposed an ANC system combined with the vehicle audio system to control the road noise. In 2002, Park et al. [10] proposed a real-time ANC system for road noise with the common FXLMS algorithm. However, most studies as discussed above used the conventional time-domain FXLMS algorithm. While it works, the FXLMS algorithm has inherent drawbacks such as the computational burden and frequency-dependent convergence speed, in particular for the road noise ANC. This is because the road noise is broadband in spectrum, which often requires a high-order adaptive filter.

T. Feng (✉) • G. Sun • M. Li • T.C. Lim
Department of Mechanical and Materials Engineering, Vibro-Acoustics and Sound Quality Research Laboratory, College of Engineering and Applied Science, University of Cincinnati, 598 Rhodes Hall, P.O. Box 210072, Cincinnati, OH 45221-0072, USA
e-mail: fengto@mail.uc.edu

A. Wicks, C. Niezrecki (eds.), *Structural Health Monitoring, Damage Detection & Mechatronics, Volume 7*,
Conference Proceedings of the Society for Experimental Mechanics Series, DOI 10.1007/978-3-319-29956-3_14

To overcome this problem, Morgan and Thi [13] proposed a delayless subband algorithm for ANC applications in 1995. Also, the signal path delay was avoided while retaining the advantage of subband algorithm. Very recently, Duan developed a time-frequency FXLMS (TF-FXLMS) algorithm for road noise ANC, which significantly reduces the computational cost as compared to the time-domain FXLMS algorithm. For road noise control, multiple reference ANC system is required to improve the system performance. However, the comparisons among the TF-FXLMS, SFXLMS and the conventional time-domain FXLMS algorithms remain unknown. Therefore, the main objective of this paper is to conduct a comparative study of the various time-frequency algorithms for road noise ANC. The performance and computational cost of the different algorithms are studied.

This paper is organized as follows. First, single-input-single-output (SISO) road noise ANC system with multi-reference signals configured with the conventional FXLMS, TF-FXLMS and SFXLMS algorithms are introduced in Sect. 14.2. Then, Sect. 14.3 compares the computational complexity of the multi-reference ANC system using different algorithms. Finally, the simulation results are discussed in Sect. 14.4.

14.2 Control System

14.2.1 FXLMS Algorithm

A configuration of the multiple-reference active road noise control system by using the conventional time-domain FXLMS algorithm is shown in Fig. 14.1, where $x(n)$ is the reference signal that is picked up by accelerometers, $d(n)$ is the primary noise and $e(n)$ is the error signal. Here, J is the number of reference sensors mounted on the vehicle body. Also, the number of adaptive filter $W(z)$ is J when only one error signal is used in this study. Hence, the residual noise $e(n)$ can be expressed as

$$e(n) = d(n) - y(n) \tag{14.1}$$

$$y(n) = \boldsymbol{S}(n) * \sum\nolimits_{j=1}^{J} \left[\boldsymbol{w}_j^T(n) \boldsymbol{x}_{\boldsymbol{j}}(n) \right] \tag{14.2}$$

where n is the time index, $\boldsymbol{S}(n)$ is the impulse response of the secondary path, and $*$ denotes linear convolution. The adaptive filter weight and the reference signal are

$$\boldsymbol{w}_{\boldsymbol{j}}(n) = \left[w_{j,0}(n)\ w_{j,1}(n) \ldots\ w_{j,L-1}(n) \right]^T \tag{14.3}$$

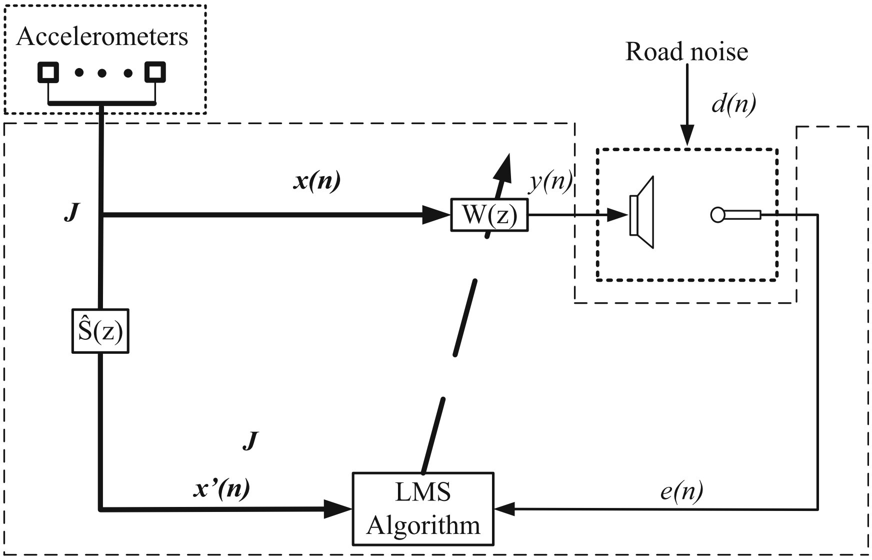

Fig. 14.1 Block diagram of the multiple-reference active road noise control system with the conventional FXLMS algorithm

$$\boldsymbol{x_j}(n) = \left[x_j(n)\, x_j(n-1) \ldots\, x_j(n-L+1)\right]^T \tag{14.4}$$

where L is the length of the adaptive filter. The objective is to minimize the mean square error (MSE), which can be estimated as follows

$$\xi(n) = E\left[e^2(n)\right] \tag{14.5}$$

where $E[\cdot]$ represents the mathematical expectation. The MSE $\xi(n)$ can be minimized, using the steepest descend method, which updates the adaptive weight vector in the negative gradient direction

$$\boldsymbol{w_j}(n+1) = \boldsymbol{w_j}(n) + \mu \boldsymbol{x'}_{\boldsymbol{j}}(n) e(n) \tag{14.6}$$

where $\boldsymbol{x}_j^{'}(n) = \boldsymbol{s}(n) * \boldsymbol{x_j}(n)$, it can be seen that the adaptive filter weight is updated by the filtered reference signal $\boldsymbol{x}_j^{'}(n)$.

14.2.2 *Time-Frequency FXLMS Algorithm*

Figure 14.2 shows the block diagram of the TF-FXLMS algorithm, proposed by Duan [11] with overlap-save implementation. The overlap-save implementation is a method, which is used to convert circular convolution to linear convolution [14]. In this study, a 50 % overlap is used. Therefore, for one update, N samples of new reference signal and error signal are accumulated in the buffer to form the $2N$ data vectors.

$$\boldsymbol{x_j}(k) = \left[\, x_j(kN-N+1)\, x_j(kN-N+2) \cdots x_j(kN)\right]^T \tag{14.7}$$

$$\boldsymbol{e}(k) = [\, e(kN-N+1)\, e(kN-N+2) \cdots e(kN)]^T \tag{14.8}$$

where k is the block index. For the input reference signal, the overlap-save implementation keeps the previous block of N samples, and pads them with the new data, to form the $2N$ vector, which is expressed as $\left[x_j(k-1)\, x_j(k)\right]^T$. However, for the error signal, it pads N -point zero data, to form the $2N$ vector, which can be expressed as $[0\ e(k)]^T$. Then, the reference signal and the error signal are transformed into frequency domain *by* 2N point FFT.

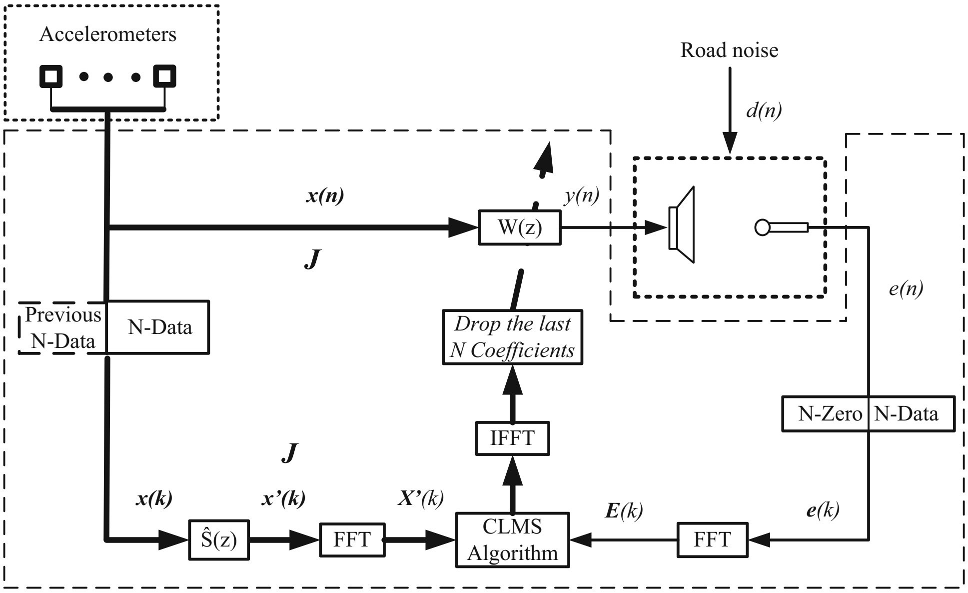

Fig. 14.2 Block diagram of the multiple-reference active road noise control system with the TF-FXLMS algorithm

$$\boldsymbol{X_j}(k) = FFT\left(\left[\boldsymbol{x_j}(k-1)\ \boldsymbol{x_j}(k)\right]^T\right) \tag{14.9}$$

$$\boldsymbol{E}(k) = FFT\left([0\ \boldsymbol{e}(k)]^T\right) \tag{14.10}$$

Therefore, the gradient can be estimated by using the frequency domain filtered reference and the error signal, expressed as

$$\widehat{\nabla}_j(n) = \mathit{first\ N\ parts\ of\ IFFT}\left\{\hat{\boldsymbol{\mu}}\,\overline{\boldsymbol{S}(k)\boldsymbol{X_j}(k)}\boldsymbol{E}(k)\right\} \tag{14.11}$$

where $\widehat{\nabla}_j$ is the block gradient estimate of the adaptive filter $\boldsymbol{w_j}$, $\overline{(\cdot)}$ denotes the complex conjugate operation, $\hat{\boldsymbol{\mu}}$ is the step size that is normalized according to the filtered reference signal in each frequency bin [15]. Then, the j -th adaptive filter coefficients can be updated by

$$\boldsymbol{w_j}(k+1) = \boldsymbol{w_j}(k) + \mu\widehat{\nabla}_j \tag{14.12}$$

Hence, each adaptive filter is updated block by block, which saves huge computational burden for multiple reference active road noise control system.

14.2.3 SFXLMS Algorithm

Figure 14.3 shows the diagram of the multiple-reference SFXLMS algorithm. As shown, the DFT analysis filter bank consists of I subbands. The reference signal $x_j(n)$ and the error signal $e(n)$ are decomposed into sets of sub-band signals, expressed as

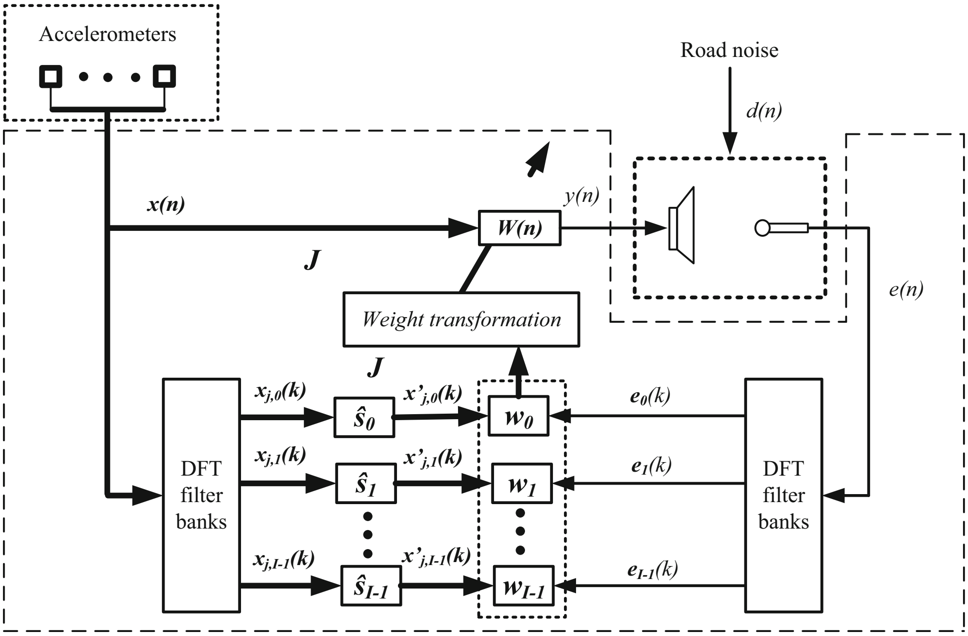

Fig. 14.3 Block diagram of the multiple-reference active road noise control system with the SFXLMS algorithm

$$\boldsymbol{x}_{j,i}(n) = \left[x_{j,i}(nD+i)\ x_{j,i}((n-1)D+i)\ \ldots\ x_{j,i}((n-K-1)D+i)\right]^T \tag{14.13}$$

$$\boldsymbol{e}_i(n) = \left[e(nD+i)\ e((n-1)D+i)\ldots\ e((n-K-1)D+i)\right]^T \tag{14.14}$$

where $i = 0, 1, \ldots, D$, the decimation factor $D = I/2$, N is the length of fullband adaptive filter, and K is the number of weights for each sub-band adaptive filter $K = N/D$.

The i-th subband adaptive filter can be updated using the complex normalized least-mean-square algorithm as

$$\boldsymbol{w}_{j,i}(n+D) = \boldsymbol{w}_{j,i}(n) + \mu \frac{\boldsymbol{x}'^{*}{}_{j,i}(n)}{\left\|\boldsymbol{x}'_{j,i}(n)\right\|^2 + \alpha} e_i(n) \tag{14.15}$$

where α is a small constant value to avoid infinite step size. Then, these subband adaptive weights are transformed to fullband via a weight transformation scheme using FFT-stacking method [13].

14.3 Computational Complexity Analysis

This section evaluates the computational complexity of the multi-reference ANC system using the TF-FXLMS algorithm, SFXLMS algorithm as well as the conventional time-domain FXLMS algorithm. For convenience, the computational complexity is based on the number of multiplies per input sample. In this analysis, the number of reference signal is J and the number of adaptive filter also is J. It is noted that the computational cost of FXLMS algorithms is mainly determined by the orders of the controller and FIR filter for the secondary path that used. Assuming order of adaptive controller is N and filter order for the secondary path is L. Hence, the total computations required in each process in FXLMS algorithm are equal to $3JN^2 + JNL$. As compared with the FXLMS algorithm, TF-FXLMS algorithm requires to process reference signal and error signal in the frequency domain and it will obviously reduce the computational burden. Therefore, to produce N sample of the output signal total computation cost for TF-FXLMS algorithm is $(2J+1) \cdot 4N \cdot \log_2(2N) + J \cdot \left(N^2 + 29N\right)$. Also, SFXLMS algorithm processes the adaptive filter at a lower decimation rate to save the computational cost. The total computational cost of SFXLMS algorithm is $(8Q + Qlog_2Q)(2+J) + 8(L+N) \cdot JQ + JN$, where Q is the number of subband adaptive filter and K is the length of each subband adaptive filter [16].

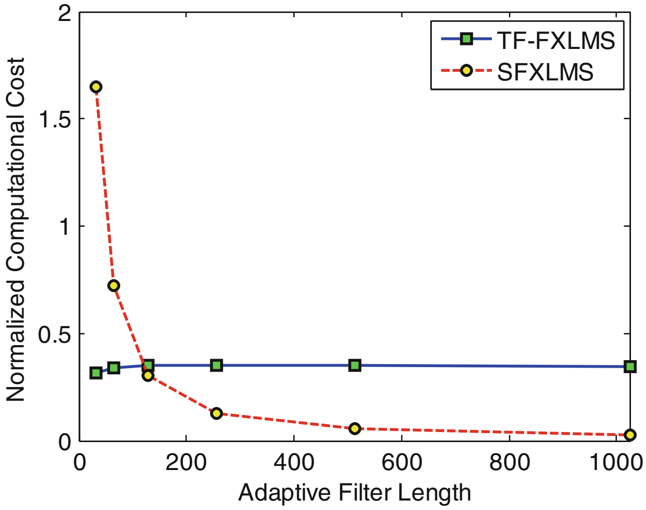

Fig. 14.4 Normalized computational complexities with different lengths of adaptive control filter ***N***

Figure 14.4 shows the comparison of the normalized computational complexity of TF-FXLMS algorithm and SFXLMS over the traditional FXLMS algorithm. Here, the length of adaptive control filter N is 32, 64, 128, 256, 512 and 1024, respectively, the number of reference signal J is 8, the length of the estimated secondary path L is 256-tap and the number of subbands Q is 8. As shown in the Fig. 14.4, the computational complexity of two time-frequency domain algorithms can save the computational cost as compared with the conventional time domain FXLMS algorithm. In addition, SFXLMS algorithm can reduce more computational burden when the length of adaptive control filter is increased to 256 taps. Therefore, SFLMS algorithm will save more computational cost when the adaptive filter length is more than 256 taps as compared with TF-FXLMS algorithm.

14.4 Numerical Results

In order to evaluate the performance of active road noise control system using different algorithms, related simulation models are built using the measured vehicle data. For demonstration purpose, the control system is composed of eight accelerometers, one secondary speaker and one error microphone to attenuate the road noise around the driver's head area. Eight accelerometers mounted on the vehicle body are selected based on the best multiple coherence function between the reference signals from accelerometer and the target road noise. The primary road noise signal and eight reference signals are recorded when the control system is off and vehicle is driven on an experimental road surface at a constant speed of 30 mph.

The transfer function of the secondary path from the control speaker to the error microphone is modeled using FIR filter with 256 taps experimentally, before the active control is implemented. The frequency response function of the measured secondary path is shown in Fig. 14.5.

To yield good reduction, the selection of the reference accelerometers is required. Hence, the multiple coherence function and principle component analysis are applied to determinate the desirable location and the number of accelerometers

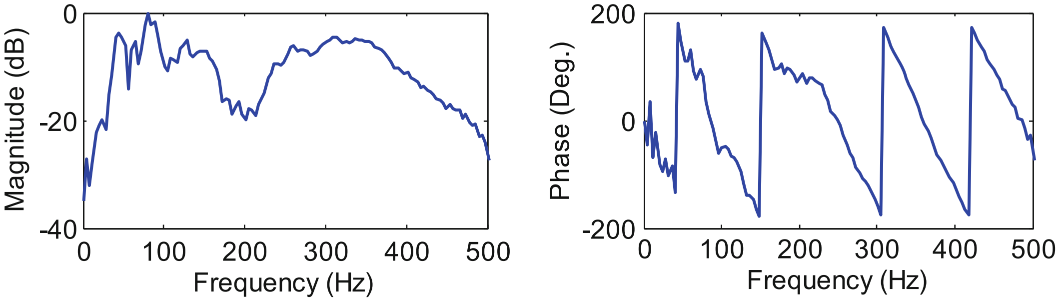

Fig. 14.5 Magnitude and phase response of the secondary path transfer functions

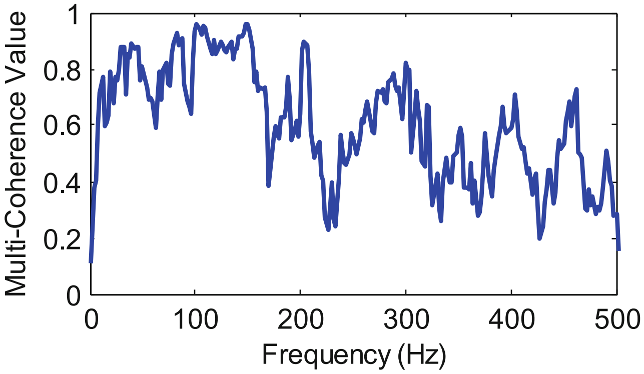

Fig. 14.6 Multiple coherence function between a set of reference signals and the targeted road noise

Fig. 14.7 Comparison of active road noise control results using different algorithms with eight reference accelerometers

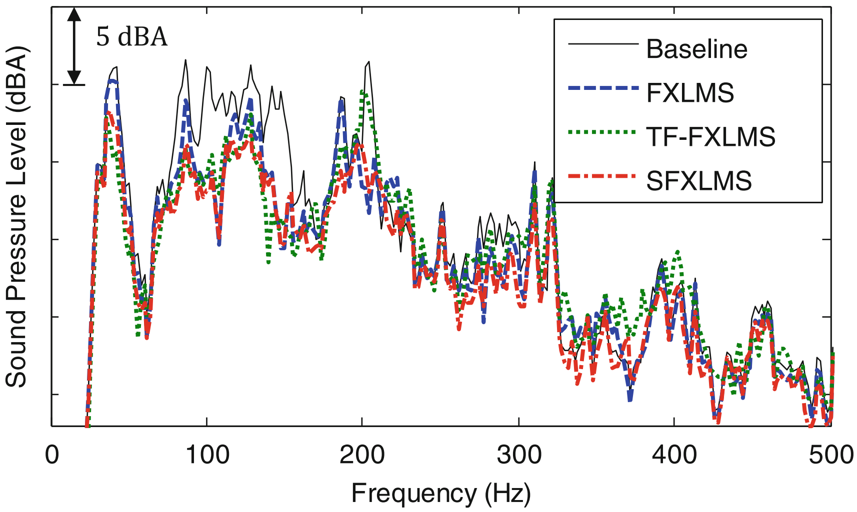

needed. Figure 14.6 shows the multiple coherence functions between the selected set the reference signals and the target road noise at the driver's error microphone.

Figure 14.7 show the simulation results using three different control algorithms at driver's head position. The black solid curve is the baseline response of road noise when the active noise is off. The blue dash line is the control result using the conventional FXLMS algorithm. The green dot curve and red dash dot curve is the resultant response using the TF-FXLMS algorithm and SFXLMS algorithm, respectively. As shown in Fig. 14.7, the SFXLMS algorithm exhibits more reductions in the broadband frequency range as compared to the conventional FXLMS algorithm and the TF-FXLMS algorithm. The reason is that subband adaptive filter will reduce the spectral dynamic range in each subband and improve the system's convergence rate.

14.5 Conclusions

This paper presents the active road noise control system using three different control algorithms. Computational complexity analysis shows that the TF-FXLMS algorithm and SFXLMS algorithm can significantly reduce the computational burden as compared to the conventional FXLMS algorithm for multiple reference active road noise control system. In order to verify the performance of the active road noise control system employed with these adaptive algorithms, numerical simulations are conducted, utilizing the measured vehicle data. The simulation results show the TF-FXLMS algorithm and SFXLMS algorithm significantly reduce the computational cost and achieve similar noise reductions as compared to the conventional FXLMS algorithm. Meanwhile, SFXLMS algorithm exhibits more reduction in the broadband frequency range. Therefore, among the three algorithms, SFXLMS algorithm shows the best performance. However, if computational cost is a concern when the adaptive filter is less than 256, the TF-FXLMS algorithm would be a better choice, due to its low computational complexity.

References

1. Rao, M.D.: Recent applications of viscoelastic damping for noise control in automobiles and commercial airplanes. J. Sound Vib. **262**(3), 457–474 (2003)
2. Dehandschutter, W., Sas, P.: Active control of structure-borne road noise using vibration actuators. J. Vib. Acoust. **120**(2), 517–523 (1998)
3. Cheer, J: Active control of the acoustic environment in an automobile cabin. Ph.D. dissertation, University of Southampton (2012)

4. Duan, J., Li, M., Lim, T., Lee, M. et al.: Control of powertrain noise using a frequency domain filtered-x LMS algorithm. SAE Technical Paper 2009-01-2145. (2009). doi:10.4271/2009-01-2145
5. Elliott, S.J.: A review of active noise and vibration control in road vehicles. ISVR Technical Memorandum No. 981, Detroit (2008)
6. Duan, J., Li, M., Lim, T., Lee, M. et al.: Control of powertrain noise using a frequency domain filtered-x LMS algorithm. SAE Technical Paper 2009-01-2145. (2009). doi:10.4271/2009-01-2145
7. Elliott, S., Nelson, P., Sutton, T., McDonald, A., Quinn, D., Stothers, I., et al.: The active control of low frequency engine and road noise inside automotive interiors. Active Noise and Vibration, ASME Winter Annual Meeting, vol. 8, pp. 125–129 (1990)
8. Sutton, T.J., Elliott, S.J., McDonald, A.M., Saunders, T.J.: Active control of road noise inside vehicles. Noise Control Eng. J. **42**(4), 137–146 (1994)
9. Sano, H., Inoue, T., Takahashi, A., Terai, K., Nakamura, Y.: Active control system for low-frequency road noise combined with an audio system. IEEE Trans. Speech Audio Process. **9**(7), 755–763 (2001)
10. Park, C., Fuller, C.R., Kidner, M.R.F.: Evaluation and demonstration of advanced active noise control in a passenger automobile. In: International Symposium on Active Control of Sound and Vibration, Southampton, pp. 275–284 (2002)
11. Duan, J., Li, M., Lim, T.C., Lee, M.-R., Cheng, M.-T., Vanhaaften, W., et al.: A computationally efficient multichannel active road noise control system. J. Dyn. Syst. Meas. Control. **137**(1), 011003(1–7) (2015)
12. Kuo, S.M., Morgan, D.: Active Noise Control Systems: Algorithms and DSP Implementations. Wiley, New York (1995)
13. Morgan, D.R., Thi, J.C.: A delayless subband adaptive filter architecture. IEEE Trans. Signal Process. **43**(8), 1819–1830 (1995)
14. Morgan, D.R.: An analysis of multiple correlation cancellation loops with a filter in the auxiliary path. IEEE Trans. Acoust. Speech Signal. Process. **28**(4), 454–467 (1980)
15. Shynk, J.J.: Frequency-domain and multirate adaptive filtering. IEEE Signal Process. Mag. **9**(1), 14–37 (1992)
16. Seon Joon, P., Jeong Hyeon, Y., Young Cheol, P., Dae Hee, Y.: A delayless subband active noise control system for wideband noise control. IEEE Trans. Speech Audio Process. **9**(8), 892–899 (2001)

Chapter 15
Wireless Monitoring of the Dynamic Behavior of Railway Catenary Systems

Anders Rønnquist and Petter Nåvik

Abstract During the last couple of decades the railways have experienced a steady growth in high-speed rail. However, there still exist a considerable amount of infrastructure that is designed for older and completely different scenarios. This is also true when considering the power supply to the electric railways where a two level catenary system is commonly used. For the power supply to be reliable and uninterrupted under higher speeds there must be strict static and dynamic requirements. The current power supply systems for old electric railway lines, often called soft catenary systems, are characterized by their design for an optimal quasi-static behaviour. This paper primarily explores the behavior of the dynamic system using a newly developed monitoring system. This includes multiple wireless sensors mounted in arbitrary positions chosen to be beneficial in the description of the fundamental motions, and with a range above 700 m. However, for any monitoring scheme to be efficient, it is important to establish relevant dynamical system conditions and to verify existing systems behavior. This requires a full-scale instrumentation program and the associated system identifications. That is, for the railway catenary system it must be included several sensors measuring response at different points within one or several spans as well as close to the cantilevered supports. The system can then assess catenary response components such as uplift, frequencies, damping and mode shapes. In the current paper this is further explored using the location of Hovin station in Norway.

Keywords Soft catenary system • Operational modal analysis • Short time Fourier analysis • Energy transfer • Catenary-pantograph interaction • Electric railways

15.1 Introduction

The international railways have seen a considerable increase in high-speed rail where several new countries around the world either are building high-speed railways or have plans to do so [1]. However, there do still exist a large volume of older infrastructure designed for completely different scenarios. The current supply systems of old electric railway lines, often called soft catenary systems, are characterized by their design for an optimal quasi-static behaviour. To increase the speed it is important to explore possible limiting factors, i.e. to identify the dynamic consequences and limitations. Excessive vibrations may produce loss of contact giving arching and increased wear, even disrupted power supply. Therefore, any significant increase in train speed must be verified by regarding effects in the catenary-pantograph interactive response [1].

The dynamic system investigated consists of the interaction between two non-linear dynamic systems, the pantograph and the catenary system. The contact interaction will give both static and dynamic loads of the combined system, and it will vary with the train speed. The complexity of this interaction and the dynamic response of the system progressively increase with increasing train speed [2]. The dynamic response of the catenary system becomes more important to address as the speed of the train is increased above design speed [3]. This is partly also due to the fact that railway catenary systems in general are considered to be low damped systems. This may become a problem when trains are running with multiple pantographs because the trailing pantographs will run into oscillations made by the first [4, 5]. It is recognized that to estimate the structural modal properties, such as damping, in the catenaries is challenging [1]. Thus, the estimated structural properties may only be evaluated from validated numerical models, then to be used to evaluate the dynamic response of different catenary systems. Other measurements are needed to evaluate the behaviour of the catenary continuously from before the train passes, as the train passes and after it passes. The importance of this is shown in a recent study [6]. An validation

---

A. Rønnquist (✉) • P. Nåvik
Department of Structural Engineering, Norwegian University of Science and Technology,
Rich. Birkelandsvei 1A, 7491 Trondheim, Norway
e-mail: anders.ronnquist@ntnu.no

A. Wicks, C. Niezrecki (eds.), *Structural Health Monitoring, Damage Detection & Mechatronics, Volume 7*,
Conference Proceedings of the Society for Experimental Mechanics Series, DOI 10.1007/978-3-319-29956-3_15

investigation by sampling displacement time series in [7] was conducted at five points within a pole span to validate the displacements in their numerical model. This was done by placing three additional poles within a span for mounting of the measuring equipment. However, acceleration measurements of the catenary as the train pass the section can also be used to assess the behaviour. Several different properties can be assessed if the sensors are well positioned. The speed of the train can be estimated by the use of the cross-correlation function if a sufficiently long distance between sampling points is used. This has been shown from analyses on numerical models that maximum displacement can be estimated by integration of sampled acceleration time series as shown by [6].

This paper explores a sensor system newly developed for examining the existing Norwegian railways. The sensor system is, at the moment, based on the inclusion of up to ten sensors that can be placed over more than 700 m on either side of the main unit. To capture the dynamic behaviour, the sensors measures accelerations in three main axes and simultaneously samples, transfer to main logging unit and further send data to a server accessible from the internet. In this investigation, the sensors are placed in the close vicinity of one span. This set-up is used to create a base line for future monitoring as well as for assessing the possibilities of increased speed. For soft contact lines, it is important to control maximum uplift at the pole support. The stiffness of the system changes between poles and along the section depending on track geometry, which makes it important to assess several points between pole supports. A range of different operational modal analysis (OMA) methods can be used on output-only data, such as the acceleration time series, for modal parameter estimation [8].

The intension has been to develop a system that is easy to mount and demount to be able to change the sampling positions. A wireless system where the sensors can be clipped on and off the wires in the system has thus been developed. Sensors have been mounted in different positions along the railway line to be able to predict different parameters. Results are presented by Power spectral densities (PSD) estimated by the Burg method [9], peak picking histograms of the PSD, spectrograms as well as stabilization plots and mode shapes estimated by the Covariance-driven Stochastic Subspace Identification (Cov-SSI) method [8]. This constitutes the base for the present investigation into properties of a railway catenary system as a train pantograph passes under. It also shows how the properties vary between pre-passage and post-passage rendering the investigation into the use of the sensor system.

15.2 Railway Catenary Systems

A railway catenary system consists of a contact wire, a messenger wire, droppers, registration arms and brackets as shown in Fig. 15.1. In the catenary, the contact wire is the conductive part that transfers the electricity to the train through the pantograph. The main purpose of the messenger wire is to carries the contact wire via the droppers, which also makes it possible to obtain the desired geometry, stiffness and thus elasticity of the system. The cantilevered brackets carrying the messenger wire are fastened to the poles along the line. The contact wire is connected to these brackets trough the registration arm. The main function of the light steady arm, besides being a fastener to the contact wire at the supports, is to obtain the right horizontal geometry of the contact wire.

To obtain the desirable geometry of the catenary system is tension introduced in both the contact wire and the messenger wire. The required tension is obtained by the use of a tensioning device consisting of weights and a transmission system like the one shown in Fig. 15.2. The droppers, the vertical wire elements in a span, are chosen such that intended sag of the contact wire between the droppers is limited to an appropriate level. Thus, the number of droppers will depend on the length of the span and the chosen tensile forces in the contact and messenger wire. For further details of contact lines system for the electric railways see also [10, 11].

For completeness, the pantograph is here also introduced. This is the device mounted on top of the train with the only purpose to ensure an uninterrupted and reliable energy transfer to the train. Furthermore, this is the second dynamic system, which introduce the vibrations in the catenary as the train moves forward. There are two bow strips of coal at the top of the pantograph that are the actual components that transfer the electricity. Simeon and Arnold [10] describes this contact as the most critical part in the transmission of the electricity to the trains of today. The contact is mainly ensured by introducing an upwards pressure in the pantograph.

The main existing catenary systems used in Norway are Tabell 54, System 35, System 20 and System 25. Only the three latter can be used in new design according to [12]. The choice of catenary system for the contact wire of a new railway sections is thoroughly specified in the technical regulations [13]. The criteria that decide which system to be use are train velocity, allowed type of pantographs, train density and type of tracks used [13, 14].

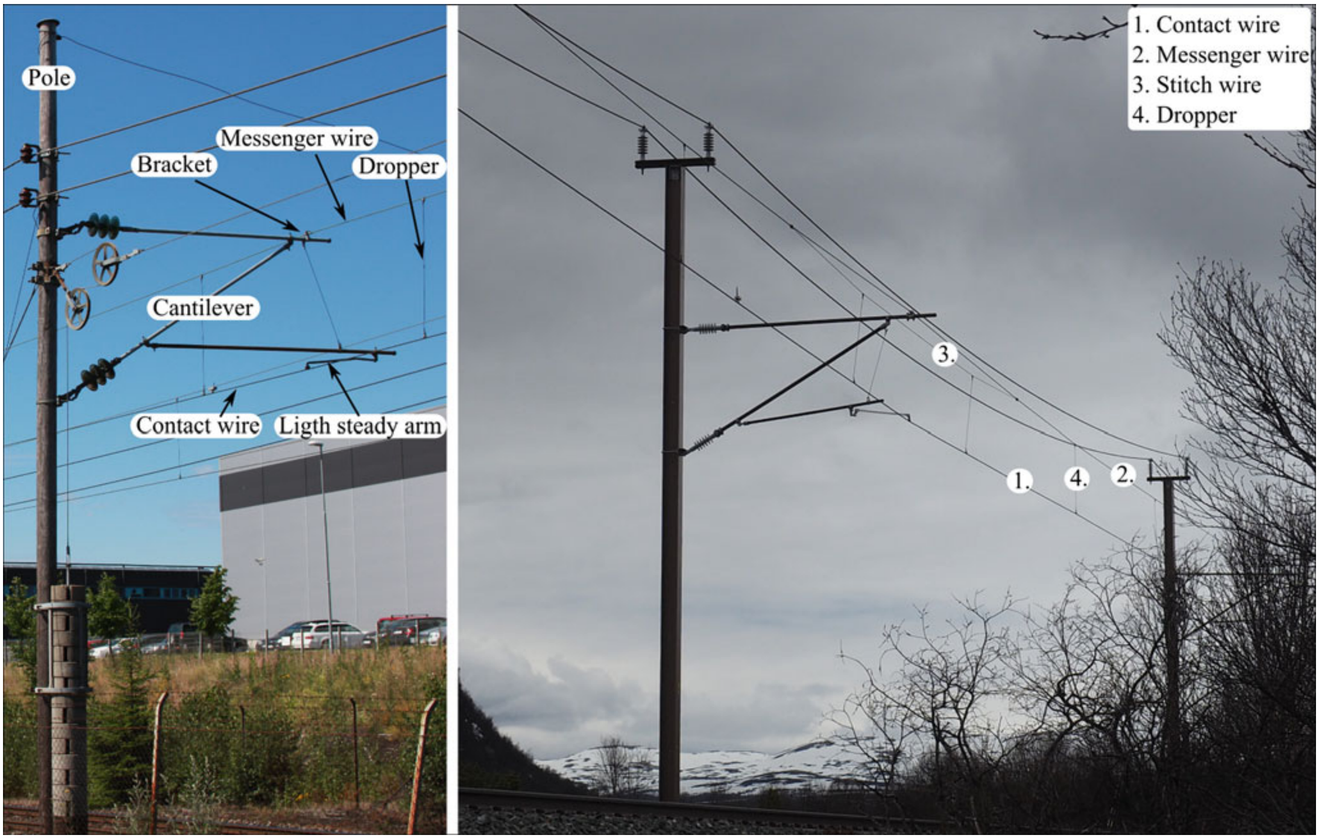

Fig. 15.1 The cantilevered bracket, registration arm as catenary support at the pole of an existing railway section in Norway

Fig. 15.2 The tensioning equipment in use at an existing railway section

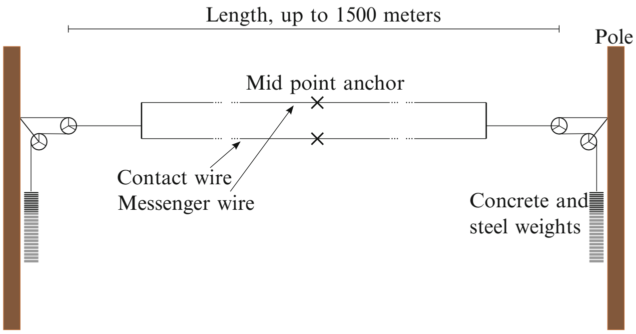

15.3 Wireless Sensors and Data Acquisition System for Electric Railway Catenaries

In this study is a newly developed wireless sensor system used. The system was developed in collaboration between the Norwegian University of Science and Technology, Norway, and Elektromotus, Lithuania [15]. The sensor system at the present consists of up to ten sensors with motion processing units (MPU) and one master unit. The MPU's are a combination of a microelectromechanical system (MEMS) based tri-axis gyroscope and a tri-axial accelerometer. These units also features inbuilt analogue-to-digital converters (ADCs). The accelerometers have a programmable full-scale range of ±2, ±4, ±8 and ±16 g, and the gyroscopes a full-scale range of ±250, ±500, and ±1000 and ±2000 °/s. The measurement width is 16 bit. The sensors transfer sampled data to the master unit using custom designed low-power 2.4 GHz radio network. The system can sample data up to 500 Hz and for 4 min. The triggering of the system can be done by exceeding a

Fig. 15.3 The catenary sensor consists of up to ten motion-processing units (MPU) as shown

boundary value, which can be chosen separately for each degree-of-freedom (DOF) in both positive and negative direction. An alternative triggering of the system is by manual triggering through a WiFi or GSM-connection. The whole system can be managed from a website through a GSM-connection in the master unit. Thus, all parameters can be set remotely, and all sampled data can equally be downloaded whenever necessary. A sampling rate of 200 Hz was used for the time series, and they were low-pass filtered at 80 % of the Nyquist frequency [16] to avoid aliasing and account for the roll-off rate of the filter [8]. Numerous sampling was done for both situations (Fig. 15.3).

15.4 Operational Modal Analysis for Dynamic Assessment of the Railway Catenary System

Frequency analysis of a time series is vital for understanding dynamic systems. Previously, it is shown that different information can be extracted from the different parts of a train passage time series, see [6, 15], then considered by numerical investigations. That is, the pre-passage data include more information about the load frequencies relevant to the section, such as the pantograph frequency and the different span-pass frequencies and fundamental frequencies. The post-passage data on the other side typically reveal the fundamental system frequencies. Otherwise, most information content do concern the motion-induced harmonic components and the structural damping, which are important parameters as the dynamic response increases. The advantage of dividing the signal with possible various information contents is also supported by the findings in [17]. The sensitivity to time variation near the peak uplift makes the important of combining pre- and post-passage segments with different operational modal analysis tools such as: power spectral density, stochastic subspace identification stabilization plots, and spectrograms in evaluating the frequency content. The combined effort of different analyses facilitates a good understanding of the energy input and transfer between frequencies originating from the train's passage.

15.4.1 Power Spectral Density (PSD) Estimation

There are several methods available for estimating PSD in structural dynamics. The method chosen to be used in estimating the PSD of pantograph passages depends to a large degree on the passage duration. Also, it is important to be aware that if the frequency distribution and energy transfer in the frequency domain are to be investigated in detail, the current time series will quickly become very short. Therefore, it is important to choose the method accordingly [8]. In parametric methods, the signal is assumed to be the output of a linear system driven by white noise, i.e., parametric methods estimate the PSD by first estimating the parameters of the linear system that is assumed to generate the signal. These methods generally produce smoother estimates of the PSD than do non-parametric methods. Commonly, parametric PSD estimation methods use an autoregressive (AR) prediction model for the signal.

In the investigation of the train passage, the Burg method is used for PSD estimation [9]. The Burg method estimates the PSD of the sampled time signal based on a pre-chosen order for the AR prediction model. The method does not apply a window function to the dataset, as is common in non-parametric methods. The Burg method may be considered better than non-parametric methods for the application to short parts of the recorded time series such as a train passage. However, it is important to be aware of some of its disadvantages. For example, the Burg method exhibits spectral line splitting, especially at high signal-to-noise ratios. In high-order systems, the Burg method can also introduce spurious spectral peaks, and when estimating sinusoids in noise, it shows a bias that is initial-phase dependent [18].

15.4.2 The Short-Time Fourier Transform (STFT) and Spectrogram Analysis

During a train's passage, the recorded time series will be, strictly speaking, non-stationary with time-varying spectral characteristics. To analyze the changing characteristics of the process, the STFT is essential. Using the STFT in the analysis of the time series provides more complete and precise information about the uplift process [6]. Calculated spectrograms give a visual representation of the displacement, providing a useful time-frequency representation. In the STFT, time series are segmented into time intervals that are sufficiently narrow to be considered stationary [19]. It is important to recognize that the time resolution, that is, how well two peaks in time can be separated from each other, and the frequency resolution, that is, how well two spectral components can be separated from each other, cannot be arbitrarily determined because they are both directly related to the time window size. It is equally important to consider the amount of overlap between the chosen windows. Avoiding overlap will result in more distinct differences between windows, whereas in overlapping windows, the results will be averaged for a better overall result. The STFT can also be used as a sliding discrete Fourier transform, conducting an analysis for each incremental shift using overlapping windows [20]. Finally, the spectrogram of from the STFT analysis is achieved by squaring the magnitude. In the following investigations, the STFT is used as a sliding discrete Fourier transform in which the STFT is evaluated for each shift of the window function. To evaluate the frequencies in the short-windowed time series, the Burg spectrum method is used.

15.4.3 Covariance Driven Stochastic Subspace Identification (Cov-SSI) Method

The covariance driven stochastic subspace identification (Cov-SSI) method [21] is used to identify modal parameters. The method is used on the data sets from all sensors at once in the identification. The Cov-SSI method uses output-only data to identify a stochastic state-space model. By assuming white noise, the discrete-time stochastic state space model can be represented as previously used in [22] and thoroughly given by Rainieri and Fabbrocino [8]. Modal parameters can be extracted from state matrices in the identified state space model including both a discrete state matrix as well as a discrete output matrix. This method requires that the order of the model is defined, but this is unknown for most practical applications. Therefore, the solution to overcome this problem is to estimate the modal parameters for all orders within a conservative interval and then show the results in a stabilization diagram [8]. The Cov-SSI method has a good ability to identify frequencies and damping of closely spaced modes that is crucial for very flexible structures, and it can also be used when there are limited amounts of data. The method as used in this investigation is by the implemented toolbox MACEC [23] for use with Matlab [24]. The abbreviation MACEC stands for Modal Analysis on Civil Engineering Constructions. In MACEC the Cov-SSI as implemented will require some user interaction such as the user has to select stable frequencies based on stabilization diagrams. This gives estimated modes, damping and mode shapes as presented.

15.5 Full-Scale Measurements of Soft Norwegian Catenaries for the Electric Railways

A railway catenary section was chosen for monitoring. The section is situated at Hovin station, numbered "wire 1". This section is part of the major railway line between Oslo and Trondheim, Dovrebanen. At this section is a catenary system called "System 35" used, which is 1411 m long. The geometry of the Hovin station section is presented in Fig. 15.4, and is here displayed without its horizontal geometry.

15.5.1 Hovin Section, Description and Instrumentation

The Hovin station section is built up by 27 spans with lengths between 40 and 60 m. Twenty-five of them are in contact with the pantograph under passage. Description of the spans and their theoretical natural frequencies for the Hovin station section is given in Table 15.1.

The horizontal geometry, from south to north, contains four curves with radii 4000, 1000, 526 and 1670 m. The allowed train speed for most of the section is 100 km/h, but it is 130 km/h in the biggest curve going south. The geometrical configuration of the sensor system at Hovin is presented in Fig. 15.5.

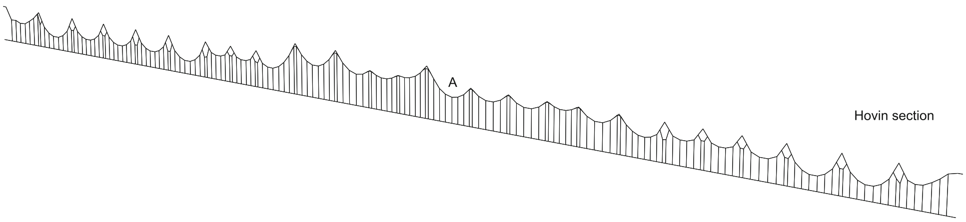

Fig. 15.4 Model of the Hovin station catenary section "wire 1"

Table 15.1 Detailed description of the spans in contact and their theoretical frequencies in Hovin section

Span length (m)	40	45	50	55	60
Number of spans	5	2	5	4	9
Length to outside dropper (m)	2	2	2	2	2
First symmetric frequency (Hz)	1.258	1.121	1.011	0.921	0.846
First non-symmetric frequency (Hz)	1.289	1.146	1.032	0.938	0.860

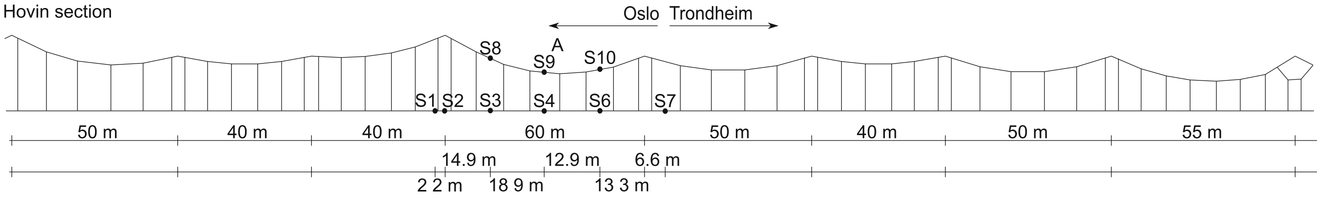

Fig. 15.5 Sensor positioning and geometry of the Hovin station catenary section

15.6 Results and Discussion

In the results are different analyses and representations shown as possible ways to process the data from the sensors and how to improve the interpretation of the data collected. The data are therefore analysed in several different manners, which includes analysis including all sensors from all passages during roughly 1 week of measuring. The sensor data are viewed both as a collective data set shown as all data in one. This is an good way to get an over view of the energy distribution over the frequencies, here assessed up to 20 Hz, where most relevant frequencies are represented. It is important to understand that this is response data from a in space stationary system excited by a secondary system (pantograph) in motion, that is both the motion in itself as well as the internal dynamic response of the secondary system will influence the result of the catenary. This means that the pre-passage data will have lower response than the post-passage data. This implies that the PSD will show low energy content for frequencies dominated by pre-passage response compare the post-passage response components. This is shown by also represent the PSD peaks by histogram, thus emphasising the number of peaks in each passage. In Fig. 15.6 this is shown by the inclusion of the PSD representation (right axis) and the peak histogram representation (left axis). Bothe are collected from all sensors and passages during the measurements.

A more detailed study of the frequency content can be achieved by employing the Cov-SSI method, here executed by using the commercial software Matlab plugin MACEC as described previously. This method is god also for dealing with closely spaced modes as well as short time series. In this investigation, the stabilization diagrams are shown for expected order up to 350. It is important to recognize that by increasing the order number the modes become stabilized and better represented. Nevertheless, overinclusion of high orders will at some point return worse results, therefore is the sensitivity of the pole estimation important to take into account when using the Cov-SSI method. Three passages are shown in Fig. 15.7 where most of the expected lower modes are captured and the mid-range closely spaced modes can be separated and investigated separately. For these catenary span analyses are the sensors positioned in S2-S6 and S9-S10 used, that is the Cov-SSI analysis is based on seven sensors, three directions rendering 21 channels.

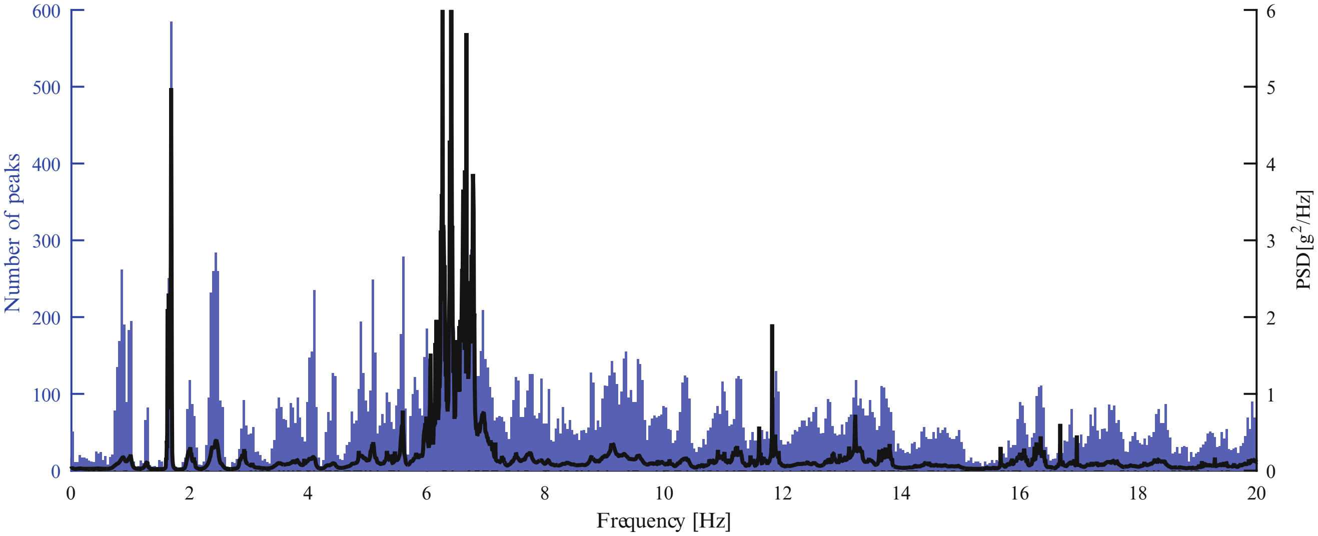

Fig. 15.6 *Left axis*: histogram representation of PSD peaks for all passages and all sensors, *right axis*: PSD of all passages and all sensors at Hovin station

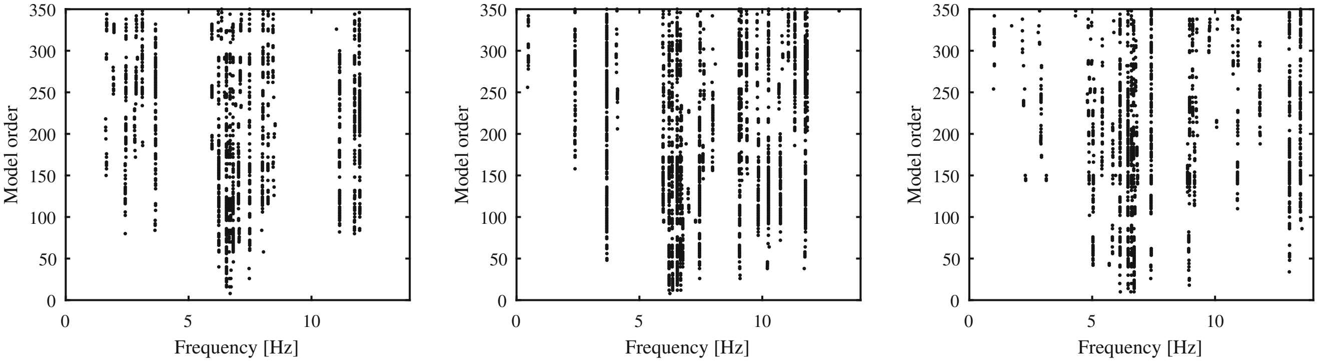

Fig. 15.7 Cov-SSI stabilization plots including all sensors at each passage, shown for three representative passages

However, it is equally important to investigate the different parts of the railway catenary as described and show in Fig. 15.1. To illustrate this also peak histogram representation for the ten highest peaks in each PSD of each passage at each representative sensor included. That is, four sensor results are from the contact wire and three sensors are from the messenger wire, all are included in Fig. 15.8. This gives a god understanding of the diversity of frequency content and the position dependency of the sensors. The wave propagation that excites the system will act differently on these two major wires and the large stiffness variation over the span of the catenary will also contribute to the dynamic response. At the same time they all include the fundamental frequencies that represent the catenary system motions such as the first and second mode of the span. It is also worth noticing that the second mode has a greater influence on the response than the first mode.

To investigate further the frequency content and position variations the three sensors S2, S4 and S9 are chosen (see Fig. 15.9). This is a representative choice of the dynamic variation over the segments in the given span. These chosen positions are at the span support and the midspan on the contact line as well as on the messenger wire at the midspan (for location of S2, S4 and S9 see also Fig. 15.5).

From Fig. 15.9 it is clear that during the short duration of the passage at the sensor will the acceleration vary considerable and reach levels of several times gravity. To identify the major frequencies and the frequency transfer zone of the passage are the corresponding spectrograms used as presented in Fig. 15.10. In this figure are both a lower order larger time window used to show main features as well as a higher order shorter time window used to show the complexity of the frequency content which is further evaluated by the PSD and the Cov-SSI analysis. Numerical models of catenary systems [6] have shown that the catenary is a slender and flexible system with many similar frequency components, including small variations. This gives similar eigenvalues from the eigenvalue analysis, which can be seen to accumulate around given frequencies.

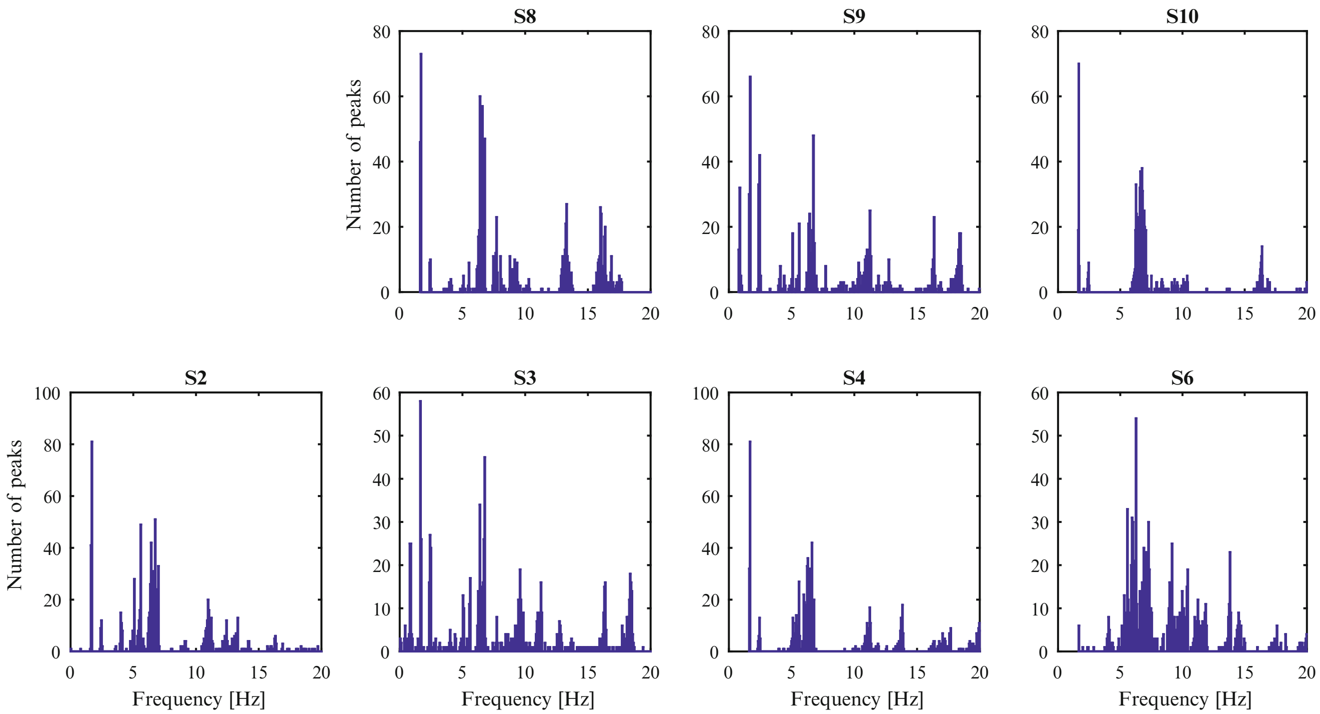

Fig. 15.8 Histogram representation of the ten highest peak at each passage for the relevant sensors (S2, S4, S5, S6, S8,S9, S10 Fig. 15.5) for all passages recorded at the Hovin station

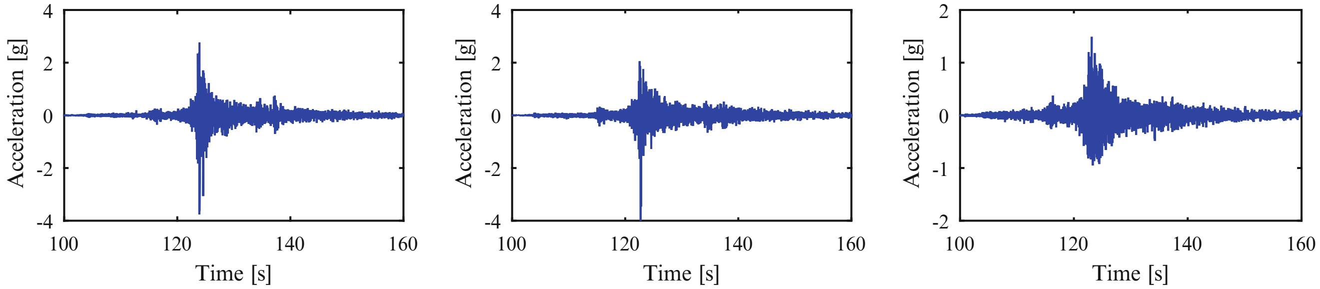

Fig. 15.9 Three representative time series form one passage given as gravity (g ≈ 9.81 m/s^2). From left to right: sensors S2, S4 and S9, Fig 15.5

With the time series of the passages (Fig. 15.9) and the results from the spectrograms (Fig. 15.10) can estimated length of the passage influence zone be determined. After the division into pre- and post-passage parts of the analysis less time-variance in remaining time series is achieved. Then, the already mentioned technics included in this investigation becomes more distinct. Here, the chosen representative pre- and post-passage PSD are presented in Fig. 15.11. These PSD's also contribute to indicate the differences in the frequency and energy distribution. For clarity in comparison are the axis are kept linear: The following diagrams in Fig. 15.11 represent the pre-passage (upper row) and the post-passage (lower row) at the Hovin station.

Finally, and for completeness are also some representative modes shapes also included. These modes shapes are estimate from the Cov-SSI analysis and their motion correspond good with expected mode shapes. Due to the geometry of the catenary system and the number of available sensors, the diagrams will not be as god to visualize as desired. The mode shapes from the catenary are complex shapes whit components in all three directions, which needs to be taken into account. However, there are some clear tendencies of sinusoidal shapes where the messenger wire is either in phase or out of phase with the contact wire. A more detailed investigation to the comparison of modes and corresponding frequencies is presented in [22] for similar railway catenary system (Fig. 15.12).

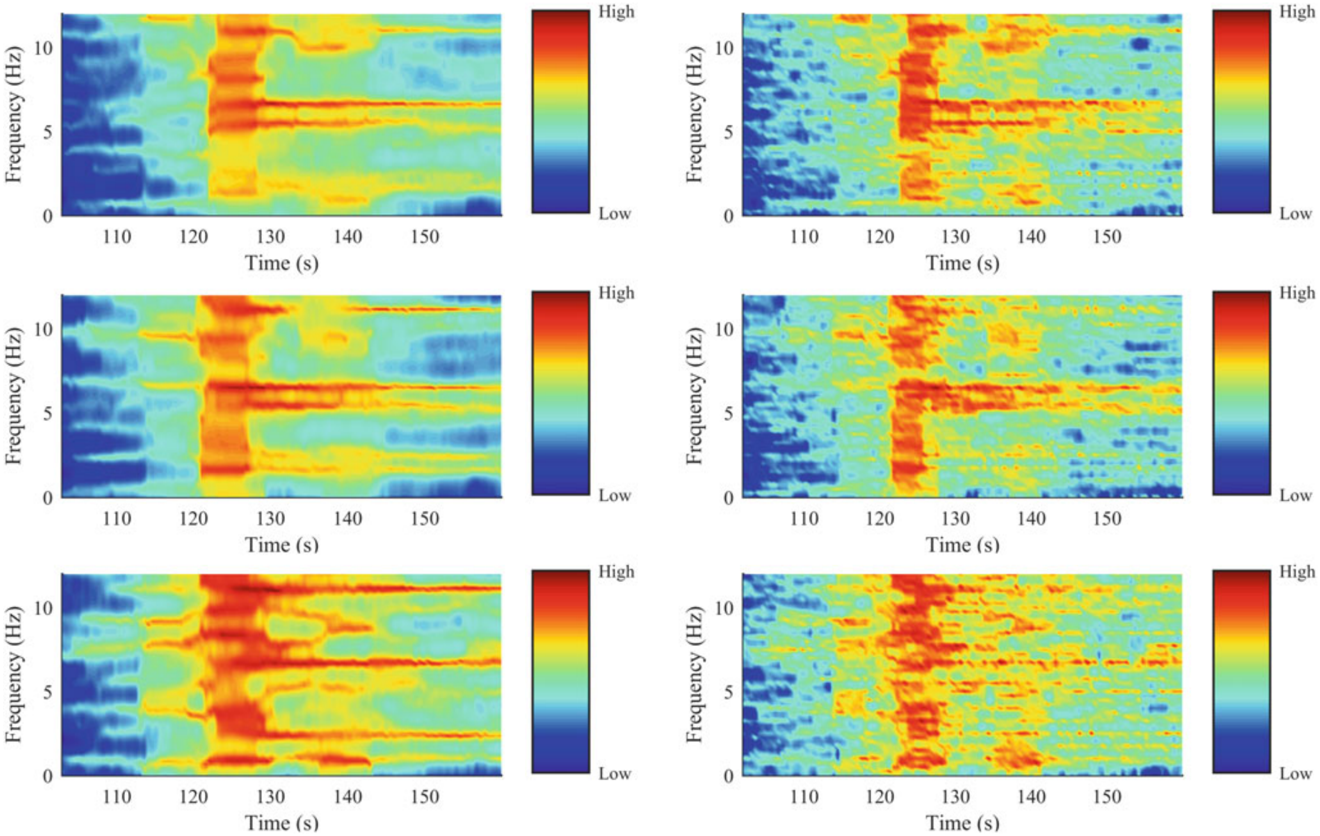

Fig. 15.10 Spectrogram representation of the frequency content through passage time series as given in Fig. 15.9; shown as lower order larger time window (*left*) and higher order shorter time window (*right*). From *top* to *bottom*: sensors S2, S4 and S9

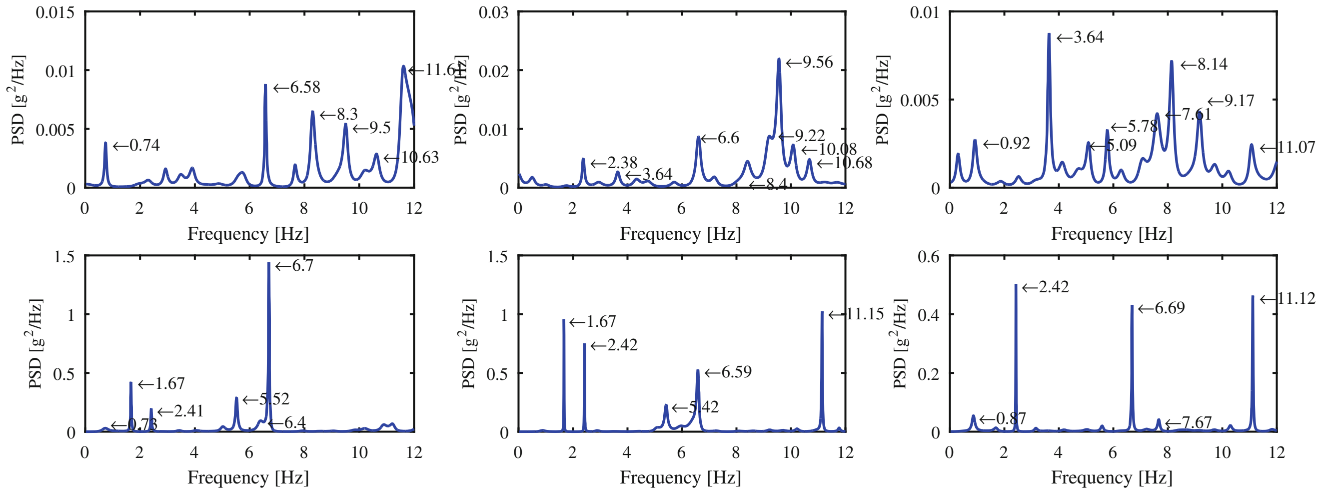

Fig. 15.11 PSD for pre-passage time series (upper three diagrams) and post-passage time series (lower three diagrams). From *left* to *right*: sensors S2, S4 and S9. Predominating frequency shifts during passage for higher and lower frequencies

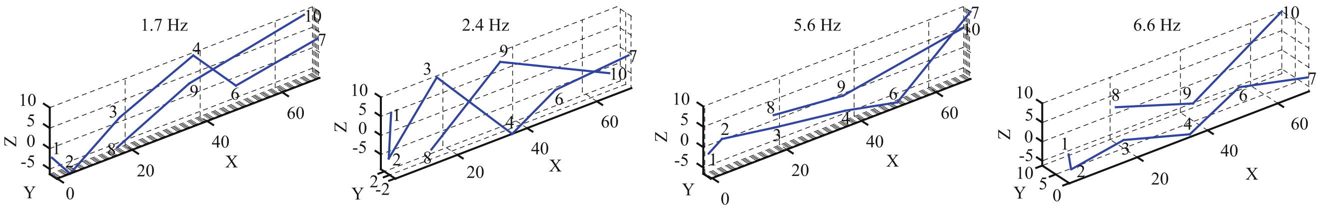

Fig. 15.12 Estimated modes shapes from the Cov-SSI analysis. From *left* to *right*, 1.7, 2,4, 5.6 and 6.6 Hz, all are dominating frequency during the passage

15.7 Conclusions

Dynamic assessment of railway catenary systems using monitoring the structural acceleration in the catenary has been suggested. Several sensors from a newly developed sensor system have been used for the recording of the measured data at the Hovin Station. The catenary system at this location is considered as a soft catenary system, which is designed for the Norwegian railways. The collected data has been used to estimate the system behaviour within one catenary span of the current location at Hovin, which includes three representative train passages. The main purpose of the investigation is to verify and further develop the new sensor system, which previously has been tested by sampling acceleration from different positions along a catenary section close to Oslo, Norway. The investigation is in its extension also intended to estimate modal parameters to verify numerical models such that they can be used to optimize each catenary.

Initially were the total passage frequency content addressed. This was done for the entire system including all sensors within the span by power spectral density estimations and peak histogram representation. Spectrograms have also been successfully included to identify important pre- and post-passage frequencies, visualising the frequency transfer of a train passage. This is also used as the basis to choose pre- and post-passage parts of the time series and to estimate separate power spectral densities. The estimation of modal parameters has been employed by the use of peak-picking from power spectral densities estimated by the Burg procedure and the stabilization diagrams constructed from several Covariance-driven Stochastic Subspace Identification analyses. The first method can be used as an initial face to locate natural frequencies, and the second used as a more thorough study for identifying both natural frequencies, corresponding damping ratios and mode shapes. Different set-up of the sensors at the different locations and different type of excitation will be investigated to improve the estimations for the future. Changing the set-up of sensors will also make it possible to identify mode shapes of parts of a railway catenary section, which in turn will help the validation of the estimated natural frequencies as physical solutions of possible problems.

Acknowledgment The Norwegian National Rail Administration is acknowledged for all their assistance on site and for funding of this project.

References

1. Ambrósio, J., Pombo, J., Pereira, M., Antunes, P., Mósca, A.: Recent developments in pantograph-catenary interaction modelling and analysis. Int. J. Railw. Technol. **1**(1), 249–278 (2012)
2. Kiessling, F.: Contact Lines for Electric Railways: Planning, Design, Implementation, Maintenance. Publicis, Munich (2009). p. 994 s.: ill., fig
3. Scott, G.A., Cook, M.: Extending the limits of pantograph/overhead performance. In: Better Journey Time - Better Business. IMechE Conference Transactions 1996-8, vol. 8, pp. 207–218 (1996)
4. Poetsch, G., Evans, J., Meisinger, R., Kortüm, W., Baldauf, W., Veitl, A., Wallaschek, J.: Pantograph/catenary dynamics and control. Veh. Syst. Dyn. **28**(2–3), 159–195 (1997)
5. Liu, Z., Jönsson, P.-A., Stichel, S., Rønnquist, A.: Implication of multiple pantograph operation on soft catenary systems in Sweden. J. Rail Rapid Transit (2014). doi:10.1177/0954409714559317. pps. 20
6. Rønnquist, A., Nåvik, P.: Dynamic assessment of existing soft catenary systems using modal analysis to explore higher train velocities: a case study of a Norwegian contact line system. J. Veh. Syst. Dyn. 756–774 (2015). doi:10.1080/00423114.2015.1013040
7. Drugge, L.: Modelling and simulation of pantograph-catenary dynamics. Luleå tekniska universitet (2000)
8. Rainieri, C., Fabbrocino, G.: Operational Modal Analysis of Civil Engineering Structures. Springer, New York (2014)
9. Burg, J.P.: Maximum entropy spectral analysis. Ph.D. thesis, Stanford University, Stanford (1975)
10. Simeon, B., Arnold, M.: Coupling DAEs and PDEs for simulating the interaction of pantograph and catenary. Math. Comput. Model. Dyn. Syst. **6**(2), 129–144 (2000)

11. Rønnquist, A., Nåvik, P.: Dynamic implications for higher speed in sharp curves of an existing Norwegian overhead contact line system for electric railways. In: The IX International Conference on Structural Dynamics, June, Porto (2014)
12. The Norwegian National Rail Administration: Mekanisk systembeskrivelse av kontaktledningsanlegg. http://www.jernbanekompetanse.no/wiki/Mekanisk_systembeskrivelse_av_kontaktledningsanlegg#Ledningsf.C3.B8ring (2015)
13. The Norwegian National Rail Administration: JD540 Teknisk regelverk, Kontaktledning/Prosjektering [Online]. https://trv.jbv.no/pdf/kontaktledning/542/vedlegg/t4205h00.pdf (2015)
14. The Norwegian National Rail Administration: Mekanisk systembeskrivelse av kontaktledningsanlegg [Online]. http://www.jernbanekompetanse.no/wiki/Mekanisk_systembeskrivelse_av_kontaktledningsanlegg#Ledningsf.C3.B8ring (2015)
15. Nåvik, P., Rønnquist, A., Stichel, S.: The use of dynamic response to evaluate and improve the optimization of existing soft railway catenary systems for higher speeds. J. Rail Rapid Transit (2015). doi:10.1177/0954409715605140. pps. 10
16. Nyquist, H.: Certain topics in telegraph transmission theory. Trans. Am. Inst. Electr. Eng. **47**(2), 617–644 (1928)
17. European Optimised Pantograph Catenary Interface (EUROPAC). Publishable Final Activity Report, International Union of Railways, Coordinator Louis-Marie Cléon, 30 March 2008
18. Jung, L.: System Identification, Theory for the User, 2nd edn. Prentice Hall, Upper Saddle River (2009)
19. Rabiner, L., Allen, J.B.: On the implementation of a short-time spectral analysis method for system identification. IEEE Trans. Acoust. Speech. Signal Process. **28**, 69–78 (1980)
20. Jacobsen, E., Lyons, R.: The sliding DFT. IEEE Signal Process. Mag. **20**, 74–80 (2003)
21. Van Overschee, P., De Moor, B.L.: Subspace Identification for Linear Systems: Theory—Implementation—Applications. Kluwer, Dordrecht (1996)
22. Nåvik, P., Rønnquist, A.: Uplift-monitoring for dynamic assessment of electric railway contact lines. In: Proceedings of IMAC XXXIII Conference and Exposition on Structural Dynamics (SEM), Orlando, 2–5 February (2015)
23. Peeters, B., Van Den Branden, B., Laquiere, A., De Roeck, G.: Output-only modal analysis: development of a GUI for Matlab. In: Proceedings of IMAC 17, Kissimmee. http://bwk.kuleuven.be/bwm/macec (1999)
24. MATLAB R2015a. The MathWorks Inc., Natick (2015)

Chapter 16
Functional Series TARMA Models for Non-stationary Tool Vibration Signals Representation and Wear Estimation

Behrang Hosseini Aghdam and Ender Cigeroglu

Abstract This article addresses the problem of tool wear estimation using vibration signals. Time dependent time series models are suitable for extraction of time varying dynamics embedded in the non-stationary signals. A version of non-stationary time series known as Functional Series Time dependent AutoRegressive Moving Average (FS-TARMA) is employed for estimation of tool vibration signals and identification of the dynamics of tool/holder system. The obtained models associated with different levels of tool wear are compared by using characteristic quantities calculated based on model parameters. In this method, called model parameter-based method wear is estimated using a feature that is a function of model parameter vector obtained from FS-TARMA models. The advantage of this method over the ARMA metric employed in a previous study is that it does not violate the non-stationarity assumption of signals. The results of this study demonstrate that the FS-TARMA models with model parameter-based method provides higher accuracy in wear estimation compared with ARMA counterpart and also FS-TARMA with ARMA metric.

Keywords Tool wear • FS-TARMA • Non-stationary • Vibration • Turning

16.1 Introduction

The cutting tool wear is one of the well-known causes of low surface quality in manufacturing. Flank wear leads to the loss of cutting edge which affects dimension in addition to surface finish quality. Online monitoring of tool wear together with estimating it can be effective in the prevention of unscheduled downtime and workpiece damage.

Tool condition monitoring (TCM) plays an important role in automation of production in advanced manufacturing technology. Methods used in TCM are either of direct types that measure tool wear directly or indirect types that estimate wear by using secondary effects such as surface quality degradation and Acoustic Emission (AE) signals. Indirect methods can be used on-line without interruption of machining process [1]. TCM has been an attractive subject of study for a number of researchers and numerous studies have been undertaken during the last two decades.

On-line tool wear estimation has important applications, such as determination of tool change policy, adaptive control, economic optimization and full automation of machining operations [2]. Employed signals are of different types; however, cutting forces, AE signals and acceleration signals are the most commonly used ones. By a review on AE-based sensing technology, Li [3] concluded that AE signals have high response rate. Nevertheless, these signals are highly dependent to cutting parameters.

Recorded signals during wear tests can be processed to reduce the high number of sample to much smaller quantities called wear sensitive features that are used to model the wear-signal correlation. These features can be extracted in time or frequency [4, 5] domain. Jemielniak et al. [6] investigated some statistical features of AE signals and reported that as a time domain feature of the signals, kurtosis was effective for wear estimation in turning.

Energy contribution of each vibration mode in total energy of the signal was introduced as a wear sensitive feature in [7] and later successfully used for the wear estimation in turning [8].

In review papers [9, 10] the effect of proper selection of wear sensitive features is discussed and it is noted that the main disadvantage with the features is their dependence on cutting conditions. Nonlinear methods have also been used by Orbay and Hayhurst [11] to obtain a relationship between cutting force and tool wear in a machining process. However, the final model could not be used in online wear estimation.

B.H. Aghdam • E. Cigeroglu (✉)
Mechanical Engineering Department, Middle East Technical University, 06800 Ankara, Turkey
e-mail: ender@metu.edu.tr

A. Wicks, C. Niezrecki (eds.), *Structural Health Monitoring, Damage Detection & Mechatronics, Volume 7*,
Conference Proceedings of the Society for Experimental Mechanics Series, DOI 10.1007/978-3-319-29956-3_16

Commercially available TCM systems are required to work in different cutting conditions and independent from a priori information or cutting data [12]. In order to fulfil the first requirement, researchers have introduced wear sensitive features that are independent from cutting conditions.

Observer-based models are of parametric methods that consider wear as output and cutting conditions as well as acquired signals as inputs have been used in some studies [13–15]. Features in frequency domain have always been attractive to authors. Alonso and Salgado [16] employed Singular Spectrum Analysis (SSA) and obtained statistical features in frequency domain that were correlated to tool wear. Nonetheless, these features are time-dependent. Kilundu et al. [17] also used SSA and found it useful in separation of different wear phases. Aghdam et al. [18] employed dispersion ratio of tool/holder set bending modes as wear sensitive features and obtained a relationship between major flank wear and the features. The most important property of proposed features is their independence from cutting conditions.

ANNs and its variants are the most commonly used methods in the tool wear estimation. Wang et al. [19] trained a fully forward neural network by modified Kalman filter to estimate tool wear in hard turning. Sensor fusion and the use of multiple sensors can increase the reliability and accuracy of wear estimation models. Aliustaoglu et al. [20] fused the data from force, sound and vibration sensors and reported more efficient results in comparison to the cases where one signal is used. To achieve higher accuracies in wear estimation, authors made progress on learning algorithms of ANNs. Purushothaman [21] employed extended Kalman filter and some other authors [22–25] used extensions of ANNs to achieve higher performance in wear estimation, although in some cases it could not guarantee the enhancement of estimations.

A more recent review paper [26] discusses the effect of choosing time or time-frequency domain features, however states that their independence from cutting conditions is still a remaining challenge.

Considering the review papers [9, 10, 26] and the literature review done based on the published papers it can be said that most of the methods used for wear estimation are based on ANNs. Moreover, it can be concluded that researchers mostly used variants of ANNs for tool wear estimation. These methods have disadvantages such as requiring high number of training samples.

Time series methods are of highly used methods for identification of dynamic systems and fault estimation. Using these methods, dynamic properties of a vibration system such as natural frequencies and modal damping values can be obtained. In addition, there are specific methods for comparing time series models and fault estimation [27]. Time series methods can be classified into stationary and non-stationary methods. Non-stationary signals can be the output response of time invariant (TI) systems which are under non-stationary excitation or the response of time varying (TV) systems [28]. Tool/holder of a turning machine can be considered as a TI system which, due to non-stationary input cutting forces, generate non-stationary vibration response. In case, where the input to the system is not measurable or observable, time series methods that only utilize the output must be used. Output-only Functional Series Time dependent AutoRegressive Moving Average (FS-TARMA) method has notable capabilities in estimation of TV dynamics and non-stationary signal estimation. In this method, assuming that the system dynamics (model parameters) vary in a deterministic way, the model parameters are estimated using a set of deterministic orthogonal basis functions that can be chosen from different families [28]. Aghdam et al. [29] employed FS-TARMA model along with ARMA metric [30] for tool wear estimation. However, ARMA metric has been used with approximations which violates the stationarity conditions of the model and thus the results may not be accurate enough. In this paper FS-TARMA method is used for prediction of tool vibration signals and instead of ARMA metric, model parameter-based method [27] employed for comparing the obtained models and wear estimation. Moreover, discrete Prolate function are considered as basis functions in the estimation of parameters which, by embedding in FS-TARMA models, provide higher accuracy compared with other orthogonal functions and stationary counterpart, i.e. ARMA models.

16.2 Functional Series TARMA Models and Their Estimation

In this section, Functional Series TARMA models are introduced for modelling tool acceleration signals which are of nonstationary type. Estimation procedure of the models is presented in the next subsection.

16.2.1 FS-TARMA Models

The response of a single-input single-output of a TV system, assuming that the input is not observable or measureable must be estimated using output only models. Once the response of the system is known, it can be modelled by FS-TARMA models that merely use the output response. An FS-TARMA $(n_a, n_c)_{[p_a, p_c, p_s]}$ model can be expressed in the following form [28]:

$$x[t] + \sum_{i=1}^{n_a} a_i[t]x[t-i] = w[t] + \sum_{i=1}^{n_c} c_i[t]w[t-i], \quad \mathrm{w[t]} \sim \mathrm{NID}\left(0, \sigma_w^2[t]\right), \quad t = 1, \ldots, N, \tag{16.1}$$

where n_a and n_c indicate AR and MA orders respectively, p_a and p_c are their corresponding functional basis dimensionalities, and p_s is dimensionality of the respective innovations variance also $x[t]$ designates the estimated non-stationary response, $w[t]$ an innovations sequence with zero mean and time-dependent variance $\sigma_w^2[t]$. Assuming that the system input is unobservable, it can be considered as a zero mean innovations (uncorrelated) sequence $w[t]$ $(f[t] \equiv w[t])$ with time-dependent variance $\sigma_w^2[t]$. $a_i[t]$ and $c_i[t]$ represent AR and MA time-dependent parameters respectively, that as well as the innovations variance $\sigma_w^2[t]$ can be estimated by the related functional subspaces represented in Eq. (16.2):

$$\begin{aligned} &\mathcal{F}_{AR} \triangleq \left\{G_{b_a(1)}[t], G_{b_a(2)}[t], \ldots, G_{b_a(p_a)}[t]\right\}, \\ &\mathcal{F}_{MA} \triangleq \left\{G_{b_c(1)}[t], G_{b_c(2)}[t], \ldots, G_{b_c(p_c)}[t]\right\}, \\ &\mathcal{F}_{\sigma_w^2} \triangleq \left\{G_{b_s(1)}[t], G_{b_s(2)}[t], \ldots, G_{b_s(p_s)}[t]\right\}. \end{aligned} \tag{16.2}$$

In the above expressions "$\mathcal{F}$" designates functional subspace of the indicated quantity and $\left\{G_j[t] : j = 0, 1, \ldots\right\}$ is a set of orthogonal basis functions which are selected from a suitable family. The indices $b_a(i)(i = 1, \ldots, p_a)$, $b_c(i)(i = 1, \ldots, p_c)$ and $b_s(i)(i = 1, \ldots, p_s)$ designate the specific basis functions of a particular family that are included in each subspace.

For an FS-TARMA model, the time-dependent AR and MA parameters and innovations variance, can be expressed based on the basis functions as follows [28]:

$$a_i[t] \triangleq \sum_{j=1}^{p_a} a_{i,j} G_{b_a(j)}[t], \quad c_i[t] \triangleq \sum_{j=1}^{p_a} c_{i,j} G_{b_c(j)}[t], \quad \sigma_w^2[t] \triangleq \sum_{j=1}^{p_a} s_j G_{b_s(j)}[t], \tag{16.3}$$

where $a_{i,j}$, $c_{i,j}$ and s_j represent the AR, MA and innovations variance coefficients of projection, respectively. By the definitions of Eq. (16.3), the model parameters consist of projection coefficients $a_{i,j}$, $c_{i,j}$ and s_j, while a specific model structure, like $\mathcal{M}$ is defined by model orders n_a, n_c and the functional subspaces $\mathcal{F}_{AR}, \mathcal{F}_{MA}, \mathcal{F}_{\sigma_w^2}$ as:

$$\mathcal{M} \triangleq \left\{n_a, n_c, \mathcal{F}_{AR}, \mathcal{F}_{MA}, \mathcal{F}_{\sigma_w^2}\right\} \tag{16.4}$$

The complete identification problem can be expressed as follows [28]: "using N vibration response measurements, $x^N = \{x[1] \ldots x[N]\}$, and the FS-TARMA model

$$\mathcal{M} \triangleq \left\{ M(\theta) : x[t] + \sum_{i=1}^{n_a} a_i[t, \theta]x[t-i] = e[t, \theta] + \sum_{i=1}^{n_c} c_i[t, \theta]e[t-i];\ \sigma_w^2 = \mathrm{E}\left\{e^2[t, \theta]\right\},\ t = 1, \ldots, N,\ \theta \in \Re^{\dim(\theta)} \right\}, \tag{16.5}$$

determine an element of $\mathcal{M}$ which best fits the data". In this expression, $\dim(\theta)$ represents the dimension of the parameter vector θ which consists of the projection coefficients $a_{i,j}$, $c_{i,j}$ and s_j, while $e[t, \theta]$ designates the one-step-ahead prediction error (residual) sequence of the model that coincides with the innovations sequence, $w[t]$, of the model.

The complete identification problem is divided into two subproblems: parameter estimation problem (for a given structure $\mathcal{M}$) and model structure selection problem.

16.2.2 FS-TARMA Parameter Estimation

The estimation of the projection coefficient vector θ, which consists of AR, MA and innovations variance projection coefficients is considered in this subsection. This estimation is realized by employing nonstationary vibration response for a given structure [34] as:

$$\begin{aligned}
&\theta \triangleq \left[\vartheta^T \middle| s^T\right]_{(n_a p_a + n_c p_c + p_s)\times 1},\ \vartheta \triangleq \left[a^T \middle| c^T\right]_{(n_a p_a + n_c p_c)\times 1},\ s \triangleq \left[s_1, \ldots, s_{p_s}\right]_{p_s \times 1},\\
&a \triangleq \left[a_{1,1}, \ldots, a_{1,p_a} \middle| \ldots \middle| a_{n_a,1}, \ldots, a_{n_a,p_a}\right]^T_{(n_a p_a)\times 1},\\
&c \triangleq \left[c_{1,1}, \ldots, c_{1,p_c} \middle| \ldots \middle| c_{n_c,1}, \ldots, c_{n_c,p_c}\right]^T_{(n_c p_c)\times 1}.
\end{aligned} \tag{16.6}$$

The AR/MA projection coefficients vector ϑ, is estimated by employing Ordinary Least Squares (OLS) method which sums up the squares of the one step ahead prediction errors of the model [28]:

$$\hat{\vartheta} = \arg\min_{\vartheta} \sum_{t=1}^{N} e^2[t, \vartheta], \tag{16.7}$$

where arg min designates "argument minimizing" meaning that the arguments are sought that minimize the criterion and $e[t,\ \vartheta]$ represents the one-step-ahead prediction error of the model.

As in the case of stationary counterpart, the estimation of ϑ for FS-TARMA is a non-linear problem. It can either be solved through non-linear optimization methods or by iterative linear methods. The Two Stage Least Squares (2SLS) method [28] is one of the linear methods that is based on an infinite order FS-TAR representation of the original FS-TARMA model. In this study, 2SLS method is employed for parameter estimation.

16.2.3 Fault Detection and Identification by Model Parameter-Based Method

In model parameter-based method, fault detection and identification is attempted using the changes in parameter vector of the models associated with different fault types and levels [27].

Let $\hat{\theta}$ represent the estimator of the parameter vector θ based on the response samples z_1^N. For sufficiently long signals, the estimated parameters, $\hat{\theta}$, have Gaussian distribution with a mean that equals its true value θ and covariance P_θ ([31], pp. 205–207)

$$\hat{\theta} \sim N(\theta, P_\theta) \tag{16.8}$$

16.2.3.1 Fault Detection

Fault is detected by testing for statistically significant changes in the parameter vector θ associated with the nominal (baseline) and current structures through the hypothesis testing problem as

$$\begin{aligned}
&H_0 : \delta\theta = \theta_o - \theta_u = 0 \quad \text{(null hypothesis - healthy structure)},\\
&H_1 : \delta\theta = \theta_o - \theta_u \neq 0 \quad \text{(alternative hypothesis - faulty structure)}.
\end{aligned} \tag{16.9}$$

It is observed that the difference of the estimated parameters associated with the nominal and current states of the structure has a Gaussian distribution

$$\delta\hat{\theta} \triangleq \hat{\theta}_o - \hat{\theta}_u \sim N(\delta\theta, \delta P), \quad \delta\theta = \theta_o - \theta_u \quad \delta P = P_o + P_u, \tag{16.10}$$

where P_o and P_u designate the estimated covariance matrices for the nominal and current structures, respectively.

In the case of the null hypothesis, $\delta\theta = \theta_o - \theta_u \sim N(0, 2P_o)$ the characteristic quantity Q defined in Eq. (16.11), Follows chi-square distribution with d degrees of freedom ([32], p. 558)

$$Q \triangleq \delta\hat{\theta}^{T}.\delta P^{-1}.\delta\hat{\theta} \sim \chi^2(d), \tag{16.11}$$

where $\delta P = 2P_o$. The covariance P_o associated with the healthy structure is not available, therefore, its estimated value $\hat{P}_o$ is used in practice. Taking the sample covariance $\hat{P}_o$ as a deterministic quantity which is realized for large number of samples, the following test at the α (Type I) risk level is constructed as [27]:

$$\begin{array}{lll} Q <\sim \chi^2_{1-\alpha}(d) & \Rightarrow & H_0 \text{ is accepted (healthy strucuture)} \\ \text{Else} & \Rightarrow & H_1 \text{ is accepted (faulty structure)} \end{array} \tag{16.12}$$

where $\chi^2_{1-\alpha}(d)$ designates the critical point $1-\alpha$ of chi-square distribution with d degrees of freedom.

16.2.3.2 Fault Identification and Estimation

Since there is only one type of fault, i.e. major flank wear, fault estimation is achieved using the characteristic magnitude Q which is computed for current value of the parameters mutually with the nominal case. The Q value itself is used as a measure of distance and also the fault magnitude.

16.3 Major Flank Wear Estimation

For the estimation of tool wear, cutting experiments are carried out and the acceleration signals corresponding with different wear levels are recorded employing miniature accelerometers enabling the measurement of tool acceleration in 3 dimensions. The procedure of wear tests is described in [18]. The experimental test setup and the cutting conditions are presented in Fig. 16.1 and Table 16.1 respectively. In order to have an insight into the cutting directions and the forces which are applied to the tool, the schematic figure of the tool/holder system is represented in Fig. 16.2.

In the experimental tests, acceleration signals are recorded for each set of cutting conditions. After each data recording, machine is stopped and the tool major flank wear VB is measured using an optical microscope with camera attachment, a stereo microscope and a digital camera equipped with a precise lens that provides the ability of high zoom rates. A sample

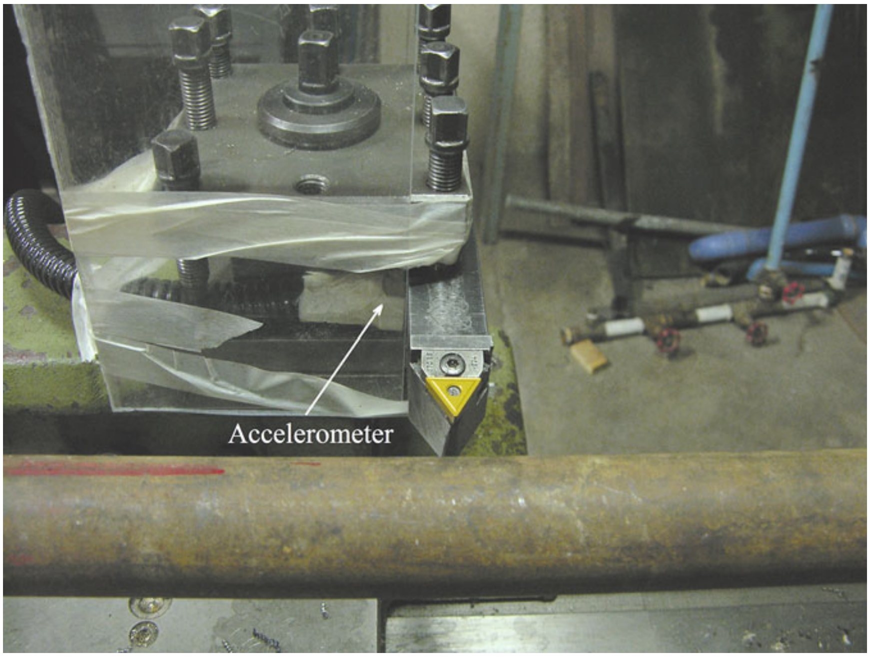

Fig. 16.1 Test setup used in the experiments

Table 16.1 Cutting conditions and machine tool specifications

Machine tool	Universal Lathe *TN*50
Tool insert type	TNMG (SANDVIK)
Work material	AISI 1045
Workpiece size	Length = 600 mm, Diameter = 50 mm
Cutting conditions	1. $n = 500$ rpm, $f = 0.2$ mm/rev, $d = 0.5$ mm
	2. $n = 710$ rpm, $f = 0.1$ mm/rev, $d = 0.5$ mm
	3. $n = 1000$ rpm, $f = 0.2$ mm/rev, $d = 0.5$ mm
	4. $n = 1000$ rpm, $f = 0.2$ mm/rev, $d = 0.1$ mm
	5. $n = 1000$ rpm, $f = 0.1$ mm/rev, $d = 0.1$ mm
Cutting fluid	No

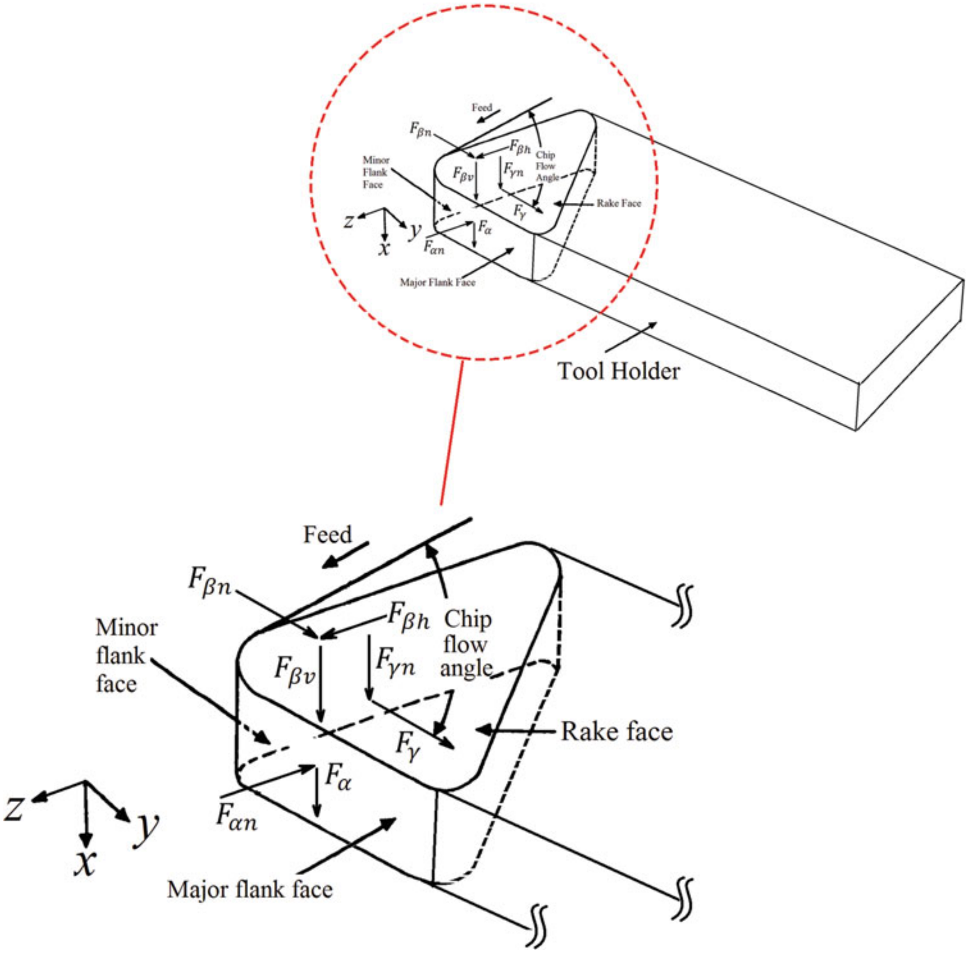

Fig. 16.2 Cutting directions and forces shown on tool/holder system [29]

photo of the worn tools is shown in the Fig. 16.3, which is taken by an optical microscope and measured major flank wear *VB* is shown on it.

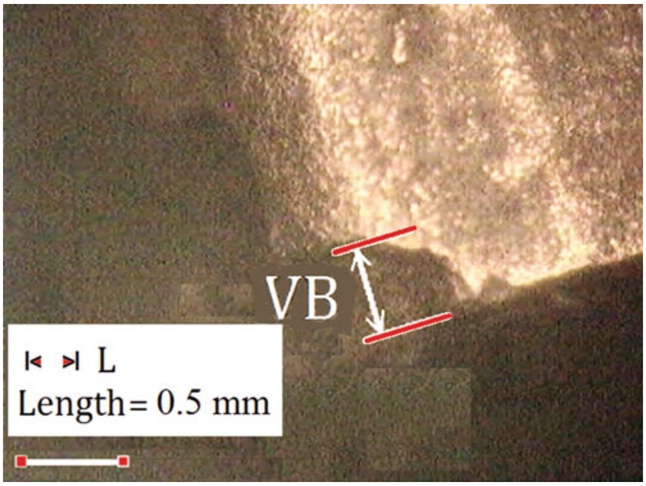

Fig. 16.3 Tool major flank wear photo taken by an optical microscope

16.3.1 Estimation of FS-TARMA Models

The FS-TARMA models are estimated for signals obtained at different wear levels. Basis functions are chosen from Discrete Prolate family of orthogonal functions. These functions which are used as window functions in time domain, have the property of carrying maximum energy in a specific frequency band [33]. The effect of different basis functions on frequency estimation accuracy in Time Varying Autoregressive (TVAR) models has been investigated in [34]. The estimation of parameters is done via 2SLS method and a subsequent nonlinear refinement is applied to achieve convergent solutions. Since the models are compared using the model parameter-based method with models of the same order, the orders and the structure are chosen based on the maximum orders obtained for the estimated models. Although the order might be higher than that is obtained for an adequate model, the order difference does not vary much between the models associated with different wear levels. The orders that are used in the models are as follows: $n_i = 52,\ p_i = 20,\ \ p_a = p_c = 14,\ n_a = n_c = 50$.

The accuracy of the models is evaluated using the ratio of the Residual Sum of Squares to the Series Sum of Squares (RSS/SSS). This value is equal to 8 % for the estimated models which is much better than those obtained for ARMA counterpart [18].

A sample of the recorded non-stationary acceleration signals is presented in Fig. 16.4. FS-TARMA model based one-step-ahead predictions for a segment of the non-stationary tool acceleration signal is presented in Fig. 16.5. The corresponding residual series along with the estimated residual variance (estimation window length 257 samples) are plotted in Figs. 16.6 and 16.7 respectively.

16.3.2 Wear Estimation via Model Parameter-Based Method

The obtained FS-TARMA models of the signals associated with different wear levels are compared with model parameter-based method. Through the comparison, a correlation between wear and the characteristic quantity defined based on the parameters can be obtained. Here, since only one type of wear is considered, the characteristic quantity defined in the Eq. (16.10), is used as a measure of the wear itself. For every set of cutting conditions, model parameters in baseline and different levels of wear are estimated. Then, the characteristic quantity Q is calculated. The plots of the obtained quantities versus wear are presented in Fig. 16.8. Since all cutting conditions provide approximately the same results, taking the 4th set (according to Table 16.1) the analysis is carried out.

In the Fig. 16.8, the characteristic quantity in x direction (squares), Q_x versus tool wear, which can be considered as a distance measure between the models associated with different wear levels and the baseline model, is given. The resulting curve has a minimum in the vicinity of wear $VB = 300$ µm. In the same interval of wear, the curve in z direction (crosses) simultaneously reaches to a maximum. The occurrence of an extremum in both curves, provides a criterion for the detection of critical wear point where the tool enters accelerating stage of wear and thus needs to be replaced with a new one. Wear values in the vicinity of $VB = 300$ µm is considered to be the critical wear in machining processes. Assuming the characteristic quantity as distance between the models, and occurrence of extremums in different directions brings the

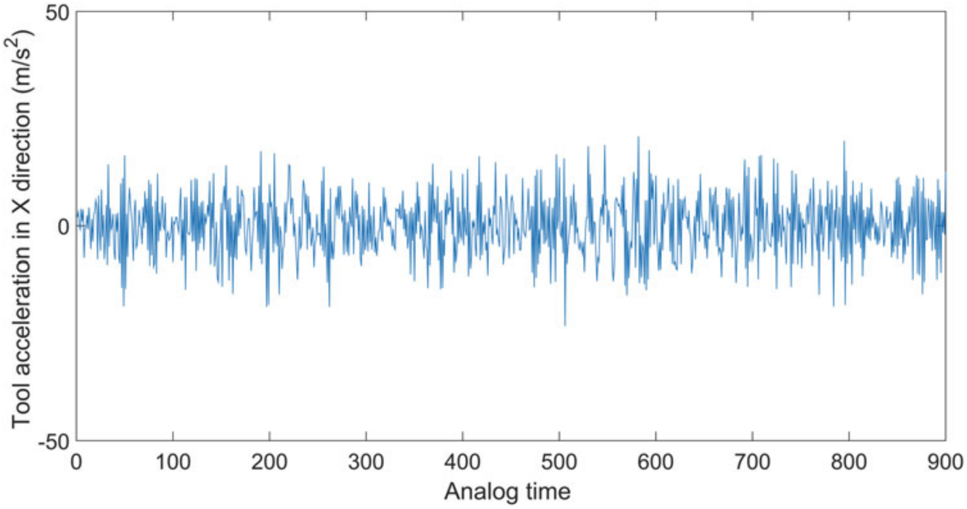

Fig. 16.4 Non-stationary acceleration response signal of the tool in *x* direction

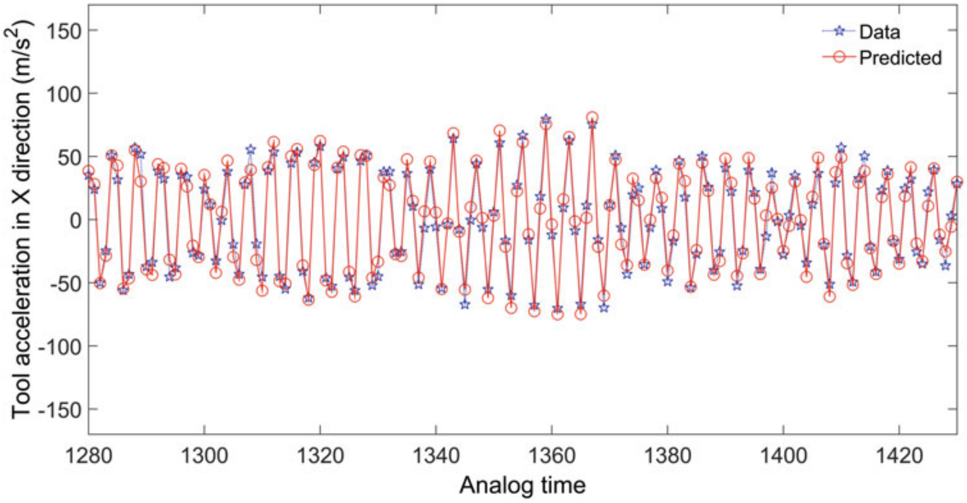

Fig. 16.5 A Segment of the non-stationary acceleration signal in *x* direction and one-step-ahead predictions based on the FS-TARMA $(50, 50)_{[14,14,10]}$

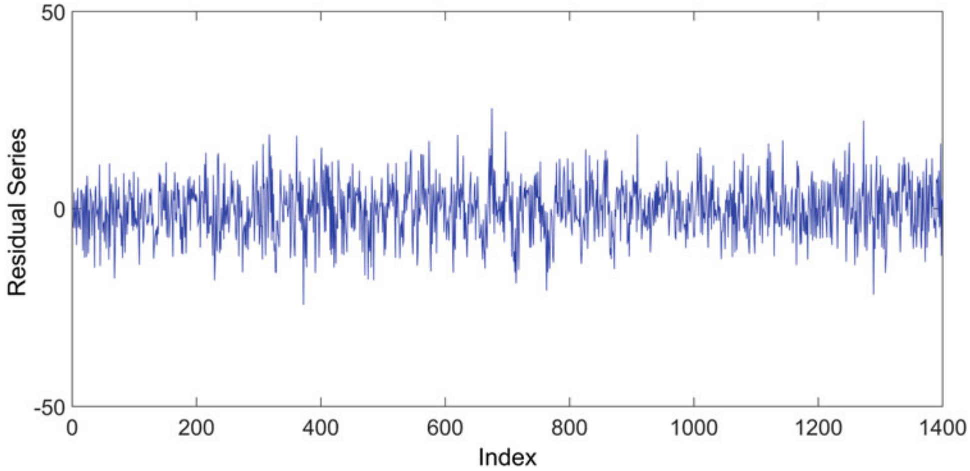

Fig. 16.6 The FS-TARMA$(50, 50)_{[14,14,10]}$ residual sequence for the modeled signal in *x* direction

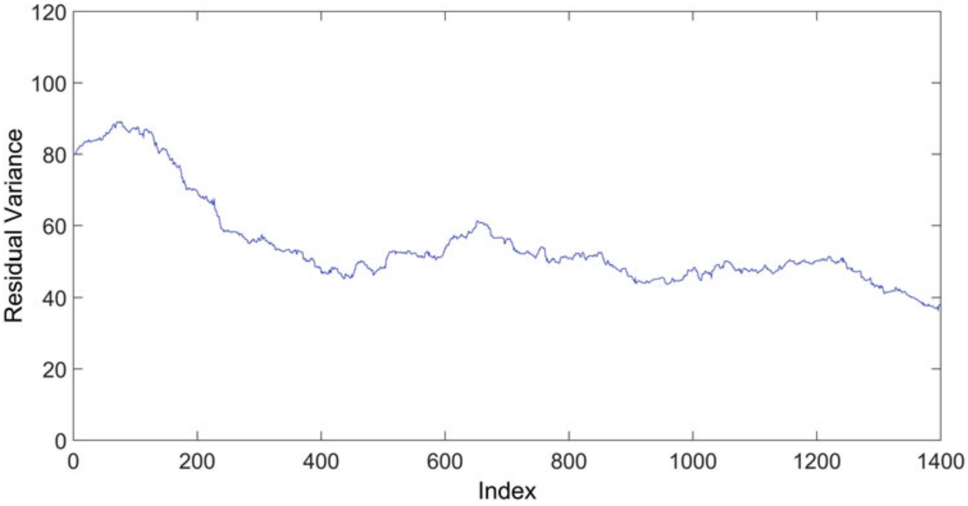

Fig. 16.7 The FS-TARMA(50, 50)$_{[14,14,10]}$ estimated residual variance

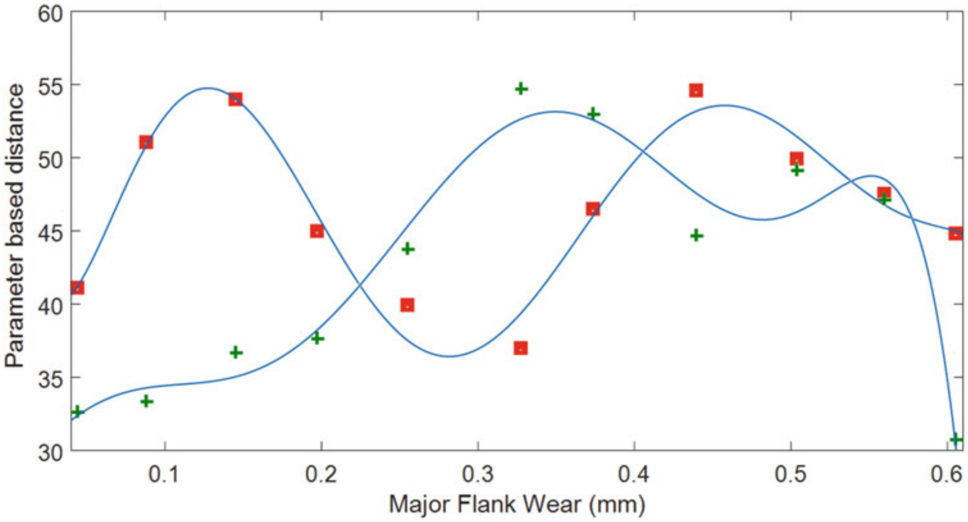

Fig. 16.8 The plot of characteristic quantity in x (*squares*) and z (*crosses*) directions, versus major flank wear

idea of occurrence of a change in dynamics of the corresponding system, i.e. tool/holder set. If the wear interval $VB = (150, 450)$ μm is considered to investigate the changes in the curve, two curves are found that vary in opposite directions. The curve in x direction has a minimum and the one in z direction has a maximum. For the curve in x direction (Fig. 16.8), arriving at a minimum means that the system behaves more or less like the baseline system at this point and after that a change in system dynamics causes an increase in the distance. Occurrence of a maximum in z direction (Fig. 16.8, crosses), which takes place with a delay with respect to the minimum observed in x direction means that the tool/holder system dynamically behaves differently compared with the baseline system in this direction. A change in vibrational behavior of the tool/holder system has been revealed in a study by Aghdam et al. [18], where it was shown that the vibration mode of the tool/holder system changes after passing the critical wear stage. Application of ARMA metric on FS-TARMA models are investigated in another study by Aghdam et al. [29]. The results of that study are presented in Figs. 16.9 and 16.10. Comparing the results obtained in [29] with those of the current study (Figs. 16.8 and 16.10, respectively), it is understood that the curves obtained in this study are smoother and the peaks are detected with higher accuracy.

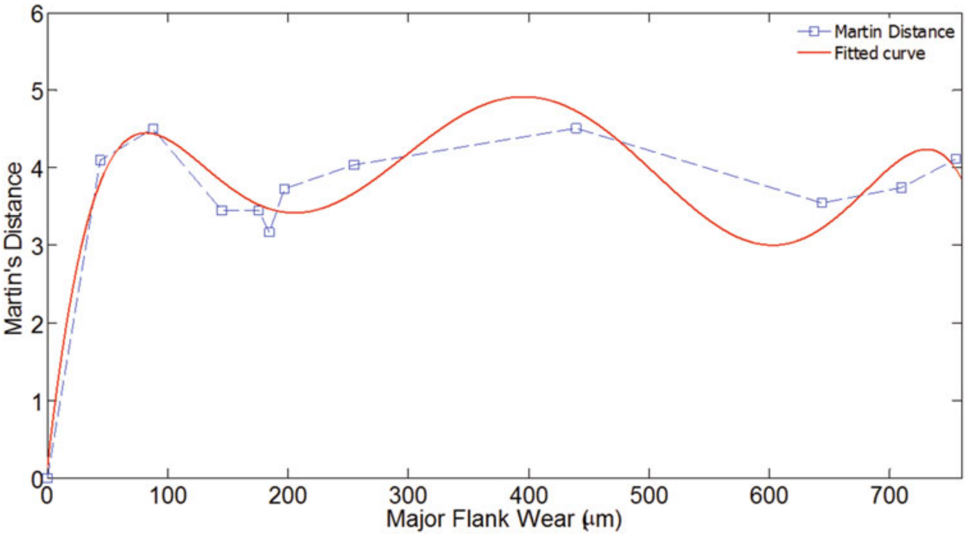

Fig. 16.9 Martin distance of worn tools from sharp one in *x* direction by FS-TARMA [29]

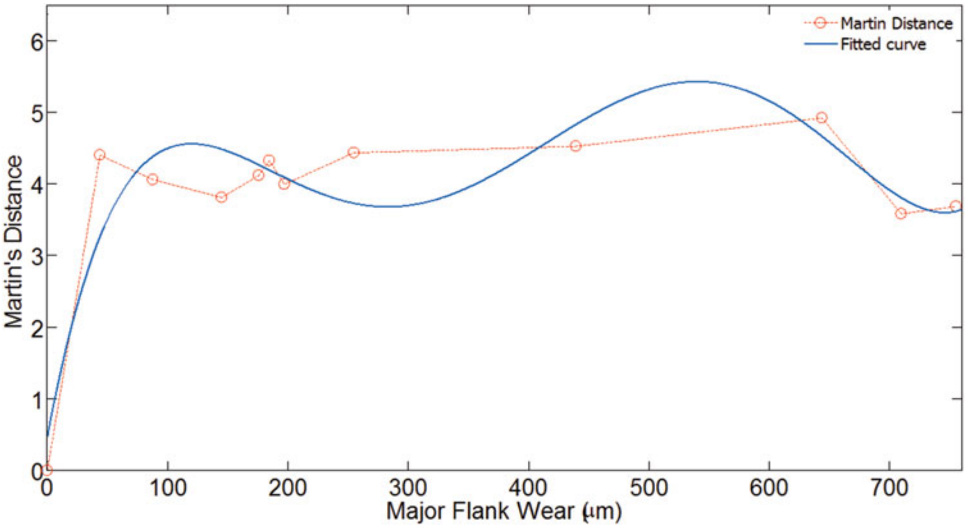

Fig. 16.10 Martin distance of worn tools from sharp one in *z* direction, FS-TARMA [29]

16.4 Conclusion

The problem of modelling tool non-stationary signals recorded during tool wear tests via FS-TARMA models and estimation of tool wear are considered in this paper. The first part of the paper which deals with the modelling reveals the good accuracy obtained in the prediction of the non-stationary response (Residual Sum of Squares to Series Sum of Squares ratio RSS/SSS = 8 %), where discrete Prolate type of basis functions are used. The comparison of the models aiming to find a correlation between wear and the signals (models) is the subject of the second part of the paper. It is shown that the application of the model-parameter based method for comparing the models provides reliable results which is also in accordance with the results obtained in the literature. The advantage of the model-parameter based method over the ARMA metric is that it does not need to satisfy the stationarity condition which is a prerequisite of the ARMA metric. The extremum points revealed in wear model curves can be used for detection of tool change time and this criterion can be included in online tool wear estimation algorithms.

Acknowledgement Authors would like to gratefully acknowledge the support provided by the TUBITAK (The Scientific and Technological Research Council of Turkey), Grant no: 2216 – Research Scholarship Program for International Researchers.

References

1. Martin, K.F.: A review by discussion of condition monitoring and fault diagnosis in machine tools. Int. J. Mach. Tool Manuf. **34**(4), 527–551 (1994)
2. Ghasempoor, A., Moore, T.N., Jeswiet, J.: On-line wear estimation using neural networks. Proc. Inst. Mech. Eng. B **212**, 105–112 (1998)
3. Li, X.: A brief review: acoustic emission method for tool wear monitoring during turning. Int. J. Mach. Tool Manuf. **42**, 157–165 (2002)
4. Pandit, S.M., Kashou, S.: A data dependent systems strategy of on-line tool wear sensing. J. Eng. Ind. **104**, 217 (1982)
5. Liang, S.Y., Dornfeld, D.A.: Tool wear detection using time series analysis of acoustic emission. J. Eng. Ind. **111**, 199 (1989)
6. Jemielniak, K., Kossakowska, J., Urbanski, T.: Application of wavelet transform of acoustic emission and cutting force signals for tool condition monitoring in rough turning of Inconel 625. Proc. IMechE B J. Eng. Manuf. **225**, 123–129 (2011)
7. Roth, J.T., Pandit, S.M.: Monitoring end-mill wear and predicting tool failure using accelerometers. J. Manuf. Sci. Eng. **121**, 559 (1999)
8. Yao, Y., Fang, X.D.: Modelling of multivariate time series for tool wear estimation in finish-turning. Int. J. Mach. Tool Manuf. **32**(4), 495–508 (1992)
9. Sick, B.: Online and indirect tool wear monitoring in turning with artificial neural networks: a review of more than a decade of research. Mech. Syst. Signal Process. **16**(4), 487–546 (2002)
10. Rehorn, A.G., Jiang, J., Orban, P.E.: State-of-the-art methods and results in tool condition monitoring: a review. Int. J. Adv. Manuf. Technol. **26**, 693–710 (2005)
11. Oraby, S.E., Hayhurst, D.R.: Tool life determination based on the measurement of wear and tool force ratio variation. Int. J. Mach. Tool Manuf. **44**, 1261–1269 (2004)
12. Szecsi, T.: A DC motor based cutting tool condition monitoring system. J. Mater. Process. Technol. **92–93**, 350–354 (1999)
13. Danai, K., Ulsoy, A.G.: An adaptive observer for on-line tool wear estimation in turning. Part I: theory. Mech. Syst. Signal Process. **1**(2), 211–225 (1987)
14. Danai, K., Ulsoy, A.G.: An adaptive observer for on-line tool wear estimation in turning. Part II: results. Mech. Syst. Signal Process. **1**(2), 227–240 (1987)
15. Huang, S.N., Tan, K.K., Wong, Y.S., et al.: Tool wear detection and fault diagnosis based on cutting force monitoring. Int. J. Mach. Tool Manuf. **47**, 444–451 (2007)
16. Alonso, F.J., Salgado, D.R.: Analysis of the structure of vibration signals for tool wear detection. Mech. Syst. Signal Process. **22**, 735–748 (2008)
17. Kilundu, B., Dehombreux, P., Chiementin, X.: Tool wear monitoring by machine learning techniques and singular spectrum analysis. Mech. Syst. Signal Process. **25**, 400–415 (2011)
18. Aghdam, B.H., Vahdati, M., Sadeghi, M.H.: Vibration-based estimation of tool major flank wear in a turning process using ARMA models. Int. J. Adv. Manuf. Technol. **76**, 1631–1642 (2015)
19. Wang, X., Wang, W., Huang, Y., et al.: Design of neural network-based estimator for tool wear modelling in hard turning. J. Intell. Manuf. **19**, 383–396 (2008)
20. Aliustaoglu, C., Ertunc, H., Ocak, H.: Tool wear condition monitoring using a sensor fusion model based on fuzzy inference system. Mech. Syst. Signal Process. **23**, 539–546 (2009)
21. Purushothaman, S.: Tool wear monitoring using artificial neural network based on extended Kalman filter weight updation with transformed input patterns. J. Intell. Manuf. **21**, 717–730 (2010)
22. Sharma, V.S., Sharma, S.K., Sharma, A.K.: Cutting tool wear estimation for turning. J. Intell. Manuf. **19**, 99–108 (2008)
23. Srikant, R.R., Krishna, P.V., Rao, N.D.: Online tool wear prediction in wet machining using modified back propagation neural network. Proc. IMechE B J. Eng. Manuf. **225**, 1009 (2011)
24. Brezak, D., Majetic, D., et al.: Tool wear estimation using an analytic fuzzy classifier and support vector machine. J. Intell. Manuf. **23**, 797–809 (2012)
25. Penedo, F., Haber, R.E., Gajate, A., Del Toro, R.M.: Hybrid incremental modeling based on least squares and Fuzzy-NN for monitoring tool wear in turning processes. IEEE Trans. Ind. Inf. **8**(4), 811–818 (2012)
26. Siddhpura, A., Paurobally, R.: A review of flank wear prediction methods for tool condition monitoring in a turning process. Int. J. Adv. Manuf. Technol. **65**, 371–393 (2013)
27. Fassois, S.D., Sakellariou, J.S.: Time-series methods for fault detection and identification in vibrating structures. Phil. Trans. R. Soc. A **365**, 411–448 (2007)
28. Poulimenos, A.G., Fassois, S.D.: Output-only stochastic identification of a time-varying structure via functional series TARMA models. Mech. Syst. Signal Process. **23**, 1180–1204 (2009)
29. Aghdam, B.H., Cigeroglu, E., Sadeghi, M.H.: Output only functional series time dependent autoregressive moving average (FS-TARMA) modelling of tool acceleration signals for wear estimation. In: Proceedings of the 33rd IMAC, A Conference and Exposition on Structural Dynamics, Springer International Publishing, vol. 7, pp. 111–122 (2015)
30. Martin, R.J.: A metric for ARMA processes. IEEE Trans. Signal Process. **48**(4), 1164–1170 (2000)
31. Soderstrom, T., Stoica, P.: System Identification. Prentice Hall, Englewood Cliffs (1989)
32. Ljung, L.: System Identification: Theory for the User, 2nd edn. PTR Prentice Hall, Upper Saddle River (1999)
33. Grenier, Y.: Time-dependent ARMA modeling of nonstationary signals. IEEE Trans. Acoust. Speech Signal Process. **31**, 899–911 (1983)
34. Reddy, G.R.S., Rao, R.: Performance analysis of basis functions in TVAR model. Int. J. Signal Process. Image Process. Pattern Recognit. **7**(3), 317–338 (2014)